Stimulated Raman Scattering in Semiconductor Nanostructures

Felix Kroeger

THÈSE

présentée pour obtenir le grade de

DOCTEUR EN SCIENCES
DE L'UNIVERSITÉ PARIS-SUD XI ORSAY

par

Felix Kroeger

le 21 décembre 2010

Stimulated Raman Scattering in Semiconductor Nanostructures

Devant le jury :

M. Philippe Boucaud	Président du jury
M. Mehdi Alouini	Rapporteur
M. Alejandro Fainstein	Rapporteur
Mme. Cornelia Denz	
M. Nicolas Dubreuil	Directeur de thèse

to Katharina

Acknowledgements and thanks

I would like to express my thanks to Gérald Roosen for offering me to join his research group Manolia at the Laboratoire Charles Fabry de l'Institut d'Optique, Campus Polytechnique, in Palaiseau near Paris, to work for my PhD thesis. Over three years, he was my PhD supervisor, and he had great confidence in me and pushed my work into the right direction.

And of course many thanks to Nicolas Dubreuil, my second and, finally, official PhD supervisor, for all his support and the many fruitful and insightful discussions. He shared all the moments of disappointment and of success with me and never stopped encouraging me on my way. Certainly, I have met only very few researchers who express their passion for their work as vividly as he does.

I also wish to thank Alejandro Fainstein and Mehdi Alouini for accepting to be the rapporteurs (i.e., the official reviewers) of my PhD thesis. Reading and evaluating a PhD thesis takes a good lot of time, and I very much appreciate their willingness to do this. Also, thanks to Philippe Boucaud and Cornelia Denz for accepting to be part of the jury.

Thanks to the whole Manolia working group for the friendly and cooperative atmosphere, which I enjoyed every day at the Institut d'Optique. They had a lot of patience with my limited French speaking skills at the beginning, and they provided something so important for professional success : an environment in which it is a pleasure to work.

I also thank my family, in particular my parents, for all the support they gave me, even though they haven't seen me very often during the past years. And last but certainly not least, so many thanks to Katharina, for having been, and still being, such an important part of my life and for always thinking positive.

Contents

Chapter 1

Introduction

"If I have seen a little further, it is by standing on the shoulders of giants," remarked Isaac Newton in 1676 in a letter to his rival Robert Hooke. This famous citation applies even more to today's research than it did to Newton when he carried out his first optical experiments on the spectral analysis of sunlight. Since then, many "giants" have joined those that Isaac Newton, one of the first researchers devoting significant attention to the field of optics, could have had in mind. Two of these giants are particularly important for the context of the present PhD thesis : *nonlinear optics* and *semiconductors nanostructures*. One could indeed say that they are the "shoulders" on which the findings of this PhD thesis are built.

At the beginning of the twentieth century, Heinrich Hertz discovered and studied the nature of electromagnetic waves. His discovery and its successful application by Guglielmo Marconi gave rise to modern communication technology, which was an essential driver of the most important technological and societal developments of the past century. While electromagnetic waves have for long times mainly been used in the form of radio waves and microwaves, today, at the beginning of the twenty-first century, it is *light* that plays a key role in the development of the future communication and information technology. With all the progress in the domain of optoelectronics during the past decades, it has become relatively easy to represent and to transmit information in the form of optical signals (e.g., in optical fibers). However, for the processing of the optical signals, they are usually converted to electrical signals. This conversion limits the overall processing speed because current data streams require switching rates above 50 GHz, where electronic compontents start to reach their limits. Moreover, the conversion introduces coupling losses at every optoelectronic interface (i.e., in every optoelectronic component), which is one of the reasons why the switching devices usually show a high energy consumption.

In order to circumvent these limitations and to improve the energy efficiency of communication technology, the next great challenge is to find ways to *process* these *signals* with *purely optical* components, i.e., without the use of electronics. As it turns out, the most promising physical effects that allow for such a purely optical signal and information processing can be found in the domain of **nonlinear optics**, as is discussed in more detail below (see section 2.1). To be of practical use for the telecommunication industry, the optical functions that are realized by means of nonlinear optics have to be integrated into highly compact devices, approximately of the same small dimensions as current microelectronics or even smaller (i.e., on a sub-micrometer scale). Therefore, both public and private sector researchers currently make great efforts and try to build on the enormous technological progress and know-how regarding **semiconductor nanostructures** to make communication

components faster, smaller, and less energy consuming [1] through the use of nonlinear optical effects. Moreover, in order to keep the production costs of these devices comparable (and competitive) with the existing optoelectronic components, it is of great interest to use existing fabrication technologies for their production. Therefore, especially the material silicon (Si) and the CMOS technology, which are the basis of all microelectronic devices, have gained great interest, giving rise to a new research domain which has in recent years become widely known as *silicon photonics.*

Among the optical functions that have already been realized, there are, for example, waveguiding [2], light emitting [3, 4], and optical filters [5]. Various studies and successful demonstrations of modulation and switching have been reported [6], be it through the thermo-optic effect [7, 8], by electro-optical modulation [9, 10, 11], or by using an all-optical approach [4, 12]. High-speed modulation of wavelengths in the telecom band has been achieved with an extremely low switching energy of only a few 100 femtojoules [13]. Even an optical memory has been demonstrated [14].

Two of the most important and still challenging functions of optical information processing are the *amplification* of optical signals, as well as the realization of an integrated (laser) *light source*, which both require a sort of *optical gain.* Since silicon is an indirect band-gap semiconductor, it is not possible to obtain a significant optical gain by exploiting the electronic transitions of the material (as, for example, in the case of GaAs). It has, however, been demonstrated that light amplification is possible using silicon in the form of quantum dots dispersed in a silicon dioxide matrix [15]. Broadband optical gain in silicon, which is useful to process larger wavelength ranges (i.e., multiple WDM channels) at the same time, has been shown through the optical process of phase-matched four-wave mixing in suitably designed SOI channel waveguides [16].

Another approach is to use **stimulated Raman scattering** (SRS) as the key element of purely silicon-based optical amplifiers and light sources [17, 18]. By means of stimulated Raman scattering, it is possible to achieve an amplification of a weak optical signal due to an efficient transfer of optical energy from a strong pump light wave to the weak signal wave (see section 2.2). This amplification is a nonlinear optical interaction between the two waves in a so-called Raman-active medium (e.g., silicon or gallium arsenide). In its simplest form, it can be expressed as an exponential increase of the signal intensity I_S by

$$I_S(l) = I_S(0) \, \exp\left\{\gamma_R \, I_P \, l\right\} , \qquad (1.1)$$

where the material-dependent coefficient γ_R is the so-called Raman gain, I_P is the intensity of the pump wave, and l is the propagation distance. Thus, in order to obtain high amplifications, it is desirable to maximize the product in the argument of the exponential function. In the perspective of highly compact telecommunication devices, the interaction lengths should be as short as possible, and the choice of the material (determining the Raman gain) is mainly given by such criteria as the maturity of the fabrication technology and the compatibility with other components. Thus, the key to obtaining high Raman amplifications lies in achieving a *local enhancement* of the pump intensity.

A fairly simple way to locally increase the pump intensitiy is to focus the light with a lens on a small focal spot in the Raman-active nonlinear medium. However, a significant increase of the intensity is only achieved within the Rayleigh length, which is directly related to the desired diameter of the focal spot through the wavelength and the refractive index of the material. A highly focused beam has inevitably a short Rayleigh length, i.e., a short effective interaction length. This significantly limits the

maximum attainable product of intensity and length occurring in the above equation. A more sophisticated approach is to inject the pump beam into a highly confined sub-lambda waveguide, i.e., into a waveguide whose cross section is small compared to the wavelength of the light. These waveguides can have lengths of several millimeters or even centimeters so that this solution circumvents the disadvantages of simple focusing by confining the increased intensity of the light in the waveguide over its full length. It should be noted that both of the above methods represent only a *transverse* confinement of the light by reducing the effective area A_{eff} of the wave.

A far more effective localization of the light can be achieved by slowing down the propagation of the light waves in the nonlinear medium so that the photons are condensed in a smaller volume. This so-called **slow light** is expressed by a reduced group velocity v_{g}, which is characterized by the group refractive index n_{gr} through $v_{\text{g}} = c/n_{\text{gr}}$, where c is the vacuum speed of light. A very strong **light localization** can be reached by the combination of sub-lambda waveguides and slow light, which leads to the so-called **slow-mode waveguides**. These slow-mode waveguides are nanostructures that are usually fabricated in semiconductor materials. They can provide very small effective mode areas A_{eff} of below 1 μm^2. Therefore, their production requires a fabrication precision of only several nanometers, whereas the waveguide lengths can be as long as several centimeters. Such fabrication precisions have only become available in the past couple of years.

The highest group refractive indices (corresponding to the strongest slowing down of the light) can be achieved in **photonic crystal structures** that are specifically designed for this purpose. In photonic crystals, the guiding of the light is not achieved by means of total internal reflection, but by the guiding effect of periodically arranged scattering centers, such as regularly arranged holes in a semiconductor slab. Because of their promising capabilities, photonic crystal waveguides are currently extensively studied both experimentally and theoretically. One of the main challenges is to obtain waveguides that show only little dispersion [19, 20, 21, 22]. Starting point for a systematic investigation of the *nonlinear* optical effects in such semiconductor nanostructures were some works on the nonlinear characterization of photonic band-gap structures [23, 24, 25, 26]. Very recently, several demonstrations of the enhancement of optical nonlinearities in photonic crystal waveguides have been published [27, 28, 29, 30].

Another way to localize the pump intensity in a small volume is to place the nonlinear medium in a **high-finesse optical cavity** and to make the light waves resonant in this cavity. As a result, a significant increase of the intensity can be achieved inside the resonator (i.e., in the medium). In the context of the present work, this approach leads to the study of stimulated Raman scattering in **semiconductor microcavities** with very short resonator lengths, being of the order of only several wavelengths. Multiple successful realizations of microcavities (or nanocavities) with ultrahigh Q factors of the order of 10^5 to 10^6 have been reported [31, 32, 33, 34].

Of particular interest is the situation where both pump and Stokes beam are resonant in the microcavity at the same time. In this case, instead of considering the local increase of the pump intensity inside the nonlinear medium, one could also interpret the influence of the microcavity as an effective prolongation of the interaction length l in Eq. (1.1) because both waves, since they are both resonant in the cavity, propagate many times back and forth in the nonlinear medium. It is worth noting that, although stimulated Raman scattering (SRS) has already been studied in doubly resonant spherical and toroid microcavities made of *silica* [35], an enhancement of SRS in *semiconductor* nanostructures has never been experimentally

studied before, although such a configuration seems to be one of the most promising steps on the route towards an ultra-compact *Raman microlaser*.

The aim of the present PhD thesis is to study the influence of the light localization on different nonlinear optical effects, especially stimulated Raman scattering, in semiconductors nanostructures. It is essentially organized in three main chapters.

The first one (chapter 2) summarizes the most important aspects of nonlinear optics that are needed to understand and interpret the results that are presented in the remainder of this document. The main focus here lies on those nonlinear effects that play a major role in semiconductors. Besides stimulated Raman scattering, this includes the two photon absorption, the Kerr effect, and the free carrier effects (absorption and refraction). The chapter also includes a formal description of the effect of light localization, and it shows how the localization enhances the optical nonlinearities through the so-called local field factor. It closes with the presentation of a simple model that illustrates how the Raman amplification can be enhanced in a doubly resonant microcavity.

In the next chapter (chapter 3), an experimental study of stimulated Raman scattering in a silicon nanowaveguide (or nanowire) is presented. I have carried out a number of nonlinear pump-probe measurements of the Raman amplification of a narrow-band probe wave in a silicon-on-insulator (SOI) nanowire. The experimental results show very clearly that, for higher pump powers, the Raman amplification of the probe wave experiences a saturation, which corresponds to a decrease of the effective Raman gain. An analytical model is developed that takes into account the finite spectral width of picosecond pump pulses in order to describe the influence of spectral broadening on the effective Raman gain. It is demonstrated that the observed saturation is caused by the fact that the pump pulses undergo a self phase modulation that is induced by the Kerr effect and free carrier refraction. With the help of a linear characterization of the nanowire, the local field factor is determined to have a value of 1.2, which corresponds to a low level of light localization. The results of the pump-probe measurements, however, can also be applied to the case of highly localized light, which has some major implications for the realization of optical functions for the all-optical information processing. As a side effect of the experiments, the Raman gain coefficient of silicon is determined.

Finally, the last of the three main chapters (chapter 4) presents an experimental study of the enhancement of stimulated Raman scattering in a doubly resonant GaAs microcavity. As in the previous case, an analytical model is developed, which is then used to simulate the nonlinear pump-probe measurements that are presented afterwards. Although the experiments, which are described in detail, agree with the simulations in certain aspects, the time dependence of the data shows some totally unexpected features. These observations can be explained by the assumption that the relaxation dynamics of the electrons in the conduction band of GaAs is profoundly modified by the presence of a coherent population of Raman phonons. A hypothesis is formulated that describes how this interaction between electrons and coherent phonons effectively influences the electron relaxation and how it could lead to a prolongation of the phonon lifetime. A second set of pump-probe measurements confirms this hypothesis, which has, to our knowledge, never been reported before in the literature.

A summary at the end of this document restates the key results of the two experimental parts and provides an exciting outlook on the next steps that have to be made towards a more complete understanding of the interplay between the different nonlinear effects and their dependence on the light localization.

Chapter 2

Basics of nonlinear optics in semiconductor nanostructures

This chapter provides an overview of the basic concepts and the most important equations of nonlinear optics in semiconductors. After a brief summary of the key concepts of nonlinear optics, it describes the central effect of the present work, the stimulated Raman scattering. Moreover, it introduces several other (third-order) nonlinear optical effects that play a vital role in the experiments presented in the following chapters. Finally, it describes the possible enhancement of the optical nonlinearities due to light localization, which is also of central importance for the present work.

Contents

2.1 Key elements of nonlinear optics

In the following chapters, we study the optical response of semiconductor nanostructures (such as waveguides and microcavities) to strong light fields. This response shows several so-called nonlinear effects. The basic theory that allows us to understand the underlying physical processes is the **theory of nonlinear optics**, which we define, for our purposes, as the interaction between light and matter in the presence of strong electromagnetic waves in the visible or near infrared spectral range. This section 2.1 summarizes the key elements of nonlinear optics that we need for the following sections.

2.1.1 Basic concept of nonlinear optics

The basic idea of nonlinear optics is the following. Consider a dielectric material, composed of microscopic dipoles (atoms and electrons). One or several electromagnetic waves (usually monochromatic waves, e.g. laser beams) are incident upon the material, where they induce a polarization of the microscopic dipoles. The dipole moment per unit volume, or polarization $\vec{P}$, of the material depends on the electric field strength $\vec{E}$ of the incident waves. In the case of conventional (i.e., linear) optics, this relationship is linear

$$\vec{P} = \epsilon_0 \underline{\chi}^{(1)} \vec{E} \, ,$$

where ϵ_0 is the permittivity of free space, and $\underline{\chi}^{(1)}$ is known as the linear susceptibility tensor. Thus, the multiplication on the right-hand side of the above equation is actually a matrix product. In nonlinear optics, the optical response can often be described as a generalization of the above equation by expressing the polarization $\vec{P}$ as a power series of the incident electric field strengths $\vec{E}$,

$$
\begin{aligned}
\vec{P} &= \epsilon_0 \left(\underline{\chi}^{(1)} \, \vec{E} + \underline{\underline{\chi}}^{(2)} : \vec{E}\vec{E} + \underline{\underline{\underline{\chi}}}^{(3)} \vdots \vec{E}\vec{E}\vec{E} + \dots \right) \\
&= \underbrace{\epsilon_0 \underline{\chi}^{(1)} \, \vec{E}}_{\vec{P}^{(1)}} + \underbrace{\epsilon_0 \, \underline{\underline{\chi}}^{(2)} : \vec{E}\vec{E}}_{\vec{P}^{(2)}} + \underbrace{\epsilon_0 \, \underline{\underline{\underline{\chi}}}^{(3)} \vdots \vec{E}\vec{E}\vec{E}}_{\vec{P}^{(3)}} + \dots \\
&= \quad\;\; \vec{P}^{(1)} \quad + \quad\;\; \vec{P}^{(2)} \quad + \quad\;\; \vec{P}^{(3)} \quad + \dots \\
&= \quad\;\; \vec{P}^{\mathrm{L}} \quad + \qquad\qquad \vec{P}^{\mathrm{NL}}
\end{aligned}
\tag{2.1}
$$

where $\underline{\underline{\chi}}^{(2)}$ and $\underline{\underline{\underline{\chi}}}^{(3)}$ are the second- and third-order nonlinear susceptibilities and

$$\vec{P}^{\mathrm{L}} = \vec{P}^{(1)} \qquad \text{and} \qquad \vec{P}^{\mathrm{NL}} = \vec{P}^{(2)} + \vec{P}^{(3)} + \dots$$

denote the linear and the **nonlinear optical response** of the medium to the incident electromagnetic waves. The nonlinear polarization $\vec{P}^{\mathrm{NL}}$ is the sum of the second-order and the third-order polarizations (and all higher orders). The N-th-order nonlinear susceptibilities are tensors of the order $N + 1$ and the vertical dots in Eq. (2.1) symbolize tensor products with the electric field strengths.

It should be noted that the electric field strength occurs several times in these tensor products. So, if there are multiple incident waves (monochromatic, plane electromagnetic waves) with different frequencies, wave vectors, and polarization directions, these waves can be combined in different ways in the tensor products. Thus, depending on the number of incident waves, we find a variety of different nonlinear optical effects, some of which will be described in more detail in the following sections.

2.1.2 Nonlinear propagation equation

The polarization induced by the incident waves acts as a source term for the generation of another electromagnetic wave. Assuming an isotropic, homogeneous medium with a frequency-dependent refractive index $n = n(\omega)$, we can derive a differential equation that describes the relationship between the nonlinear polarization of the material and the electric field of the generated wave. The complete derivation, from Maxwell's equations to the propagation equation, can be found in numerous standard text books on nonlinear optics [36, 37]. Here, we simply present the key results.

In the Fourier domain (i.e., in the frequency space), the propagation of an electromagnetic wave (represented by the electric field strength $\vec{E}$) that is driven by the nonlinear polarization $\vec{P}^{\text{NL}}$ (which acts as the source term) is described by the differential equation

$$\nabla^2 \vec{E}(\vec{r}, \omega) + \frac{\omega^2 n(\omega)^2}{c^2} \vec{E}(\vec{r}, \omega) = -\frac{\omega^2}{c^2 \epsilon_0} \vec{P}^{\text{NL}}(\vec{r}, \omega) \,, \tag{2.2}$$

where c is the speed of light in free space. We assume that all waves propagate in the z direction and that the incident waves and the solutions of the above differential equation are **monochromatic electromagnetic waves** of the form

$$\vec{E}(z, t) = A(z)\, \hat{e}\, e^{i(kz - \omega t)} + \text{c.c.} \,, \tag{2.3}$$

where A is the amplitude of the electric field strength and where ω, k, and $\hat{e}$ are the angular frequency, the wave vector, and the polarization vector of the wave.[1] We can then derive the so-called **nonlinear propagation equation** for the field amplitudes, given by

$$\boxed{\frac{\partial A}{\partial z} = \frac{i\omega}{2n(\omega)c\epsilon_0} \vec{P}^{\text{NL}}(\omega) \cdot \hat{e}\, e^{-ikz}} \,. \tag{2.4}$$

The derivation of this important equation is essentially based on the so-called slowly varying envelope approximation (SVEA). It is demonstrated with all the details in the above-mentioned references. The nonlinear propagation equation (2.4) describes the evolution of the amplitude A (i.e., the envelope) of the generated electromagnetic wave during its propagation in the nonlinear optical material along the z direction. As can be seen from the equation, the change of the amplitude is proportional to the product of the imaginary unit i and the nonlinear polarization $\vec{P}^{\text{NL}}(\omega)$. The latter is, in general, a complex vector that can be decomposed into its real part and its imaginary part. The real part affects the phase of the generated electromagnetic wave, while the imaginary part changes the amplitude of the wave. This conclusion is very important for the understanding of the nonlinear effects that are presented in sections 2.2 and 2.3.

In order to solve the nonlinear propagation equation, we have to insert an expression for the nonlinear polarization $\vec{P}^{\text{NL}}(\omega)$, which depends on the particular nonlinear effect under consideration.

$\vec{E}$

A

$\omega, k, \hat{e}$

---

[1]*Remark:* In scientific reports such as PhD theses, it is practically unavoidable to introduce a large number of different symbols whose precise and sometimes subtle differences in meaning are essential to the understanding of the text. The present work is no exception to this rule. Thus, in order to reduce the possibly arising confusion between similar symbols (i.e., those that resemble one another) and to minimize searching for frequently referenced equations, the first appearances of the most important symbols are indicated in the margin of this document, thus facilitating the reading and the browsing through the text. In certain cases, instead of the *first* appearance, it is the *most meaningful* appearance that is shown in the margin.

2.1.3   Third-order nonlinear polarization

In the present work, we mainly study nonlinear effects of the third order. Therefore, the third-order nonlinear polarization $\vec{P}^{(3)}$ is of particular importance here, as is explained in more detail below. A formal and technical derivation [37] yields the **general form of the third-order nonlinear polarization**[2]

$$\vec{P}^{\mathrm{NL}}(\omega) = D^{(3)}\,\epsilon_0\,\underline{\underline{\chi}}^{(3)}(\omega;\omega_1,\omega_2,\omega_3)\vdots\vec{E}(\omega_1)\vec{E}(\omega_2)\vec{E}(\omega_3) \tag{2.5}$$

where the factor $D^{(3)}$ is the so-called third-order degeneracy factor, which can have three possible values, depending on the number of (in)distinguishable incident electric fields [37]:

$D^{(3)}$

$$
\begin{aligned}
D^{(3)} &= 1 \quad \text{if} \quad \text{all three fields are indistinguishable} \\
&= 3 \quad \text{if} \quad \text{two fields are distinguishable} \\
&= 6 \quad \text{if} \quad \text{all three fields are distinguishable .}
\end{aligned}
$$

Equation (2.5) also contains the so-called **third-order nonlinear susceptibility** at the frequency ω

$\underline{\underline{\chi}}^{(3)}$

$$\underline{\underline{\chi}}^{(3)}(\omega;\omega_1,\omega_2,\omega_3) \;,$$

which is, as mentioned in section 2.1.1, a fourth-order tensor. The four arguments of the third-order nonlinear susceptibility indicate that the sum of the three frequencies behind the semicolon gives the frequency before the semicolon

$$\omega = \omega_1 + \omega_2 + \omega_3 \;.$$

Therefore, it is actually not necessary to write the first argument explicitly (i.e., the one before the semicolon), but we use this notation because it is a widely used convention. Equation (2.5) can also be expressed for one single component of the nonlinear polarization as

$$P_i^{\mathrm{NL}}(\omega) = D^{(3)}\,\epsilon_0 \sum_{jkl} \chi^{(3)}_{ijkl}(\omega;\omega_1,\omega_2,\omega_3)E_j(\omega_1)E_k(\omega_2)E_l(\omega_3) \;.$$

The electric fields $\vec{E}(\omega)$ are the Fourier amplitudes of the three incident electromagnetic waves at the frequencies ω_1, ω_2, and ω_3. They are implicitly defined by

$$\vec{E}(z,t) = \vec{E}(\omega)\,e^{-i\omega t}\;+\;\text{c.c.} \;. \tag{2.6}$$

and can be explicitly written as

$$\vec{E}(\omega) = A\,\hat{e}\,e^{ikz} \;. \tag{2.7}$$

In the next sections 2.2 and 2.3 we present several nonlinear optical effects and their corresponding expressions of the nonlinear polarization $\vec{P}^{\mathrm{NL}}(\omega)$. These expressions are then used to solve the nonlinear propagation equation (2.4).

---

[2]*Remark:* As is common for scientific reports, the present PhD thesis contains numerous equations, calculations, and conclusions. To improve the readability of this document, the reader will find important equations framed in oval boxes (i.e., boxes with rounded edges), while numerical results as well as logical conclusions are framed in boxes with sharp edges (see the following chapters).

2.2 Raman scattering and Raman amplification

The central effect that is studied in the present work is the so-called **Raman scattering**. This section 2.2 therefore introduces the Raman scattering and explains the fundamental physics behind it. The section comprises three subsection, covering the spontaneous Raman scattering, the stimulated Raman scattering (SRS), and a particular application of the SRS, the Raman amplification. In order to focus on the physical understanding and not only on the equations, we approach these subjects by simple classical models, which are then refined using more rigorous theoretical approaches.

2.2.1 Spontaneous Raman scattering

Among the various interactions between light and matter is the so-called **spontaneous Raman scattering**, named after its discoverer, Chandrasekhra Venkata Raman, who first experimentally demonstrated this "new type of secondary radiation" in 1928 [38].

Observation of Stokes and Anti-Stokes scattering

Consider a liquid or a gas, composed of molecules, and an incident light wave at a frequency ω_L. The light is scattered by the molecules and is emitted isotropically in all directions. A spectral analysis of the scattered light shows essentially the elastic scattering of the incident light wave, i.e., a strong spectral line at the frequency ω_L of the incident light (Rayleigh scattering). However, there are also some other spectral components whose intensities are usually several orders of magnitude weaker than the Rayleigh peak. Some of these new spectral lines have frequencies lower than the frequency of the incident light (the so-called **Stokes** lines), and some of them have frequencies which are higher than the incident frequency (the so-called **Anti-Stokes** lines). In other words, part of the scattered light loses some energy during the scattering process (Stokes), the other part gains energy (Anti-Stokes). Figures 2.1(a) and 2.1(b) illustrate a Raman scattering experiment and the resulting spectrum. The frequency differences between the incident wave and the new spectral lines are independent of the incident frequency ω_L. They are characteristic of the material in which the scattering occurs. The exact values of these frequency shifts depend on the chemical composition and on the structure of the molecules (more precisely, on the spectrum of rotational-vibrational eigenstates of the molecules, which itself depends on the composition and on the geometry). The same effect is observed with solids. In that case, the incident light does not interact with the vibrational eigenstates of single molecules but with the whole crystal lattice of the solid. Therefore, the crystal has to possess optical phonon branches, which allow for dipole interactions with the incident electromagnetic wave. Since the present work presents a study of semiconductor materials, we will in the following mainly consider solids rather than molecules.

The process of Raman scattering can be explained with the energy diagram that is depicted in Figure 2.1(c). Here, we consider only the simple case of one Stokes wave and one Anti-Stokes wave. The Stokes wave is generated by the annihilation of an incident photon at the frequency ω_L and the creation of a photon at the Stokes frequency ω_S. At the same time, a phonon at the Raman frequency Ω_R is created so that after the interaction, the material is in an excited state. In terms of energy, this scattering process can be expressed as $\hbar\omega_S = \hbar\omega_L - \hbar\Omega_R$. Conversely, the Anti-Stokes wave corresponds to the simultaneous annihilation of an incident photon at
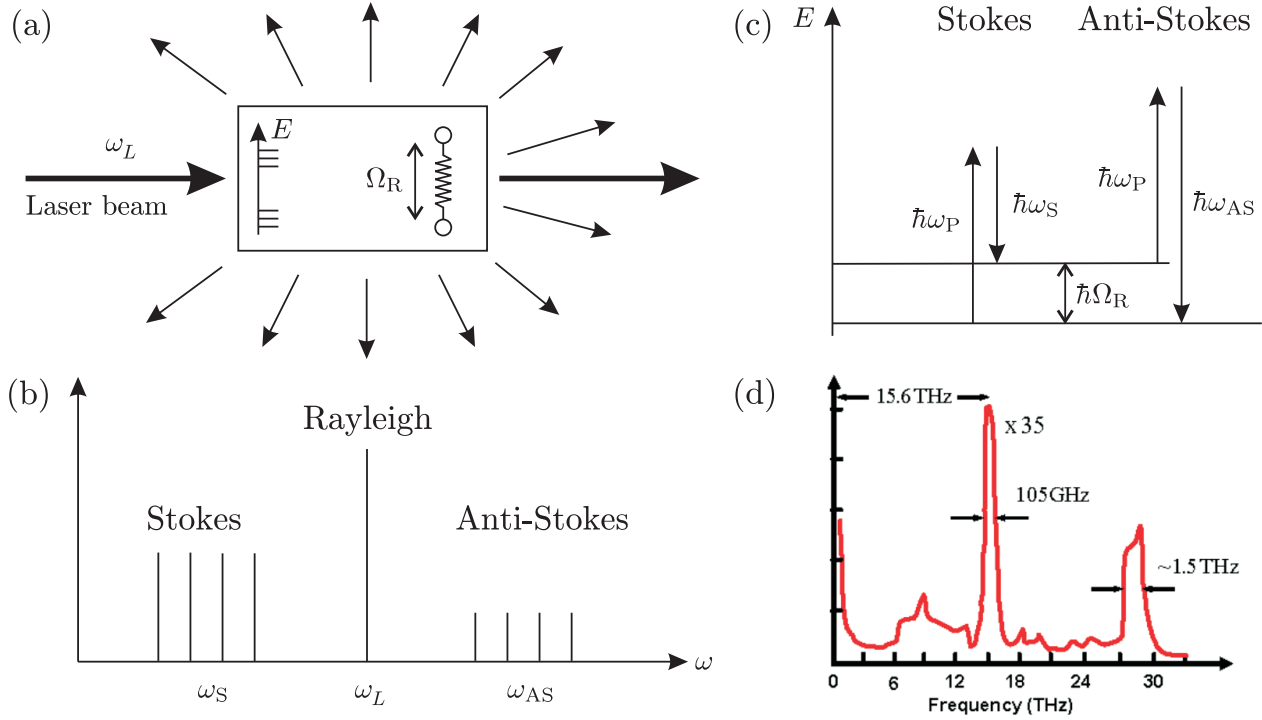
Fig. 2.1. Spontaneous Raman scattering. (a) An incident monochromatic light wave (e.g. laser beam) is scattered by molecules or by the crystal lattice of a solid that possess a spectrum of rotational-vibrational eigenstates. The scattered light is emitted isotropically. (b) In the spectrum, there are new components whose energies (i.e., frequencies) are higher and lower than the energy of the incident light. The components with less energy than the incident wave are called Stokes waves, whereas those with more energy are called Anti-Stokes waves. (c) They correspond to the transitions between the vibrational eigenstates of the material. Real crystals have more complex Raman spectra with multiple Raman resonances. In the spectrum of Si shown in (d), there are two peaks, the first of which is at a frequency of 15.6 THz [39].

ω_L and a phonon with Ω_R, leading to the creation of a photon at the Anti-Stokes frequency ω_{AS}. Energetically speaking, this is described by $\hbar\omega_{AS} = \hbar\omega_L + \hbar\Omega_R$. So, the Anti-Stokes scattering is the de-excitation (decay) of a previously exited state of the material. It should be noted that there is no electronic resonance of the material involved in this process.

As is known from solid state physics, the higher the temperature of a crystal is, the more excited phonon states of the crystal are populated. Therefore, the probability of Anti-Stokes scattering compared to the probability of Stokes scattering is given by the Boltzmann function $\exp\{-(\hbar\Omega_R)/(k_B T)\}$. With the relationship $\hbar\Omega_R \gg k_B T$, which is valid at room temperature, the Raman scattering is dominated by the Stokes waves. Because of the complex structure of molecules and crystals, there are usually many possible transitions, each of which corresponds to a different phonon mode with its own phonon energy. Figure 2.1(d) shows the first two Raman resonances of silicon [39]. Since the Raman transitions usually correspond to mid-infrared or far-infrared frequencies, the energies of the involved phonons are much smaller than the energies of the interacting light waves

$$\hbar\Omega_R \ll \hbar\omega_L, \hbar\omega_S, \hbar\omega_{AS} \qquad \Longleftrightarrow \qquad \Omega_R \ll \omega_L, \omega_S, \omega_{AS} \,,$$

which is thus also valid for the involved frequencies, as the above equation shows.

Classical model of a Raman oscillator

A simple classical interpretation of the Raman scattering process can be given by describing the modulation of the polarizability of a simple dipole (e.g., a diatomic

molecule). Consider two atoms which are bound by a spring of length q_0. The displacement of this oscillator from its equilibrium position can be expressed as

$$q(t) = \hat{q}\cos(\Omega_R t) \tag{2.8}$$

where Ω_R is the eigenfrequency (i.e., the Raman frequency) of the system. We assume that the optical polarizability of the dipole (which is typically predominantly electronic in origin) is not constant, but depends on the displacement q according to the equation

$$\alpha(q) = \alpha_0 + \left(\frac{\partial\alpha}{\partial q}\right)_0 q + \ldots \tag{2.9}$$

where α_0 is the polarizability at equilibrium and $(\partial\alpha/\partial q)_0$ represents the first term in a Taylor series expansion of the polarizability in terms of the displacement q. Inserting Eq. (2.8) into Eq. (2.9) yields

$$\alpha(t) = \alpha_0 + \left(\frac{\partial\alpha}{\partial q}\right)_0 \hat{q}\cos(\Omega_R t) + \ldots \ .$$

Consider a monochromatic electromagnetic wave, e.g. a laser beam at the frequency ω_L, that is incident upon the dipole. Thus, the dipole is excited by an oscillating electric field

$$E(t) = \hat{E}\cos(\omega_L t)$$

which induces a dipole moment that is given by

$$
\begin{aligned}
p(t) &= \alpha(t)\,E(t) = \left[\alpha_0 + \left(\frac{\partial\alpha}{\partial q}\right)_0 \hat{q}\cos(\Omega_R t)\right]\hat{E}\cos(\omega_L t) \\[2mm]
&= \alpha_0\hat{E}\cos(\omega_L t) + \left(\frac{\partial\alpha}{\partial q}\right)_0 \hat{q}\hat{E}\frac{1}{2}\left(\cos\left(\Omega_R t - \omega_L t\right) + \cos\left(\Omega_R t + \omega_L t\right)\right) \\[2mm]
&= \underbrace{\alpha_0\hat{E}\cos(\omega_L t)}_{\text{incident wave}} + \underbrace{\frac{1}{2}\left(\frac{\partial\alpha}{\partial q}\right)_0 \hat{q}\hat{E}\cos(\omega_S t)}_{\text{Stokes wave}} + \underbrace{\frac{1}{2}\frac{\partial\alpha}{\partial q'}\hat{q}'\hat{E}\cos(\omega_{AS} t)}_{\text{Anti-Stokes wave}} \ .
\end{aligned}
\tag{2.10}
$$

Thus, the dipole oscillates not only at the incident frequency ω_L, but also at the **Stokes frequency** ω_S and the **Anti-Stokes frequency** ω_{AS}, given by

$$\boxed{\omega_S = \omega_P - \Omega_R} \qquad \text{and} \qquad \boxed{\omega_{AS} = \omega_P + \Omega_R}, \tag{2.11}$$

ω_S, ω_{AS}

which correspond to the Stokes and the Anti-Stokes waves with a vibrational eigenfrequency Ω_R. As this simple model shows, the Raman scattering has its origins in the fluctuations of the polarizability of the material under study.

Ω_R

2.2.2 Stimulated Raman scattering (SRS)

We consider again the situation described in the previous section. But this time, we suppose that there are two light waves incident upon the dipole (or solid, respectively): a powerful laser beam with a given frequency ω_P, the so-called **pump beam** (or pump wave), and another beam at the Stokes frequency ω_S, which we call the **Stokes beam** (or Stokes wave). In other words, the situation is similar to the spontaneous Raman scattering, except that both the initial laser beam and the Stokes wave are incident upon the medium [40]. Unlike in the case of spontaneous Raman scattering, here the Stokes wave is a laser beam and thus has a well-defined

Fig. 2.2. Stimulated Raman scattering (SRS). (a) In the case of stimulated Raman scattering there are two incident light waves whose difference in frequency corresponds exactly to the Raman frequency: $\omega_P - \omega_S = \Omega_R$. (b) Thus, the energy difference between the two waves equals the energetic difference between two vibrational eigenstates of the material.
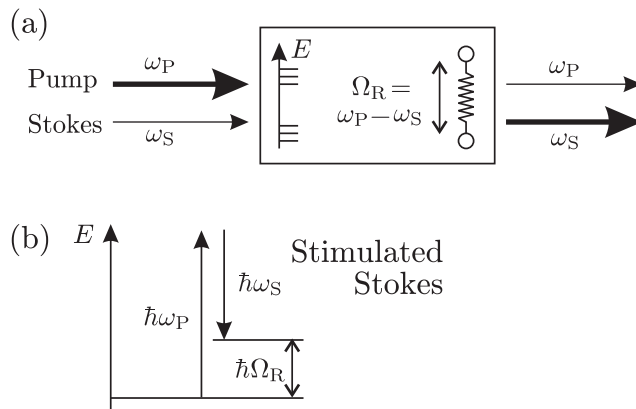
propagation direction. In this situation, which is depicted in Fig. 2.2, the Stokes scattering can be stimulated, and therefore this process is called the **stimulated Raman scattering (SRS)**.

Since SRS is the central subject of the present work, it is introduced in this section in three steps. In a first subsection, we present a classical model of a simple stimulated Raman oscillator, in order to describe the physical origin of the SRS. This leads to the fundamental notion of the Raman susceptibility, whose key properties are discussed in a second subsection. After these phenomenological considerations, we derive in a third subsection a more systematic approach to describe the nonlinear Raman polarization.

Classical description of stimulated Raman scattering

As in the case of the spontaneous Raman scattering, we can describe the stimulated Raman scattering with a simple classical model [36]. This simple description yields some valuable insight in the underlying processes and into the properties of the central material constant describing the Raman scattering, the so-called Raman susceptibility. The complete derivation of the classical model of SRS is presented in appendix A. Here, we only summarize the most important points.

As in the case of spontaneous Raman scattering, we consider a two-atom molecule with an vibrational eigen-frequency Ω_R. The molecule can be described by the equation of motion of a driven harmonic oscillator of the form

$$\frac{d^2}{dt^2} q + 2\Gamma \frac{d}{dt} q + \Omega_R^2 q = \frac{F(t)}{m} \tag{2.12}$$

where q is the displacement of the oscillator from its equilibrium position, Γ is a damping constant, m is the mass of the oscillator, and $F(t)$ is a time-dependent driving force. As is shown in the complete derivation in appendix A, the driving force can be expressed in terms of the amplitudes and oscillatory parts of the two incident electromagnetic waves. As a result, we obtain an expression for the time-varying part at the beat frequency $\omega_P - \omega_S$, given by

$$F(t) = \left(\frac{\partial \alpha}{\partial q}\right)_0 \left[A_P A_S^* e^{i(Kz - \Omega t)} + \text{c.c.}\right], \tag{2.13}$$

where we have introduced the notation

K, Ω $$K = k_P - k_S \qquad \text{and} \qquad \Omega = \omega_P - \omega_S . \tag{2.14}$$

By inserting Eq. (2.13) into the equation of motion (2.12), we obtain an oscillating solution for the displacement of the molecule,

$$q = q(\Omega)\, e^{i(Kz-\Omega t)}\; +\; \text{c.c.}\;, \tag{2.15}$$

where the amplitude of the molecular vibration is given by

$$q(\Omega) = \frac{(1/m)\,(\partial\alpha/\partial q)_0}{\Omega_R^2 - \Omega^2 - 2i\Omega\Gamma}\, A_P A_S^*\;. \tag{2.16}$$

With Eqs. (2.15) and (2.16) we have found a solution to the equation of motion of our model oscillator, i.e., a single molecule. In order to describe a medium such as a gas or a liquid, we want to calculate the dipole moment per unit volume, or polarization P, of the medium. With the particle density N, the polarization of the material is given by

$$P(z,t) \;=\; N\,p(z,t) \;=\; N\left[\alpha_0 + \left(\frac{\partial\alpha}{\partial q}\right)_0 q(z,t)\right] E(z,t)\;.$$

By expanding all the parentheses in the above equation, we find an expression for the nonlinear response of the material at the Stokes frequency ω_S, given by

$$P_S^{NL}(z,t) = P^{NL}(\omega_S)\, e^{-i\omega_S t}\; +\; \text{c.c.}\;, \tag{2.17}$$

where the complex amplitude of the **nonlinear Stokes polarization** can then be written as

$$P^{NL}(\omega_S) = 6\,\epsilon_0\,\chi_R(\omega_S)\,|A_P|^2\, A_S\, e^{ik_S z}\;, \tag{2.18}$$

and the so-called **Raman susceptibility** is defined as

$$\chi_R(\omega_S) \;=\; \frac{1}{6\epsilon_0}\frac{(N/m)\,(\partial\alpha/\partial q)_0^2}{\Omega_R^2 - \Omega^2 + 2i\Omega\Gamma} \;=\; \frac{Q_0}{\Omega_R^2 - \Omega^2 + 2i\Omega\Gamma}\;. \tag{2.19}$$

$\chi_R(\omega_S)$

For the sake of convenience, we have summarized several material dependent quantities as $Q_0 = (N/6\,m\,\epsilon_0)\,(\partial\alpha/\partial q)_0^2 \in \mathbb{R}$. The above expressions for the nonlinear Stokes polarization and the Raman susceptibility are those that we need to know in order to solve the nonlinear propagation equation (2.4). The ϵ_0 in Eq. (2.18) has been introduced to keep the result of our simple classical model consistent with the meaning of the susceptibility as it has been introduced in section 2.1. The factor 6 is the so-called degeneracy factor, which is properly introduced and explained below.

Raman susceptibility

The Raman susceptibility given by Eq. (2.19) is a **material constant** that describes the stimulated Raman scattering. It should be noted that it is a **complex number**, which depends on the difference frequency, or beat frequency, between the two incident waves $\Omega = \omega_P - \omega_S$. If this difference frequency is exactly equal to the vibrational eigenfrequency, $\Omega = \Omega_R$, the susceptibility is purely negative imaginary,

$$\bar{\chi}_R \;=\; \chi_R(\omega_S = \omega_P - \Omega_R) \;=\; \frac{Q_0}{2\,i\,\Omega_R\Gamma} \;=\; -\,i\,\frac{Q_0}{2\,\Omega_R\Gamma}\;, \tag{2.20}$$

$\bar{\chi}_R$

and it thus represents an amplification of the Stokes wave during its propagation along the z direction, as we shall see in section 2.2.3.

If the frequencies of the incident electromagnetic waves are detuned from the Raman frequency, $\Omega \neq \Omega_R$, the Raman susceptibility has a non-vanishing real part so that we can decompose it into its real part and its imaginary part as

$$\chi_R(\omega_S) = \chi'_R(\omega_S) + i\,\chi''_R(\omega_S) \;. \tag{2.21}$$

As can be clearly seen from Eq. (2.18), the nonlinear Stokes polarization $P^{NL}(\omega_S)$ is proportional to the Raman susceptibility, and it is consequently also a *complex* quantity. Because of the proportionality, the imaginary part of the Raman susceptibility affects the amplitude of the Stokes wave, whereas the real part introduces a phase shift (see also discussion in section 2.1.2).

By multiplying the definition of the Raman susceptibility given by Eq. (2.19) with the complex conjugate of its denominator, we find an explicit expression for the decomposition of the Raman susceptibility, given by

$$\chi_R(\omega_S) = \frac{Q_0}{2\,\Omega\,\Gamma} \left(\frac{\Delta}{1+\Delta^2} - \frac{i}{1+\Delta^2} \right) \;, \tag{2.22}$$

where the parameter Δ is defined as

$$\Delta = \frac{\Omega_R^2 - \Omega^2}{2\,\Omega\,\Gamma} \;. \tag{2.23}$$

Figure 2.3 shows the real and the imaginary part of the Raman susceptibility as a function of the difference frequency $\Omega = \omega_P - \omega_S$. As can be seen from the graph, the imaginary part of the Raman susceptibility has a resonant lineshape. The center of the resonance curve is at $\Omega = \Omega_R$ and its full width at half maximum (FWHM) is given by $\delta\Omega_R$.

Near the Raman resonance (i.e., for $\Omega = \omega_P - \omega_S \approx \Omega_R$) we define the detuning of the pump wave from the Raman resonance for a given (and fixed) Stokes frequency ω_S as

$$\Delta\omega_P = \Omega - \Omega_R = \omega_P - \omega_S - \Omega_R = \omega_P - (\omega_S + \Omega_R) \;, \tag{2.24}$$

so that we can approximate the Δ parameter as

$$\Delta = \frac{(\Omega_R - \Omega)(\Omega_R + \Omega)}{2\,\Omega\,\Gamma} \;\approx\; \frac{(\Omega_R - \Omega)\,2\Omega_R}{2\Omega_R\Gamma} = \frac{\Omega_R - \Omega}{\Gamma} = -\frac{\Delta\omega_P}{\Gamma} \;. \tag{2.25}$$

Therefore, the Raman susceptibility can be approximated near the Raman resonance as

$$\chi_R(\omega_S) \approx -\frac{Q_0}{2\Omega_R} \left(\frac{\Delta\omega_P}{\Delta\omega_P^2 - \Gamma^2} + i\,\frac{\Gamma}{\Delta\omega_P^2 - \Gamma^2} \right) \;. \tag{2.26}$$

Fig. 2.3.   Real part $\chi'_R(\omega_S)$ and imaginary part $\chi''_R(\omega_S)$ of the Raman susceptibility as a function of the difference frequency $\Omega = \omega_P - \omega_S$. As can be seen from the curves, the susceptibility shows a resonance for $\omega_S = \omega_P - \Omega_R$ that has a full width at half maximum of $\delta\Omega_R$. At resonance it is purely negative imaginary.
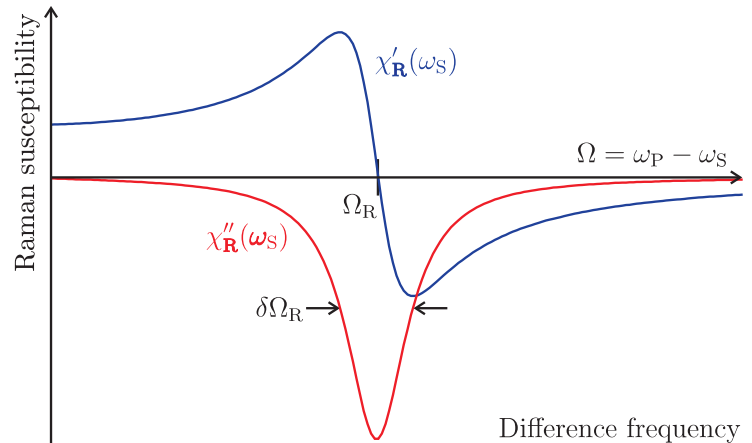
As can be seen from this representation, the Raman resonance (i.e., the imaginary part of χ_R) is approximately a Lorentzian function whose **full width at half maximum (FWHM)** is given by

$$\delta\Omega_\mathrm{R} = 2\,\Gamma\;.$$

Therefore, the Δ parameter given by Eq. (2.25) simply corresponds to the normalized detuning of the pump frequency from the Raman resonance (i.e., in units of the half width at half maximum of the resonance given by $\Gamma = \delta\Omega_\mathrm{R}/2$). Hence, in the vicinity of the Raman resonance we can express the **dimensionless detuning parameter** as

$$\Delta \;\approx\; -\frac{\Delta\omega_\mathrm{P}}{\delta\Omega_\mathrm{R}/2} \;=\; -2\,\frac{\Delta\omega_\mathrm{P}}{\delta\Omega_\mathrm{R}} \;=\; -2\,\frac{\Delta\nu_\mathrm{P}}{\delta\nu_\mathrm{R}}\;, \qquad (2.27)$$

where we have inserted the relationship $\omega = 2\pi\nu$ between angular frequency ω and frequency ν. Thus, the Raman linewidth can be given either in the *frequency* or in the *angular frequency* domain, related by $\delta\nu_\mathrm{R} = \delta\Omega_\mathrm{R}/2\pi$.

Third-order nonlinear polarization of stimulated Raman scattering

The above two subsections have described the physical origin of stimulated Raman scattering as well as the properties of the material constant describing this effect, the Raman susceptibility. Here we present a more systematic approach that follows the theoretical framework given in the introductory section 2.1. This systematic approach is also used in the next section 2.3 where we introduce several other nonlinear effects.

We can interpret the stimulated Raman scattering (SRS) as the interaction between two input waves and two output waves through the nonlinear Raman susceptibility of the material. In this sense, it is a four-wave interaction and can be theoretically described as a third-order nonlinear optical effect. In the stimulated scattering process, a Stokes wave with the frequency ω_S is created by the interaction of three waves at the frequencies ω_P, $-\omega_\mathrm{P}$, and ω_S so that the sum of the three frequencies is

$$\omega_\mathrm{S} = \omega_\mathrm{P} - \omega_\mathrm{P} + \omega_\mathrm{S}\;.$$

All three interacting waves are distinguishable, and therefore the degeneracy factor is

$$D^{(3)} = 6 \qquad \text{for SRS,} \qquad (2.28)$$

which is the reason why we have introduced this factor 6 in our derivation of the classical model in Eq. (2.19). As has been shown by Eq. (2.7), we can write the non-oscillating parts (i.e., the Fourier amplitudes) of the electric fields as

$$\vec{E}(\omega_\mathrm{P}) = A_\mathrm{P}\,\hat{e}_\mathrm{P}\,e^{ik_\mathrm{P}z} \qquad \text{and} \qquad \vec{E}(\omega_\mathrm{S}) = A_\mathrm{S}\,\hat{e}_\mathrm{S}\,e^{ik_\mathrm{S}z}\;. \qquad (2.29)$$

By inserting Eqs. (2.28) and (2.29) into the general form of the nonlinear polarization given by Eq. (2.5), we obtain the third-order nonlinear polarization at the Stokes frequency

$$\vec{P}^\mathrm{NL}(\omega_\mathrm{S}) = 6\,\epsilon_0\left(\underline{\underline{\chi}}^{(3)}(\omega_\mathrm{S};\omega_\mathrm{P},-\omega_\mathrm{P},\omega_\mathrm{S})\vdots\hat{e}_\mathrm{P}\hat{e}_\mathrm{P}\hat{e}_\mathrm{S}\right)|A_\mathrm{P}|^2 A_\mathrm{S}\,e^{ik_\mathrm{S}z}\;, \qquad (2.30)$$

which is similar to the result of our classical model given by Eq. (2.18), except that instead of the Raman susceptibility, there is now a complicated tensor product including the third-order nonlinear susceptibility and the polarization vectors of the incident waves. It should be noted that, in general, this tensor product contains

contributions from all possible third-order nonlinear optical effects that are induced by the pump wave on the Stokes wave. The stimulated Raman scattering, whose particularity is that it shows a resonance for $\omega_P - \omega_S = \Omega_R$, is only one of these effects. The nonlinear polarization in Eq. (2.30) can therefore be decomposed into

$$\vec{P}^{\mathrm{NL}}(\omega_S) = \vec{P}_R^{\mathrm{NL}}(\omega_S) + \vec{P}_{NR}^{\mathrm{NL}}(\omega_S) , \qquad (2.31)$$

where the index "R" denotes the Raman contribution and "NR" stands for the non-Raman components. The latter are described in detail in section 2.3. Here, we are only interested in the Raman component of the third-order nonlinear polarization

$\vec{P}_R^{\mathrm{NL}}(\omega_S)$

$$\vec{P}_R^{\mathrm{NL}}(\omega_S) = 6\,\epsilon_0 \left[\underline{\underline{\chi}}^{(3)}(\omega_S; \omega_P, -\omega_P, \omega_S) \vdots \hat{e}_P \hat{e}_P \hat{e}_S \right]_R |A_P|^2 A_S\, e^{ik_S z} . \qquad (2.32)$$

We insert the above expression (2.32) into the nonlinear propagation equation for the Stokes wave, which is given by Eq. (2.4) as

$$\frac{\partial A_S}{\partial z} = \frac{i\omega_S}{2 n_S c \epsilon_0}\, \vec{P}_R^{\mathrm{NL}}(\omega_S) \cdot \hat{e}_S\, e^{-ik_S z} , \qquad (2.33)$$

where $n_S = n(\omega_S)$ is the index of refraction of the material at the frequency of the Stokes wave, and obtain

$$\begin{aligned}
\frac{\partial A_S}{\partial z} &= \frac{i\omega_S}{2 n_S c \epsilon_0} \left(6\,\epsilon_0 \left[\underline{\underline{\chi}}^{(3)}(\omega_S; \omega_P, -\omega_P, \omega_S) \vdots \hat{e}_P \hat{e}_P \hat{e}_S \right]_R |A_P|^2 A_S\, e^{ik_S z} \right) \cdot \hat{e}_S\, e^{-ik_S z} \\
&= \frac{3 i \omega_S}{n_S c} \underbrace{\left(\left[\underline{\underline{\chi}}^{(3)}(\omega_S; \omega_P, -\omega_P, \omega_S) \vdots \hat{e}_P \hat{e}_P \hat{e}_S \right]_R \cdot \hat{e}_S \right)}_{\chi_R^{(3)}(\omega_S)} |A_P|^2 A_S . \qquad (2.34)
\end{aligned}$$

Here we have introduced the **Raman susceptibility** as

$\chi_R^{(3)}(\omega_S)$

$$\chi_R^{(3)}(\omega_S) = \left(\left[\underline{\underline{\chi}}^{(3)}(\omega_S; \omega_P, -\omega_P, \omega_S) \vdots \hat{e}_P \hat{e}_P \hat{e}_S \right]_R \cdot \hat{e}_S \right) \quad \in \mathbb{C} . \qquad (2.35)$$

This tensorial definition of the Raman susceptibility can be considered as the general and physically correct form of the expression that was given in the context of the classical model of stimulated Raman scattering by Eq. (2.19). As already stated above, the **Raman susceptibility** is a complex number (i.e., a scalar) that **depends on** the properties of **the nonlinear material** under study **and on the frequencies** of the incident electromagnetic waves.

   It is worth noting here that the two exponential functions in the first line of Eq. (2.34) cancel each other for all possible choices of k_P and k_S, no matter what material is considered. Therefore, the phase matching condition

$$\Delta k = (k_S - k_S) \equiv 0 \qquad \Longrightarrow \qquad e^{i\,\Delta k\, z} \equiv 1 \qquad (2.36)$$

is automatically fulfilled in the case of stimulated Raman scattering.

While the classical model presented above describes a simple two-atom molecule, the general definition given here applies to the oscillations in a three-dimensional multibody system with many degrees of freedom (e.g., a crystal), which therefore strongly depend on the crystallographic structure of the material (e.g., on the symmetry class). Consequently, as can be seen from Eq. (2.35), this general form of the Raman susceptibility $\chi_R^{(3)}(\omega_S)$ **also depends on the polarization states** of

the pump and the probe waves with respect to the crystallographic orientation of the material. Because of the high complexity of these multiple dependencies, it is often desirable to separate the polarization-state dependence from the influence of the frequencies and the material properties. Depending on the symmetry class of the solid under study (here the semiconductor material), this separation is often possible and can be expressed in the form

$$\chi_R^{(3)}(\omega_S) = \Sigma \, \chi_R(\omega_S) \, . \tag{2.37}$$

The resonance-like behavior of the Raman scattering is thus included in the Raman susceptibility $\chi_R(\omega_S)$ as given by Eq. (2.19), whereas the dependence on the polarization states of the two incident beams is expressed by the coefficient Σ. The latter is proportional to the spontaneous Raman scattering efficiency, and in the case of Si and GaAs, it can be calculated by [41]

$$\Sigma = \sum_{l=1}^{3} \left[\hat{e}_P \, R^l \, \hat{e}_S \right]^2 \, , \tag{2.38}$$

Σ

where the $\hat{e}_P$ and $\hat{e}_S$ are the polarization vectors of pump and Stokes wave (in the crystallographic coordinate system) and the R^l matrices are defined by

$$R^1 = \begin{pmatrix} 0 & 1 & 0 \\ 1 & 0 & 0 \\ 0 & 0 & 0 \end{pmatrix} \quad R^2 = \begin{pmatrix} 0 & 0 & 1 \\ 0 & 0 & 0 \\ 1 & 0 & 0 \end{pmatrix} \quad R^3 = \begin{pmatrix} 0 & 0 & 0 \\ 0 & 0 & 1 \\ 0 & 1 & 0 \end{pmatrix} \, . \tag{2.39}$$

For a given choice of pump and Stokes polarization, the maximum attainable value of the scattering efficiency is $\Sigma = 1$. For the two semiconductor materials that are studied in the present work, i.e., silicon (Si) and galium arsenide (GaAs), we can comfortably describe the stimulated Raman scattering with the above equations, as is demonstrated in detail in the following chapters.

2.2.3 Raman amplification

In the process of stimulated Raman scattering, the pump wave transfers part of its energy to the Stokes wave through the interaction with the nonlinear medium. As a result, it is possible to amplify a weak Stokes beam by the pump beam, which is called **Raman amplification**. In the following we derive an equation that describes the amplification of the Stokes wave intensity via stimulated Raman scattering.

Using the definition of $\chi_R^{(3)}(\omega_S)$ given by Eq. (2.35), we can write Eq. (2.34) in a shorter form, yielding the nonlinear **propagation equation for the Stokes wave**

$$\frac{\partial A_S}{\partial z} = \frac{3i\omega_S}{n_S c} \, \chi_R^{(3)}(\omega_S) \, |A_P|^2 A_S \, . \tag{2.40}$$

We assume in the following that the polarization directions remain unchanged so that the above equation is valid for all times.

Nonlinear propagation of the Stokes intensity

The intensity of an electromagnetic wave with the frequency ω can be expressed as a function of the field amplitude

$$I_\omega \;=\; 2 \, n(\omega) \, c \, \epsilon_0 \, |A_\omega|^2 \;=\; 2 \, n(\omega) \, c \, \epsilon_0 \, A_\omega A_\omega^* \, , \tag{2.41}$$

where $n(\omega)$ is the frequency-dependent refractive index and the asterisk * denotes the complex conjugate. We differentiate the above equation (2.41) with respect to the propagation in the z direction and insert the nonlinear propagation equation (2.40) for the Stokes wave. As a result, we obtain the nonlinear propagation equation for the Stokes intensity I_S, given by

$$
\begin{aligned}
\frac{\mathrm{d}}{\mathrm{d}z} I_S &= 2 n_S c \epsilon_0 \frac{\mathrm{d}}{\mathrm{d}z} \left(A_S A_S^* \right) = 2 n_S c \epsilon_0 \left[A_S^* \frac{\mathrm{d}}{\mathrm{d}z} A_S + A_S \frac{\mathrm{d}}{\mathrm{d}z} A_S^* \right] \\
&= \frac{3\,i\,\omega_S}{n_S c} 2 n_S c \epsilon_0 |A_S|^2 |A_P|^2 \underbrace{\left[\chi_R^{(3)}(\omega_S) - \left(\chi_R^{(3)}(\omega_S) \right)^* \right]} \\
&= \frac{3\,i\,\omega_S}{n_S c} 2 n_S c \epsilon_0 |A_S|^2 |A_P|^2 \times \left[2\,i\,\mathrm{Im}\left(\chi_R^{(3)}(\omega_S) \right) \right] .
\end{aligned} \tag{2.42}
$$

By using again the relationship between intensity and amplitude of an electromagnetic wave, $I = 2 n c \epsilon_0 |A|^2$, we can rewrite the propagation equation as a function of the pump and Stokes intensities instead of the field strengths, yielding

$$
\frac{\mathrm{d}}{\mathrm{d}z} I_S = - \left(\frac{3\omega_S}{n_S n_P c^2 \epsilon_0} \right) \mathrm{Im}\left(\chi_R^{(3)}(\omega_S) \right) I_P I_S ,
$$

where $n_P = n(\omega_P)$ is the index of refraction at the pump frequency, and I_P is the intensity of the pump wave. By introducing the so-called **Raman gain of the Stokes wave** as

$$
\boxed{\gamma_R = - \frac{3\omega_S}{n_S n_P c^2 \epsilon_0} \mathrm{Im}\left(\chi_R^{(3)}(\omega_S) \right)} , \tag{2.43}
$$

we obtain the **propagation equation for the Stokes intensity** in the compact form

$$
\boxed{\frac{\mathrm{d}}{\mathrm{d}z} I_S = \gamma_R I_P I_S} . \tag{2.44}
$$

Since the Raman gain is a function of the imaginary part of the Raman susceptibility $\chi_R^{(3)}(\omega_S)$, it also inherits from the susceptibility all the dependencies mentioned on page 16. For the sake of simplicity, we assume in the following that the pump wave and the Stokes waves have polarizations such that the scattering efficiency is maximal, $\Sigma = 1$, so that we can henceforth use the identity

$$
\chi_R^{(3)}(\omega_S) = \chi_R(\omega_S)
$$

This allows us to express the imaginary part of the Raman susceptibility according to Eq. (2.22) as

$$
\mathrm{Im}\left(\chi_R(\omega_S) \right) = \frac{-Q_0}{2\,\Omega\,\Gamma} \frac{1}{1 + \Delta^2} .
$$

For a zero detuning (i.e., for $\Delta = 0$), the imaginary part takes its maximum value, which we define as the so-called **Raman gain coefficient**

$$
\boxed{\bar{\gamma}_R = - \frac{3\omega_S}{n_S n_P c^2 \epsilon_0} \mathrm{Im}\left(\bar{\chi}_R \right) = \frac{3\omega_S}{n_S n_P c^2 \epsilon_0} \frac{Q_0}{2\,\Omega_R\,\Gamma}} . \tag{2.45}
$$

Thus, near the Raman resonance we can describe the **frequency dependence of the Raman gain** as

$$
\boxed{\gamma_R \approx \bar{\gamma}_R \frac{1}{1 + \Delta^2}} \quad \text{with} \quad \boxed{\Delta \approx \frac{\Omega_R - \Omega}{\Gamma} = \frac{\Omega_R - \omega_P + \omega_S}{\delta\Omega_R/2}} . \tag{2.46}
$$

γ_R

$I_S,\ I_P$

$\bar{\gamma}_R$

The equations (2.44), (2.45), and (2.46) provide a very convenient way to describe the effect of Raman amplification. The intensities of the pump and the Stokes beam are simply related through the Raman gain γ_R, which is characterized by three parameters: the Raman gain coefficient $\bar{\gamma}_R$, the Raman frequency Ω_R, and the linewidth of the Raman resonance $\delta\Omega_R$.

Propagation equation for the pump intensity

In order to find the propagation equation for the intensity of the pump wave, we consider the stimulated Raman scattering as a scattering process between a pump photon, a Stokes photon, and a Raman phonon, satisfying

$$\hbar\omega_P = \hbar\omega_S + \hbar\Omega_R \qquad \text{and} \qquad \hbar k_P = \hbar k_S + \hbar K_R \ ,$$

where K_R is the quasi-wave vector that can be attributed to the phonon. If $\widetilde{N}$ denotes the number of photons per unit area per time, we can express the intensites of the two electromagnetic waves at each position z as

$$I_P = \hbar\omega_P \widetilde{N}_P \qquad \text{and} \qquad I_S = \hbar\omega_S \widetilde{N}_S \ ,$$

which yields the following equations for the photon numbers per unit area per time

$$\widetilde{N}_P = \frac{I_P}{\hbar\omega_P} \qquad \text{and} \qquad \widetilde{N}_S = \frac{I_S}{\hbar\omega_S} \ .$$

In the elementary scattering process, one pump photon "decays" into one Stokes photon and one Raman phonon. Thus, the photon numbers satisfy the differential equation

$$\frac{\mathrm{d}}{\mathrm{d}z}\widetilde{N}_P = -\frac{\mathrm{d}}{\mathrm{d}z}\widetilde{N}_S \ ,$$

which yields directly the **propagation equation for the pump intensity**

$$\boxed{\frac{\mathrm{d}}{\mathrm{d}z}I_P = -\frac{\omega_P}{\omega_S}\gamma_R I_S I_P = -\frac{\lambda_S}{\lambda_P}\gamma_R I_S I_P} \ . \tag{2.47}$$

The above equation is essentially the same result as for the Stokes wave, given by Eq. (2.44), except that the right-hand side is multiplied by the ratio of the wavelengths (or frequencies) of the two waves and that it has a negative sign. The latter means that the pump intensity decreases during the propagation because it transfers its energy to the Stokes wave, whose intensity increases.

Raman amplification of the Stokes wave

In summary, the intensities of the Stokes wave and the pump wave are described by the following set of coupled differential equations:

$$\frac{\mathrm{d}}{\mathrm{d}z}I_S = \gamma_R I_P I_S \qquad \text{and} \qquad \frac{\mathrm{d}}{\mathrm{d}z}I_P = -\frac{\lambda_S}{\lambda_P}\gamma_R I_S I_P \ .$$

In what follows, we assume that the intensity of the pump wave does not change substantially during its propagation in the medium (**non-depleted pump approximation**),

$$I_P(z) \approx \text{const} \ .$$

In this case, we can easily integrate the propagation equation of the Stokes intensity (2.44), and we obtain an expression for the **intensity of the Stokes beam as a function of the distance** z, given by

$$I_S(z) = I_S(0) \exp\left\{\gamma_R \, I_P \, z\right\},\tag{2.48}$$

where $I_S(0)$ is the incident signal intensity at $z = 0$. Thus, the Stokes intensity experiences an **exponential amplification** that depends on the Raman gain, the intensity of the pump wave, and the length of the medium.

Raman phase shift of the Stokes wave

As mentioned above, the Raman scattering affects not only the intensity but also the phase of the Stokes wave. We can calculate the Raman-induced phase shift by using the nonlinear propagation equation for the Stokes wave, given by Eq. (2.40) as

$$\frac{\partial A_S}{\partial z} = \frac{3i\omega_S}{n_S c} \chi_R^{(3)}(\omega_S) |A_P|^2 A_S \,.\tag{2.49}$$

In the non-depleted pump approximation (i.e., $|A_P|^2 \approx$ const.), this equation can be easily integrated, resulting in

$$A_S(z) = A_S(0) \exp\left\{i \frac{3\omega_S}{2 n_S n_P c^2 \epsilon_0} \chi_R^{(3)}(\omega_S) \, I_P \, z\right\} \,.\tag{2.50}$$

We can express the accumulated phase shift after the propagation of the distance z as

$$\Delta\varphi_R(z) = \frac{1}{2} \frac{3\omega_S}{n_S n_P c^2 \epsilon_0} \mathrm{Re}\!\left(\chi_R^{(3)}(\omega_S)\right) I_P \, z \,.\tag{2.51}$$

Assuming again an optimal choice of the polarization states of pump and Stokes wave (i.e., $\Sigma = 1$), the real part of the Raman susceptibility can be expressed according to Eq. (2.22) as

$$\mathrm{Re}\!\left(\chi_R(\omega_S)\right) = \frac{Q_0}{2\,\Omega\,\Gamma} \frac{\Delta}{1 + \Delta^2} \,,\tag{2.52}$$

so that the **frequency-dependent Raman-induced phase shift** near the Raman resonance is given by

$$\Delta\varphi_R \qquad \boxed{\Delta\varphi_R(z) = \frac{\bar{\gamma}_R}{2} \frac{\Delta}{1 + \Delta^2} \, I_P \, z} \quad \text{with} \quad \boxed{\Delta \approx \frac{\Omega_R - \omega_P + \omega_S}{\delta\Omega_R/2}}.\tag{2.53}$$

As in the case of the Raman gain, the phase shift for a given choice of the pump and Stokes polarizations is described by the three central parameters $\bar{\gamma}_R$, Ω_R, and $\delta\Omega_R$, as well as by the pump intensity I_P. It is worth noting here that the Raman *gain*, which was derived in the context of the description of the Stokes *intensity*, also serves to quantify the Raman-induced *phase* shift.

2.3   Other nonlinear optical effects occurring in semiconductors (Kerr, TPA, FCA, FCR)

Besides the stimulated Raman scattering (SRS), there are also several other nonlinear optical effects that can occur in semiconductor materials (such as Si and GaAs). Of particular interest for the present work are the Kerr effect, the two-photon absorption

(TPA), the free-carrier absorption (FCA), and the free-carrier refraction (FCR). Like the Raman scattering, all of these effects can be derived from the general form of the third-order nonlinear polarization that has been introduced in section 2.1.3. As in the case of the stimulated Raman scattering (SRS), they can modify the amplitude (absorptive or amplifying effect) and/or the phase (dispersive effect) of the waves. In this section, we properly derive these effects and describe their influence on the propagation of the pump and the Stokes wave. However, since they are not of *central* importance for the present work, the introductions to these effects are much shorter than the description of the Raman scattering in section 2.2.

Although the term "*Stokes* wave" does not have a specific meaning in the context of the other nonlinear effects (it is only related to SRS), we consider in the following the same two waves that have been discussed above (i.e., the pump and the Stokes wave) in order to develop a complete description of the nonlinear processes that occur in the experiments. As before, we assume that the pump wave is much stronger than the Stokes wave,

$$ I_\mathrm{P} \gg I_\mathrm{S} \, . $$

We therefore suppose that **all nonlinear optical effects are caused by the pump wave**, whereas the Stokes wave only *experiences* the effects (i.e., is affected by them). Moreover, we consider a semiconductor material that is transparent at the pump and Stokes wavelengths so that both waves can propagate without linear absorption in the nonlinear medium.

Non-Raman nonlinear polarization affecting the Stokes wave

As has been explained in section 2.2.2, the pump-induced third-order nonlinear polarization at the Stokes frequency can be decomposed into its Raman and non-Raman components, as given by Eq. (2.31). While the Raman contribution has been extensively discussed in the previous section, we consider here the non-Raman (i.e., non-resonant) part, which can be written as

$$ \vec{P}_\mathrm{NR}^\mathrm{NL}(\omega_\mathrm{S}) = 6 \, \epsilon_0 \left[\underline{\underline{\chi}}^{(3)}(\omega_\mathrm{S}; \omega_\mathrm{P}, -\omega_\mathrm{P}, \omega_\mathrm{S}) \vdots \hat{e}_\mathrm{P} \hat{e}_\mathrm{P} \hat{e}_\mathrm{S} \right]_\mathrm{NR} |A_\mathrm{P}|^2 A_\mathrm{S} \, e^{ik_\mathrm{S}z} \, . \tag{2.54} $$

By inserting the above expression into the nonlinear propagation equation, we obtain

$$ \frac{\partial A_\mathrm{S}}{\partial z} = i \frac{3\omega_\mathrm{S}}{n_\mathrm{S}c} \underbrace{\left(\left[\underline{\underline{\chi}}^{(3)}(\omega_\mathrm{S}; \omega_\mathrm{P}, -\omega_\mathrm{P}, \omega_\mathrm{S}) \vdots \hat{e}_\mathrm{P} \hat{e}_\mathrm{P} \hat{e}_\mathrm{S} \right]_\mathrm{NR} \cdot \hat{e}_\mathrm{S} \right)}_{\chi_\mathrm{NR}^{(3)}(\omega_\mathrm{S}) \, \in \, \mathbb{C}} |A_\mathrm{P}|^2 A_\mathrm{S} \, , \tag{2.55} $$

and we define the complex **non-Raman third-order susceptibility at the Stokes frequency** as

$$ \boxed{ \chi_\mathrm{NR}^{(3)}(\omega_\mathrm{S}) = \left(\left[\underline{\underline{\chi}}^{(3)}(\omega_\mathrm{S}; \omega_\mathrm{P}, -\omega_\mathrm{P}, \omega_\mathrm{S}) \vdots \hat{e}_\mathrm{P} \hat{e}_\mathrm{P} \hat{e}_\mathrm{S} \right]_\mathrm{NR} \cdot \hat{e}_\mathrm{S} \right) \quad \in \mathbb{C} } \, . \tag{2.56} $$

$$ \chi_\mathrm{NR}^{(3)}(\omega_\mathrm{S}) $$

In the following sections, we examine the influence of this susceptibility on the propagation of the Stokes wave.

Pump-induced nonlinear polarization affecting the pump wave

In addition, we may be interested in the *pump*-induced third-order nonlinear polarization at the *pump* frequency itself,

$$ \vec{P}^\mathrm{NL}(\omega_\mathrm{P}) = 3 \, \epsilon_0 \left[\underline{\underline{\chi}}^{(3)}(\omega_\mathrm{P}; \omega_\mathrm{P}, -\omega_\mathrm{P}, \omega_\mathrm{P}) \vdots \hat{e}_\mathrm{P} \hat{e}_\mathrm{P} \hat{e}_\mathrm{P} \right] |A_\mathrm{P}|^2 A_\mathrm{P} \, e^{ik_\mathrm{P}z} \, , \tag{2.57} $$

which is similar to the nonlinear Stokes polarization given by Eq. (2.54), except that the Stokes frequency has been replaced by the pump frequency. Because there are only two distinguishable waves (i.e., ω_P and $-\omega_P$), the degeneracy factor is 3 in this case. Insertion into the nonlinear propagation equation yields

$$\frac{\partial A_P}{\partial z} = i\,\frac{3\omega_P}{2n_P c}\,\underbrace{\left(\left[\underline{\underline{\chi}}^{(3)}(\omega_P;\omega_P,-\omega_P,\omega_P)\vdots\hat{e}_P\hat{e}_P\hat{e}_P\right]\cdot\hat{e}_P\right)}_{\chi^{(3)}(\omega_P)\in\mathbb{C}}|A_P|^2 A_P\,,\qquad(2.58)$$

where $\chi^{(3)}(\omega_P)$ is the complex **third-order susceptibility at the pump frequency**

$\chi^{(3)}(\omega_P)$

$$\chi^{(3)}(\omega_P) = \left(\left[\underline{\underline{\chi}}^{(3)}(\omega_P;\omega_P,-\omega_P,\omega_P)\vdots\hat{e}_P\hat{e}_P\hat{e}_P\right]\cdot\hat{e}_P\right)\quad\in\mathbb{C}\,.\qquad(2.59)$$

We discuss in the following sections the effects of this susceptibility on the propagation of the *pump* wave.

Stokes-induced nonlinear polarizations

It should be noted that, in principle, we could also consider the nonlinear polarizations at the Stokes and pump frequency that are *induced by the Stokes* wave, given by

$$\vec{P}^{NL}(\omega_S) = 3\,\epsilon_0\left[\underline{\underline{\chi}}^{(3)}(\omega_S;\omega_S,-\omega_S,\omega_S)\vdots\hat{e}_S\hat{e}_S\hat{e}_S\right]|A_S|^2 A_S\,e^{ik_S z}\,,$$

$$\vec{P}^{NL}(\omega_P) = 6\,\epsilon_0\left[\underline{\underline{\chi}}^{(3)}(\omega_P;\omega_S,-\omega_S,\omega_P)\vdots\hat{e}_S\hat{e}_S\hat{e}_P\right]|A_S|^2 A_P\,e^{ik_P z}\,.$$

However, since we assume the Stokes wave to be much weaker than the pump wave, we henceforth ignore these contributions. Therefore, all of the nonlinear effects presented in the following sections are caused by the pump wave alone and can be derived from Eqs. (2.55) and (2.58).

2.3.1   Kerr effect and cross-Kerr effect (Kerr, X-Kerr)

The strong pump beam can induce a modification of the refractive index of the material, which is known as the optical Kerr effect. Due to the optical Kerr effect, the refractive index of the material changes for both the pump and the Stokes wave. Therefore, we distinguish between the so-called **cross-Kerr effect**, where the pump beam induces a change of the refractive index for the Stokes wave, and the self-Kerr effect, or simply **Kerr effect**, which is a self-induced index change of the pump beam.

Kerr effect and nonlinear refractive index

The Kerr effect can be described by the real part of the third-order susceptibility at the pump frequency given by Eq. (2.59). We introduce the **Kerr susceptibility** as

$\chi_K^{(3)}(\omega_P)$

$$\chi_K^{(3)}(\omega_P) = \mathrm{Re}\left(\chi^{(3)}(\omega_P)\right)\,.\qquad(2.60)$$

so that the nonlinear propagation equation becomes

$$\frac{\partial A_P}{\partial z} = i\,\frac{3\omega_P}{2n_P c}\,\chi_K^{(3)}(\omega_P)|A_P|^2 A_P = i\,\frac{\omega_P}{c}\,\frac{3\,\chi_K^{(3)}(\omega_P)}{4\,n_P^2\,c\,\epsilon_0}\,I_P A_P\,,$$

where we have, again, used the relationship $I = 2nc\epsilon_0 |A|^2$. For the sake of convenience, we define the **nonlinear refractive index** as

$$n_2 = \frac{3\,\chi_K^{(3)}(\omega_P)}{4\,n_P^2\,c\,\epsilon_0},$$

(2.61) n_2

so that the nonlinear propagation equation becomes

$$\frac{\partial A_P}{\partial z} = i\frac{2\pi}{\lambda_P}\,n_2\,I_P A_P\,.$$

Since the right-hand side of this equation is purely imaginary, it describes a phase shift of the pump wave. Assuming a non-depleted propagation of the pump beam (i.e., $I_P(z) \approx$ const.), we can easily integrate the propagation equation and obtain

$$A_P(z) = A_P(0)\,\exp\left\{i\frac{2\pi}{\lambda_P}\,n_2\,I_P\,z\right\}\,.$$

This corresponds to a **pump-induced phase shift at the pump wavelength** after the propagation of the distance z, given by

$$\Delta\varphi_K(z) = \frac{2\pi}{\lambda_P}\,n_2\,I_P\,z\,.$$

(2.62) $\Delta\varphi_K$

We can describe the Kerr effect by a phase shift given by Eq. (2.62), which is characterized by the nonlinear refractive index n_2 expressed by Eq. (2.61).

Cross-Kerr effect (X-Kerr)

The cross-Kerr effect is described by the real part of the non-Raman third-order susceptibility at the Stokes frequency given by Eq. (2.56), and we define the **cross-Kerr susceptibility** as

$$\chi_{XK}^{(3)}(\omega_S) = \mathrm{Re}\left(\chi_{NR}^{(3)}(\omega_S)\right)\,.$$

(2.63) $\chi_{XK}^{(3)}(\omega_S)$

By following the same approach as in the case of the Kerr effect, we define the **nonlinear cross-Kerr index** as

$$n_{2X} = \frac{3\,\chi_{XK}^{(3)}(\omega_S)}{4\,n_P\,n_S\,c\,\epsilon_0},$$

(2.64) n_{2X}

and we find the **pump-induced phase shift at the Stokes wavelength** to be

$$\Delta\varphi_{XK}(z) = \frac{2\pi}{\lambda_S}\,2\,n_{2X}\,I_P\,z\,.$$

(2.65) $\Delta\varphi_{XK}$

If we ignore dispersion, we can approximate $n_S \approx n_P$ and $\chi_{XK}^{(3)}(\omega_S) \approx \chi_K^{(3)}(\omega_P)$. In this case, a comparison between Eq. (2.65) and Eq. (2.62) shows that the influence of the pump wave is twice as strong on the Stokes wave (factor 2 in the cross-Kerr phase shift) as on the pump wave itself. The reason for this difference is the fact that the degeneracy factor is 6 for the cross-Kerr effect and only 3 in the case of the self-induced Kerr effect.

2.3.2 Two-photon absorption (TPA, XTPA)

As shown above, the *real* part of the third-order nonlinear polarization given by Eqs. (2.54) and (2.57) causes the Kerr effect and the cross-Kerr effect, which affect the *phase* of the two waves. The *imaginary* part of the nonlinear polarization, however, describes another nonlinear effect, which modifies the *intensity* of the light waves during their propagation. It is, for reasons that become clear below, called the two-photon absorption.

Like the Kerr effect, the two photon absorption is induced by the pump wave, and it affects the pump wave itself as well as the Stokes wave. In order to derive propagation equations for the intensities, we follow the same approach as presented for the Raman amplification in section 2.2.3. This leads to

$$
\frac{\mathrm{d}}{\mathrm{d}z} I_\mathrm{P} = -\frac{3\omega_\mathrm{P}}{2n_\mathrm{P}^2 c^2 \epsilon_0}\, \chi_\mathrm{TPA}^{(3)}(\omega_\mathrm{P})\, I_\mathrm{P}\, I_\mathrm{P}\ ,
$$

$$
\frac{\mathrm{d}}{\mathrm{d}z} I_\mathrm{S} = -\frac{3\omega_\mathrm{S}}{n_\mathrm{S} n_\mathrm{P} c^2 \epsilon_0}\, \chi_\mathrm{XTPA}^{(3)}(\omega_\mathrm{S})\, I_\mathrm{P}\, I_\mathrm{S}\ ,
$$

where we have introduced the **two photon absorption susceptibility** as

$\chi_\mathrm{TPA}^{(3)}(\omega_\mathrm{P})$

$$
\chi_\mathrm{TPA}^{(3)}(\omega_\mathrm{P}) = \mathrm{Im}\left(\chi^{(3)}(\omega_\mathrm{P})\right) \quad \in \mathbb{R}\ , \tag{2.66}
$$

and the so-called **cross-two photon absorption susceptibility** as

$\chi_\mathrm{XTPA}^{(3)}(\omega_\mathrm{S})$

$$
\chi_\mathrm{XTPA}^{(3)}(\omega_\mathrm{S}) = \mathrm{Im}\left(\chi_\mathrm{NR}^{(3)}(\omega_\mathrm{S})\right) \quad \in \mathbb{R}\ . \tag{2.67}
$$

These nonlinear susceptibilities can then be used to define coefficients that describe the two photon absorption, leading to the so-called **two-photon absorption coefficient**

β_TPA

$$
\beta_\mathrm{TPA} = \frac{3\omega_\mathrm{P}}{2n_\mathrm{P}^2 c^2 \epsilon_0}\, \chi_\mathrm{TPA}^{(3)}(\omega_\mathrm{P})\ , \tag{2.68}
$$

and the **cross-two photon absorption coefficient**

β_XTPA

$$
\beta_\mathrm{XTPA} = \frac{3\omega_\mathrm{S}}{2n_\mathrm{S} n_\mathrm{P} c^2 \epsilon_0}\, \chi_\mathrm{XTPA}^{(3)}(\omega_\mathrm{S})\ . \tag{2.69}
$$

Thus, we obtain two equations describing the effect of **two-photon absorption** on the pump intensity

$$
\frac{\mathrm{d}}{\mathrm{d}z} I_\mathrm{P} = -\beta_\mathrm{TPA}\, I_\mathrm{P}^2 \tag{2.70}
$$

and the **cross-two photon absorption**[3] on the Stokes intensity

$$
\frac{\mathrm{d}}{\mathrm{d}z} I_\mathrm{S} = -2\,\beta_\mathrm{XTPA}\, I_\mathrm{P} I_\mathrm{S}\ . \tag{2.71}
$$

---

[3] In the literature, the cross-two photon absorption (XTPA) is also referred to as the "non-degenerate two photon absorption", whereas the TPA, in contrast to this, is called the "degenerate two photon absorption" because both involved photons have the same energy.

Again, by neglecting dispersion, we see that the pump-induced absorption of the *Stokes* wave is stronger by a factor 2 than the absorption of the *pump* wave. As in the case of the Kerr effect and the cross-Kerr effect, this difference is due to the different degeneracy factors.

In the process of the two photon absorption in a semiconductor (or cross-two photon absorption, respectively), a pair of photons is absorbed by the nonlinear medium, which means that an electron is excited from the valence band (VB) into the conduction band (CB). In order for this process to happen, the sum of the two photon energies has to be greater than the band gap energy, while the energy of the photons individually is below the gap energy. This condition can be expressed as

$$\hbar\omega_1, \hbar\omega_2 \; < \; E_\mathrm{g} \; < \; \hbar\omega_1 + \hbar\omega_2 \; ,$$

where the angular frequencies ω_1 and ω_2 can be either one of the two involved frequencies (i.e., ω_P or ω_S). When considering for example GaAs, which is a direct band-gap semiconductor, and a pump and a probe beam whose wavelengths are 920 nm and 950 nm, respectively, we calculate the pump energy to be $E_\mathrm{P} = 1.348$ eV and a probe energy of $E_\mathrm{S} = 1.305$ eV. Obviously, both of these energies are smaller than the gap energy of $E_\mathrm{g} = 1.424$ eV, while $2\,E_\mathrm{P}$ as well as $E_\mathrm{P} + E_\mathrm{S}$ are greater than E_g. Thus, the above-stated condition is fulfilled. The TPA and XTPA processes in such a situation are schematically illustrated in Fig. 2.4.
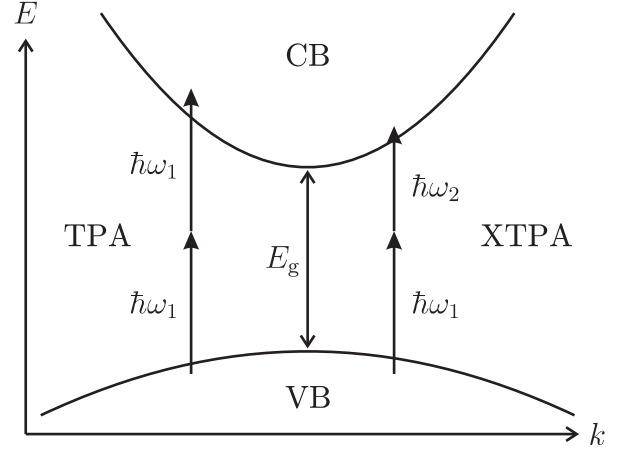
Fig. 2.4. Illustration of the two photon absorption (TPA) and the cross-two photon absorption (XTPA). Electrons in the valence band (VB) of semiconductors (here a direct band-gap semiconductor, e.g., GaAs) are excited into the conduction band (CB).

It should be noted that the right hand side of Eq. (2.71), which describes the influence of XTPA on the evolution of the Stokes intensity, is proportional to the product of the pump intensity and the Stokes intensity. By comparison with Eq. (2.44), we see that it has, therefore, to be taken into account in the same situations as the stimulated Raman scattering. Because of the negative sign in Eq. (2.71), cross-two photon *absorption* and Raman *amplification* are in this sense *competing processes*.

2.3.3 Free carrier effects (FCA, FCR)

As stated above, the two-photon absorption excites one electron from the valence band to the conduction band, and it thus leads to the creation of an electron-hole pair in the semiconductor material. Therefore, the two-photon absorption creates free charge carriers, which also affect the propagation of the pump and the Stokes wave, as is demonstrated in the following.

The evolution of the **free carrier densitiy** (i.e., the number of electrons and holes per unit volume) N_FC is described by the differential equation [42]

$$\frac{\mathrm{d}}{\mathrm{d}t} N_\mathrm{FC} = -\frac{1}{\tau_\mathrm{e}} N_\mathrm{FC} + \beta_\mathrm{TPA} \frac{I_\mathrm{P}^2}{2\hbar\omega_\mathrm{P}} \qquad (2.72) \qquad\qquad N_\mathrm{FC}$$

where τ_e is the lifetime of the free carriers (i.e., the recombination time of the electrons in the conduction band and the holes in the valence band). The first term in the

above equation describes the *decay* of the free carrier density due to recombination processes, whereas the second term corresponds to the *creation* of an electron-hole pair by the absorption of two photons of the energy $\hbar\omega_P$. In principle, we could also consider the free carriers created by the *cross*-two photon absorption (XTPA), described by $\beta_{XTPA} I_P I_S / \hbar(\omega_S + \omega_P)$. However, since we assume that the pump intensity is much higher than the Stokes intensity, we can reasonably ignore the XTPA-generated free carriers compared to the TPA contribution.

The free carriers induce a modification of the linear susceptibility of the material [43]. This modification can be expressed as

$$\chi_{FC} = 2n_0 \left(\sigma_n(\omega) \, N_{FC} + i\frac{c}{2\omega} \, \sigma_a(\omega) \, N_{FC} \right) , \qquad (2.73)$$

where n_0 represents the linear refractive index. The first term in the parentheses represents a modification of the refractive index of the material, while the second term describes a free-carrier induced absorption. The quantities σ_n and σ_a can be expressed in terms of the effective masses and the mobilities of the electrons and the holes as [44, 45]

$$\sigma_n = -\frac{q^2}{2\epsilon_0 n_0 \omega^2} \left(\frac{1}{m_e} + \frac{1}{m_h} \right) \frac{E_g^2}{E_g^2 - (\hbar\omega)^2} , \qquad (2.74)$$

$$\sigma_a = \frac{q^3}{\epsilon_0 c n_0 \omega^2} \left(\frac{1}{\mu_e m_e^2} + \frac{1}{\mu_h m_h^2} \right) \frac{E_g^2}{E_g^2 - (\hbar\omega)^2} . \qquad (2.75)$$

Here E_g is the band gap energy of the semiconductor, $q = 1.602 \times 10^{-19}$ C is the elementary charge, m_e and m_h are the effective masses, and μ_e and μ_h the mobilities of electrons and holes, respectively. Moreover, the assumption has been made that the number of electrons is equal to the number of holes. Although the free carriers modify the *linear* susceptibility (effect), they are created by a the two photon absorption, which is a *nonlinear* process (cause). Therefore, we define a free-carrier induced (nonlinear) polarization at the Stokes frequency ω_S as

$$P_{FC}^{NL}(\omega_S) = \epsilon_0 \, \chi_{FC} \, A_S \, e^{ik_S z} . \qquad (2.76)$$

We insert the free-carrier susceptibility χ_{FC} given by Eq. (2.73) and obtain

$$P_{FC}^{NL}(\omega_S) = 2n_0\epsilon_0 \, \sigma_n \, N_{FC} \, A_S \, e^{ik_S z} + 2n_0\epsilon_0 \, i \, \frac{c}{2\omega} \, \sigma_a \, N_{FC} \, A_S \, e^{ik_S z} . \qquad (2.77)$$

The first term in the above equation represents the modification of the refractive index of the material, or free carrier refraction (FCR), and the second term describes the absorption by the free carriers, or free carrier absorption (FCA).

Free carrier refraction (FCR)

According to the previous equation (2.77), the nonlinear polarization of the free carrier refraction is given by

$$P_{FCR}^{NL}(\omega_S) = 2n_0\epsilon_0 \, \sigma_n \, N_{FC} \, A_S \, e^{ik_S z} . \qquad (2.78)$$

We insert this nonlinear polarization into the nonlinear propagation equation of the Stokes wave, yielding

$$\frac{\partial}{\partial z} A_S = i \frac{\omega_S}{c} \sigma_n \, N_{FC} \, A_S .$$

We can easily integrate this differential equation and obtain

$$A_S(z) = A_S(0) \, \exp\left\{ i \, \frac{\omega_S}{c} \sigma_n \, N_{FC} \, z \right\} \; .$$

Using the relationship $\omega = 2\pi c/\lambda$, the **free carrier induced phase shift** at the Stokes wavelength after the propagation of the distance z is given by

$$\Delta\varphi_{FC}(z) = \frac{2\pi}{\lambda_S} \sigma_n \, N_{FC} \, z \; . \qquad (2.79)$$

$\Delta\varphi_{FC}$

As can be seen from the above equation, the product of σ_n and the carrier density N_{FC} has the physical meaning of a refractive index. We can therefore define the **free carrier refractive index**

$$n_{FC} = \sigma_n \, N_{FC} \; , \qquad (2.80)$$

n_{FC}

which describes the modification of the index of refraction that is caused by the presence of free charge carriers in the semiconductor material.

Free carrier absorption (FCA)

As can be seen from Eq. (2.77), the nonlinear polarization of the free carrier absoption is given by

$$P_{FCA}^{NL}(\omega_S) = 2n_0\epsilon_0 \, i \, \frac{c}{2\omega} \, \sigma_a \, N_{FC} \, A_S \, e^{ik_S z} \; . \qquad (2.81)$$

We insert this expression into the nonlinear propagation equation of the Stokes wave and obtain

$$\frac{\partial}{\partial z} A_S = - \frac{\sigma_a}{2} \, N_{FC} \, A_S \; ,$$

which can be integrated and yields an equation describing the evolution of the amplitude of the Stokes wave as a function of the propagation along the z direction

$$A_S(z) = A_S(0) \, \exp\left\{ -\frac{\sigma_a}{2} \, N_{FC} \, z \right\} \; .$$

Using the relationship between the amplitude and the intensity of an electromagnetic wave, $I = 2nc\epsilon_0 |A|^2$, we obtain an equation describing the influence of the TPA-induced free-carrier absorption on the Stokes intensity,

$$I_S(z) = I_S(0) \, \exp\left\{ -\sigma_a N_{FC} \, z \right\} \; ,$$

where the factor $\sigma_a N_{FC}$ in the exponent indicates how efficient the Stokes wave is absorbed in the material. We can, therefore, define a **free carrier absorption coefficient**

$$\alpha_{FC} = \sigma_a \, N_{FC} \qquad (2.82)$$

α_{FC}

for the intensity of an electromagnetic wave. The inverse of $\sigma_a N_{FC}$ thus represents a characteristic length after which the incident intensity $I_S(0)$ decreases to $1/e \approx 37\,\%$ of its initial value. This characteristic length may serve as an indicator to see whether the FCA has to be included in a mathematical model of the nonlinear effects or not (see also chapter 4).

Time dependence of free carrier effects

An important particularity of the free carrier effects (i.e., FCR and FCA) compared to the other nonlinear optical effects presented in this chapter is their time dependence. For pulses with a duration of about 10 ps or more, the Kerr (and cross-Kerr)
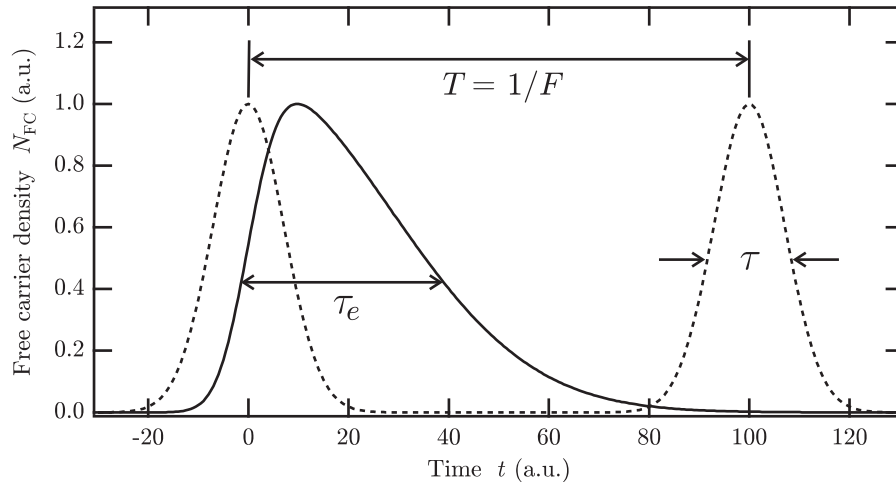
Fig. 2.5. Illustration of the time dependence (with the carrier life time τ_e) of free carriers that are generated by a pulsed laser beam. The dotted line represents a regular pulse train with a pulse duration τ and a repetition rate $F = 1/T$, where T is the time between two consecutive pulses.

effect and the two photon absorption (and cross-two photon absorption) process can be considered as *instantaneous* effects. This means that they occur only as long as the pump wave is present in the nonlinear medium. The free carrier effects, however, depend on the free carrier density in the semiconductor, which is only indirectly, through the two photon absorption (TPA), a function of the pump intensity. Once the free carriers are created by TPA, their evolution in time is described by Eq. (2.72). The relaxation of the electrons, i.e., their recombination with the holes in the valence band, is governed by the carrier lifetime τ_e.

It is therefore interesting to examine the influence of the free carrier effects in the case of a pulsed pump beam. For this purpose, we consider Gaussian pump pulses with a maximum transmission $I_{P,0}$ and a duration $\widetilde{\tau}_P$ (full width at $1/e$) of the form

$$I_P(t) \;=\; I_{P,0} \, \exp\left\{-\frac{t^2}{(\widetilde{\tau}_P/2)^2}\right\} \;.$$

We then find the solution to the differential equation (2.72) to be[4]

$$N_{FC}(t) \;=\; e^{-t/\tau_e} \, e^{(\widetilde{\tau}_P/\sqrt{8}\,\tau_e)^2} \left[\widetilde{\tau}_P \, \sqrt{\frac{\pi}{8}} \, \frac{\beta_{TPA}}{2\hbar\omega_P} \, I_{P,0}^2 \left(1 + \mathrm{erf}\left(\sqrt{2}\frac{t}{\widetilde{\tau}_P} - \frac{1}{\sqrt{8}}\frac{\widetilde{\tau}_P}{\tau_e}\right)\right)\right] \;,$$

where $\mathrm{erf}()$ is the error function (i.e., the integral over the Gauss function). If the pulse duration is much shorter than the free carrier lifetime (i.e., for $\widetilde{\tau}_P \ll \tau_e$), the time dependence of the free carrier density is essentially proportional to

$$N_{FC}(t) \;\propto\; e^{-t/\tau_e} \left(1 + \mathrm{erf}\left(\sqrt{2}\frac{t}{\widetilde{\tau}_P}\right)\right) \;, \tag{2.83}$$

which describes the creation of the free carriers through the $\mathrm{erf}()$ function with a simple exponential damping. We further assume that the pump pulses represent a regular pulse train with the repetition rate F, which corresponds to a time $T = 1/F$ between two consecutive pulses. Figure 2.5 illustrates the typical time dependence of the TPA-induced free carrier density N_{FC}, where the dotted lines indicate time dependence of the pump intensity (i.e., the pulse train).

$\mathcal{DC}$ It is common to characterize such a pulse train by the so-called **duty cycle** $\mathcal{DC}$, which is simply the ratio

$$\mathcal{DC} \;=\; \frac{\tau}{T} \;=\; \tau \, F \;. \tag{2.84}$$

For experimental studies of nonlinear optical effects, it is often desirable to work with short pulses whose duration is much shorter than the free carrier life time,

---

[4]determined by using the symbolic differential equation solver of the software Mathematica

$\tau \ll \tau_{\mathrm{e}}$, because this provides the necessary high pump intensities without requiring a transient description and modeling of the observed phenomena. However, in order to avoid any cumulative free carrier effects from one pulse to the next, which would bias the measurements, we require that the time between two consecutive pulses be long compared to the free carrier life time, $\tau_{\mathrm{e}} \ll T = \tau/\mathcal{DC}$. By combining these two conditions, we find

$$\tau \ \ll \ \tau_{\mathrm{e}} \ \ll \ T = \frac{\tau}{\mathcal{DC}} \qquad \Longrightarrow \qquad \mathcal{DC} \ll 1 \,,$$

which means that the duty cycle of an appropriately configured pulsed pump laser should be small. However, as the following considerations show, it should not be *too* small either.

Besides the pulse duration and repetition rate, the duty cycle also relates the average power P_{avg} of a pulse train to the peak power P_{max} of the individual pulses. Supposing that the pulses have a Gaussian time dependence, we can calculate the total optical energy of one pulse approximately by $E_{\mathrm{pulse}} = P_{\mathrm{max}}\tau$, with the peak power P_{max} and the duration τ (full width at half maximum). Since the average power P_{avg} corresponds to the pulse energy divided by the time between two pulses, $P_{\mathrm{avg}} = E_{\mathrm{pulse}}/T$, we find the relationship between peak power and the average power

$$P_{\mathrm{avg}} \ = \ \frac{\tau}{T} \, P_{\mathrm{max}} \ = \ \tau \, F \, P_{\mathrm{max}} \ = \ \mathcal{DC} \, P_{\mathrm{max}} \,. \tag{2.85}$$

From an experimental point of view, this relationship can be very useful because it indicates whether the experiment can work with average powers (which are relatively easy to detect) or whether it is necessary to treat each pulse individually (which makes the data acquisition and processing rather complex). As is explained in the following chapters, both approaches are used for the experiments presented in this work.

2.4 Enhancement of nonlinear effects through light localization in semiconductor nanostructures

In the previous sections 2.1, 2.2, and 2.3, we have introduced and used the basic equations of nonlinear optics, notably the nonlinear propagation equation (2.4) and the nonlinear polarization given by Eq. (2.5). These equations describe the nonlinear response of a material to strong incident light fields. We will see in the following what we have to take into account if we want to use these equations to describe the nonlinear optical effects in the case of highly localized light. This leads to the notion of the local field factor, which is useful for the description of light localization in waveguides, as well as to the so-called intensity magnification factor, which we will use when describing the nonlinear effects in a microcavity.

2.4.1 Local field factor and group refractive index

On a microscopic level, the nonlinear optical effects are caused by the *local* (i.e., *microscopic*) nonlinear response of the elementary dipoles, atoms, moelcules etc. So far, however, we have used the *macroscopic* electric fields $\vec{E}$ and the macroscopic nonlinear polarization $\vec{P}^{\mathrm{NL}}$ to describe these phenomena. This approximation works well in diluted media, where a single microscopic dipole experiences essentially the macroscopic fields. In the case of dense media or highly localized light, however, we have to distinguish between the external, macroscopic fields $\vec{E}$ and $\vec{P}^{\mathrm{NL}}$ and the local, microscopic fields $\vec{E}_{\mathrm{loc}}$ and $\vec{P}^{\mathrm{NL}}_{\mathrm{loc}}$ [46].

Enhancement of nonlinear effects due to light localization

We have demonstrated in section 2.1 that we can express the polarization $\vec{P}$ of a medium (i.e., the dipole moment per unit volume) as a power series in the incident electric field strengths, which can be written in the simple form

$$\vec{P} = \vec{P}^{\text{L}} + \vec{P}^{\text{NL}} \qquad \text{where} \qquad \vec{P}^{\text{NL}} = \vec{P}^{(2)} + \vec{P}^{(3)} + \dots ,$$

as shown by Eq. (2.1). The nonlinear contributions are given by

$$\vec{P}^{(2)} = \epsilon_0 \, D^{(2)} \, \underline{\underline{\chi}}^{(2)}(\omega; \omega_1, \omega_2) : \vec{E}(\omega_1)\vec{E}(\omega_2)$$

$$\vec{P}^{(3)} = \epsilon_0 \, D^{(3)} \, \underline{\underline{\chi}}^{(3)}(\omega; \omega_1, \omega_2, \omega_3) \vdots \, \vec{E}(\omega_1)\vec{E}(\omega_2)\vec{E}(\omega_3) ,$$

so that the nonlinear polarization can be written in the simplified form

$$\vec{P}^{\text{NL}} = \sum_{n=2}^{\infty} \vec{P}^{(n)} = \sum_{n=2}^{\infty} \epsilon_0 \, D^{(n)} \, \chi^{(n)} \, \vec{E}^n . \tag{2.86}$$

In the case of dense media or strong light localization, the local electric field is not equal to the external electric field. We can, however, assume a linear relationship of the form [47]

f
$$\vec{E}_{\text{loc}}(\omega) = f(\omega) \, \vec{E}(\omega) , \tag{2.87}$$

where we have introduced the so-called **local field factor** $f(\omega)$, which **relates the microscopic to the macroscopic electric field**.

It is important to note that the source term of the nonlinear propagation equation (2.2) (which describes the propagation of the electromagnetic wave that is generated through the nonlinear interaction in the medium) is given by the microscopic (i.e., *local*) nonlinear polarization $\vec{P}_{\text{loc}}^{\text{NL}}$. It can be shown that the latter is related to the macroscopic nonlinear polarization $\vec{P}^{\text{NL}}$ through [36]

$$\vec{P}_{\text{loc}}^{\text{NL}}(\omega) = f(\omega) \, \vec{P}^{\text{NL}}(\omega) , \tag{2.88}$$

where the local field factor f corresponds to the generated electromagnetic wave. Based on the above equations, it can further be shown that the nonlinear susceptibility has to be modified in order to fulfill the nonlinear propagation equation [36]. In the present work, we are mainly interested in the third-order nonlinear susceptibility, which becomes, thus, in the case of light localization [48]

$$\boxed{\underline{\underline{\chi}}^{(3)}(\omega; \omega_1, \omega_2, \omega_3) \quad \longrightarrow \quad f(\omega)f(\omega_1)f(\omega_2)f(\omega_3)\underline{\underline{\chi}}^{(3)}(\omega; \omega_1, \omega_2, \omega_3)}$$

with the local field factors $f(\omega_i)$ for the corresponding frequencies ω_i. Thus, we find that the n-th order contribution to the *local* nonlinear polarization contains a product of $n+1$ local field factors. If we insert the above expression in the case of stimulated Raman scattering into the nonlinear propagation equation of the Stokes wave, we obtain

$$\frac{\partial A_{\text{S}}}{\partial z} = \frac{3i\omega_{\text{S}}}{n_{\text{S}}c} \, f_{\text{P}}^2 f_{\text{S}}^2 \, \chi_{\text{R}}^{(3)}(\omega_{\text{S}}) \, |A_{\text{P}}|^2 A_{\text{S}} \tag{2.89}$$

where f_{P} and f_{S} are the local field factors for the pump wave and for the Stokes wave, respectively. By following the same steps as presented in the derivation of

the Raman amplification and the Raman gain (see section 2.2.3), this leads to an equation describing the **Stokes amplification in the case of light localization**, given by

$$I_S(L) = I_S(0) \, \exp\left(f_P^2 f_S^2 \, \gamma_R \, I_P \, l\right) \, .$$
(2.90)

Effect	Factor	Order
SRS	$f_P^2 f_S^2$	3
TPA	f_P^4	3
XTPA	$f_P^2 f_S^2$	3
Kerr	f_P^4	3
Cross-Kerr	$f_P^2 f_S^2$	3
FCR on pump	f_P^6	5
FCR on Stokes	$f_P^4 f_S^2$	5
FCA on pump	f_P^6	5
FCA on Stokes	$f_P^4 f_S^2$	5

Tab. 2.1. Enhancement factors and effective order of the nonlinear optical effects.

Thus, depending on the values of the local field factors for the pump and the Stokes wave, we can obtain a **significantly higher amplification** of the Stokes wave during its propagation in the nonlinear medium **because of the localization** of the light. By comparing the propagation equation *without* light localization, given by Eq. (2.40), to Eq. (2.89), one can clearly see that the two equations are identical except for the four f factors on the right hand side of Eq. (2.89). Thus, the influence of the light localization is an **enhancement of the nonlinear effects** that is completely described by the product of the local field factors, which we call the enhancement factor. Tab. 2.1 summarizes the enhancement factors of the nonlinear effects considered in the present work, as well as their effective order. As the table shows, the enhancement factors of the free carrier effects (FCA, FCR) contain products of six local field factors (f factors). They are, therefore, effectively *fifth*-order nonlinear effects.

Obviously, the description of the nonlinear optical effects *without* light localization, as presented in section 2.2 and 2.3, can be obtained from the description *with* light localization by setting all the local field factors to $f = 1$, as can be seen by comparing Eq. (2.48) and (2.90).

Light localization due to reduced group velocity

After having seen what consequences the localization of light can have, we are interested in the relationship between the local field factor and the propagation of light in a slow-mode waveguide. Experimentally, the intensities of the pump and Stokes waves are only accessible outside the waveguide, while the nonlinear optical interaction is governed by the internal intensities. Therefore, we need to relate the intensity of an electromagnetic wave *inside* a slow mode waveguide to its intensity measured *outside* the waveguide, as illustrated in Fig. 2.6. We consider a waveguide with an effective mode area A_{eff} in which a light pulse with a pulse duration τ (FWHM) is propagating along the z direction. The waveguide consists of two parts which are characterized by different group velocities $v_{\text{gr},1}$ and $v_{\text{gr},2}$ of the pulse. The group velocities are determined by the group refractive indices $n_{\text{gr},1}$ and $n_{\text{gr},2}$ through

$$v_{\text{gr},1} \; = \; \frac{c}{n_{\text{gr},1}} \qquad \text{and} \qquad v_{\text{gr},2} \; = \; \frac{c}{n_{\text{gr},2}} \, .$$
(2.91)

In both parts, we consider a volume that corresponds to the effective mode area of the waveguide multiplied by the length (Δz_1 and Δz_2, respectively) of the pulse in the respective part (FWHM). We can then easily express the energy density U in each part as

$$U_1 = \frac{\hbar \omega \, N_1}{A_{\text{eff}} \, \Delta z_1} \qquad \text{and} \qquad U_2 = \frac{\hbar \omega \, N_2}{A_{\text{eff}} \, \Delta z_2} \, ,$$
(2.92)

where N_1 and N_2 is the number of photons in the respective part. For simplicity, all photons are assumed to have the same energy $\hbar \omega$. Within the pulse duration τ, all the photons in the above-described volumes move exactly the distances Δz_1 and Δz_2, which are given by

$$\Delta z_1 = v_{\text{gr},1} \, \tau \qquad \text{and} \qquad \Delta z_2 = v_{\text{gr},2} \, \tau \, .$$
(2.93)

Fig. 2.6. Illustration of the intensity enhancement due to light localization in a slow mode waveguide. Source: C. MONAT [30].

With Eqs. (2.91), (2.92), and (2.93), we then find that the ratio of the maximum intensities (which are proportional to the energy densities) in the two parts is given by

$$\frac{I_2}{I_1} \;=\; \frac{U_2}{U_1} \;=\; \frac{N_2/\Delta z_2}{N_1/\Delta z_1} \;=\; \frac{N_2}{N_1}\,\frac{v_{\mathrm{gr},1}}{v_{\mathrm{gr},2}} \;=\; \frac{N_2}{N_1}\,\frac{n_{\mathrm{gr},2}}{n_{\mathrm{gr},1}} \;.$$

We consider one single pulse that propagates through the first part and then enters the second part, where we assume that there are no losses at the interface between the two parts. This means that we require the total number of photons in the pulse to be conserved, i.e., $N_1 = N_2$. Thus, the intensity ratio is simply

$$\frac{I_2}{I_1} \;=\; \frac{n_{\mathrm{gr},2}}{n_{\mathrm{gr},1}} \;=\; S \;, \tag{2.94}$$

where S is called the slow down factor [30], since it indicates by how much the pulse propagation has been slowed down (in the case that $n_{\mathrm{gr},2} > n_{\mathrm{gr},1}$). In other words, the pulse is effectively compressed (or expanded) along its propagation direction, and therefore its peak intensity increases (or decreases, respectively). Figure 2.6 illustrates this increase of the intensity in a photonic crystal waveguide [30].

We now compare the situation where the first part corresponds to a bulk medium (e.g., a semiconductor) and the second part represents a waveguide that provides a certain amount of light localization. According to Eq. (2.94), we obtain the intensity ratio

$$\frac{I_{\mathrm{guide}}}{I_{\mathrm{bulk}}} \;=\; \frac{n_{\mathrm{gr}}}{n_{\mathrm{bulk}}} \;,$$

where n_{bulk} is the (normal) refractive index of the bulk material[5]. However, we can also express the intensities as a function of the electric field strengths, including the local field factor according to Eq. (2.87), yielding

$$\frac{I_{\mathrm{guide}}}{I_{\mathrm{bulk}}} \;=\; \frac{(f\,|\vec{E}|)^2}{|\vec{E}|^2} \;=\; f^2\,\frac{|\vec{E}|^2}{|\vec{E}|^2} \;=\; f^2 \;,$$

so that we find the relationship between the local field factor and the group refractive index in semiconductor nanostructures (e.g., slow-mode waveguides)

$$\boxed{\,f \;=\; \sqrt{\frac{n_{\mathrm{gr}}}{n_{\mathrm{bulk}}}}\,} \;. \tag{2.95}$$

With this expression, we can experimentally determine the local field factor f of a silicon waveguide (see chapter 3) by measuring its group refractive index n_{gr}.

---

[5]In the case of a low-dispersion material, which we assume here, we can approximately identify the bulk refractive index with the group refractive index, $n_{\mathrm{bulk}} \approx n_{\mathrm{gr}}$.

2.4.2 Simple model of SRS in a semiconductor microcavity

In this section we develop a simple analytical model that describes the effect of stimulated Raman scattering in a semiconductor microcavity. Using this model, we then present a comparison between different resonance configurations and demonstrate that the Raman amplification of the Stokes wave can be significantly enhanced in a *doubly* resonant microcavity.

Starting point of our considerations is a simple Fabry-Perot resonator consisting of two mirrors M_1 and M_2 with an optical gain medium in between. We are interested in an expression for the (intensity) transmission coefficient T of the resonator as a function of the (intensity) gain coefficient G of the medium. The full derivation of this expression is presented in appendix B, including several graphical illustrations of the geometry, the involved electrical fields, and the resonance behavior of such a Fabry-Perot resonator. Here, we only summarize the key results of this derivation.

The transmission and reflectivity coefficients (for the intensities of the electromagnetic waves) are denoted by T_1, R_1 (first mirror) and T_2, R_2 (second mirror). Furthermore, we assume the mirrors to be loss-free, which means that $T_1 + R_1 = 1$ and $T_2 + R_2 = 1$. We can then express the **transmission of a resonator containing a gain medium** as a function of the intensity reflectivities as

$$T = \frac{(1 - R_1)(1 - R_2)\, e^{Gl}}{\left| 1 - \sqrt{R_1 R_2}\, e^{Gl}\, e^{2i\varphi_{\mathrm{FP}}} \right|^2}, \tag{2.96}$$

where the propagation distance l is given by

$$l = L/\cos\vartheta \tag{2.97}$$

with L the distance between the two mirrors (i.e. the resonator length) and ϑ as the angle of incidence of the light. As is demonstrated in appendix B, the **Fabry-Perot phase**, which describes the resonance behavior of the transmission coefficient T, can be expressed as

$$\varphi_{\mathrm{FP}} = n\, L\, k \cos\vartheta = \frac{2\pi\, n\, L \cos\vartheta}{\lambda}, \tag{2.98}$$

Raman amplification in a Fabry-Perot resonator

We now specify that the optical gain G is provided by stimulated Raman scattering. In other words, we consider a resonator that contains a Raman-active medium, which is in the present case a semiconductor material (e.g., Si or GaAs). Pump and Stokes wave are assumed to be monochromatic CW laser beams injected in the cavity, and we consider them as plane waves with a constant beam diameter. As shown in section 2.2.3, the Stokes wave experiences an exponential Raman amplification so that we can express the gain coefficient G according to Eq. (2.48) as

$$G = \gamma_{\mathrm{R}}\, I_{\mathrm{P,c}}, \tag{2.99}$$

where γ_{R} is the Raman gain and $I_{\mathrm{P,c}}$ the intensity of the pump wave inside the cavity (intracavity intensity). The pump beam itself, as it is the origin of the optical gain, is *not* amplified. It can, however, be resonant in the cavity. In that case, the intra-cavity pump intensity is higher than the intensity outside of the cavity. We

Fig. 2.7. Intensity of an electromagnetic wave in a Fabry-Perot resonator (with gain). The graph illustrates the relationship between the incident intensity I_i, the reflected intensity I_r, the forward and backward propagating intra-cavity intensity I_f and I_b, and the transmitted intensity I_t as a function of the position z. The total intensity inside the cavity I_c is composed of the forward and the backward propagating parts.
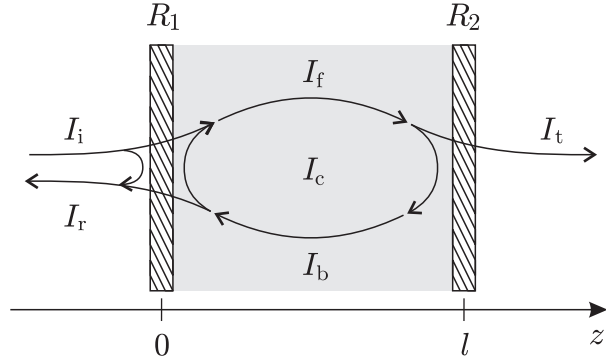
consider the intra-cavity pump intensity $I_{P,c}$ as the sum of intensities of the forward propagating and the backward propagating pump wave

$$I_{P,c} = I_{P,f} + I_{P,b} \, , \tag{2.100}$$

as illustrated in Fig. 2.7. Both the forward and the backward propagating contribution can be expressed in terms of the transmitted pump intensity $I_{P,t}$ in the form

$$I_{P,t} = T_{2,P}\, I_{P,f} = (1 - R_{2,P})\, I_{P,f} \quad\Longrightarrow\quad I_{P,f} = \frac{1}{1 - R_{2,P}}\, I_{P,t}$$

$$I_{P,b} = R_{2,P}\, I_{P,f} = R_{2,P}\, \frac{1}{1 - R_{2,P}}\, I_{P,t} = \frac{R_{2,P}}{1 - R_{2,P}}\, I_{P,t} \, ,$$

where $R_{1,P}$ and $R_{2,P}$ are the reflectivities of the two mirrors for the pump wave, i.e., at the pump wavelength. Using the above expressions, the intra-cavity pump intensity is given by

$$I_{P,c} = \frac{1}{1 - R_{2,P}}\, I_{P,t} + \frac{R_{2,P}}{1 - R_{2,P}}\, I_{P,t} = \frac{1 + R_{2,P}}{1 - R_{2,P}}\, I_{P,t} = \frac{1 + R_{2,P}}{1 - R_{2,P}}\, T_P\, I_{P,i} \, , \tag{2.101}$$

where we have also introduced the overall transmission coefficient of the resonator for the pump wave,

$$T_P = \frac{I_{P,t}}{I_{P,i}} \, , \tag{2.102}$$

with the incident pump intensity $I_{P,i}$. For the transmission coefficient, we now use Eq. (2.96), where we assume that the pump beam is at resonance, $\varphi_{FP} = 0$, and that it experiences *no* gain, $G \equiv 0$ (the gain is experienced by the Stokes wave, not by the pump wave), so that we obtain the pump transmission

$$T_P = \frac{I_{P,t}}{I_{P,i}} = \frac{(1 - R_{1,P})(1 - R_{2,P})}{\left(1 - \sqrt{R_{1,P} R_{2,P}}\right)^2} \, .$$

By inserting the above expression into Eq. (2.101), we find

$$I_{P,c} = \frac{(1 + R_{2,P})}{(1 - R_{2,P})}\, \frac{(1 - R_{1,P})(1 - R_{2,P})}{(1 - \sqrt{R_{1,P} R_{2,P}})^2}\, I_{P,i} = \frac{(1 - R_{1,P})(1 + R_{2,P})}{\left(1 - \sqrt{R_{1,P} R_{2,P}}\right)^2}\, I_{P,i}$$

so that we can express the **intra-cavity intensity of the pump wave** by

$$I_{P,c} = M_P\, I_{P,i} \tag{2.103}$$

with the so-called **intensity magnification factor** [49] for the pump wave

$$M_{\mathrm{P}} = \frac{(1 - R_{1,\mathrm{P}})(1 + R_{2,\mathrm{P}})}{\left(1 - \sqrt{R_{1,\mathrm{P}}R_{2,\mathrm{P}}}\right)^2}.$$ (2.104) M_{P}

This means that, although the pump beam itself does not experience any gain, its intensity inside the cavity is increased by a factor M_{P} if the pump wave is at resonance. As an example, we obtain an almost 200-fold higher intra-cavity intensity, compared to the incident intensity, for the reflectivity values $R_{1,\mathrm{P}} = 0.99$ and $R_{2,\mathrm{P}} = 0.99$. By inserting Eqs. (2.103) and (2.104) into Eq. (2.99) and by using the expression (2.97) for the effective propagation distance, $l = L/\cos\vartheta$, we obtain an expression for the **transmission of the Stokes wave at resonance**, given by

$$T_{\mathrm{S}} = \frac{(1 - R_{1,\mathrm{S}})(1 - R_{2,\mathrm{S}})\,e^{\gamma_{\mathrm{R}} M_{\mathrm{P}} I_{\mathrm{P,i}} L/\cos\vartheta_{\mathrm{S}}}}{\left(1 - \sqrt{R_{1,\mathrm{S}}R_{2,\mathrm{S}}}\,e^{\gamma_{\mathrm{R}} M_{\mathrm{P}} I_{\mathrm{P,i}} L/\cos\vartheta_{\mathrm{S}}}\right)^2},$$ (2.105)

where $R_{1,\mathrm{S}}$ and $R_{2,\mathrm{S}}$ are the reflectivities of the two mirrors for the Stokes wave, i.e., at the Stokes wavelength.

The above equation is the ratio of the output intensity $I_{\mathrm{S,t}}$ to the input intensity $I_{\mathrm{S,i}}$ of a Fabry-Perot resonator containing a medium that provides Raman gain ($I_{\mathrm{S,t}} = T_{\mathrm{S}} I_{\mathrm{S,i}}$). Therefore, it is actually not quite correct to refer to it as a *transmission* coefficient. If greater than unity, it is actually rather an *amplification* coefficient that describes by how much the Stokes wave is amplified during its propagation in the gain medium, and we will in such cases refer to it as the "transmission enhancement factor".

Comparison of singly and doubly resonant microcavities

The reflectivities of the two mirrors for the pump and the Stokes beam have a strong influence on the Stokes "transmission" defined by Eq. (2.105). The Stokes reflectivities can be found directly in the Airy-type transmission function, while the pump reflectivities go into the intensity magnification factor. In the following, we study several cases of different resonance situations (i.e., different choices of the reflectivities for pump and Stokes wave) to see how efficient the Stokes beam can be amplified in a Raman-active semiconductor microcavity.

For this purpose, we determine the so-called **on-off gain** $G_{\text{on-off}}$, which characterizes the influence of the pump intensity on the achievable amplification. In the context of this simple model, the on-off gain is defined as the ratio of the transmitted Stokes intensity *with* an incident pump intensity $I_{\mathrm{P,i}}$ ("on") to the transmitted Stokes intensity *without* the pump beam ("off"),

$$G_{\text{on-off}} = \frac{I_{\mathrm{S,t}}(I_{\mathrm{P,i}})}{I_{\mathrm{S,t}}(I_{\mathrm{P,i}} = 0)} = \frac{T_{\mathrm{S}}(I_{\mathrm{P,i}})}{T_{\mathrm{S}}(I_{\mathrm{P,i}} = 0)},$$ (2.106) $G_{\text{on-off}}$

where we have assumed that the *incident* Stokes intensity is constant. Furthermore, we assume that the Stokes wavelength is $\lambda_{\mathrm{S}} = 950$ nm and that we are at normal incidence, $\vartheta_{\mathrm{S}} = 0$. Since the two semiconductor materials studies in the present work are Si and GaAs, we use a refractive index of $n \approx 3.5$ (which is valid for both). The thickness is supposed to be $L = 5\lambda_{\mathrm{S}}/n$. For the Raman gain γ_{R}, we assume that the polarizations of pump and Stokes wave are optimally chosen (i.e., $\Sigma = 1$) and use a numerical value of the Raman gain of 27 cm/GW, which is a value arbitrarily chosen in the middle

$\lambda_{\mathrm{S}} = 950$ nm
$\vartheta_{\mathrm{S}} = 0$
$n \approx 3.5$ (Si, GaAs)
$L = 5\lambda_{\mathrm{S}}/n$ ($m = 10$)
$\gamma_{\mathrm{R}} = 27$ cm/GW

between the Raman gain coefficient of GaAs (50 cm/GW, see chapter 4 for details) and Si (approximately 9 cm/GW, as we show in chapter 3).

Case 1: Not resonant at all. In this situation, we consider simply a semiconductor slab that has a natural Fresnel reflectivity at the front side and that is anti-reflection coated on the back side. Therefore, the reflectivities are given by

$$R_{1,S} \approx R_{1,P} \approx \frac{(n-1)^2}{(n+1)^3} \approx 0.31 \qquad \text{and} \qquad R_{2,S} = R_{2,P} = 0 \,,$$

yielding a pump intensity magnification factor of

$$M_P = \frac{(1 - 0.31)(1 + 0)}{\left(1 - \sqrt{0.31 \times 0}\right)^2} = 0.69 \,,$$

which is actually rather a reduction factor than a magnification factor because it is smaller than unity. The Stokes transmission can then be expressed as a function of the incident pump intensity as

$$T_S(I_{P,i}) = \frac{(1 - 0.31)(1 - 0) \, e^{0.69 \, \gamma_R I_{P,i} L / \cos 0}}{\left(1 - \sqrt{0.31 \times 0} \, e^{0.69 \, \gamma_R I_{P,i} L / \cos 0}\right)^2} = 0.69 \, \exp\left\{0.69 \, \gamma_R \, I_{P,i} \, L\right\} \,,$$

which is a simple exponential amplification. Since we are interested in the influence of the pump intensity, we compare the above expression to the Stokes transmission *without pump* wave by calculating the on-off gain in the non-resonant case

$$G_{\text{on-off, NR}} = \exp\left\{0.69 \, \gamma_R \, I_{P,i} \, L\right\} \,.$$

Case 2: Pump resonant. In this situation, we assume for the Stokes wave a Fresnel reflectivity at the front side and the anti-reflection coating on the back side. The pump beam, however, is assumed to be resonant in the cavity so that the reflectivities are

$$R_{1,S} \approx 0.31, \ R_{1,P} = 0.99 \qquad \text{and} \qquad R_{2,S} = 0, \ R_{2,P} = 0.99 \,,$$

which yields a pump intensity magnification factor of $M_P = 199$, meaning an almost two-hundred-fold increase of the pump intensity inside the cavity. According to Eq. (2.106), this yields an on-off gain of

$$G_{\text{on-off, PR}} = \exp\left\{199 \, \gamma_R \, I_{P,i} \, L\right\} \,.$$

Case 3: Stokes resonant. This is the inverse situation of the previous case, i.e., the Stokes wave alone is resonant. Hence, the reflectivities are given by

$$R_{1,S} = 0.99, \ R_{1,P} \approx 0.31 \qquad \text{and} \qquad R_{2,S} = 0.99, \ R_{2,P} = 0 \,,$$

which yields again a pump intensity magnification factor of $M_P = 0.69$, as in the first case, and we obtain an on-off gain of

$$G_{\text{on-off, SR}} = \frac{0.01^2 \, e^{0.69 \, \gamma_R I_{P,i} L}}{\left(1 - 0.99 \, e^{0.69 \, \gamma_R I_{P,i} L}\right)^2} \,.$$
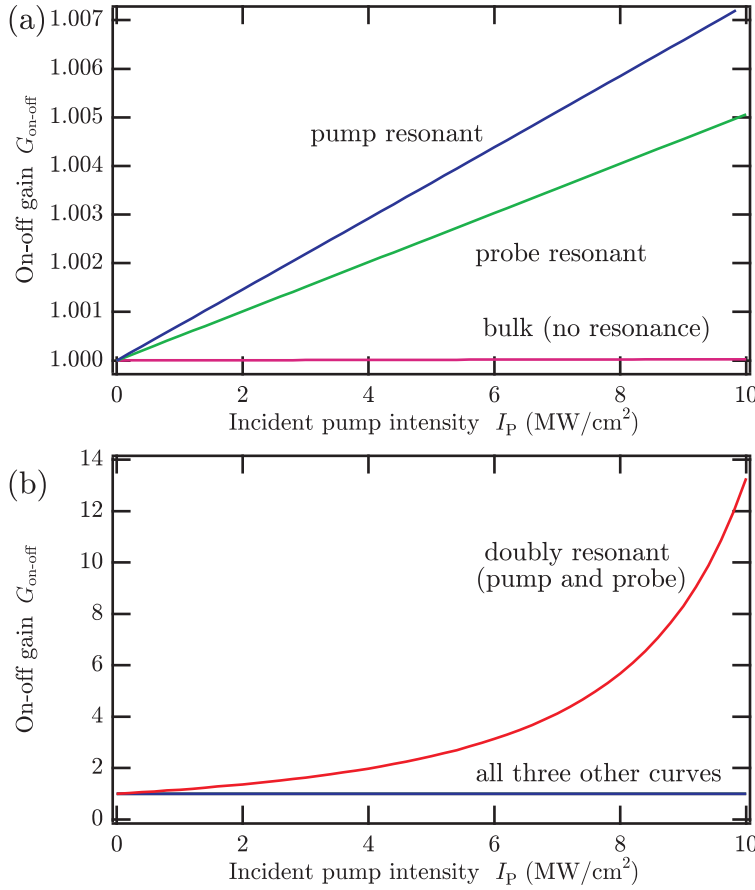
Fig. 2.8. On-off gain $G_{\text{on-off}}$ as a function of the incident pump intensity $I_{\text{P,i}}$ for four different resonance situations.

(a) The three curves correspond to the cases of a bulk semiconductor (no beam resonant), the pump beam alone resonant, and the Stokes beam alone at resonance.

(b) The graph shows the on-off gain $G_{\text{on-off, DR}}$ in the case of a doubly resonant microcavity (i.e., pump and Stokes beam resonant at the same time) compared to the three other cases, which are so close to each other that they cannot be separated from one another.

Case 4: Double resonance. Both beams are resonant in the cavity with the reflectivities

$$R_{1,\text{S}} = 0.99, \ R_{1,\text{P}} = 0.99 \qquad \text{and} \qquad R_{2,\text{S}} = 0.99, \ R_{2,\text{P}} = 0.99$$

so that the pump intensity magnification factor is again $M_{\text{P}} = 199$, as in the second case, resulting in an on-off gain of

$$G_{\text{on-off, DR}} = \frac{0.01^2 \, e^{199 \, \gamma_{\text{R}} I_{\text{P,i}} L}}{\left(1 - 0.99 \, e^{199 \, \gamma_{\text{R}} I_{\text{P,i}} L}\right)^2} \, .$$

Figure 2.8 illustrates the dependence of the on-off gain $G_{\text{on-off}}$ on the incident pump intensity $I_{\text{P,i}}$ for all four cases. Compared to the last case (doubly resonant), the three other curves are so close together that they cannot be distinguished from one another. As can be seen from the graph, in a doubly resonant microcavity containing a Raman gain medium, we can achieve a **significant amplification** of the Stokes beam for pump intensities in the MW/cm² range, which are easily attainable in experiments. To our knowledge, this particular situation (i.e., Raman amplification in a *doubly* resonant semiconductor microcavity) has never been experimentally studied before. In chapter 4, we present an experimental study of such a situation in a GaAs microcavity as well as some totally unexpected results.

In the simple model presented in this section, the amplification of the Stokes wave increases with $I_{\text{P,i}}$ without any limit because we have made the approximation of a non-depleted pump beam, which means effectively an infinite source of energy. Moreover, no other nonlinear effects have been taken into account, especially not

those that affect the phase of the waves (such as the Kerr effect and the free carrier refraction). Therefore, although this simple model motivates very well the interest in a study of Raman amplification in a doubly resonant semiconductor microcavity, we need a better model in order to describe the physical processes occurring during the propagation of the pump and the Stokes waves. In chapter 4, we present such an improved model that is partially based on the above findings.

* * *

Chapter 3

Saturated Raman amplification in a silicon-on-insulator nanowire

This chapter presents an experimental study of stimulated Raman scattering in a silicon-on-insulator (SOI) nanowire. We demonstrate that the Raman amplification of a narrow-band Stokes wave experiences a saturation effect for high pump intensities because of self phase modulation of the pump beam. Moreover, an analytical model is presented that describes the experimental results remarkably well. The model furthermore provides an estimation of the Raman gain coefficient $\bar{\gamma}_{\mathrm{R}}$ of silicon.

Contents

Silicon-on-insulator (SOI) is widely regarded as one of the most promising technologies for the realization of key functions for the optical processing of information [39]. What makes this technology platform particularly attractive is its compatibility with existing CMOS fabrication technology in combination with the possibility to achieve an extremely strong confinement of the light in waveguides whose cross sections are as small as 0.1 to 0.2 μm^2 [50]. This significantly reduces the optical powers that are necessary to control the optical functions and thus allows for the design of highly compact components with low command powers.

The first experimental demonstration of Raman amplification in silicon nanowaveguides (or "nanowires") [51] has lead to the realization of the first Raman lasers in silicon, both in the pulsed regime [52] as well as continuous wave [53, 54]. A large number of studies have shown that the two main limitations are caused by two photon absorption (TPA) and the absorption by the free carriers (FCA) which are generated by TPA [55, 56, 57]. The influence of FCA can be reduced by working with pulses whose repetition time (i.e., the time between two consecutive pulses) is very long compared to the free carrier lifetime [58, 59, 60, 61]. Moreover, several studies have been carried out on the reduction of the free carrier lifetime by ion implantation [62] and by the integration of a reverse-biased p-i-n junction in the waveguide [63]. With the latter method, the free carrier lifetime has been successfully reduced from the order of nanoseconds to only several picoseconds.

However, in the perspective of high-speed optical information processing, it is surprising to see that there are no publications studying how the performance of optical functions, especially Raman amplification, is influenced by nonlinear phase shifts. With the lifetime of optical phonons in silicon being of the order of 2 to 3 picoseconds, it should be possible to amplify optical pulses of several picoseconds in duration through stimulated Raman scattering. However, such pulses are expected to experience nonlinear phase shifts due to the Kerr effect and the free carrier refraction (FCR). These variations of the phase induce a temporal deformation of the pulses and, as a result, a spectral broadening (self phase modulation, SPM). When the resulting spectral width of the pulse is of the same order of magnitude as the Raman resonance, which is 105 GHz in silicon [39], we expect to observe a reduction of the effective amplification. Although such a reduction of the Raman gain represents a key issue concerning the realization of functional nanostructures (slow mode waveguides or microcavities), where the spectral broadening due to the Kerr effect and FCR is strongly enhanced, it has to our knowledge never been studied up to now.

Recent studies have demonstrated the enhancement of *amplified spontaneous* Raman scattering [64, 65, 66] in silicon-based photonic crystal waveguides. As these publications show, the enhancement of the Raman scattering is caused by a strong reduction of the group velocity v_{gr}. However, a reduced group velocity also leads to a stronger self phase modulation (SPM), which effectively limits the enhancement of the Raman amplification. Therefore, it is of crucial importance to study the interplay between these effects in the perspective of the realization of slow-mode photonic crystal structures for Raman amplification.

In this chapter, I experimentally demonstrate the above-mentioned effect, i.e., a saturation of the Raman amplification of a narrow-band Stokes wave in a silicon nanowire (which is basically a ridge waveguide with a sub-lambda cross section). I show that this saturation is caused by the self-phase modulation of the pump beam due to the Kerr effect and the free carrier refraction. Furthermore, I demonstrate that, because of the light localization, the influence of two photon absorption on the pump wave is enhanced. Moreover, I present an analytical model of the propagation

of the Stokes wave, which shows a very good agreement with the experimental results. As a side effect, the model also yields a value of the bulk Raman gain coefficient $\bar{\gamma}_{R}$ of silicon, whose currently reported values in the literature are spread over a large range between 4 and 70 cm/GW [67].

The present work illustrates the interest to take into account the interplay between the different nonlinear effects in the case of localized light (i.e., slow v_{gr}). As the results clearly show, it is not sufficient to simply slow down the light in order to enhance the nonlinear effects (e.g., Raman amplification). It is also crucial to study their interactions among each other. Although the experiments presented in this chapter have been carried out with a nanowire in a *weakly* slow-light regime, our results can also be applied to a situation with a *strong* light localization (i.e., in a strongly slow-light regime), which makes them very useful for applications in photonic crystal structures.

The work presented in this chapter has been part of the ANR project MIRA-MAN, which was a research collaboration between the Laboratoire Charles Fabry de l'Institut d'Optique (LCFIO) in Palaiseau, notably the research groups MANO-LIA and NAPHEL, the research laboratory SiNaPS of the Commissariat à l'Énergie Atomique (CEA) in Grenoble, and the Laboratoire des Technologies de la Microélectronique (LTM) of the CNRS in Grenoble. The aim of the project was to improve the design of slow mode waveguides and microcavities in silicon-on-insulator (SOI), as well as to study the nonlinear optical interactions in silicon-based waveguides and slow mode structures. For the experimental study presented here, the group NAPHEL has numerically simulated and optimized the design of an appropriate sample that is based on the silicon-on-insulator (SOI) technology. The sample has then been fabricated by the LTM. It is described in more detail in section 3.2.1.

The experimental nonlinear characterization of the silicon nanowire, which I have carried out in the research group MANOLIA at the Laboratoire Charles Fabry de l'Institut d'Optique (LCFIO), uses the so-called pump-probe technique. This means that a strong laser beam (pump beam) is used to induce nonlinear optical effects in the semiconductor sample, and the (nonlinear) response of the sample is measured with a weak probe beam. For the study of the stimulated Raman scattering, **the probe beam corresponds to the Stokes wave**. In order to obtain high pump intensities, we work with almost Fourier-transform limited picosecond laser pulses whose pulse duration is such that their spectral width corresponds to the linewidth of the Raman resonance. To avoid any cumulative effects of free charge carriers, the time between two consecutive pulses is chosen to be long compared to the free carrier lifetime.

The chapter starts with the analytical model, which describes the Raman gain of silicon in the picosecond domain (i.e., when using picosecond pulses as the pump beam). After a detailed description of the experimental setup and the semiconductor sample, a linear characterization of the latter is presented, including a determination of the local field factor of the Stokes wave. Then, the chapter shows the nonlinear pump-probe measurements and demonstrates the Raman gain saturation, which is equivalent to a decrease of the effective Raman gain. By applying the analytical model to the measurement data, we find an excellent agreement between experiment and theory and determine the bulk Raman gain coefficient of silicon. The results of this chapter have been subject of a publication in Applied Physics Letters [68].

3.1   Analytical model of SRS in a silicon nanowire

Before presenting the experimental results of the pump-probe measurements, we develop a model of Raman amplification in the case of Fourier-transform limited picosecond pump pulses whose duration is significantly shorter than the duration of the probe pulse (i.e., $\tau_P \ll \tau_S$)[1]. In that case, the spectral width of the pump pulses is larger than the width of the probe pulses (i.e., $\delta\omega_P \gg \delta\omega_S$). Since we assume furthermore that the spectral width of the pump pulses is larger than the linewidth of the Raman resonance (i.e., $\delta\omega_P > \delta\Omega_R$), this effectively reduces the Raman gain experienced by the probe beam, as is demonstrated in the following. In order to describe this phenomenon mathematically, the theory of stimulated Raman scattering that has been derived in section 2.2.1 must be slightly modified. Using this modified theory of SRS, we derive an equation that describes the evolution of the Stokes wave in a silicon nanowire. These results are then used to develop a model of the pump-probe experiments that are presented in section 3.4.

3.1.1   Effective Raman gain with a polychromatic pump wave

In a first step, we are interested in the Raman gain experienced by the Stokes wave in the case where the pump wave is polychromatic (in the sense that the pump wave has a finite spectral linewidth of at least the same order of magnitude as the spectral lineshape of the Raman resonance). The Stokes wave is assumed as monochromatic (i.e., continuous wave or spectrally very fine). Thus, we express the Stokes wave as

$$\vec{E}_S(z,t) = A_S(z)\, \hat{e}_S\, e^{ik_S z}\, e^{-i\omega_S t}\, +\, \text{c.c.}$$

and the polychromatic pump wave as

$$\vec{E}_P(z,t) = \sum_{\omega_P} A_P(z,\omega_P)\, \hat{e}_P\, e^{ik_P z}\, e^{-i\omega_P t}\, +\, \text{c.c.}\, ,$$

where the symbol $\sum$ represents the sum over all frequency components of the pump spectrum. Both beams are assumed to propagate in the z direction (collinear propagation). As in section 2.2.3, we assume that the pump beam is significantly stronger than the probe beam and that the pump intensity is therefore approximately constant (non-depleted pump approximation),

$$\frac{\mathrm{d}}{\mathrm{d}z} A_P \approx 0 \quad \Longrightarrow \quad A_P(z,\omega_P) = A_P(\omega_P)\, .$$

We write down the scalar propagation equation of the Stokes wave, which is given by Eq. (2.33), yielding

$$\frac{\partial A_S}{\partial z} = \frac{i\omega_S}{2n_S c\epsilon_0}\, P_R^{NL}(\omega_S)\, e^{-ik_S z}\, .$$

We express the nonlinear polarization at the Stokes frequency as the sum of all the contributions from the different spectral components of the pump spectrum

$$P_R^{NL}(\omega_S) = 6\,\epsilon_0 \sum_{\omega_P} \chi_R^{(3)}(\omega_S; \omega_P, -\omega_P, \omega_S)\, \frac{I_P}{2\, n_P\, c\, \epsilon_0}\, A_S\, e^{ik_S z}\, ,$$

where $\omega_P - \omega_P + \omega_S = \omega_S$ is satisfied for all frequency components ω_P. Alternatively, we can also describe the spectrum of the pump wave by a continuous spectral

---

[1]In the experiments presented in section 3.4, the pump pulse duration is about $\tau_P = 15$ ps, while the probe pulses are about ten times longer, i.e., $\tau_S = 150$ ps, which is in fact *significantly* longer.

distribution function $S(\omega)$ instead of discrete frequencies. In this case, the nonlinear polarization is given by the integral over the spectrum

$$P_\mathrm{R}^\mathrm{NL}(\omega_\mathrm{S}) = 6\,\epsilon_0 \int_{-\infty}^{\infty} \chi_\mathrm{R}^{(3)}(\omega_\mathrm{S}; \omega_\mathrm{P}, -\omega_\mathrm{P}, \omega_\mathrm{S}) \frac{I_\mathrm{P,0}\,S(\omega_\mathrm{P})}{2\,n_\mathrm{P}\,c\,\epsilon_0} A_\mathrm{S}\,e^{ik_\mathrm{S}z}\,\mathrm{d}\omega_\mathrm{P}\;,$$

where $I_\mathrm{P,0}$ is the total pump intensity of one pulse (over the whole spectrum), and the spectral distribution function $S(\omega_\mathrm{P})$ is normalized by

$$\int_{-\infty}^{\infty} S(\omega)\,\mathrm{d}\omega = 1\;.$$

Following the derivation given in section 2.2.3, we obtain the propagation equation for the Stokes intensity with a polychromatic pump wave

$$\frac{\mathrm{d}}{\mathrm{d}z}I_\mathrm{S} = -\frac{3\,\omega_\mathrm{S}}{n_\mathrm{P}n_\mathrm{S}c^2\epsilon_0} \int_{-\infty}^{\infty} \mathrm{Im}\Big(\chi_\mathrm{R}^{(3)}(\omega_\mathrm{S}; \omega_\mathrm{P}, -\omega_\mathrm{P}, \omega_\mathrm{S})\Big)\,S(\omega_\mathrm{P})\,\mathrm{d}\omega_\mathrm{P}\,I_\mathrm{P,0}\,I_\mathrm{S}\;. \qquad (3.1)$$

By comparing this equation to the result for a monochromatic pump wave, given by Eqs. (2.44) and (2.43),

$$\frac{\mathrm{d}}{\mathrm{d}z}I_\mathrm{S} = \gamma_\mathrm{R}\,I_\mathrm{P}\,I_\mathrm{S} \qquad \text{with} \qquad \gamma_\mathrm{R} = -\frac{3\omega_\mathrm{S}}{n_\mathrm{S}n_\mathrm{P}c^2\epsilon_0}\,\mathrm{Im}\left(\chi_\mathrm{R}^{(3)}(\omega_\mathrm{S}; \omega_\mathrm{P}, -\omega_\mathrm{P}, \omega_\mathrm{S})\right)\;,$$

we can express Eq. (3.1) in the form

$$\frac{\mathrm{d}}{\mathrm{d}z}I_\mathrm{S} = \underbrace{\left[\int_{-\infty}^{\infty} \gamma_\mathrm{R}(\omega_\mathrm{P} - \omega_\mathrm{S})\,S(\omega_\mathrm{P})\,\mathrm{d}\omega_\mathrm{P}\right]}_{\widetilde{\gamma}_\mathrm{R}(\omega_\mathrm{S})}\,I_\mathrm{P,0}\,I_\mathrm{S}\;,$$

where we have defined the **effective Raman gain** with a polychromatic pump wave

$$\boxed{\widetilde{\gamma}_\mathrm{R}(\omega_\mathrm{S}) = \int_{-\infty}^{\infty} \gamma_\mathrm{R}(\omega_\mathrm{P} - \omega_\mathrm{S})\,S(\omega_\mathrm{P})\,\mathrm{d}\omega_\mathrm{P}}\;. \qquad (3.2) \qquad\qquad \widetilde{\gamma}_\mathrm{R}(\omega_\mathrm{S})$$

The above equation (3.2) is the convolution integral between the frequency dependence of the Raman gain and the spectrum of the pump wave. As shown in section 2.2.3, the frequency dependence of the Raman gain is given by

$$\gamma_\mathrm{R}(\omega_\mathrm{P} - \omega_\mathrm{S}) \approx \bar{\gamma}_\mathrm{R}\,\frac{1}{1 + \Delta^2}\;, \qquad (3.3)$$

where $\bar{\gamma}_\mathrm{R}$ is the material-dependent Raman gain coefficient, and the frequency detuning parameter Δ can be approximated as

$$\Delta \approx \frac{\Omega_\mathrm{R} - \omega_\mathrm{P} + \omega_\mathrm{S}}{\delta\Omega_\mathrm{R}/2} = 2\,\frac{\nu_\mathrm{R} - \nu_\mathrm{P} + \nu_\mathrm{S}}{\delta\nu_\mathrm{R}} \qquad (3.4)$$

with the Raman frequency ν_R and the full width at half maximum (FWHM) of the Raman resonance $\delta\nu_\mathrm{R}$. In the present work, we study the zone center optical phonon of silicon with a Raman frequency of $\nu_\mathrm{R} = 15.6$ THz and a linewidth of $\delta\nu_\mathrm{R} = 105$ GHz [39, 69, 70, 71].

3.1.2   Evolution of the Stokes intensity in a silicon nanowire

We now use the above findings to derive a model that describes the nonlinear propagation of the pump and the Stokes wave in a silicon nanowire. The pump intensity can be described by the propagation equation

$$\frac{\mathrm{d}}{\mathrm{d}z}I_{\mathrm{P},0} = -\beta' \, I_{\mathrm{P},0}^2 \; - \; \alpha'_{\mathrm{P}} I_{\mathrm{P},0} \,, \tag{3.5}$$

where the first term represents the auto-induced two photon absorption and the second term is the linear attenuation in the waveguide.

$\alpha'_{\mathrm{P}}, \, \beta'$

The nanowire is a waveguide of very small dimensions compared to the pump and Stokes wavelengths (which are in the range between 1.4 and 1.6 μm). The propagation of the pump and Stokes waves in the waveguide is significantly slower than in bulk silicon, which is expressed by the **group refractive index** $n_{\mathrm{gr}} > n_{\mathrm{bulk}}$ [72] and leads to the **local field factor** f of the waves in the waveguide. Thus, for a correct description of the nonlinear propagation in the nanowire, we have to take into account the effects of the **light localization**, which has not been done in the previous studies of SRS in SOI waveguides. In the above equation, the light localization is included in the coefficient $\beta' = f_{\mathrm{P}}^4 \beta_{\mathrm{TPA}}$ with the two-photon absorption coefficient β_{TPA} and the local field factor f_{P} of the pump wave. As has been mentioned in section 2.4.1, even a relatively small local field factor f_{P} can lead to a significant enhancement of the two photon absorption because it is raised to the fourth power. For example, a value of $f_{\mathrm{P}} = 1.2$ leads to a two-fold increase of the two-photon absorption coefficient, $\beta' = f_{\mathrm{P}}^4 \beta_{\mathrm{TPA}} \approx 2 \beta_{\mathrm{TPA}}$.

Notice that the intrinsic linear attenuation coefficient α'_{P} of the waveguide implicitly takes into account the effect of light localization. The evolution of the Stokes intensity is described by

$$\frac{\mathrm{d}}{\mathrm{d}z}I_{\mathrm{S}} = \left(\gamma' \, - \, 2\,\beta'_{\mathrm{X}}\right) \, I_{\mathrm{P},0}(z)\, I_{\mathrm{S}} \; - \; \alpha'_{\mathrm{S}} I_{\mathrm{S}} \,, \tag{3.6}$$

α'_{S}

where the last term with α'_{S} represents the linear attenuation. As mentioned in section 2.3.2, the stimulated Raman scattering and the cross-two photon absorption compete with one another, as can be seen in the parentheses of the first term. The stimulated Raman scattering (Raman amplification) is given by $\gamma' = f_{\mathrm{P}}^2 f_{\mathrm{S}}^2 \widetilde{\gamma}_{\mathrm{R}}(\omega_{\mathrm{S}})$ with the local field factor of the Stokes wave f_{S} and the effective Raman gain $\widetilde{\gamma}_{\mathrm{R}}(\omega_{\mathrm{S}})$ as defined by Eq. (3.2). The term $\beta'_{\mathrm{X}} = f_{\mathrm{P}}^2 f_{\mathrm{S}}^2 \beta_{\mathrm{XTPA}}$ represents the cross-two photon absorption.

$\beta'_{\mathrm{X}}, \, \gamma'$

In the following, we solve the two coupled differential equations (3.5) and (3.6). In our experiments, typical input pump intensities are on the order of a few gigawatts per square centimeter, with 15 ps pulses and a repetition rate of 80 MHz. Therefore, following the arguments provided by Yin et al. [43], the free carrier effects (FCA and FCR) can reasonably be neglected, which allows us to find an *analytical* solution of the above set of equations. Moreover, since we will not measure the phase of the pump beam and the Stokes beam experimentally, we do not include the Kerr effect and the dispersive Raman effect, which is described by the real part of the Raman susceptibility, in the quantitative model presented here. However, as the experimental results in section 3.4 show, we observe a self-phase modulation (SPM) of the pump pulses leading to a spectral broadening of the pump spectra. Although *not* included quantitatively in the model of the beam propagation, the spectral broadening clearly influences the effective Raman gain given by Eq. (3.2) through the spectral distribution function $S(\omega_{\mathrm{P}})$. This influence is discussed in more detail in section 3.4.3.

Two photon absorption of the pump beam

In order to solve the propagation equation (3.6) for the Stokes wave, we first have to integrate Eq. (3.5) for the pump wave. The latter is independent of the Stokes intensity and can be written as

$$\frac{\mathrm{d}I_{\mathrm{P},0}}{I_{\mathrm{P},0}\,(\beta'\,I_{\mathrm{P},0} - \alpha'_{\mathrm{P}})} = -\,\mathrm{d}z \;. \tag{3.7}$$

The integrand on the left hand side of the above equation can be transformed to

$$\frac{1}{I_{\mathrm{P},0}\,(\beta'\,I_{\mathrm{P},0} - \alpha'_{\mathrm{P}})} = \frac{1}{\alpha'_{\mathrm{P}}}\left(\frac{1}{I_{\mathrm{P},0}} - \frac{\beta'}{\beta'\,I_{\mathrm{P},0} - \alpha'_{\mathrm{P}}}\right)$$

so that the integration of Eq. (3.7) yields

$$\ln\left(\frac{I_{\mathrm{P},0}(z)}{I_{\mathrm{P},0}(0)}\right) - \ln\left(\frac{\beta'\,I_{\mathrm{P},0}(z) + \alpha'_{\mathrm{P}}}{\beta'\,I_{\mathrm{P},0}(0) + \alpha'_{\mathrm{P}}}\right) = -\alpha'_{\mathrm{P}}\,z \;.$$

By defining the so-called **effective length of the nanowire** [73] as

$$\boxed{L_{\mathrm{eff}} = \frac{1 - e^{-\alpha'_{\mathrm{P}}L}}{\alpha'_{\mathrm{P}}}}\;, \tag{3.8} \qquad L_{\mathrm{eff}}$$

we obtain an equation for the pump intensity at the exit of the nanowire (i.e., at $z = L$),

$$I_{\mathrm{P},0}(L) = I_{\mathrm{P},0}(0)\,\frac{e^{-\alpha'_{\mathrm{P}}L}}{(1 \,+\, \beta'\,L_{\mathrm{eff}}\,I_{\mathrm{P},0}(0))} \;. \tag{3.9}$$

For simplicity, we summarize the factors in the denominator as the **X parameter**

$$\boxed{X_{\mathrm{P}} = \beta'\,L_{\mathrm{eff}}\,I_{\mathrm{P},0}(0) = f_{\mathrm{P}}^4\,\beta_{\mathrm{TPA}}\,L_{\mathrm{eff}}\,I_{\mathrm{P},0}(0)}\;, \tag{3.10} \qquad X_{\mathrm{P}}$$

which is, for a given nanowire and its properties, essentially a measure of the initial pump intensity $I_{\mathrm{P},0}(0)$. By inserting this definition into Eq. (3.9), we find an equation of the **evolution of the pump intensity** in the nanowire,

$$\boxed{I_{\mathrm{P},0}(L) = I_{\mathrm{P},0}(0)\,\frac{e^{-\alpha'_{\mathrm{P}}L}}{(1 \,+\, X_{\mathrm{P}})}}\;, \tag{3.11}$$

which describes the pump intensity at the position $z = L$ as a function of the intensity at $z = 0$, the linear attenuation coefficient α'_{P}, and the parameter X_{P}.

Raman amplification of the probe beam

With the above solution for the pump intensity, we can solve the propagation equation of the Stokes wave. We insert Eqs. (3.10) and (3.11) into Eq. (3.6) and obtain

$$\frac{\mathrm{d}I_{\mathrm{S}}}{I_{\mathrm{S}}} = \alpha'_{\mathrm{P}}\,(\gamma' - 2\beta'_{\mathrm{X}})\,I_{\mathrm{P},0}\,\frac{e^{-\alpha'_{\mathrm{P}}z}\,\mathrm{d}z}{\alpha'_{\mathrm{P}} + \beta'\,I_{\mathrm{P},0}(0)\,(1 - e^{-\alpha'_{\mathrm{P}}z})} - \alpha'_{\mathrm{S}}\,\mathrm{d}z \;. \tag{3.12}$$

This equation can be integrated directly, yielding

$$\ln\left(\frac{I_{\mathrm{S}}(z)}{I_{\mathrm{S}}(0)}\right) = \alpha'_{\mathrm{P}}\,(\gamma' - 2\beta'_{\mathrm{X}})\,I_{\mathrm{P},0}\,J - \alpha'_{\mathrm{S}}\,z \;, \tag{3.13}$$

where the symbol J stands for

$$J = \int_0^L \frac{e^{-\alpha'_P z}}{\alpha'_P + \beta' I_{P,0}(0)\,(1 - e^{-\alpha'_P z})}\,\mathrm{d}z\;.\qquad(3.14)$$

The above integration has the solution

$$J\;=\;\frac{1}{\alpha'_P\,\beta'\,I_{P,0}}\;\ln\left(1 + \beta'\,I_{P,0}\,L_{\mathrm{eff}}\right)\;=\;\frac{1}{\alpha'_P\,\beta'\,I_{P,0}}\;\ln\left(1 + X_P\right),\qquad(3.15)$$

so that Eq. (3.13) yields an equation describing the **evolution of the Stokes intensity** in the nanowire,

$$\boxed{\ln\left(\frac{I_S(L)}{I_S(0)}\right) = \frac{\gamma'_R - 2\,\beta'_X}{\beta'}\,\ln\left(1 + X_P\right)\;-\;\alpha'_S L}\;.\qquad(3.16)$$

This means that we can plot the ratio $I_S(L)/I_S(0)$ as a function of $(1+X_P)$ in a log-log scale and, if the Raman gain γ' and the two photon absorption coefficients β', β'_X are independent of the parameter X_P (i.e., independent of the pump intensity $I_{P,0}(0)$), we shall obtain a straight line whose properties are illustrated in Fig. 3.1 (the linear attenuation coefficient is assumed to be independent of X_P and $I_{P,0}(0)$). The slope of the straight line is given by $(\gamma'_R - 2\beta'_X)/\beta'$, and its y-intercept is $-\alpha'_S L$.

If we want to plot this graph based on the data of a experiment with a real nanowire sample, we face the problem that it is usually very difficult or even impossible to know the pump and Stokes intensities inside the waveguide. Therefore, it is necessary to find a way to determine X_P as a function of the injected pump power P_{Pin}, as is described in the following.

Fig. 3.1. Illustration of Eq. (3.16), showing $I_S(L)/I_S(0)$ as a function of $(1 + X_P)$ in a log-log scale. The parameter X_P is proportional to the initial pump intensity $I_P(0)$. The slope and the y-intercept of the line yield some information about the Raman gain, the two-photon absorption coefficient, and the linear attenuation in the nanowire.
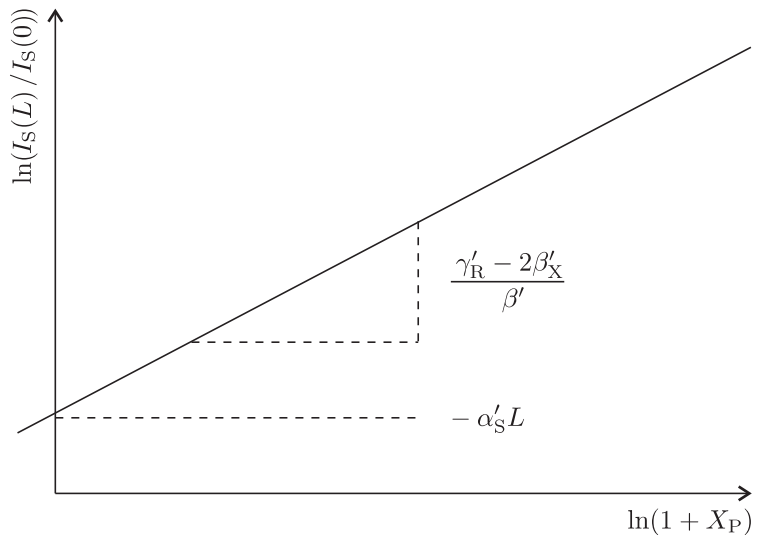
3.1.3 Model of the Raman amplification experiments

In a next step, we extend the above model to describe the pump-probe experiments with a nanowire sample. This means that we take into account the injection of the two beams into the nanowire and the extraction of the light at the exit of the sample. Furthermore, we consider both pump and probe wave as pulsed laser beams consisting of pulses with durations τ_P and τ_S, respectively, and a common repetition rate F. The principle of the experimental setup is illustrated in Fig. 3.2. The incident average power P_{Pin} of the pump beam is coupled into the nanowire (i.e., the sample)

$\tau_P,\ \tau_S,\ F$
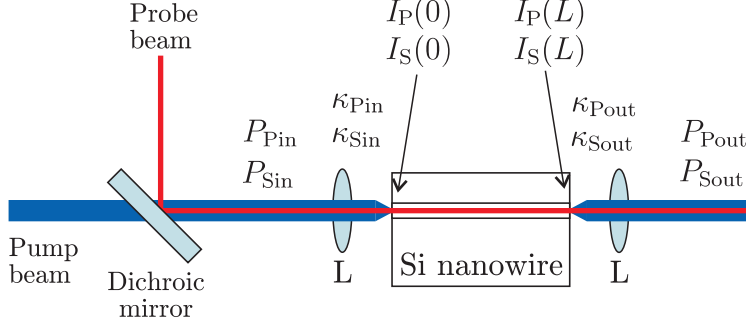
Fig. 3.2. Schematical experimental setup of the pump-probe experiments showing the injection and extraction of the pump and the probe beam. L lens. For details see text.

with a coupling efficiency κ_{Pin}. Thus, according to Eq. (2.85), the peak intensity in the waveguide is given by $I_{\mathrm{P},0}(0) = \kappa_{\mathrm{Pin}} P_{\mathrm{Pin}}/A_{\mathrm{eff}} \tau_{\mathrm{P}} F$, where A_{eff} is the effective mode area. A lens behind the exit of the waveguide collects the pump light with a coupling efficiency κ_{Pout}. Altogether, this can be described by the following set of equations

$$I_{\mathrm{P},0}(0)\, A_{\mathrm{eff}} = \kappa_{\mathrm{Pin}}\, P_{\mathrm{Pin}}/\tau_{\mathrm{P}}\, F \qquad (3.17\mathrm{a})$$

$$P_{\mathrm{Pout}}/\tau_{\mathrm{P}}\, F = \kappa_{\mathrm{Pout}}\, I_{\mathrm{P},0}(L)\, A_{\mathrm{eff}}\,, \qquad (3.17\mathrm{b})$$

where L is the length of the nanowire waveguide. Similarly, the injected and extracted power of the probe beam (which corresponds to the Stokes wave) is given by

$$I_{\mathrm{S}}(0)\, A_{\mathrm{eff}} = \kappa_{\mathrm{Sin}}\, P_{\mathrm{Sin}}/\tau_{\mathrm{S}}\, F \qquad (3.18\mathrm{a})$$

$$P_{\mathrm{Sout}}/\tau_{\mathrm{S}}\, F = \kappa_{\mathrm{Sout}}\, I_{\mathrm{S}}(L)\, A_{\mathrm{eff}}\,. \qquad (3.18\mathrm{b})$$

It should be noted that in this notation, all powers P are actually **average powers**, while the intensities I represent **peak intensities**. This notation makes sense because the experimentally measurable quantities are *average* powers (we work with a repetition rate of $F = 80$ MHz), whereas the physical nonlinear effects depend on the *peak* intensities, not on average values.

Probe (Stokes) intensity as a function of the X parameter

With the above coupling efficiencies, we find

$$\ln\left(\frac{I_{\mathrm{S}}(L)}{I_{\mathrm{S}}(0)}\right) = \ln\left(\frac{P_{\mathrm{Sout}}}{P_{\mathrm{Sin}}}\right) - \ln\left(\kappa_{\mathrm{Sin}}\,\kappa_{\mathrm{Sout}}\right), \qquad (3.19)$$

which yields, by inserting Eq. (3.16), an equation describing the ratio of the output power to the input power of the probe beam,

$$\ln\left(\frac{P_{\mathrm{Sout}}}{P_{\mathrm{Sin}}}\right) = \frac{\gamma_{\mathrm{R}}' - 2\,\beta_{\mathrm{X}}'}{\beta'}\,\ln\left(1 + X_{\mathrm{P}}\right) - \alpha_{\mathrm{S}}' L + \ln\left(\kappa_{\mathrm{Sin}}\,\kappa_{\mathrm{Sout}}\right). \qquad (3.20)$$

We summarize the last two terms as

$$-\alpha_{\mathrm{S}}' L + \ln\left(\kappa_{\mathrm{Sin}}\,\kappa_{\mathrm{Sout}}\right) = \ln\left(\kappa_{\mathrm{Sin}}\,\kappa_{\mathrm{Sout}}\, e^{-\alpha_{\mathrm{S}}' L}\right) = \ln\left(\kappa_{\mathrm{S}}\right), \qquad (3.21)$$

where we have introduced the **total end-to-end loss of the probe beam** as κ_{S}

$$\boxed{\kappa_{\mathrm{S}} = \kappa_{\mathrm{Sin}}\,\kappa_{\mathrm{Sout}}\, e^{-\alpha_{\mathrm{S}}' L}}\,. \qquad (3.22)$$

Thus, Equation (3.20) can be written in the form

$$\ln\left(\frac{P_{\text{Sout}}}{P_{\text{Sin}}}\right) = \frac{\gamma_{\text{R}}' - 2\,\beta_{\text{X}}'}{\beta'}\,\ln\left(1 + X_{\text{P}}\right) \,+\, \ln\left(\kappa_{\text{S}}\right)\,, \tag{3.23}$$

where the parameter X_{P} is a measure of the input pump power P_{Pin} according to

$$X_{\text{P}} \,=\, \beta'\,L_{\text{eff}}\,I_{\text{P},0}(0) \,=\, \frac{\beta'\,L_{\text{eff}}\,\kappa_{\text{Pin}}}{A_{\text{eff}}\,\tau_{\text{P}}\,F}\,P_{\text{Pin}}\,. \tag{3.24}$$

Like Eq. (3.16), we can plot Eq. (3.23) as a function of the parameter $(X_{\text{P}} + 1)$ in a log-log graph, yielding a straight line whose slope is determined by the Raman gain and the two photon absorption and whose y-intercept is given by the linear losses.

Method for the determination of the X parameter

In order to determine X_{P} as a function of P_{Pin}, we insert the coupling efficiencies of the pump beam, given by Eq. (3.17), into Eq. (3.11) and obtain

$$P_{\text{Pout}} \,=\, \frac{\kappa_{\text{Pin}}\kappa_{\text{Pout}}\,e^{-\alpha_{\text{P}}'L}}{1 + X_{\text{P}}}\,P_{\text{Pin}} \,=\, \frac{\kappa_{\text{P}}}{1 + X_{\text{P}}}\,P_{\text{Pin}}\,, \tag{3.25}$$

κ_{P} where we have also introduced the **total end-to-end loss of the pump beam** as

$$\kappa_{\text{P}} = \kappa_{\text{Pin}}\kappa_{\text{Pout}}\,e^{-\alpha_{\text{P}}'L}\,. \tag{3.26}$$

We write Eq. (3.25) in the form

$$\frac{P_{\text{Pin}}}{P_{\text{Pout}}} \,=\, \frac{1}{\kappa_{\text{P}}}\left(1 + X_{\text{P}}\right) \,=\, \frac{1}{\kappa_{\text{P}}} \,+\, \frac{\beta'\,L_{\text{eff}}\,\kappa_{\text{Pin}}}{A_{\text{eff}}\,\tau_{\text{P}}\,F\,\kappa_{\text{P}}}\,P_{\text{Pin}}\,, \tag{3.27}$$

which corresponds to a straight line. Thus, by plotting the ratio of the input pump power to the pump power measured behind the nanowire (both experimentally accessible) for different input powers, we shall see a linear dependence that can be fitted by a function of the type $y = a + b\,x$, as is schematically illustrated in Fig. 3.3. As a result, we can calculate an experimentally determined value of the parameter X_{P} for each input pump power P_{Pin} according to

$$X_{\text{P}} \,=\, \kappa_{\text{P}}\,\frac{P_{\text{Pin}}}{P_{\text{Pout}}} \,-\, 1 \,=\, \frac{1}{a}\left(a + b\,P_{\text{Pin}}\right) - 1 \,=\, \frac{b}{a}\,P_{\text{Pin}}\,, \tag{3.28}$$

where a and b are the resulting fit parameters. These values of X_{P} can then be used to plot and analyze the experimental data of the probe beam according to Eq. (3.23).

Fig. 3.3. Illustration of Eq. (3.27). The ratio $P_{\text{Pin}}/P_{\text{Pout}}$ is plotted as a function of the input pump power P_{Pin}, yielding a straight line. We can use this linear dependence to determine the value of X_{P} for each input pump power P_{Pin}.
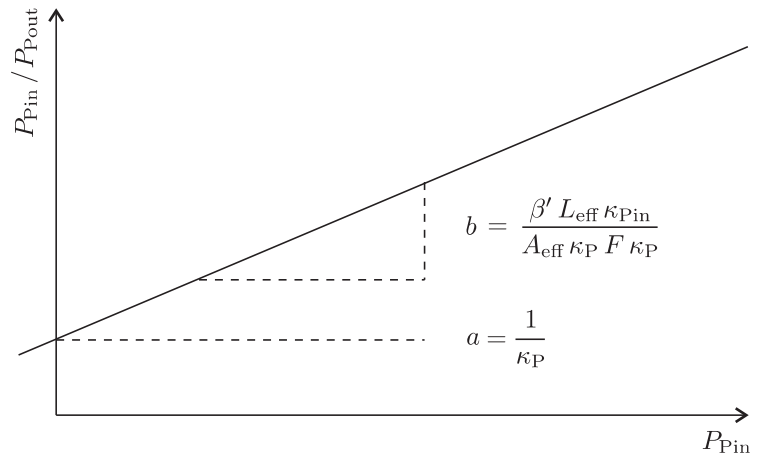
3.2 SOI sample and experimental setup

In this section we present the silicon-on-insulator (SOI) sample that is used for the experiments. Furthermore, this section describes the light source that delivers the pump and probe pulses as well as the data acquisition and processing that is used to obtain the experimental results presented in section 3.4. As is explained in more detail in section 3.3, part of the experimental setup is also used for the determination of the linear attenuation of the waveguide.

3.2.1 Silicon-on-insulator (SOI) nanowire sample

The sample that is used for the experiments has been specifically designed for this research project. In this section, we present the preliminary considerations that have lead to the actual design of the sample. Moreover, the fabricated sample that is actually used for the experiments is described.

Considerations regarding the sample design

As has been shown in section 2.2.2, the Raman gain depends on the polarization states of the pump and the Stokes wave with respect to the crystallographic axes of the semiconductor material. This dependence is described by the scattering efficiency Σ given by Eq. (2.38) as

$$\Sigma = \sum_{l=1}^{3} \left[\hat{e}_\mathrm{P} \, R^l \, \hat{e}_\mathrm{S} \right]^2 , \tag{3.29}$$

where the $\hat{e}_\mathrm{P}$ and $\hat{e}_\mathrm{S}$ are the polarization vectors of pump and Stokes wave and the R^l matrices are defined by Eq. (2.39). We suppose in the following that the nanowires are fabricated on an [001] surface of a silicon waver. Moreover, we assume that the polarization vectors of pump and probe are purely transverse and that the wave vectors of pump and probe are parallel (i.e., collinear propagation). This leads to the following expressions for the propagation vector $\hat{k} = \hat{k}_\mathrm{P} = \hat{k}_\mathrm{S}$ and the unit vectors $\hat{e}_\mathrm{TE}$ and $\hat{e}_\mathrm{TM}$, which correspond to the polarization directions of the TE mode and the TM mode of the waveguides :

$$\hat{k} = \begin{pmatrix} \cos\varrho \\ \sin\varrho \\ 0 \end{pmatrix} \qquad \hat{e}_\mathrm{TE} = \begin{pmatrix} \sin\varrho \\ -\cos\varrho \\ 0 \end{pmatrix} \qquad \hat{e}_\mathrm{TM} = \begin{pmatrix} 0 \\ 0 \\ 1 \end{pmatrix} ,$$

where ϱ is the angle between the propagation direction $\hat{k}$ and the crystallographic direction [100]. The relationships between these vectors are illustrated in Fig. 3.4.
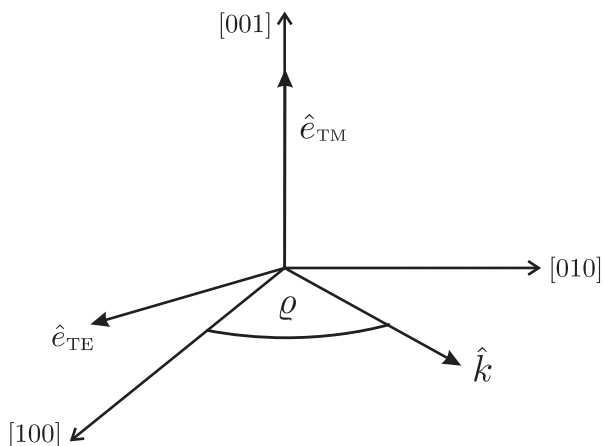

Fig. 3.4. Illustration of the relationship between the vector $\hat{k}$ (i.e., the propagation direction of pump and the probe beam) and the polarization vectors of the TE and the TM mode of the silicon waveguide. The latter is assumed to be parallel to an [001] surface.

The above definitions satisfy the orthogonality conditions $\hat{k}\cdot\hat{e}_{\mathrm{TE}} = 0$, $\hat{k}\cdot\hat{e}_{\mathrm{TM}} = 0$, and $\hat{e}_{\mathrm{TE}} \cdot \hat{e}_{\mathrm{TM}} = 0$. Based on these definitions, we can calculate the scattering efficiency Σ for four different cases.

- **TM-TM :** In this case, we consider both pump and Stokes wave as TM-polarized, and we set $\hat{e}_{\mathrm{P}} = \hat{e}_{\mathrm{TM}}$ and $\hat{e}_{\mathrm{S}} = \hat{e}_{\mathrm{TM}}$. By inserting this into Eq. (3.29), we calculate the scattering efficiency $\boxed{\Sigma \equiv 0,}$ which is independent of the angle ϱ of the propagation direction.

- **TM-TE :** In this case, we consider the probe wave as TE-polarized, which is expressed by $\hat{e}_{\mathrm{P}} = \hat{e}_{\mathrm{TM}}$ and $\hat{e}_{\mathrm{S}} = \hat{e}_{\mathrm{TE}}$. The resulting scattering efficiency is $\boxed{\Sigma \equiv 1}$, which is again independent of the angle ϱ.

- **TE-TM :** This is the inverse of the previous case, expressed by $\hat{e}_{\mathrm{P}} = \hat{e}_{\mathrm{TE}}$ and $\hat{e}_{\mathrm{S}} = \hat{e}_{\mathrm{TM}}$, yielding a scattering efficiency of $\boxed{\Sigma \equiv 1.}$ As in the previous two cases, the result is independent of ϱ.

- **TE-TE :** This last combination, given by $\hat{e}_{\mathrm{P}} = \hat{e}_{\mathrm{TE}}$ and $\hat{e}_{\mathrm{S}} = \hat{e}_{\mathrm{TE}}$, yields a scattering efficiency of $\boxed{\Sigma = \sin^2(2\varrho),}$ which obviously depends on the propagation direction defined by ϱ. Thus, $\boxed{\text{for } \varrho = \pi/4 = 45°,}$ we obtain the maximum value of $\boxed{\Sigma = 1}$, as in the previous two cases.

In conclusion, a propagation along the [110] direction (i.e., $\varrho = 45°$) offers the most flexible configuration. It enables us to excite the stimulated Raman scattering with three different combinations of the polarization directions (TM-TE, TE-TM, and TE-TE), and the scattering efficiency should be maximal ($\Sigma = 1$) in all three cases. Moreover, by using a TE polarized pump beam, we are sure to obtain a maximal scattering efficiency, no matter how the probe beam is polarized.

Silicon-on-insulator (SOI) sample used for the experiments

The sample that we use for the experiments has been fabricated by our collaboration partner David PEYRADE at the LTM in Grenoble [74]. On the sample, there are several identical silicon ridge waveguides on top of a 2-μm thick oxide layer (i.e., SiO$_2$), which in turn is deposited on a silicon substrate. All waveguides have a width of 500 nm and a height of 340 nm, which are both small compared to the wavelengths used (around 1.5 μm). This means that the effective mode area is only about $A_{\mathrm{eff}} \approx 0.17$ μm^2. The waveguides are 11 mm long, and the propagation
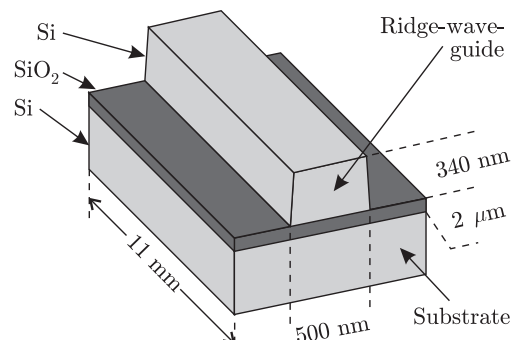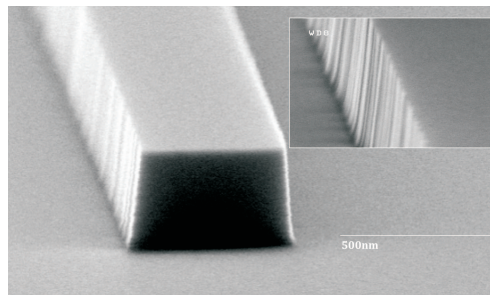

Fig. 3.5. Silicon-on-insulator (SOI) nanowire sample. SEM picture and schematic illustration showing the guide on top of the SiO$_2$ layer (insulator). The SOI sample provides several identical ridge waveguides of this type, which are all oriented along the crystallographic [110] direction, i.e., parallel to a [001] surface. The dimensions in the illustration are **not to scale**.

direction (i.e., the direction of the guides) is oriented along the [110] crystallographic direction of silicon. Figure 3.5 shows a SEM photo and an illustration of the structure of the SOI sample.

3.2.2 Synchronous hybrid picosecond light source

The pump and probe pulses are generated by a hybrid laser light source that is composed of a picosecond optical parametric oscillator (OPO) and an intensity-modulated tunable diode laser (telecom test laser). This section describes both components as well as the method that is used to synchronize the pulses with respect to each other, i.e., to control the time delay between the probe pulses and the pump pulses.

Picosecond optical parametric oscillator (OPO) as pump beam

The picosecond OPO has been previously designed and built as a general-purpose tunable light source for nonlinear characterization experiments [75]. It is synchronously pumped by a commercial mode-locked Ti:Sapphire laser (Spectra Physics TSUNAMI), which delivers Fourier-transform limited pulses of a duration of 10 picoseconds (FWHM) at a wavelength of 725 nm with a spectral width of $\Delta\lambda = 0.06$ nm, a repetition rate of $F = 80$ MHz, and maximum output power 1.7 W.

The OPO is designed as a ring cavity in a bow-tie geometry, as is illustrated in Fig. 3.6. It consists of a pair of concave mirrors CM, each with a radius of curvature of 25.9 cm, and a plane mirror PM. These elements have been chosen to be highly reflective in the 1300-1600 nm range. The cavity is singly resonant at the signal wavelength, for which the output coupler OC has a reflectivity of 80%. Due to the relatively long pulse duration, the dispersion of the mirrors and the output coupler can be considered negligible. The beam from the Ti:Sapphire laser is injected into the cavity through a lens with a focal length of 15 cm. The active medium of the OPO is a 20-mm long PPLN crystal, which is anti-reflection coated from 1300 to 1650 nm. The crystal period is 18 μm, and the temperature of the crystal can be controlled for the fine tuning of the signal wavelength. Both the signal and the idler wave are provided as output beams of the OPO with approximately equal power. The average output power of the OPO is up to 500 mW (total power of signal *and* idler), depending on the alignment of the mirrors and on the operating wavelengths. We use an optical spectrum analyzer (ANDO AQ6317B) to measure the spectral linewidth of the OPO as 0.25 nm. Because of the repetition rate of 80 MHz, the OPO represents a *quasi-continuous* light source. Therefore, all power measurements in the remainder of this chapter are average powers, which is consistent with the model presented in section 3.1.3.
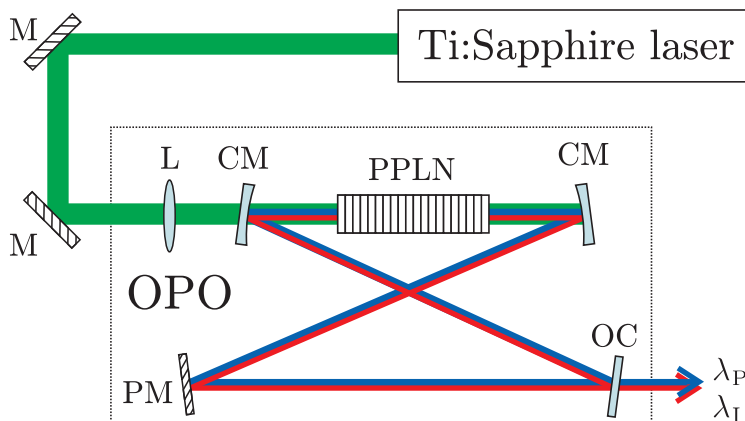

Fig. 3.6. Optical parametric oscillator (OPO) generating the pump pulses for the pump-probe experiments. CM concave mirrors, L lens, PM plane mirror, OC output coupler, PPLN periodically poled lithium niobate crystal, λ_P pump wavelength, and λ_I idler wavelength. The drawing is not to scale.

Synchronously modulated tunable diode laser as probe beam

The preparation of the probe beam has been developed specifically for the experiments presented in this chapter. In order to use the beam for Raman amplification measurements, we need a very high precision regarding the wavelength tuning. As mentioned above, we consider the zone center optical phonon of silicon with a Raman frequency of $\nu_R = 15.6$ THz and a linewidth of $\Delta\nu_R = 105$ GHz [39]. Thus, for a given pump wavelength λ_P, the probe wavelength has to be controlled with a relative accuracy of 105 GHz/15.5 THz $\approx 10^{-2} = 1\%$.

Therefore, the probe beam is generated by a commercial tunable diode laser (NetTest TUNICS-PRI) that emits a single-frequency continuous-wave laser beam at a freely tunable wavelength in the range between 1530 and 1600 nm. Its fiber-coupled output is connected to a polarization maintaining fiber and is then coupled into a LiNbO$_3$ intensity modulator from EOSPACE (see also illustration in Fig. 3.8). The LiNbO$_3$ modulator is driven by a synchronization signal (sync) coming from the OPO output. For this purpose, we use the idler beam from the OPO that is transmitted by a dichroic mirror behind the OPO output. The idler beam is then injected into a single mode fiber that is connected to a fast photodetector of the type PP10G from Nortel with a 12-GHz bandwidth. The electrical signal from this photodetector is superimposed with a constant DC voltage of 4.4 V in a so-called "bias T" (or "bias tee") from Picosecond Pulse Labs and then connected to the RF input of the modulator. The optical output of the modulator (i.e., the 80-MHz modulated diode laser signal) is extracted by a lens and serves as the probe beam for the pump-probe experiments. To set the correct polarization, the probe beam passes a half-wave plate and a Glan-Taylor polarizer.

In order to determine the pulse duration of the probe pulses, we use a fiber-coupled fast photodetector of the type Agilent 83440C (20 GHz bandwidth) and a fast digital oscilloscope of the type Tektronix CSA 8000, including a high-speed sampling module

Fig. 3.7. Typical time dependence of the probe pulses.

(a) Two probe pulses follow each other with a delay of 12.5 ns (corresponding to the repetition rate of the hybrid light source of $F = 80$ MHz).

(b) The main peak has a pulse duration (FWHM) of 150 ps.
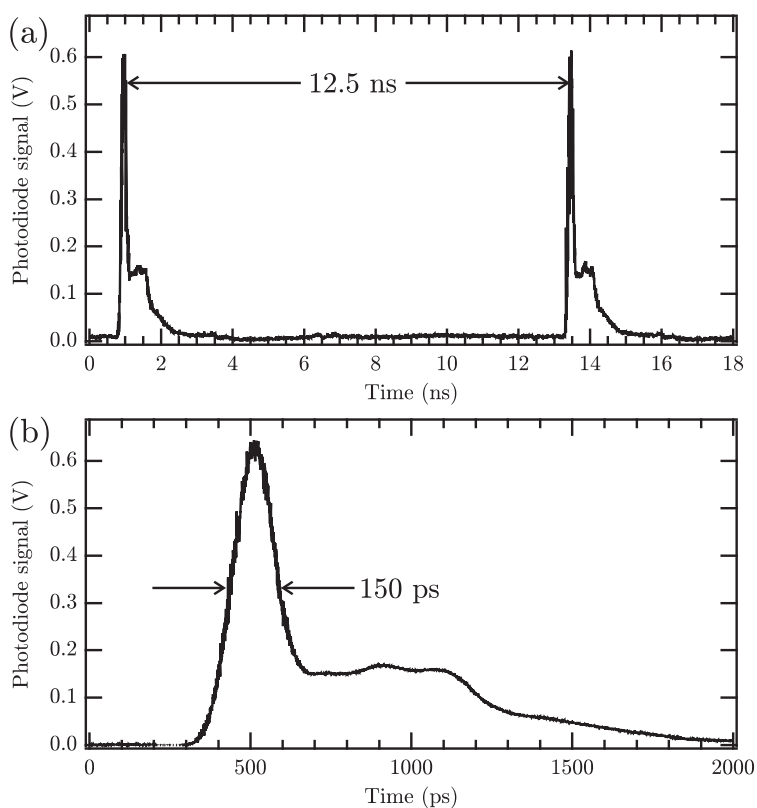
with a 100-ps time resolution. The measured time dependence of the probe pulses is shown in Fig. 3.7 with two different time resolutions. As can be seen from the upper graph, the time difference between two consecutive probe pulses is 12.5 nm, which is consistent with the synchronization with the pump pulses at the repetition rate of 80 MHz. As the high-resolution measurement in the lower graph shows, the main peak has a duration of about 150 ps. It is followed by a 850-ps long plateau that is caused by a saturation of the photodetector, which leads to a longer relaxation time. In the following, we consider only the main peak of the probe pulses.

In summary, the above-described hybrid picosecond light source provides two synchronized pulsed laser beams. The wavelengths of the two beams can be tuned independently; the pulse durations are 15 ps (pump) and 150 ps (probe). The linewidth of the pump beam is about 0.25 nm, whereas the linewidth of the probe beam is about 0.03 nm. The average power of the probe beam is 10 mW, and the average output power of the OPO (pump beam) is several hundreds of milliwatts.

3.2.3 Pump-probe setup and data acquisition

As is illustrated in Fig. 3.8, the light from the OPO is guided to an optical delay line consisting of four mirrors. Two of these mirrors can be translated, in order to increase or decrease the optical path for the pump beam. Given that the pump pulses and the probe pulses have a fixed phase relation to each other, we can control the temporal overlap between the pump and the probe pulses by adjusting the position r of the movable mirrors.

After the delay line, the light is injected into a single mode fiber whose other end is connected to the experimental pump-probe setup. The light is extracted from the fiber and passes a combination of a half-wave plate and a Glan-Taylor polarizer. The latter fixes the polarization state of the pump pulses, whereas the former can be used to control the pump power (or intensity, respectively).

In a next step, the two beams have to be spatially superimposed for the pump-probe experiments. This spatial superposition is achieved in free space through a dichroic mirror. The pulses of both beams are then injected into the nanowire sample using a microscope objective with a numerical aperture of 0.85. An identical microscope objective is used to collect the transmitted light at the output of the waveguide. The collected light is injected into a single-mode fiber that is connected to an optical spectrum analyzer (OSA), which is an ANDO AQ6317B with a 0.01-nm spectral resolution. By selecting the wavelength range of the OSA, we can record spectra of the transmitted pump and probe beams. The input polarization of the pump pulses is chosen to excite the TE modes of the waveguide, whereas TM polarization is used for the probe pulses. We experimentally observed a slightly better Raman amplification efficiency for this polarization configuration than for the pump and probe beams being polarized along the TE-TE or TM-TE directions.

The dichroic mirror that is used for the superposition of the two beams does not reflect all of the pump light. Therefore, we can use the weak transmitted part to monitor the input pump power P_{Pin} during the experiments. The average power is read manually with a calibrated power meter. The output spectra are recorded with the optical spectrum analyzer and saved in data files for further data processing.
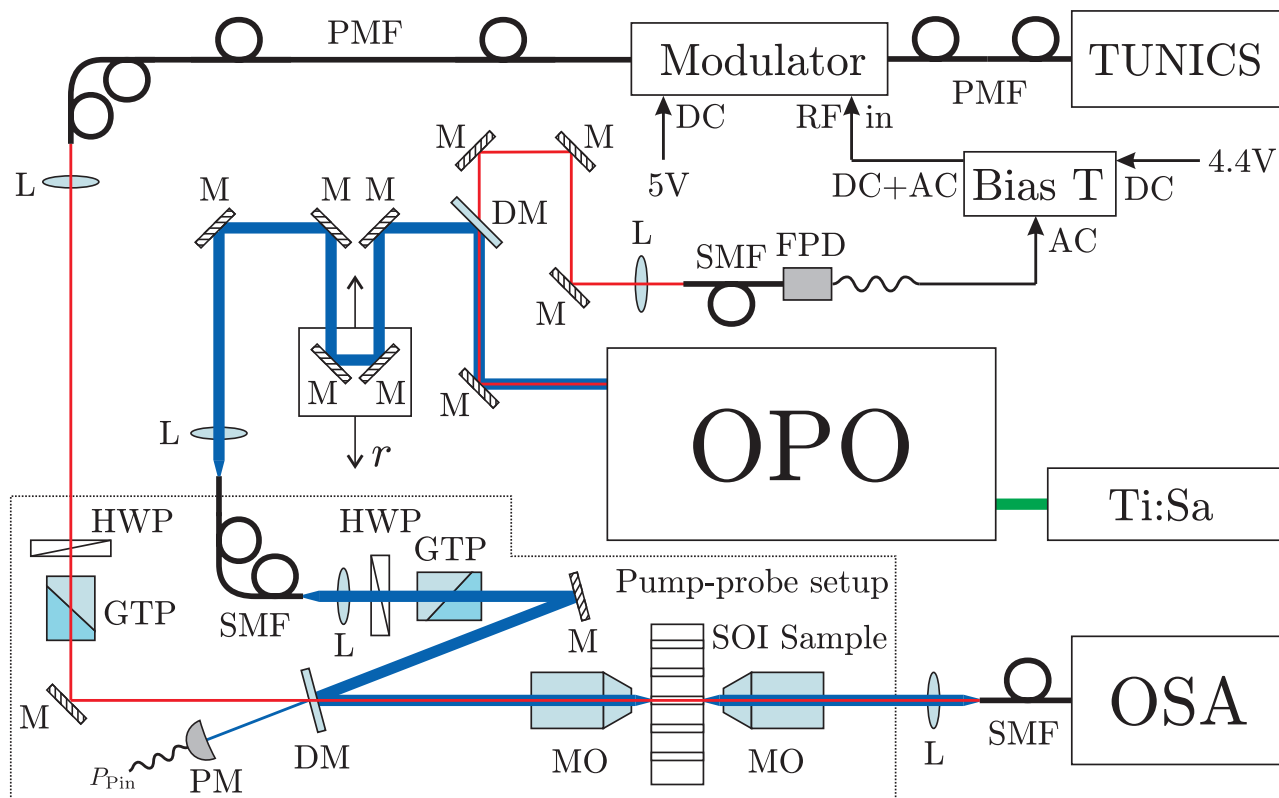
Fig. 3.8. Experimental setup for the pump-probe experiments with the silicon nanowire. The synchronous hybrid light source consists of an optical parametric oscillator (OPO) delivering the pump pulses and a cw tunable diode laser (TUNICS), which is intensity-modulated by a LiNbO₃ modulator to generate the probe pulses. M mirror, L lens, SMF single mode fiber, PMF polarization maintaining fiber, FPD fast photo detector (fiber-coupled), HWP half wave plate, GTP Glan-Taylor polarizer, DM dichroic mirror, MO microscope objective, PM calibrated power meter measuring the input pump power P_{Pin}, OSA optical spectrum analyzer. The dimensions are not to scale. For more details see text.

3.3 Linear characterization of the silicon nanowire

Before presenting the experimental results of the *nonlinear* pump-probe experiments in section 3.4, we characterize the *linear* optical properties of the silicon nanowire in a preliminary experiment. As a result, we determine the linear attenuation coefficient α' and the local field factor f_{S} at the Stokes wavelength.

3.3.1 Fabry-Perot transmission spectra of the nanowire

According to our collaboration partners who have designed and simulated the SOI sample, the entry and the exit facet of the waveguide have reflectivities of about 30 %[2]. Thus, we can consider the silicon nanowire as a low-finesse Fabry-Perot resonator whose mirrors are actually the two facets of the guide.

Thus, if we inject a weak monochromatic laser beam into the waveguide, we can measure its linear transmission coefficient as a function of the wavelength of the laser beam (linear transmission spectroscopy). As a result, we shall obtain a typical Fabry-Perot fringe pattern that can be used to determine the absorption coefficient in the waveguide. The transmission of a Fabry-Perot cavity containing a medium

---

[2]Calculation by Philippe Lalanne of the group NAPHEL at the LCFIO.

with a non-zero linear attenuation can be described by[3]

$$T = \frac{T_1 T_2 \, e^{-\alpha' L}}{\left| 1 - \sqrt{R_1 R_2} \, e^{-\alpha' L} \, e^{2i\varphi} \right|^2} \, , \tag{3.30}$$

where α' is the linear attenuation (or absorption) coefficient, and where we have assumed that the wave is injected and propagates at normal incidence to the facets (i.e., the angle of incidence is $\vartheta = 0$), which implies that $l = L$. By expanding the square of the absolute value in the denominator, Eq. (3.30) can be written in the form

$$T = \frac{T_1 T_2 \, e^{-\alpha' L}}{1 + R_1 R_2 e^{-2\alpha' L} - 2\sqrt{R_1 R_2} \, e^{-\alpha' L} \, \cos(2\varphi)} \, .$$

With the reflectivities of $R_1 = R_2 = 30\,\%$, we find $R_1 R_2 \ll 1$. Therefore, we ignore in the following the second term in the denominator, yielding

$$T \approx \frac{T_1 T_2 \, e^{-\alpha' L}}{1 - 2\sqrt{R_1 R_2} \, e^{-\alpha' L} \cos(2\varphi)} \, . \tag{3.31}$$

This can be further simplified by assuming that the last term in the denominator is small compared to 1, i.e.,

$$2\sqrt{R_1 R_2} \, e^{-\alpha' L} \, \cos(2\varphi) \ \ll \ 1 \, .$$

In that case, we can expand Eq. (3.31) in a power series and obtain

$$T \approx T_1 T_2 \, e^{-\alpha' L} \left(1 + 2\sqrt{R_1 R_2} \, e^{-\alpha' L} \cos(2\varphi) \right) .$$

The transmission coefficient T is defined as the ratio between the transmitted and the incident optical power,

$$T = \frac{P(L)}{P(0)} \, .$$

By using the coupling efficiencies κ_{in} and κ_{out}, which take into account the coupling losses due to the injection and the extraction of the light,

$$P(0) = \kappa_{\text{in}} \, P_{\text{in}} \qquad \text{and} \qquad P_{\text{out}} = \kappa_{\text{out}} \, P(L) \, ,$$

we can describe the output power by the expression

$$P_{\text{out}} = \frac{\kappa_{\text{out}}}{\kappa_{\text{in}}} \, P_{\text{in}} \, T_1 T_2 \, e^{-\alpha' L} \left(1 + 2\sqrt{R_1 R_2} \, e^{-\alpha' L} \cos(2\varphi) \right) , \tag{3.32}$$

where P_{in} is the incident power before the injection into the nanowire. The phase of the cosine function is given by

$$2\varphi = 2\pi \frac{\lambda}{\Delta\lambda_{\text{M}}} + \varphi_0 \, ,$$

where $\Delta\lambda_{\text{M}}$ is the mode spacing between the resonator modes, i.e., the free spectral range of the cavity given in the wavelength domain. Thus, the output power P_{out} given by Eq. (3.32) is a function of the wavelength λ. It represents a cosine function with an offset

$$P_0 = (\kappa_{\text{out}}/\kappa_{\text{in}}) \, P_{\text{in}} \, T_1 T_2 \, e^{-\alpha' L} \, ,$$

---

[3]See also appendix B, where we show a complete derivation of this equation in the case of an optical gain G instead of an attenuation $-\alpha'$, given by Eq. (B.5).

which corresponds to the power that is transmitted after one single propagation through the waveguide. By defining the modulation amplitude

$$\widetilde{m} = 2\sqrt{R_1 R_2}\, e^{-\alpha' L}\,, \tag{3.33}$$

we can write Eq. (3.32) as

$$P_{\text{out}} = P_0 + P_0\, \widetilde{m}\, \cos\left(2\pi \frac{\lambda}{\Delta\lambda_{\text{M}}} + \varphi_0\right). \tag{3.34}$$

Since we know the mirror reflectivities R_1 and R_2, as well as the cavity length L, we can use Eq. (3.33) to calculate the linear attenuation coefficient by determining the modulation amplitude $\widetilde{m}$. In order to do that, we use the Fourier transformation.

It is clear that the Fourier spectrum of Eq. (3.34) should contain two frequency components : a DC component at $\omega = 0$ and a component at the modulation frequency $\omega_{\text{M}} = 2\pi/\Delta\lambda_{\text{M}}$, which corresponds to the Fabry-Perot oscillations (i.e., the constructive and destructive interferences). By comparing the heights of these two components, we can determine the modulation amplitude $\widetilde{m}$ even without knowing the power P_0. In the following, we use this method on some experimental data in order to determine the linear attenuation coefficient α'.

The mode spacing $\Delta\lambda_{\text{M}}$ is a measure for the group refractive index of the waveguide according to

$$n_{\text{gr}} = \frac{1}{2L} \frac{\lambda^2}{\Delta\lambda_{\text{M}}}. \tag{3.35}$$

Thus, by comparing the Fourier frequency ω_{M} of the measured Fabry-Perot fringes to the Fourier frequency ω'_{M} of a reference function given by Eq. (3.34) with a known mode spacing $\Delta\lambda'_{\text{M}}$, we can also determine the group refractive index of the silicon nanowire at a given wavelength λ. From the group refractive index, we can then derive the local field factor f at that wavelength.

3.3.2   Measurement of attenuation and local field factor

We use the experimental setup illustrated in Fig. 3.9 to measure the transmitted power of the silicon nanowire as a function of the wavelength of the injected light (linear transmission spectroscopy). The light source is a single-frequency cw diode laser (ANDO AQ4320D), which can be freely tuned between 1540 and 1580 nm. The fiber-coupled output of the laser is connected to a polarization maintaining fiber. At

Fig. 3.9. Experimental setup for the linear characterization of the silicon nanowire. The optical spectrum analyzer (OSA) commands the tunable diode laser through the data link cable. This allows for automatic transmission spectroscopies of the silicon nanowire. L lens, MO microscope objective, PMF polarization maintaining fiber, SMF single mode fiber.
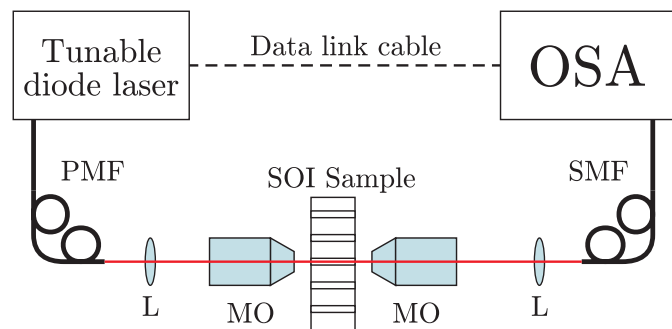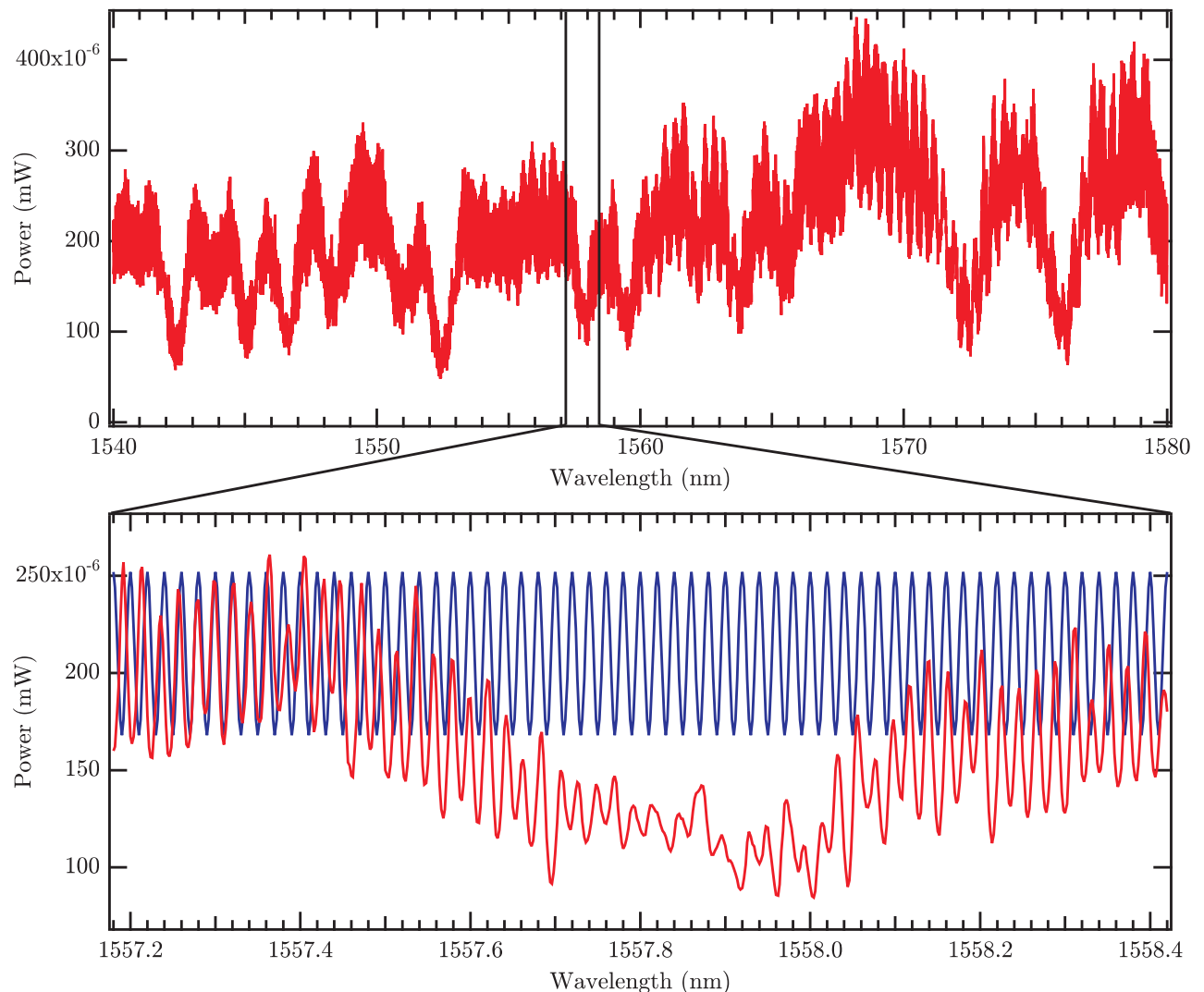
Fig. 3.10. Fabry-Perot fringes of the silicon nanowire, i.e., output power as a function of the wavelength. *Top:* Full range between 1540 and 1580 nm with a wavelength resolution of 0.002 nm. *Bottom:* Zoom between 1557.2 and 1558.4 nm. The red traces represent the experimental data; the blue trace corresponds to a reference function whose parameters yield the same modulation characteristics as the experimental data, except for the modulation frequency, which is slightly different.

the other end of the fiber, the light is extracted with a lens (fiber collimator) and then injected into the nanowire sample through a microscope objective (the one described in section 3.2). We inject the beam in TM polarization. Behind the sample, the light is collected by another microscope objective and injected into a single mode fiber that is connected to an optical spectrum analyzer (OSA) of the type ANDO AQ6317B (as in section 3.2). It it worth noting that the microscope objectives are not anti-reflection coated. We can connect the OSA and the tunable diode laser with a data link cable, which allows for automatic transmission measurements over a user-defined wavelength range.

The experimental results, i.e., the measured linear transmission spectroscopy of the nanowire, are shown in the top panel of Fig. 3.10 between 1540 and 1580 nm with a wavelength resolution of 0.002 nm. The resolution is given by the minimum wavelength step of the tunable diode laser. The Fabry-Perot fringes (i.e., the intensity modulation) with the modulation frequency ω_M becomes visible in the zoom that is shown in the bottom panel. As can be seen from the graphs, the experimental

Fig. 3.11. Fourier spectrum of the Fabry-Perot fringes. The red trace corresponds to the experimental data, the blue trace shows the spectrum of the reference function. The inset shows a zoom on the two peaks at ω_M and ω'_M.
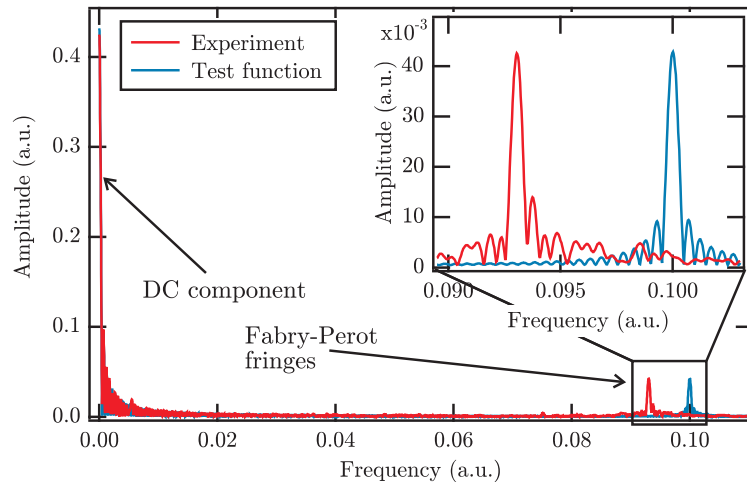
data do not exactly correspond to the theoretical function given by Eq. (3.34). They obviously contain some low frequency impurities which cause a slow variation of the envelope of the Fabry-Perot fringes. These impurities originate most probably from the fact that the microscope objectives are neither anti-reflection coated nor adapted to the wavelengths used. This might create some parasite reflections and also cause the injection quality to vary as a function of the wavelength.

Linear attenuation coefficient of the silicon nanowire

We perform a Fast Fourier Transform of the experimental data and obtain the corresponding Fourier spectrum, which is shown in Fig. 3.11. By comparing the height of the Fourier component at the frequency ω_M to the height of the DC component, we obtain the modulation amplitude of the Fabry-Perot fringes, which is

$$\widetilde{m} \; = \; 2 \times 0.099 \; \approx \; 0.20 \; . \tag{3.36}$$

The factor 2 is necessary because the data in Fig. 3.11 show only the nonnegative half of the of the FFT spectrum. Using Eq. (3.33) with the reflectivities $R_1 = R_2 = 30$ % and the resonator length $L = 1.1$ cm, we obtain a linear attenuation coefficient of

$$\alpha' \; = \; 1.0 \; \text{cm}^{-1} \; ,$$

which is in good agreement with published values for silicon nanowires at wavelengths around 1.5 μm [76]. We assume that the absorption coefficients for pump and probe wave are equal (i.e., $\alpha'_P = \alpha'_S$) so that the above result yields the **experimentally determined linear attenuation coefficient** for the pump and the probe beam

$$\boxed{\alpha'_P \; = \; \alpha'_S \; = \; 1.0 \; \text{cm}^{-1}} \; . \tag{3.37}$$

Group refractive index and local field factor at the Stokes wavelength

Besides the linear attenuation coefficient, we can extract from the experimental data the value of the group refractive index n_{gr} at the Stokes wavelength (i.e., of the probe beam). For this purpose we define a reference test function according to Eq. (3.34), whose parameters P'_0, $\widetilde{m}'$, and φ'_0 are such that they produce Fabry-Perot fringes with the same characteristics as the experimental data. The mode spacing $\Delta\lambda'_M$ is chosen as 0.02 nm, which yields a modulation frequency ω'_M that is slightly different from

the one of the experimental data. The reference function and its Fourier spectrum
are shown as the blue traces in Fig. 3.10 and Fig. 3.11, respectively.

As can be clearly seen in Fig. 3.11, the peak of the reference function in the
Fourier spectrum is at a frequency of $\omega'_{\mathrm{M}} = 0.1$, corresponding to a mode spacing
of $\Delta\lambda'_{\mathrm{M}} = 0.02$ nm. The Fourier peak of the experimental data in Fig. 3.11 is at
$\omega_{\mathrm{M}} = 0.0930$. Since the modulation frequency is given by $\omega_{\mathrm{M}} = 2\pi/\Delta\lambda_{\mathrm{M}}$, we can
calculate the corresponding mode spacing of the waveguide resonator as

$$\Delta\lambda_{\mathrm{M}} \;=\; \frac{0.1}{0.093}\, 0.02 \text{ nm} \;=\; 0.0215 \text{ nm} . \qquad (3.38)$$

Using this value of the mode spacing and a wavelength of $\lambda = 1558$ nm (which is
approximately the wavelength of the probe beam in section 3.4), we can calculate the
group refractive index of the silicon nanowire at the Stokes wavelength
according to Eq. (3.35), yielding

$$n_{\mathrm{gr}}(\lambda_{\mathrm{S}}) \;=\; 5.13 \;, \qquad (3.39)$$

which is in good agreement with published values for the wavelengths used [72]. With
a bulk refractive index of silicon of $n_{\mathrm{bulk}} = 3.48$ at 1.55 μm [77], we use Eq. (2.95)
to calculate the **local field factor of the Stokes wave** to be

$$\boxed{f_{\mathrm{S}} \;=\; \sqrt{\frac{n_{\mathrm{gr}}}{n_{\mathrm{bulk}}}} \;=\; 1.21} \;. \qquad (3.40)$$

Since the tunable diode laser used for this linear transmission spectroscopy cannot
emit light at wavelengths below 1530 nm, it is not possible to use the above-presented
setup to determine the group refractive index and the local field factor at the pump
wavelength. However, it is reasonable to assume that the local field factors of the
pump and the probe beam are approximately equal $f_{\mathrm{P}} \approx f_{\mathrm{S}}$ because the variation
between the pump and probe group velocities is expected to be less than 2 % [57]. In
addition to that, we present in the following section a method to estimate the value
of f_{P} using the transmitted nonlinear pump spectra.

3.4 Nonlinear pump-probe measurements of saturated Raman amplification due to self phase modulation of the pump beam

Using the SOI nanowire sample and the experimental setup described in section 3.2,
we have carried out a series of pump-probe experiments, whose results are presented
in this section.

3.4.1 Pump and probe spectra behind the nanowire

We have recorded the spectra of the pump and the probe beam after the passage
of the silicon nanowire for different input pump powers P_{Pin}, varying from 60 μW
to 120 mW (before the injection into the nanowire). The input pump wavelength
is set at $\lambda_{\mathrm{P}} = 1441.0$ nm, whereas the input probe wavelength λ_{S} and time delay
have been adjusted such as to maximize the Raman amplification. This optimum
has been found for a probe wavelength $\lambda_{\mathrm{S}} = 1558.2$ nm.

Measured spectra of pump and probe beam behind the nanowire

The resulting pump spectra and the probe spectra are shown in Fig. 3.12 for 29 different input pump intensities P_{Pin} between 7 mW and 120 mW. Since the facets of the waveguide are not anti-reflection coated (see section 3.3), the measured raw spectra contain small Fabry-Perot fringes.

As can be seen from Fig. 3.12(a), the pump spectra are broadened due to self phase modulation (SPM). This broadening obviously increases with increasing input pump power P_{Pin}. It originates from the combination of the Kerr effect and the TPA-induced free-carrier refraction (FCR). The intensity-dependent nonlinear phase shift induced by the Kerr effect is instantaneous and broadens the spectrum symmetrically, whereas the time-dependent buildup of the carrier density creates a nonlinear phase contribution that shifts the spectrum towards shorter wavelengths (blueshift) [78],[79].

In the probe spectra in Fig. 3.12(b), we can clearly see a narrow peak, which corresponds to the injected probe beam. This main peak appears to be identical in all probe spectra. Apart from that, there is a second spectral component that shows up on the left hand side (shorter wavelengths) of the main peak. It becomes stronger and larger as the pump power increases. Moreover, it is blueshifted with respect to the initial wavelength, and this blueshift also increases with the pump power.

This second component is a part of the injected probe pulse which is amplified by stimulated Raman scattering. Given that the probe pulse duration ($\tau_{\text{S}} = 150$ ps) is significantly longer than the pump pulse duration ($\tau_{\text{P}} = 15$ ps), we expect that only the temporally overlapping part of the probe pulse is amplified by SRS. This means that the Raman-amplified part of the probe light has effectively a pulse duration of about 15 ps, which is shorter than the non-amplified probe light. Consequently, the spectral component corresponding to the Raman-amplified probe light should be spectrally broader than the non-amplified part, which is exactly what we observe. Moreover, the cross-Kerr effect between the pump and the probe pulses induces a spectral broadening. As is explained in section 2.3.1, the cross-Kerr contribution affecting the probe wave is expected to be two times larger than the auto-induced Kerr effect for the pump pulses. Moreover, like the pump pulses, the Raman-amplified probe light experiences an FCR-induced phase shift towards shorter wavelengths, exactly like the pump beam.

Considering the 15.6 THz Raman shift of the zone center optical phonon in silicon, the maximum Raman gain for a pump wavelength of $\lambda_{\text{P}} = 1441$ nm should be observed at

$$\lambda_{\text{S}} = (1/\lambda_{\text{P}} - \nu_{\text{R}}/c)^{-1} = (1/\lambda_{\text{P}} - 15.6 \text{ THz}/c)^{-1} = 1557.8 \text{ nm} .$$

In a preliminary experiment, we have measured the amplified *spontaneous Raman spectrum* for an input pump power of 100 mW *without probe* beam. The spontaneous Raman spectrum showed a maximum at 1557.3 nm, which is slightly below the theoretical value. In presence of the probe beam and for the same pump power, the Raman amplification has been maximized adjusting the input probe wavelength at 1558.2 nm, for which the blueshifted Raman-amplified part of the probe light is centered at 1557.3 nm (see the top spectrum in Fig. 3.12(b)) [68].
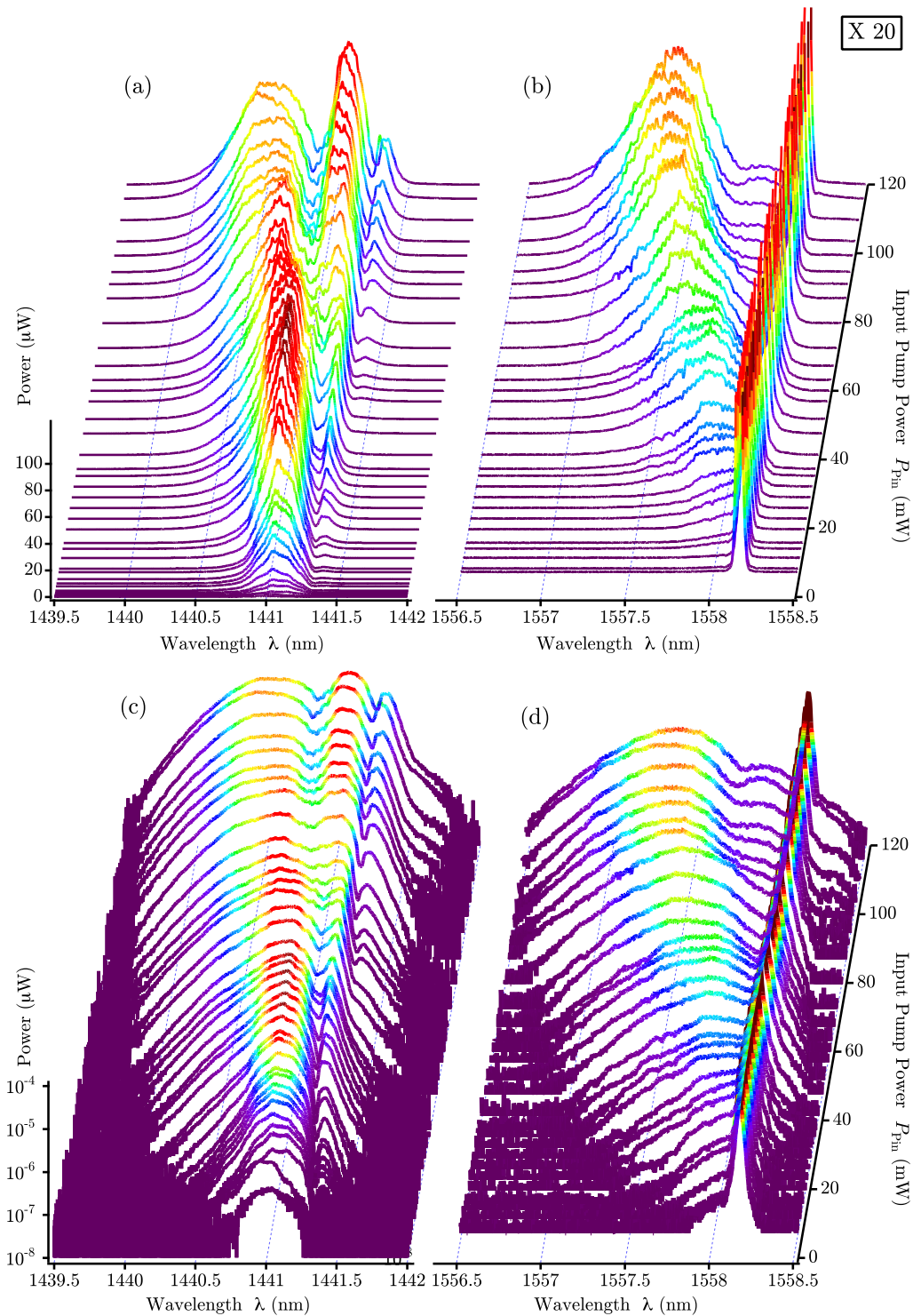
Fig. 3.12. Output spectra of the pump pulses (a) and the amplified probe pulses (b), measured after the passage of the silicon nanowire for different input pump powers (varying from 7 mW to 120 mW). The probe spectra have been multiplied by a factor 20. In (c) and (d) the same spectra are shown in a logarithmic vertical scale, for illustration purposes.

Group refractive index and local field factor at the pump wavelength

As an example, Figure 3.13 shows a zoom of the output pump spectrum for $P_{\mathrm{Pin}} = 120$ mW. As can be seen from the graph, the measured spectrum shows some small oscillations, which are caused by the fact that the entry facet and the exit facets

Fig. 3.13. Zoom in the output spectrum of the pump beam for $P_{\mathrm{Pin}} = 120$ mW. The graph clearly shows some weak Fabry-Perot oscillations, which are caused by the fact that the nanowire represents a Fabry-Perot resonator with weak mirrors at both ends. The thick line shows the smoothing of the spectrum that is used in section 3.4.3.
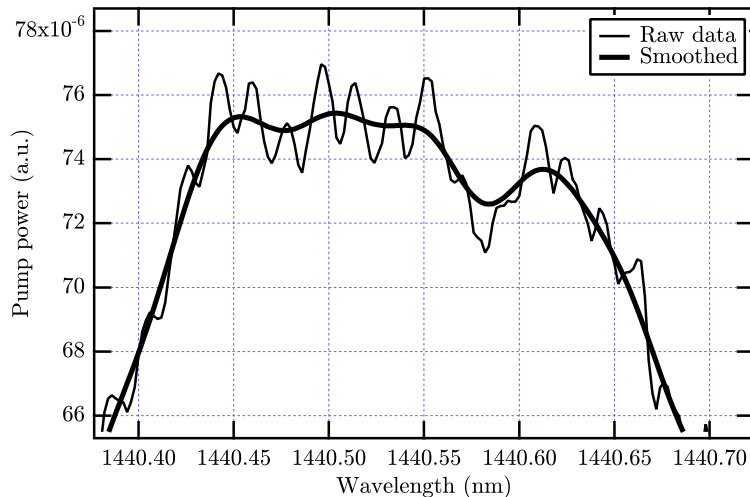
of the nanowire are not anti-reflection coated. Hence, these oscillations are Fabry-Perot fringes, which we can use to determine the local field factor f_{P} at the pump wavelength.

For this purpose, we apply the method that has already been presented in section 3.3.2. Thus, we calculate numerically the fast Fourier transform (FFT) of the measured spectrum shown in Fig. 3.13, which yields a peak at the modulation frequency of the Fabry-Perot fringes at $\omega_{\mathrm{M}} = 0.108$. We synthetize a sinusoidal reference function according to Eq. (3.34) with a mode spacing of $\Delta\lambda'_{\mathrm{M}} = 0.02$ nm. Its Fourier spectrum has a sharp peak at a position of $\omega'_{\mathrm{M}} = 0.1$. By comparison with this reference function, we can calculate the mode spacing of the Fabry-Perot fringes to be $\Delta\lambda_{\mathrm{M}} = 0.0185$ nm. Using this value of the mode spacing and the pump wavelength of $\lambda = 1441.0$ nm, we can calculate the **group refractive index of the silicon nanowire at the pump wavelength** of

$$n_{\mathrm{gr}}(\lambda_{\mathrm{P}}) = 5.10 . \tag{3.41}$$

With a bulk refractive index of silicon of $n_{\mathrm{bulk}} = 3.49$ at 1.44 μm [77], we obtain a **local field factor of the pump wave** of

$$\boxed{f_{\mathrm{P}} = \sqrt{\frac{n_{\mathrm{gr}}}{n_{\mathrm{bulk}}}} = 1.21} , \tag{3.42}$$

which is equal to the local field factor of the probe wave, $f_{\mathrm{P}} = f_{\mathrm{S}}$. It should be noted, however, that the spectra which have been examined here represent *nonlinear* spectroscopies, as opposed to the linear measurements in section 3.3.2. Therefore, several nonlinear effects (especially SPM, SRS, and FCR) can bias the measurements, which makes the calculated value of the local field factor of the pump beam less reliable than the one of probe beam. In any case, as has already been mentioned above, it is sensible to assume that $f_{\mathrm{P}} \approx f_{\mathrm{S}}$ [57], and we will therefore use this equality in the following.

3.4.2 Two photon absorption and Raman amplification

In a next step, we quantitatively analyze the above-presented experimental data. According to the model presented in section 3.1.2, we expect mainly two nonlinear optical effects influencing the spectra of the pump and the probe beam during the propagation in the waveguide : two photon absorption (TPA) and stimulated Raman scattering (SRS).

Decreasing pump transmission due to two photon absorption

For each of the curves shown in Fig. 3.12(a), we integrate the total transmitted power of the pump beam. For this purpose, we determine for each curve the zero level corresponding to the background signal of the OSA. Then we perform a numerical integration over the whole spectrum, yielding the transmitted pump power P_{Pout}. In Fig. 3.14(a), P_{Pout} is plotted versus the input pump power P_{Pin}. As can be clearly seen from the graph, the transmission of the silicon nanowire is nonlinear, with a decreasing transmission coefficient $P_{\text{Pout}}/P_{\text{Pin}}$ for higher input pump powers.

In order to check whether this is (only) due to two photon absorption, we plot the data in a different way. As has been shown in section 3.1.3, the ratio of the transmitted pump power to the input pump power $P_{\text{Pin}}/P_{\text{Pout}}$ should be proportional to the parameter $X_{\text{P}} = \kappa_{\text{Pin}} \beta' L_{\text{eff}} P_{\text{Pin}}/A_{\text{eff}} \tau_{\text{P}} F$. This relationship is given by Eq. (3.27) as

$$\frac{P_{\text{Pin}}}{P_{\text{Pout}}} = \frac{1}{\kappa_{\text{P}}} \left(1 + X_{\text{P}}\right) = \frac{1}{\kappa_{\text{P}}} + \frac{\kappa_{\text{Pin}} f_{\text{P}}^4 \beta_{\text{TPA}} L_{\text{eff}}}{\kappa_{\text{P}} A_{\text{eff}} \tau_{\text{P}} F} P_{\text{Pin}} , \qquad (3.43)$$

where we have inserted the relationship $\beta' = f_{\text{P}}^4 \beta_{\text{TPA}}$. Figure 3.14(b) shows the ratio $P_{\text{Pin}}/P_{\text{Pout}}$ as a function of the input pump power P_{Pin} for the experimental data. The points show very well a linear dependence over the whole range of input pump powers, which is exactly what we would expect.
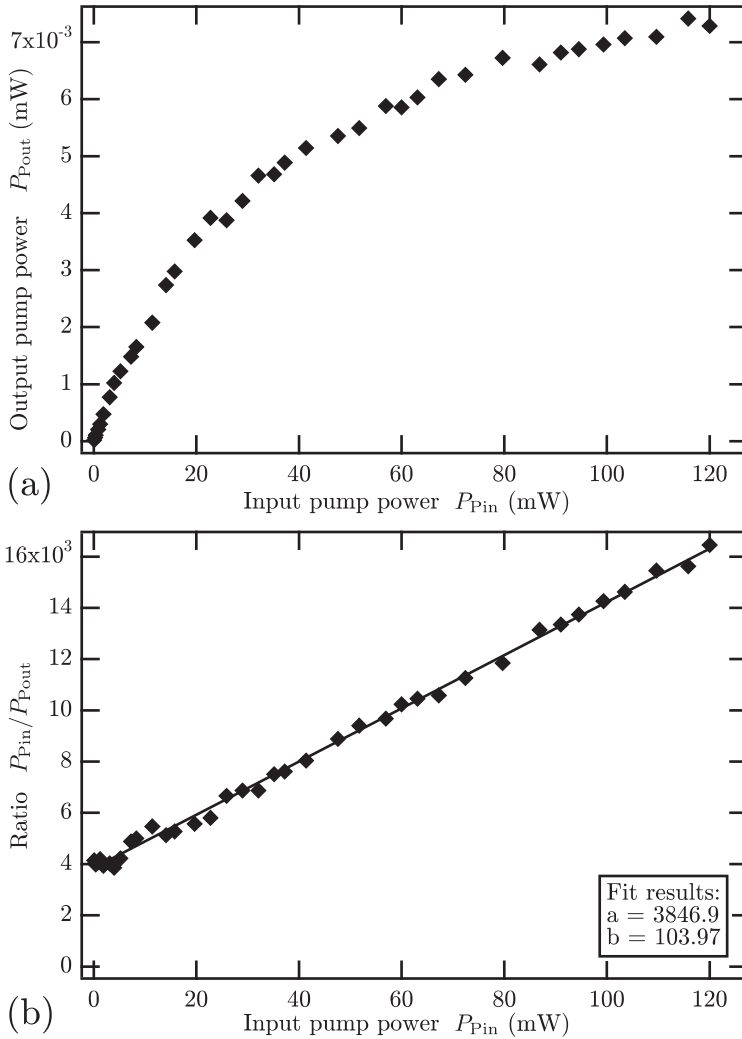

Fig. 3.14. (a) Transmitted pump power P_{Pout} as a function of the input pump power P_{Pin}. The output power increases nonlinearly.

(b) Ratio $P_{\text{Pin}}/P_{\text{Pout}}$ as a function of the input pump power P_{Pin}. The experimental data points show very well the linear dependence that we would expect according to Eq. (3.27).

> We conclude that the pump beam experiences two photon absorption (if not the slope would be zero) **and** that the pump beam is *not* depleted by the Raman amplification (otherwise the curve should show a nonlinear increase).

Therefore, we can fit a linear function of the form $y = a + b\,x$ to the data, yielding the following values for the fit parameters :

$$a = 3847 \pm 53 \qquad \text{and} \qquad b = (103 \pm 0.9)\,\text{mW}^{-1}\,. \tag{3.44}$$

With these results, we can calculate the value of the parameter X_{P} for each input pump power P_{Pin} according to Eq. (3.28), given by

$$X_{\mathrm{P}} \;=\; \frac{b}{a}\,P_{\mathrm{Pin}}\,. \tag{3.45}$$

These values are needed for the analysis of the probe spectra, as is demonstrated in the next section. Moreover, the fit parameters a and b enable us to determine the end-to-end loss of the pump beam as

$$\kappa_{\mathrm{P}} \;=\; 1/a \;=\; 2.6 \times 10^{-4}\,. \tag{3.46}$$

Using the expression for the slope parameter

$$b \;=\; \frac{\kappa_{\mathrm{Pin}}\, f_{\mathrm{P}}^4\, \beta_{\mathrm{TPA}} L_{\mathrm{eff}}}{\kappa_{\mathrm{P}}\, A_{\mathrm{eff}}\, \tau_{\mathrm{P}} F}\,,$$

we can also calculate the injection coupling efficiency of the pump beam as

$$\kappa_{\mathrm{Pin}} \;=\; \frac{\kappa_{\mathrm{P}}\, A_{\mathrm{eff}}\, \tau_{\mathrm{P}} F}{f_{\mathrm{P}}^4\, \beta_{\mathrm{TPA}} L_{\mathrm{eff}}}\, b\,. \tag{3.47}$$

By using the definition of the effective length L_{eff} given by Eq. (3.8) and with the values $\kappa_{\mathrm{P}} = 2.6 \times 10^{-4}$, $A_{\mathrm{eff}} = 0.17\,\mu\text{m}^2$, $\tau_{\mathrm{P}} = 15$ ps, $F = 80$ MHz, $f_{\mathrm{P}} = 1.21$, $\beta_{\mathrm{TPA}} = 0.8$ cm/GW [80], $L = 1.1$ cm, and $\alpha_{\mathrm{P}}' = 1.0$ cm^{-1}, we obtain

$$\kappa_{\mathrm{Pin}} \;=\; 4.8\,\%\,, \tag{3.48}$$

which is a reasonable order of magnitude, given the very small lateral dimensions of the nanowire. In a last step, we use Eq. (3.26) to calculate the extraction coupling efficiency of the pump beam as

$$\kappa_{\mathrm{Pout}} \;=\; \frac{\kappa_{\mathrm{P}}}{\kappa_{\mathrm{Pin}}\, e^{-\alpha_{\mathrm{P}}' L}} \;=\; 1.6\,\%\,, \tag{3.49}$$

which is only 33 % of the coupling efficiency at the injection. Given that the extraction efficiency κ_{Pout} accounts for the overall coupling from the nanowire sample to the OSA, including the injection into the single mode fiber, the value of 1.6 % seems to be reasonable.
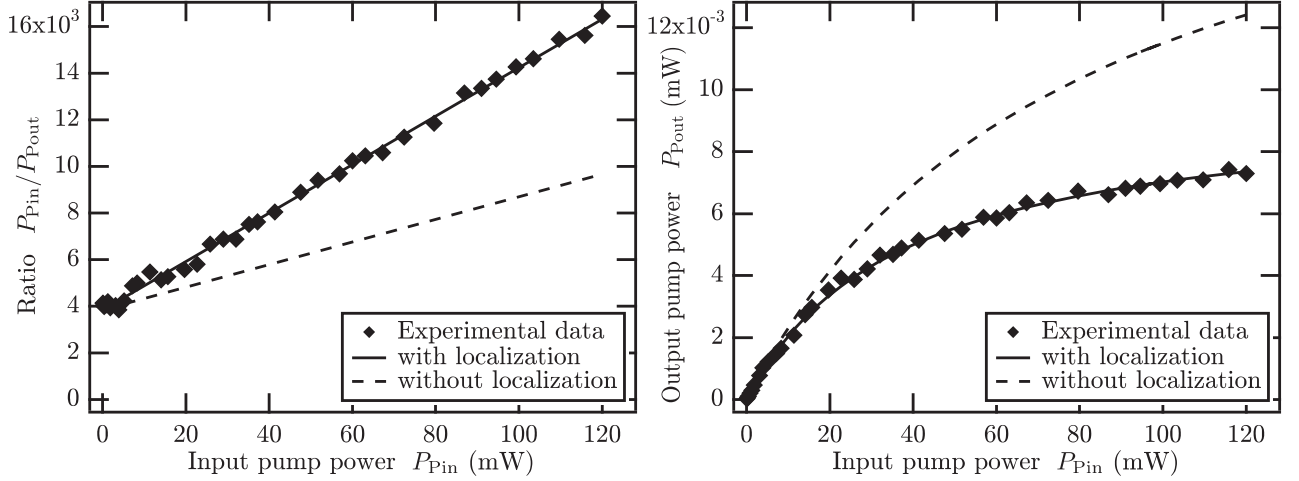
Fig. 3.15. Simulations of the graphs in Fig. 3.14 for a local field factor of $f_P = 1$ (i.e., *without* light localization).

Having determined all the constituents of the slope parameter b, we can illustrate the influence of the light localization by calculating the slope $\widetilde{b}$ that corresponds to a local field factor of $f_P = 1$ (i.e., *without* localization)

$$\widetilde{b} = \frac{\kappa_{\mathrm{Pin}}\,\beta_{\mathrm{TPA}}L_{\mathrm{eff}}}{\kappa_{\mathrm{P}}\,A_{\mathrm{eff}}\,\tau_{\mathrm{P}}F} = \frac{b}{f_{\mathrm{P}}^4}\;.$$

This allows us to simulate how the graphs in Fig. 3.14 would look like in the case of no light localization. The results are shown in Fig. 3.15. Clearly, the light localization *significantly* enhances the two photon absorption. For example, for an input pump power $P_{\mathrm{Pin}} = 120$ mW, the theoretical output pump power should be 12 μW, whereas we have measured 7 μW, which is only about 60 % of the theoretical value (i.e., a reduction by almost a factor 2).

Raman-amplified and blueshifted probe beam

In order to examine the effect of stimulated Raman scattering quantitatively, we are interested in the total optical power of the Raman-amplified part of the transmitted probe spectrum. Here, we utilize the observed blueshift by applying a low-pass filter to the spectrum (i.e., a filter function) that cuts all spectral information above the threshold wavelength $\lambda_{\mathrm{cut}} = 1558.11$ nm. We thus isolate the Raman-amplified part and ignore the main peak corresponding to the non-amplified part. We then carry out a numerical integration as in the case of the pump spectra. Figure 3.16 illustrates the filter function and the integration method.

Since we know the relationship between the parameter X_P and the input pump power P_{Pin} according to Eq. (3.45), we can now quantitatively analyze the calculated output probe power, as has been explained in section 3.1.3. For this purpose, we use Eq. (3.23), which can be expressed in the form

$$\underbrace{10\log\left(\frac{P_{\mathrm{Sout}}}{1\text{ mW}}\right)}_{P_{\mathrm{Sout}}\text{ in dBm}} = \underbrace{\frac{\gamma'_{\mathrm{R}} - 2\,\beta'_{\mathrm{X}}}{\beta'}}_{C}\underbrace{10\log\left(1 + X_{\mathrm{P}}\right)}_{(1 + X_{\mathrm{P}})\text{ in dB}}$$

$$+ \underbrace{10\log\left(\kappa_{\mathrm{S}}\right)}_{\kappa_{\mathrm{S}}\text{ in dB}} + \underbrace{10\log\left(\frac{P_{\mathrm{Sin}}}{1\text{ mW}}\right)}_{P_{\mathrm{Sin}}\text{ in dBm}}, \quad (3.50)$$

Fig. 3.16. Schematical illustration of the integration method used to determine the total optical power of the Raman-amplified part of the transmitted probe spectrum. A low-pass filter is applied to isolate the blueshifted Raman-amplified component, which is then numerically integrated (shaded area). This spectrum corresponds to an input pump power $P_{\mathrm{Pin}} = 120$ mW.
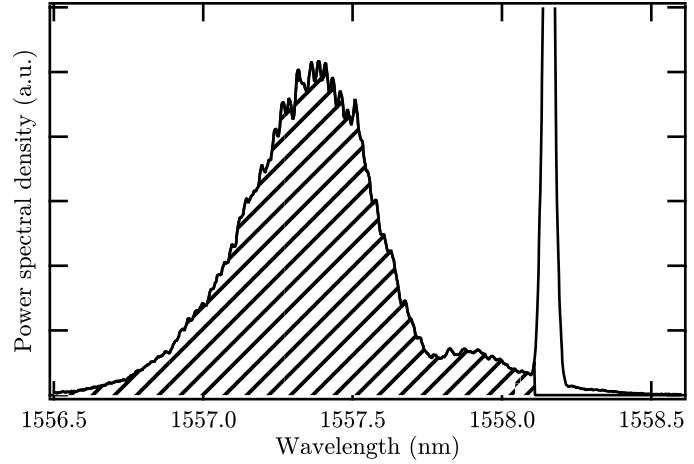
and we plot the Raman-amplified transmitted probe power in dBm (i.e., compared to the reference power of 1 mW) versus the parameter $(1 + X_{\mathrm{P}})$ in dB. The result is depicted in Fig. 3.17. As the graph clearly shows, the first seven data points (i.e., for $(1 + X_{\mathrm{P}}) \leq 2.1$ dB) can be described by a linear dependence, which is exactly what we expect according to the above equation. However, the points above 2.1 dB show clearly a nonlinear behavior such that

> **the Raman amplification of the probe beam saturates**

for higher values of X_{P} (i.e., for increasing input pump powers P_{Pin}). Assuming that the end-to-end loss of the probe beam κ_{S} and the injected probe power P_{Sin} do not depend on X_{P} or P_{Pin}, respectively (which are reasonable assumptions), we conclude

Fit results
a'= -62.03
b' = 7.841
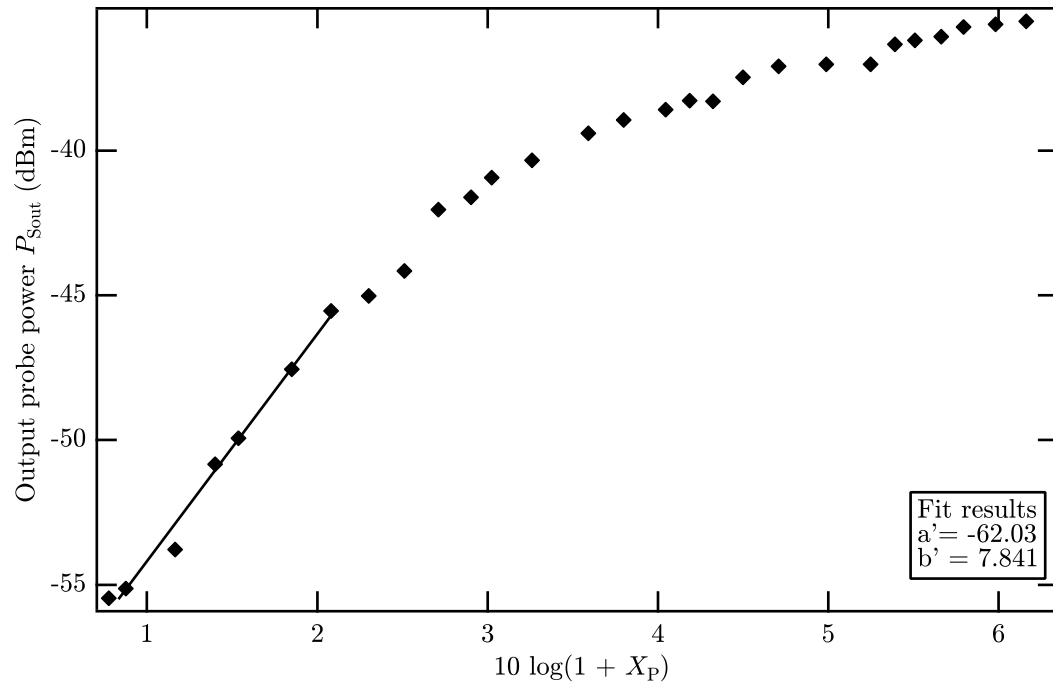
Fig. 3.17. Raman-amplified transmitted probe power in dBm as a function of $(1+X_{\mathrm{P}})$ in dB. The straight line represents a linear fit through the first seven data points, corresponding to a constant effective Raman gain $\widetilde{\gamma}_{\mathrm{R}}(\omega_{\mathrm{S}})$.

that the reason of the nonlinearity is included in the slope coefficient

$$C \;=\; \frac{\gamma_{\mathrm{R}}' - 2\,\beta_{\mathrm{X}}'}{\beta'} \;=\; \frac{f_{\mathrm{S}}^2}{f_{\mathrm{P}}^2}\,\frac{\widetilde{\gamma}_{\mathrm{R}}(\omega_{\mathrm{S}}) - 2\,\beta_{\mathrm{XTPA}}}{\beta_{\mathrm{TPA}}} \;. \tag{3.51}$$

We can furthermore consider the two photon absorption coefficients β_{TPA} and β_{XTPA}, as well as the local field factors f_{P} and f_{S}, as independent of the input pump power (i.e., independent of the parameter X_{P}). Therefore, it must be the effective Raman gain $\widetilde{\gamma}_{\mathrm{R}}(\omega_{\mathrm{S}})$ that causes the nonlinearity. From the saturation of the Raman amplification we deduce that the effective Raman gain decreases with increasing input pump power, which can be qualitatively understood by considering the SPM-induced broadening of the pump spectrum : The higher the input pump power, the broader the pump spectrum and, consequently, the smaller the overlap between the pump spectrum and the spectral shape of the Raman gain at the probe wavelength (see Eq. (3.2)).

> We conclude that the probe beam is amplified by stimulated Raman scattering. The measured Raman amplification of the probe beam saturates because of an SPM-induced spectral broadening of the pump beam, which leads to a decrease of the achievable Raman gain. This saturation effect of the Raman amplification with picosecond pump pulses in silicon (SOI) nanowires has never been explicitly reported or studied before.

For those points in Fig. 3.17 that show a linear dependence (i.e., the first seven data points), the pump spectrum is not broadened by SPM, and thus the effective Raman gain is constant, $\widetilde{\gamma}_{\mathrm{R}}(\omega_{\mathrm{S}}) = \mathrm{const.}$. Therefore, we fit a linear function of the form $y = a' + b'\,x$ to these points, which is also shown in the graph. The fit yields a y-intercept and a slope of

$$a' = (-62.0 \pm 0.5)\ \mathrm{dBm} \qquad \text{and} \qquad b' = 7.8 \pm 0.4 \;. \tag{3.52}$$

The y-intercept a' is a measure for the coupling losses κ_{S} (in dB) and the input pump power P_{Sin} (in dBm) in Eq. (3.50), whereas the slope b' corresponds to the coefficient C given by Eq. (3.51). With the values of the local field factors determined above, $f_{\mathrm{P}} = f_{\mathrm{S}} = 1.21$, the ratio of the local field factors is $f_{\mathrm{S}}/f_{\mathrm{P}} = 1$. Moreover, in the present case we can neglect the dispersion of the two photon absorption and assume $\beta_{\mathrm{XTPA}} \approx \beta_{\mathrm{TPA}}$ [81]. Therefore, the coefficient C is approximately given by

$$C \;\approx\; \frac{\widetilde{\gamma}_{\mathrm{R}}(\omega_{\mathrm{S}}) - 2\,\beta_{\mathrm{TPA}}}{\beta_{\mathrm{TPA}}} \;. \tag{3.53}$$

By using a value of $\beta_{\mathrm{TPA}} = (0.8 \pm 0.12)\ \mathrm{cm/GW}$ [80] and by inserting $b' = C$, we calculate an **effective Raman gain for a non-broadened pump beam** of

$$\widetilde{\gamma}_{\mathrm{R}}(\omega_{\mathrm{S}}) \approx \beta_{\mathrm{TPA}}\left(b' + 2\right) = 7.87\ \mathrm{cm/GW} \;. \tag{3.54}$$

In the following, we determine the effective Raman gain for the points in Fig. 3.17 for which the amplification of the probe power saturates (i.e., for $(1 + X_{\mathrm{P}}) > 2.1$ dB).

3.4.3 Saturated Raman amplification due to self phase modulation of the pump beam

In order to describe the observed saturation of the Raman amplification quantitatively, we apply our model (see section 3.1) to the experimental data. As a result, we also obtain a numerical value of the Raman gain coefficient $\bar{\gamma}_{\mathrm{R}}$ of silicon.

Calculation of the effective Raman gain

According to Eqs. (3.2), (3.3), and (3.4), the effective Raman gain of a polychromatic pump beam can be calculated by

$$\widetilde{\gamma}_{R}(\omega_{S}) = \bar{\gamma}_{R} \int_{-\infty}^{\infty} \frac{S(\omega_{P})}{1 + \Delta^2} \, d\omega_{P} \quad \text{with} \quad \Delta \approx \frac{2}{\Delta\nu_{R}} \left(\nu_{R} - \frac{c}{\lambda_{P}} + \frac{c}{\lambda_{S}} \right) , \quad (3.55)$$

where we have inserted the relationship between frequency and wavelength, $\nu = c/\lambda$, with c as the speed of light. We now use the above expressions to calculate the effective Raman gain for different input pump powers. We determine the power spectral densities $S(\omega_{P})$ based on the measured pump spectra. For this purpose, all pump spectra have to be normalized in order to satisfy the normalization condition

$$\int_{-\infty}^{\infty} S(\omega) \, d\omega = 1 .$$

Therefore, a smoothing algorithm is applied to all the pump spectra in order to eliminate the weak Fabry-Perot oscillations (for an illustration of the smoothing, see Fig. 3.13), and each spectrum is then divided by the total transmitted pump power, which is determined by numerically integrating the whole spectrum. For the Raman resonance of the zone center optical phonon in silicon, we use a Raman shift (i.e., Raman frequency) of $\nu_{R} = 15.6$ THz and a width of the Raman resonance (FWHM) of $\Delta\nu_{R} = 105$ GHz [39].

The factor $\bar{\gamma}_{R}$ before the integral in Eq. (3.55) is, in principle, an adjustable parameter. As is demonstrated below, the best agreement with the experimental data is achieved with a value of the **Raman gain coefficient of silicon** of

$$\boxed{\bar{\gamma}_{R} = 8.9 \, \frac{\text{cm}}{\text{GW}}} .$$

The top panel of Fig. 3.18 shows the result of the calculation, i.e., the dependence of the convolution integral $\widetilde{\gamma}_{R}(\Delta\lambda_{R})$ on the detuning $\Delta\lambda_{R} = (1/\lambda_{P} - 1/\lambda_{S} - \nu_{R}/c)^{-1}$ from the Raman resonance for different input pump powers P_{Pin}. As can be clearly seen from the graph, exactly at Raman resonance (i.e., at the position $\Delta\lambda_{R} = 0$), the value of the effective Raman gain $\widetilde{\gamma}_{R}(\omega_{S})$ decreases with increasing pump power. This is exactly what we expect in order to explain the nonlinear behavior in Fig. 3.17. To illustrate this effect, we plot the calculated values of $\widetilde{\gamma}_{R}(\omega_{S})$ at the probe wavelength (i.e., for $\Delta\lambda_{R} = 0$) as a function of $(1 + X_{P})$ in dB. The result is depicted in the bottom panel of Fig. 3.18. It is clearly visible that the effective Raman gain decreases with increasing $(1 + X_{P})$ and, thus, with increasing input pump power P_{Pin}.

Theoretical description of the pump-probe experiments

We use the above findings to verify our model. For this purpose, we insert the calculated values of $\widetilde{\gamma}_{R}(\omega_{S})$ into the formula for the slope coefficient C given by Eq. (3.53) with a two photon absorption coefficient $\beta_{TPA} = 0.8$ cm/GW (as before). By adding the offset a' that we have determined with the linear fit, given by Eq. (3.52), we can calculate the theoretical values of the Raman-amplified output probe power according to

$$P_{Sout}\Big[\text{dBm}\Big] = \frac{\widetilde{\gamma}_{R}(\omega_{S}) - 2\,\beta_{TPA}}{\beta_{TPA}} \left(1 + X_{P}\right)\Big[\text{dB}\Big] + a' . \quad (3.56)$$
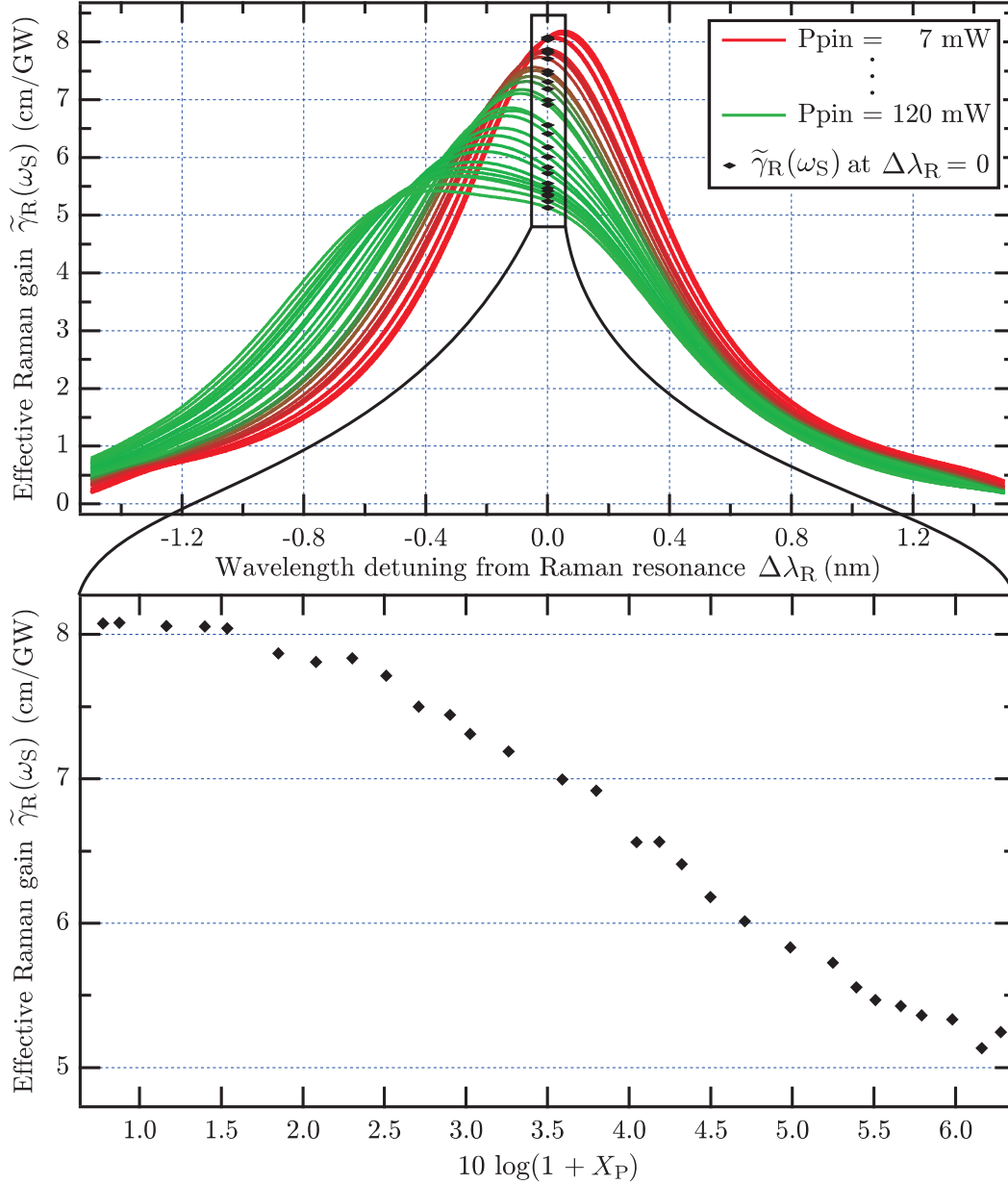
Fig. 3.18. Effective Raman gain $\widetilde{\gamma}_R(\omega_S)$ experienced by the probe beam, calculated according to Eq. (3.55). *Top:* $\widetilde{\gamma}_R(\omega_S)$ as a function of the detuning $\Delta\lambda_R$ from the Raman resonance. *Bottom:* $\widetilde{\gamma}_R(\omega_S)$ as a function of $(1+X_P)$ in dB, which corresponds to P_{Pin}.

The results are plotted versus $(1+X_P)$ in dB in Fig. 3.19, along with the experimental data. As is clearly visible in the graph, the values calculated with our model of the SPM-broadened pump beam show an **excellent agreement** with the experimental data. The graph also contains a straight line corresponding to the extrapolation of the Raman amplification with a non-broadened pump beam (see fit in Fig. 3.17). By comparing the straight line to the results of our model with the SPM-induced broadening, one sees very clearly the saturation effect of the Raman amplification. It it worth noting that this effect has never been properly described nor explicitly studied in the previous publications on Raman amplification in silicon nanowires.

It is common to characterize amplifying effects or devices in terms of the so-called "on-off gain" $G_{\text{on-off}}$, which has already been introduced in section 2.4.2. In the present case, the on-off gain of the Raman amplification in the silicon nanowire is
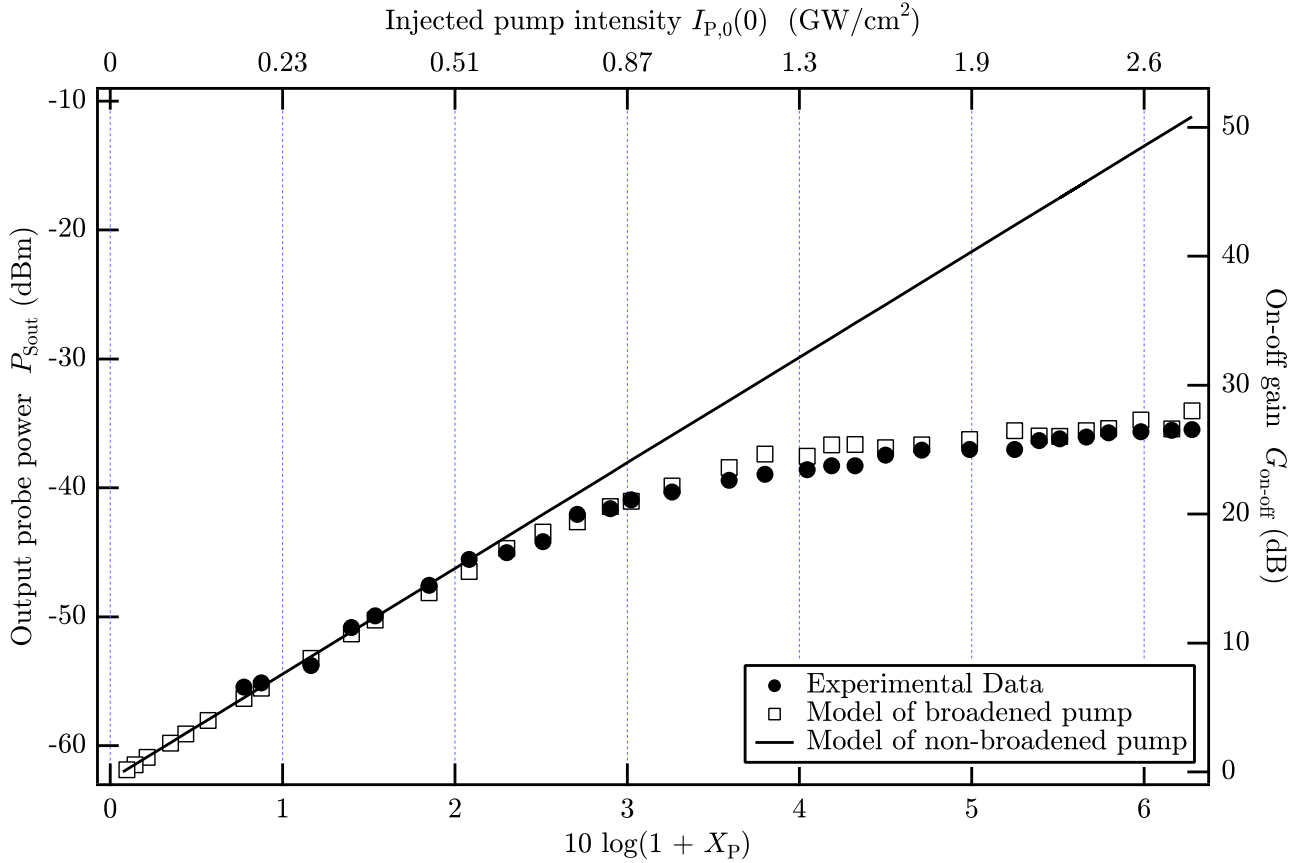
Fig. 3.19. Raman-amplified transmitted probe power in dBm as a function of the experimentally determined parameter $(1 + X_P)$ in dB. The filled circles represent the experimental data (see also Fig. 3.17); the white squares show the values that have been calculated with the model presented in section 3.1. The straight line corresponds to the extrapolation of the Raman amplification with a non-broadened pump beam. The right axis shows the on-off gain $G_{\text{on-off}}$ defined by Eq. (3.57). The top axis shows the corresponding injected pump intensities at the beginning of the nanowire $I_{P,0}(0)$.

defined as the ratio of the output probe power *in presence of the pump beam* ("on") to the output probe power *without the pump beam* ("off"). As is common, we express the on-off gain here in dB so that we obtain

$$G_{\text{on-off}} \;=\; 10 \, \log \left(\frac{P_{\text{Sout}}(P_{\text{Pin}})}{P_{\text{Sout}}(P_{\text{Pin}} = 0)} \right) \; .$$

Using Eqs. (3.50) and (3.56), we find an expression for the on-off gain of Raman amplification in the silicon nanowire, yielding

$$G_{\text{on-off}} \;=\; \frac{\widetilde{\gamma}_R(\omega_S) - 2 \, \beta_{\text{TPA}}}{\beta_{\text{TPA}}} \left(1 + X_P \right) \Big[\text{dB} \Big] \;=\; P_{\text{Sout}} \Big[\text{dBm} \Big] \;-\; a' \, , \qquad (3.57)$$

which is basically the same as the output probe power P_{Sout} in dBm, only shifted by the constant offset a'. Figure 3.19 indicates the on-off gain $G_{\text{on-off}}$ of the experimental data and of the values calculated with our model on the right axis of the graph. As can be seen from the data points, the silicon nanowire provides a maximum amplification of about 27 dB, corresponding to a 500-fold increase of the probe power due to the stimulated Raman scattering, which is a good performance compared to previous studies [82]. Given that the silicon nanowire has a length of only 11 mm, this is a quite remarkable result.

With Eqs. (3.17) and (3.45), we know the relationship between the parameter X_P and the injected pump intensity at the beginning of the nanowire $I_{P,0}(0)$. We can,

therefore, also plot the output probe power P_{Sout} and the on-off gain $G_{\text{on-off}}$ as a function of the injected pump intensity $I_{\text{P,0}}(0)$, which is indicated on the top axis in Fig. 3.19. As can be seen from the graph, the maximum amplification of 27 dB is achieved for an intensity of about 2.8 GW/cm^2.

It should be noted that the good agreement between the model and the experimental data in Fig. 3.19 depends on our choice of the material-dependent Raman gain coefficient of $\bar{\gamma}_{\text{R}} = 8.9$ cm/GW, as mentioned above. According to the expression of the slope parameter C given by Eq. (3.53), a different value of $\bar{\gamma}_{\text{R}}$ would have produced a less good agreement. In addition to that, the calculated values of C also depend on the numerical value of the two-photon absorption coefficient β_{TPA}, which was chosen as 0.8 cm/GW here [80]. However, the choice of these two parameters affects only the vertical scaling of the curve. Thus, the general form of the nonlinear dependence (i.e., the saturation effect) is caused by the decreasing overlap of the pump spectrum and the Raman resonance in the convolution integral, which is very well predicted by our (purely analytical) model.

3.5   Conclusion and outlook

In this chapter, I have experimentally demonstrated a **saturation of the Raman amplification** in a silicon-on-insulator (SOI) nanowire in the picosecond regime. The saturation of the amplification, which corresponds to a decrease of the effective Raman gain $\widetilde{\gamma}_{\text{R}}(\omega_{\text{S}})$, is caused by the self-phase modulation (SPM) of the pump pulses during their propagation in the nanowire. The self-phase modulation is induced by the (optical) Kerr effect and by the free carrier refraction (FCR), which in turn is caused by the two photon absorption of the pump photons.

An analytical model has been established which describes the evolution of the pump and the Stokes intensities in the nanowire. Based on the measured output spectra of the pump pulses, this model reproduces very well the saturation of the on-off gain of the Raman amplification. Moreover, although the experiments have been carried out with a 15-picosecond pulse duration, which corresponds to a slightly transient regime for SRS, the model allows us to determine the steady-state **Raman gain coefficient** of silicon. We obtain an excellent agreement between model and experiment for a value of $\bar{\gamma}_{\text{R}} = 8.9$ cm/GW. Given that the previously published values vary over a very large range between 4 and 70 cm/GW [67], this is an excellent result, which confirms the correct order of magnitude.

The above results have been obtained by using a two photon absorption coefficient of $\beta_{\text{TPA}} = 0.8$ cm/GW [80]. It should be noted, however, that the measurement method and data processing presented here yield only a result for the *ratio* of the Raman gain to the TPA coefficient, as given by Eq. (3.53),

$$C \approx \frac{\widetilde{\gamma}_{\text{R}}(\omega_{\text{S}}) - 2\,\beta_{\text{TPA}}}{\beta_{\text{TPA}}} = \frac{\widetilde{\gamma}_{\text{R}}(\omega_{\text{S}})}{\beta_{\text{TPA}}} - 2\,,$$

so that the determination of the Raman gain, thus, *depends* on the TPA coefficient β_{TPA}. However, the latter has not only been used for the modeling of the saturated Raman amplification, but also for the calculation of the coupling efficiency κ_{Pin} of the pump beam in Eq. (3.47). Therefore, we can also reverse the order of the logical reasoning. This means that, if we could measure the coupling efficiency κ_{Pin} independently of the value of β_{TPA}, we would then be able to *determine* the two photon absorption coefficient by ourselves by using the above-presented data analysis (i.e., by using Eq. (3.47) in the reverse direction). Thus, besides the observed saturation of the Raman amplification and the determination of the Raman gain coefficient $\bar{\gamma}_{\text{R}}$,

which are the main results of the pump-probe experiments, the measurement and **data analysis method** itself is another important and very useful result of this chapter. A major advantage of this method is that it can also be applied to situations with a much stronger light localization and, therefore, with much slower group velocities (e.g., in photonic crystal waveguides). Thus, we can determine the Raman gain based on the knowledge of either the coupling efficiency κ_{Pin} or the two photon absorption coefficient β_{TPA}.

Moreover, the present work provides insight in the **enhancement of optical non-linearities** due to light localization, and it shows how the order of importance of the different nonlinear effects changes with increasing light localization. As has been shown above, the two photon absorption is significantly stronger in the nanowire than in bulk silicon because of the localization of the light, i.e., because of the reduced group velocity of the pump pulses in the nanowire. This slow-down effect on the pump pulses is expressed by the group refractive index n_{gr}, which is related to the local field factor f_{P}. Similarly, we can qualitatively discuss the influence of the light localization on the other nonlinear optical effects, especially those that cause the self phase modulation of the pump pulses. In section 2.4.1, we have discussed the enhancement factors of the different nonlinear effects. Some of these factors are summarized again in Tab. 3.1. We can see from the composition of the enhancement factors that, depending on the (effective) order of the different nonlinear effects and on the exact values of the involved local field factors (here f_{P} and f_{S}), an effect that appears negligible in a bulk semiconductor may become predominant in the case of high localization, due to a high enhancement factor.

Effect	Factor	Order
Kerr	f_{P}^4	3
Cross-Kerr	$f_{\mathrm{P}}^2 f_{\mathrm{S}}^2$	3
FCR on pump	f_{P}^6	5
FCR on Stokes	$f_{\mathrm{P}}^4 f_{\mathrm{S}}^2$	5

Tab. 3.1. Enhancement factors of the nonlinear optical effects affecting the phase of the pump and the Stokes wave, as well as the effective order of the effects (see also Tab. 2.1).

As Tab. 3.1 shows, the enhancement factors of the Kerr effect and the free carrier refraction are at least of the same order of magnitude as the ones of TPA (f_{P}^4) and SRS ($f_{\mathrm{P}}^2 f_{\mathrm{S}}^2$), which have been taken into account by our analytical model. This means that a stronger localization of the light (i.e., higher local field factors) would result in an even stronger self phase modulation. Thus, although the light localization does not affect the Raman on-off gain *directly* (as long as $f_{\mathrm{S}}/f_{\mathrm{P}} \approx 1$, which is often a reasonable assumption [57]), a high localization *indirectly* limits the maximum attainable Raman amplification through the SPM-induced spectral broadening of the pump beam (because the latter leads to a reduced effective Raman gain). It is important to note that this is an **intrinsic limitation concerning Raman amplification**, which originates in the dependence of the nonlinear effects on the local field factors. This important result has major implications for the design of slow-mode Raman devices because it conflicts with the ever-growing need for high compactness and low command power of the optical signal processing components.

In order to gather a better understanding of the influence of the light localization on the Raman amplification in silicon or SOI nanowires, the above-presented analytical model should be extended by explicitly taking into account the phase of the pump and probe waves during their propagation. Moreover, it would be necessary to include the free carrier effects (free carrier refraction and free carrier absorption) in the equations. Because of the increased complexity of such a model, the solutions have to be found numerically, for example by using the so-called split-step Fourier method (SSFM) [83]. In other words, the next steps towards a detailed understanding and design of Raman-based devices in the field of silicon photonics consist in extensive numerical simulations in order to fully describe the underlying physical processes.

Such simulations have been outside of the scope of the present PhD thesis, but they have been subject of the PhD thesis of Alexandre BARON (group Manolia of the Laboratoire Charles Fabry de l'Institut d'Optique), who compares the results of such simulations[4] to an advanced analytical model that takes into account the SPM broadening due to Kerr and FCR and its influence on the reduction of the Raman gain [84].

* * *

---

[4]These numerical simulations have been part of a collaboration with Govind P. AGRAWAL.

Stimulated Raman scattering in a doubly resonant GaAs microcavity

This chapter presents the experimental study of stimulated Raman scattering in a doubly resonant planar GaAs microcavity. An analytical model is developed and used to simulate the interplay between the different nonlinear optical effects and their influence on the microcavity transmission. In the main part of this chapter, we present a series of pump-probe experiments that show some totally unexpected results. A detailed analysis of the measurement data demonstrates that the relaxation of the electrons in the conduction band of GaAs is significantly modified through the interaction with a population of coherently excited Raman phonons.

Contents

In the previous chapter, we have seen how a tight confinement of light waves in a semiconductor ridge waveguide leads to a slowing down of light, which results in a significant enhancement of several nonlinear optical effects (especially TPA and SRS). Another situation that is favorable to the enhancement of the nonlinear interactions consists in an optical microcavity in which the interacting waves coincide with cavity resonances. Although optical cavities in the nonlinear regime have been the subject of numerous studies, they currently regain interest because of the recent technological progress in the fabrication technology of semiconductor nanostructures. In particular, the use of photonic band-gap structures has proven to allow for the realization of microcavities with extremely high Q factors in SOI (including SOI on membrane), GaAs, and AlGaAs materials [31, 32, 33, 34, 85, 86, 87]. Low command power optical switches have already been demonstrated in GaAs [88] and AlGaAs [89] microcavities. Very recently, it has been demonstrated [90] that in ultrahigh-Q photonic crystal microcavities in GaAs, optical nonlinearities can already appear at a microwatt-level.

The enhancement of *spontaneous* Raman scattering due to the confinement of the incident and/or the scattered photons in a cavity has first been observed for molecular vibrations in external cavities [91] and in micro-droplets [92]. In the latter case, a doubly resonant situation has been obtained by adjusting the size of the objects in such a way that the photons energies of two resonant whispering gallery modes coincide with the energies of the incident and scattered photons.

More recently, *stimulated* Raman scattering (SRS) has been studied in ultra high-Q spherical and toroid microcavities in silica [35]. As already mentioned in the previous chapter, the optical gain provided by SRS has been successfully used to demonstrate Raman lasers in silicon-on-insulator nanowaveguides [93, 94, 95]. The lengths of the resonators in these works have been of the order of several centimeters. In the perspective of applications in information and communication technology, another approach consists in realizing doubly resonant *microcavities* with resonator lengths in the micrometer range. *Spontaneous* Raman scattering in such planar semiconductor microcavities has been subject of several studies [96, 97, 98]. More recently, WONG and YANG have proposed a design of a microcavity for Raman amplification and lasing that is based on photonic crystal structures [99, 100], and CHERCOURY *et al.* have experimentally demonstrated the *enhancement* of the amplified spontaneous Raman scattering in a doubly resonant cavity, based on a photonic crystal waveguide [101].

The central aim of the work presented in this chapter is *not* to develop a *new design* of a microcavity or a photonic crystal waveguide, *but* rather to study a simple *model system* to investigate the interplay between Raman scattering and the other nonlinear optical effects in a situation where they are strongly enhanced by light localization. For this purpose, we have chosen to use a geometry that has already been successfully used for many experiments by our collaboration partner Bernard JUSSERAND, who is a renowned expert in the study of enhanced spontaneous Raman scattering in 2D semiconductor microcavities.

As in the previous chapter, the measurement technique that I have used for the experiments is the so-called pump-probe method. This means that a strong pump beam is incident upon a semiconductor sample and excites several nonlinear optical effects in the semiconductor material, whose response is then measured with a weak probe beam. Here again, **the probe beam corresponds to the Stokes wave**. However, unlike in the previous chapter, here the semiconductor sample is not a waveguide, but it is a planar semiconductor microcavity, consisting of a thin GaAs layer enclosed by two highly reflective AlGaAs/AlAs Bragg mirrors. The main advantage of a *planar* cavity is that this is the simplest way to obtain a doubly resonant situation, where pump and Stokes wave are resonant at the same time. The double resonance can be achieved by injecting the pump and the probe (Stokes) beam at two different angles of incidence. Because of its simplicity, the situation described here serves as a model system for more complex configurations such as doubly resonant microcavities etched in ridge waveguides. It is worth noting that, to our knowledge, this is the first experimental investigation of *stimulated* Raman scattering in a doubly resonant semiconductor microcavity.
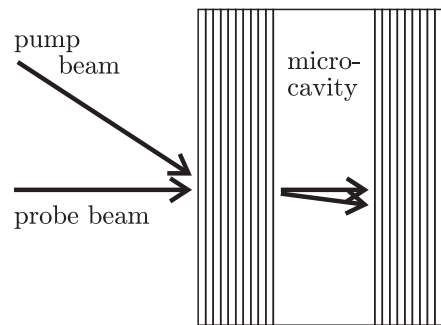
The chapter starts with a description of the sample, followed by the presentation of an analytical model describing the nonlinear optical effects that we expect to observe in the pump-probe measurements. It explains in detail the experimental setup, including the light source and the preparation of the pump beam and the probe beam, as well as the different optical signals and the data acquisition and processing. An experimental linear characterization of the semiconductor sample is presented, yielding the key characteristics of the GaAs microcavity.

Then, the experimental results of several series of nonlinear pump-probe measurements are presented and compared to the predictions of the analytical model introduced before. Although many of the key characteristics of the experimental results are well described by the simulations, we observe several features which differ very clearly from what we would expect according to the model. A detailed analysis of the measurement results indicates that the dynamics of the free carriers in the central semiconductor layer are modified due to Raman scattering. More precisely, it is demonstrated that TPA-generated free carriers in the conduction band interact with a population of coherent Raman phonons, which are created by the enhancement of amplified spontaneous Raman scattering, and that this interaction leads to a significant slowing down of the relaxation of the electrons towards the band edge. Besides the modification of the relaxation dynamics of the *free carriers*, we expect that the interaction between electrons and coherent phonons also causes a prolongation of the lifetime of the involved *phonons* (typical phonon lifetimes in bulk GaAs are of the order of 3 to 7 picoseconds).

The observed modification of the electron dynamics is a consequence of the strong light localization, which is caused by the microcavity. It illustrates the impact that the localization effect can have on the interplay between the different optical nonlinearities.

These observations, especially the electron-phonon interaction and its influence on the free carriers, is a **totally unexpected result**, which has, to our knowledge, never been reported in previous studies. The results of this chapter are subject of a publication that is currently in preparation.

4.1   Doubly resonant planar microcavity

The sample that is used for the experiments has been designed and fabricated specifically for the pump-probe measurements presented in this chapter. In order to determine its optimal design, we have carried out numerical simulations, which are presented in the following.

4.1.1   Considerations regarding the sample design

Basically, the sample is a simple planar resonator that consists of a thin semiconductor layer which is enclosed by two planar Bragg mirrors. The most important properties of the cavity are the thickness of the central semiconductor layer, the reflectivities of the two Bragg mirrors, and the choice of the semiconductor material. With respect to the experiments, a certain number of criteria has to be taken into account.

- The choice of the semiconductor material of the central layer and of the mirrors should be such that the fabricating technology is well-known and that it is possible to produce high quality structures and Bragg mirrors with very high reflectivities. For the present PhD thesis, the access to the fabrication technology via collaboration partners has also been of crucial importance. Moreover, the optical properties of the semiconductor material should be well known. Hence, the choice of the material (as well as the doubly resonant cavity geometry) is based on the experience of one of our collaboration partners (Bernard JUSSERAND) so that GaAs has been chosen for the microcavity's central layer and the AlGaAs/AlAs material system for the surrounding Bragg mirrors.

- In principle, it is possible that the two Bragg mirrors have different reflectivities (asymmetric resonator). This means that they have different numbers of layers. Since the Raman interaction between the pump and the Stokes wave depends on the pump intensity inside the microcavity, we want to minimize injection losses caused by scattering at the interfaces between the Bragg layers. Therefore, the number of layers of the front mirror N_{front} should be lower than the number of layers of the rear mirror N_{rear}.

- For the same reason, i.e., to maximize the intracavity pump intensity, the pump beam should be TM-polarized because this minimizes the losses due to the reflection at the air-sample interface. This is of particular importance because we work near Brewster's angle. Since the Raman scattering efficiency of a material depends, in general, on the polarizations of the pump and the Stokes wave, this condition yields some other constraints concerning the crystallographic orientation of the semiconductor sample, as is demonstrated below.

- For the pump-probe experiments, we suppose that the pump and the probe beam consist of Gaussian pulses with a pulse duration of $\tau \approx 12$ ps (full width at half maximum, FWHM). Since the time-bandwidth product of the pulse duration τ and the linewidth $\delta\nu$ (FWHM) of Gaussian pulses is $\tau\,\delta\nu = 0.44$, this corresponds to a linewidth of 0.11 nm. Therefore, the resonance curve of the microcavity should also have a spectral width of at least 0.11 nm (or larger) in order to maximize the coupling of the pulse into the cavity resonance.

- The band gap energy of GaAs is $E_{\mathrm{gap}} \approx 1.424$ eV, which corresponds to a wavelength of $\lambda_{\mathrm{gap}} \approx 870$ nm. In order to make sure that neither the pump nor the probe beam experiences linear absorption in the sample, both wavelengths should be reasonably far from the band edge. We choose to work

with a Stokes wavelength of $\lambda_S \approx 950$ nm that is resonant in the microcavity at normal incidence. With the Raman shift in GaAs at room temperature of $\bar{\nu}_R = 292$ cm^{-1} [102], this corresponds to a pump wavelength of $\lambda_P = (1/\lambda_S + \bar{\nu}_R)^{-1} \approx 924$ nm, which is sufficiently far from the band edge so that the sample is nearly transparent for both wavelengths.

- The last requirement concerns the thickness of the central layer, i.e. the length L of the microcavity. On the one hand, it is desirable to have long interaction length of the two beams, which would be an argument for a long cavity, i.e., a thick GaAs layer. On the other hand, it follows from the resonance condition that the longer the cavity is, the smaller is the mode spacing of the resonances, i.e., the denser are the resonances in the frequency or wavelength domain. We want to be sure that pump and probe beam "see" only the same longitudinal mode (resonance order). Therefore, the free spectral range of the resonator modes should be greater than the Raman shift, which is approximately the difference between pump and probe frequency. This requirement favors a thin GaAs layer. Moreover, since pump and probe beam are injected with different angles of incidence, it is important to have enough spatial overlap of the different round-trips of both waves in the resonator. This is also an argument for a short resonator length. In the wavelength range used (i.e., around 1 μm), a good compromise is a cavity length of $5\lambda_S/n_S$, where $n_S \approx 3.5$ (GaAs). This corresponds to the tenth resonance order, i.e., $m = 10$ (for more explanations see appendix B).

As has been mentioned above, we want to work in a *doubly resonant* situation, where both beams, Stokes and pump, are resonant in the microcavity at the same time. This can be achieved by injecting the two beams at different angles of incidence. In the present case, we work with the probe beam (i.e., the Stokes wave) with a wavelength $\lambda_S \approx 950$ nm at normal incidence ($\vartheta_S = 0°$). According to Eqs. (B.11) and (B.12), which are derived in appendix B, the so-called Fabry-Perot phase of the microcavity at the tenth-order resonance can be expressed as

$$\frac{2\pi \, n \, L}{\lambda} \cos(\vartheta) \;=\; \varphi_{FP} \;=\; m \, \pi \;=\; 10\pi \; .$$

This equation enables us to calculate for each wavelength the corresponding angle of incidence for which this wavelength is resonant in the microcavity. For a pump wavelength of $\lambda_P \approx 924$ nm, we obtain an internal angle of incidence $\vartheta_P \approx 13.4°$, which corresponds to an external angle of incidence $\vartheta_P' = \arcsin(n_P \sin(\vartheta_P)) \approx 54.4°$, where we have assumed $n_P \approx n_S \approx 3.5$.

Since pump and Stokes beam are not parallel to each other (as opposed to the situation presented in chapter 3), the propagation vectors k_P and k_S of the pump and Stokes beam define a plane of incidence. The directions corresponding to the TE and the TM polarization are thus given relative to this plane of incidence. As has been shown in section 2.2.2, the Raman gain depends on the polarization states of the pump and the Stokes wave with respect to the crystallographic axes of the semiconductor material. This dependence is described by the scattering efficiency Σ given by Eq. (2.38) as

$$\Sigma = \sum_{l=1}^{3} \left[\hat{e}_P \, R^l \, \hat{e}_S \right]^2 ,$$

where the $\hat{e}_P$ and $\hat{e}_S$ are the polarization vectors of pump and Stokes wave and the R^l matrices are defined by Eq. (2.39). We suppose in the following that the planar

microcavity is fabricated perpendicular to a [001] surface of a GaAs waver. In other words, we suppose that a beam which is at normal incidence upon the microcavity propagates in the [001] direction. Moreover, we assume that the polarization vectors of pump and Stokes are purely transverse. This leads to the following general form of the propagation vector $\hat{k}$ and the polarization vectors $\hat{e}_{\mathrm{TE}}$ and $\hat{e}_{\mathrm{TM}}$:

$$\hat{k} = \begin{pmatrix} \sin\vartheta \sin\varrho \\ \sin\vartheta \cos\varrho \\ \cos\vartheta \end{pmatrix} \quad \hat{e}_{\mathrm{TE}} = \begin{pmatrix} \cos\varrho \\ -\sin\varrho \\ 0 \end{pmatrix} \quad \hat{e}_{\mathrm{TM}} = \begin{pmatrix} \cos\vartheta \sin\varrho \\ \cos\vartheta \cos\varrho \\ -\sin\vartheta \end{pmatrix} ,$$

where ϑ is the angle of incidence, and ϱ is the angle between the TE polarization vector $\hat{e}_{\mathrm{TE}}$ and the crystallographic direction [100]. The relationships between these vectors are illustrated in Fig. 4.1. The above definitions satisfy the orthogonality conditions $\hat{k} \cdot \hat{e}_{\mathrm{TE}} = 0$, $\hat{k} \cdot \hat{e}_{\mathrm{TM}} = 0$, and $\hat{e}_{\mathrm{TE}} \cdot \hat{e}_{\mathrm{TM}} = 0$. The angle ϱ is a degree of freedom representing the orientation of the semiconductor lattice (crystalline structure) with respect to the propagation direction of two beams (pump and Stokes). We first consider the case where $\varrho = 45°$. As in section 3.2.1 in the previous chapter, we can calculate the scattering efficiency Σ for four different cases, where we suppose that the Stokes beam is always at normal incidence, i.e., $\vartheta_{\mathrm{S}} = 0$.

- **TE-TE :** We assume that both beams are TE polarized. Then, the polarization vector of both beams is given by $\hat{e}_{\mathrm{P}} = \hat{e}_{\mathrm{S}} = \left(1/\sqrt{2}, -1/\sqrt{2}, 0\right)$, yielding a scattering efficiency of $\boxed{\Sigma \equiv 1}$, which is independent of the angle of incidence ϑ_{P}.

- **TE-TM :** The pump polarization is still TE (as in the previous case), given by $\hat{e}_{\mathrm{P}} = \left(1/\sqrt{2}, -1/\sqrt{2}, 0\right)$, but the Stokes beam is TM polarized, which means that the Stokes polarization vector is $\hat{e}_{\mathrm{S}} = \left(1/\sqrt{2}, 1/\sqrt{2}, 0\right)$. The result is a vanishing scattering efficiency $\boxed{\Sigma \equiv 0}$ for all possible angles of incidence ϑ_{P} of the pump beam.

- **TM-TE :** This is the inverse of the previous configuration. The polarization vector of the pump beam is given by $\hat{e}_{\mathrm{P}} = \left(\cos\vartheta_{\mathrm{P}}/\sqrt{2}, \cos\vartheta_{\mathrm{P}}/\sqrt{2}, -\sin\vartheta_{\mathrm{P}}\right)$, while the Stokes beam is TE polarized, i.e., $\hat{e}_{\mathrm{S}} = \left(1/\sqrt{2}, -1/\sqrt{2}, 0\right)$. We obtain the scattering efficiency $\boxed{\Sigma = \sin^2\vartheta_{\mathrm{P}}.}$

Fig. 4.1. Illustration of the relationship between the propagation vector $\hat{k}$ of the pump or the Stokes beam and the unit vectors $\hat{e}_{\mathrm{TE}}$ and $\hat{e}_{\mathrm{TM}}$, which represent the TE and the TM polarization of the beams with respect to the plane of incidence. The angle ϑ is the angle of incidence of the beam. The direction [001] corresponds to normal incidence in the microcavity (i.e., as the Stokes beam, $\vartheta_{\mathrm{S}} = 0$). The angle ϱ determines the orientation of the semiconductor sample (i.e., its crystallographic axes) with respect to the plane of incidence. It is defined as the angle between the TE polarization vector $\hat{e}_{\mathrm{TE}}$ and the [100] direction. We assume that $\hat{k}$, $\hat{e}_{\mathrm{TE}}$, and $\hat{e}_{\mathrm{TM}}$ are perpendicular to one another.
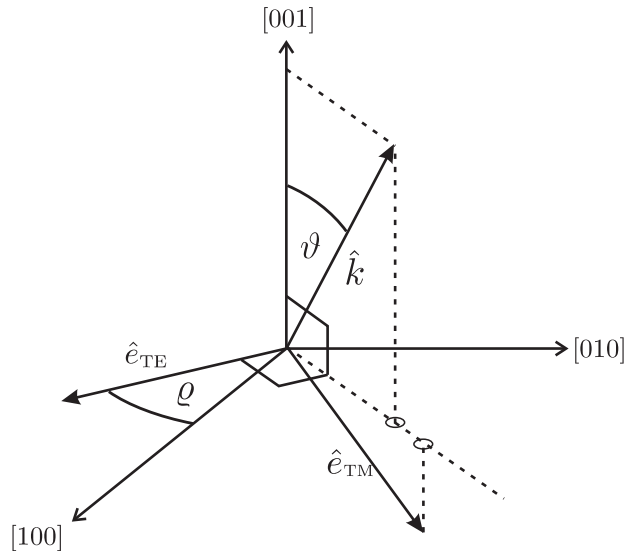
- **TM-TM :** In this case, we consider both beams as TM polarized. The resulting scattering efficiency is $\boxed{\Sigma \equiv 1}$, independently of ϑ_P, as in the first case.

As can be clearly seen from these results, the TE-TM combination does not show any stimulated Raman scattering at all, and TM-TE is the only combination that depends on the angle of incidence of the pump beam. For $\vartheta_P = 13.4°$, as we have calculated above, the scattering efficiency is only about 5 %. This is very small compared to the TE-TE and the TM-TM configurations, which both have the maximum efficiency of $\Sigma = 1$. As has been explained above (see the list of requirements regarding the sample design), it is reasonable to use a TM polarized pump beam. Thus, in conclusion, the TM-TM combination is the preferred choice of the polarization states for a sample orientation given by $\varrho = 45°$.

The above calculations can also be carried out for other sample orientations, such as $\varrho = 0°$ and $\varrho = 90°$. For both of these cases, we have calculated the scattering efficiency Σ for all of the four different combinations of the polarizations. In either case, the results are again $\Sigma \equiv 0$, $\Sigma \equiv 1$, or $\Sigma = \sin^2 \vartheta_P$, as in the detailed discussion of the $\varrho = 45°$ configuration, but for different polarization settings. For practical reasons, we consider in the remainder of this chapter only the configuration where the GaAs sample is aligned according to $\varrho = 45°$ because the real sample used for the experiments has a mark indicating the crystallographic direction [110].

4.1.2 Optimal design of the semiconductor sample

Taking the above-mentioned considerations and criteria into account, we have determined the final design of the sample by simulating its linear optical properties. For these simulations, we use a transfer-matrix method that has been previously developed in our group for the modeling of four-wave mixing in planar semiconductor nanostructures [103]. The method describes each layer (GaAs, AlGaAs, or AlAs) by its refractive index n, which depends on the polarization and on the wavelength of the light. All layers in the Bragg mirrors have a thickness of $\lambda/(4n)$. Each interface between the layers is described by an estimated scattering loss. The whole sample is then simulated by numerically calculating the forward and backward propagating electric fields in each layer, which is done by extensive matrix multiplications. This method also provides the wavelength dependence of the transmission and reflectivity coefficients of the microcavity as a whole, as well as the intracavity intensity.

In order to find the optimal design of the sample with respect to the above-described criteria, we have carried out many different simulations by varying the number of layers N_{front} and N_{rear} of both mirrors, the polarization states of the incident waves, and the composition of the $Al_x Ga_{1-x} As$ layers. As a result of this optimization, the front mirror consists of 15 pairs of $Al_{0.2} Ga_{0.8} As / AlAs$ layers and the rear mirror of 25 pairs of such layers. Also, we have verified that the maximum intracavity pump intensity is achieved with a TM polarized pump beam. As has been demonstrated above, we therefore work with TM polarization for both beams. Figure 4.2 shows the epitaxial structure (i.e., the sequence of the different layers) of the final optimal sample design.

By performing similar simulations for varying external angles of incidence ϑ', we find out that the external angle of incidence corresponding to a resonance wavelength of $\lambda = 924$ nm (pump wavelength) is actually $\vartheta'_P \approx 58°$ instead of the estimated 54.4°. In Fig. 4.3, we present the simulated transmission and reflection spectra of the optimal sample design at two different (external) angles of incidence, corresponding

Al$_{0.2}$Ga$_{0.8}$As	($e = 69.28$ nm)
AlAs	($e = 80.12$ nm)
Al$_{0.2}$Ga$_{0.8}$As	($e = 69.28$ nm)
AlAs	($e = 80.12$ nm)
•	
•	
•	
Al$_{0.2}$Ga$_{0.8}$As	($e = 69.28$ nm)
AlAs	($e = 80.12$ nm)

BM 15 pairs

GaAs	($e = 1340.25$ nm)

[001]

micro-cavity

AlAs	($e = 80.12$ nm)
Al$_{0.2}$Ga$_{0.8}$As	($e = 69.28$ nm)
•	
•	
•	
•	
•	
•	
AlAs	($e = 80.12$ nm)
Al$_{0.2}$Ga$_{0.8}$As	($e = 69.28$ nm)
AlAs	($e = 80.12$ nm)
Al$_{0.2}$Ga$_{0.8}$As	($e = 69.28$ nm)

BM 25 pairs

GaAs	($e = 500$ μm)

wafer sub-strate
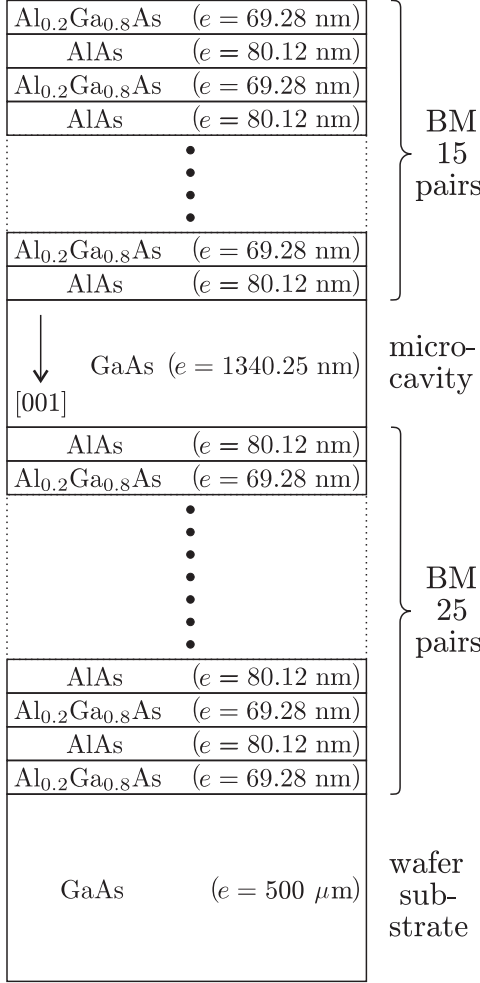
Fig. 4.2. Epitaxial structure of the optimal sample design showing the different layers and their thicknesses. The front Bragg mirror (BM) consists of 15 pairs of AlGaAs/AlAs layers, the rear Bragg mirror is composed of 25 pairs of layers. The thickness of each Bragg layer is $e = \lambda/(4n)$ with a wavelength of $\lambda = 950$ nm. The central GaAs layer is $5\lambda/n$ thick. The direction of the crystallographic [001] direction of the GaAs layer is indicated by the little arrow.

to the pump beam ($\vartheta' = 58°$) and the Stokes beam (normal incidence, $\vartheta' = 0°$). The graph clearly shows the two resonance peaks at the probe wavelength $\lambda_S = 950$ nm and at the pump wavelength $\lambda_P = 924$ nm. A detailed analysis of these spectra enables us to determine the resonance wavelength λ_0, the maximum transmission coefficient T_{max}, and the linewidth $\delta\lambda$ of the resonance (FWHM) for each external angle of incidence. Since we work at the tenth-order resonance (i.e., $m = 10$), we can also calculate the finesse $\mathcal{F}$ of the resonances according to

$$\mathcal{F} = \frac{\lambda_0}{10\,\delta\lambda} \ .$$

Moreover, knowing the finesse $\mathcal{F}$ and the maximum transmission T_{max}, we can also calculate the reflectivities of the front mirror R_1 and of the rear mirror R_2 individually. As is demonstrated in appendix B, the maximum transmission T_{max} and the finesse $\mathcal{F}$ can be expressed as

$$T_{max} = \frac{(1-R_1)(1-R_2)}{\left(1-\sqrt{R_1 R_2}\right)^2} \tag{4.1a}$$

$$\mathcal{F} = \frac{\pi \sqrt[4]{R_1 R_2}}{1-\sqrt{R_1 R_2}} \tag{4.1b}$$

where we have inserted $G \equiv 0$ (i.e., we consider the linear case without gain or loss in the medium) as well as $T_1 + R_1 = 1$ and $T_2 + R_2 = 1$ (i.e., both mirrors are assumed to be loss-free). As can be clearly seen, Eq. (4.1) is a system of two equations for two variables : R_1 and R_2. The second equation (4.1b) depends exclusively on the product $R_1 R_2$ so that we can define the geometric mean

$$R = \sqrt{R_1 R_2}$$

and find the solution

$$R = \left(-\frac{\pi}{2\mathcal{F}} + \sqrt{\frac{\pi^2}{4\mathcal{F}^2} + 1}\right)^2 ,$$
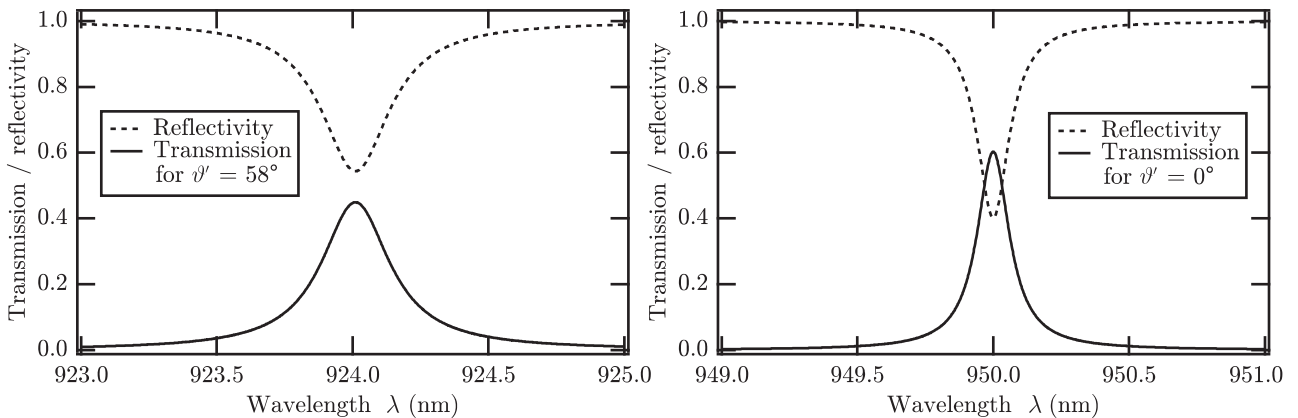
Fig. 4.3. Results of the simulations of the microcavity. Simulated spectrum of the optimal design, showing the transmission and reflectivity coefficients as a function of the wavelength at two different external angles of incidence : $\vartheta'_P = 58°$ (corresponding to the pump beam) and $\vartheta'_S = 0°$ (corresponding to the Stokes beam).

which depends only on the finesse $\mathcal{F}$. By using $R_1 = R^2/R_2$, the first equation (4.1a) leads to a quadratic equation in R_2, which has the solution

$$R_2 = \frac{1 + R^2 - T_{\max}(1 - R)^2}{2} + \sqrt{\frac{\left(1 + R^2 - T_{\max}(1 - R)^2\right)^2 - 4\,R^2}{4}}\,.$$

The solution for R_1 is then easily obtained by using again

$$R_1 = \frac{R^2}{R_2}$$

With the above equations, we can easily calculate the reflectivities of both Bragg mirrors for the pump and the Stokes beam. The following table summarizes all the results of the simulations :

	ϑ'	λ_0/nm	$T_{\max}$	$\delta\lambda$/nm	$\mathcal{F}$	R_1	R_2
Stokes	0°	950.0	0.60	0.14	680	0.9925	0.9983
Pump	58°	924.0	0.44	0.31	298	0.9817	0.9974

As these numbers clearly show, the optimal microcavity design fulfills all of the key requirements that we have mentioned in section 4.1.1, especially the resonance linewidths $\delta\lambda$ and the asymmetric reflectivities of the front and the rear mirror.

For the nonlinear pump-probe experiments that are presented in section 4.5, we use a semiconductor sample that corresponds to the above-described optimal sample design. It has been fabricated by our collaboration partners at the Laboratoire de Photonique et de Nanostructures (LPN) using a molecular epitaxy on a GaAs wafer. In section 4.4, we present an experimental *linear* characterization of the sample.

4.2 Analytical model of the pump-probe experiments with the GaAs microcavity

Before showing the experimental results, we develop in this section an analytical model of the nonlinear propagation of the Stokes wave in the GaAs microcavity. The purpose of the model is to provide a theoretical description of the pump-probe experiments, which is then used to simulate the measurements. The simulations yield valuable insights in *how* the measurements have to be carried out in order to provide the most meaningful results.

It should be noted that the model does not take into account any transient effects. As will be shown in section 4.5, the main results of the pump-probe experiments are related to the refractive effect due to free carriers at long delays ($\Delta t \gg 0$), for which a transient model is not necessary. For this reason, however, the model developed here does *not* provide an exact description of the effects for time delays around zero ($\Delta t \approx 0$). The latter would require a numerical solution of the coupled equations in the transient regime.

4.2.1 Pump and probe pulses and nonlinear effects

The central quantity of interest of the model is the Stokes transmission T_{S} of the microcavity. In section 2.4.2, we have presented a very simple model of SRS in a semiconductor microcavity, where we have assumed that pump and Stokes are continuous waves. Here, we have to take into account that the pump and the Stokes (i.e., the probe) beam come from a pulsed light source. Therefore, we first describe

the pump and probe pulses, then we reuse and extend the simple model from section 2.4.2, and finally we find a mathematical description of the nonlinear response of the semiconductor material, which depends on the pump wavelength, on the pump intensity, and on the time delay between the probe and the pump pulses.

Pump and probe picosecond pulses

Both pump and probe pulses are assumed to be Gaussian pulses. The time dependence of the probe intensity can therefore be expressed as

$$
I_S(t) \;=\; I_{S,0} \, \exp\left\{ - \frac{t^2}{(\widetilde{\tau}_S/2)^2} \right\} \,,
$$

where $I_{S,0}$ is the peak probe intensity, and $\widetilde{\tau}_S$ is the pulse duration (full width at $1/e$) of the pulses. The latter is related to the full width at half maximum τ_S through $\tau_S = \widetilde{\tau}_S \sqrt{\ln 2}$ so that we can express the time dependence of the probe intensity as

$$
I_S(t) \;=\; I_{S,0} \, \exp\left\{ - \frac{t^2}{(\tau_S/2\sqrt{\ln 2})^2} \right\} \;=\; I_{S,0} \, \exp\left\{ - 4\ln(2) \, \frac{t^2}{\tau_S^2} \right\} \,, \qquad (4.2)
$$

where the pulse duration τ_S is the full width at half maximum (FWHM). Pump and probe pulses do *not* arrive at the same time at the semiconductor sample. The delay of the probe pulse with respect to the pump pulse is given by Δt. It is negative in the case that the probe pulse arrives before the pump pulses, and vice versa. In its own time frame t', the pump pulses are described by

$$
I_P(t') = I_{P,0} \, \exp\left\{ - 4\ln(2) \, \frac{t'^{\,2}}{\tau_P^2} \right\} \,,
$$

where $I_{P,0}$ is the peak pump intensity and τ_P is the pulse duration (FWHM) of the pulses. Thus, in the time frame t of the probe pulses, the above expression becomes

$$
I_P(t') \;=\; I_P(t + \Delta t) \;=\; I_{P,0} \, \exp\left\{ - 4\ln(2) \, \frac{(t + \Delta t)^2}{\tau_P^2} \right\} . \qquad (4.3)
$$

In the following calculations, we use Eqs. (4.2) and (4.3) with pulse durations of $\tau_S = \tau_P = 12$ ps. Figure 4.4 illustrates the time dependence of the pulses. We furthermore assume that the repetition rate of the pump and probe pulses is $F = 10$ Hz, which corresponds to a time between two consecutive pulses of $T = 100$ ms. The delay Δt is one of the independent parameters of the model, as will become clear in the following.

Fig. 4.4. Illustration of the time dependence of the pump and probe intenstiy. The curve shows a gaussian pulse whose pulse duration (FWHM) is $\tau = 12$ ps.
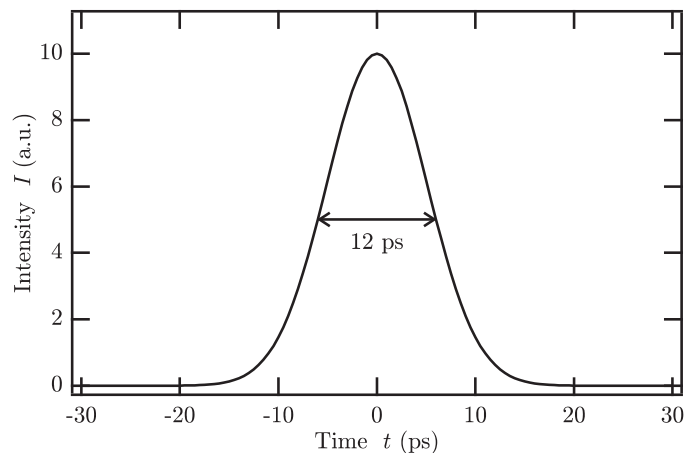
Stokes transmission of the semiconductor microcavity

We consider a planar GaAs microcavity that corresponds to the optimal design determined in section 4.1. The cavity length (i.e., the thickness of the central layer) is assumed to be $L = 5 \times 950$ nm$/3.5 \approx 1357$ nm. Hence, the probe beam, which is incident upon the microcavity at normal incidence ($\vartheta_{\mathrm{P}} = 0°$), is exactly at the tenth-order resonance if it has the so-called *optimal* probe wavelength $\lambda_{\mathrm{S}}^* = 950$ nm. As will be demonstrated below, it can be sensible to use probe wavelengths λ_{S} that are slightly off resonance, i.e., $\lambda_{\mathrm{S}} \neq \lambda_{\mathrm{S}}^*$. In that case, we define the *probe wavelength detuning* as the difference between the probe wavelength used and the optimal probe wavelength,

$$\Delta\lambda_{\mathrm{S}} = \lambda_{\mathrm{S}} - \lambda_{\mathrm{S}}^* .$$

λ_{S}^*

$\Delta\lambda_{\mathrm{S}}$

In the description of the simple model in section 2.4.2 we have derived an expression for the intensity transmission coefficient of a microcavity containing a gain medium. By introducing a nonlinear phase shift $\Delta\varphi_{\mathrm{NL}}$ into Eq. (2.96), we can express the Stokes transmission of the microcavity as

$$T_{\mathrm{S}} = \frac{(1 - R_{1,\mathrm{S}})(1 - R_{2,\mathrm{S}})\, e^{GL}}{\left|1 - \sqrt{R_{1,\mathrm{S}}R_{2,\mathrm{S}}}\, e^{GL}\, e^{2i(\varphi_{\mathrm{FP}} + \Delta\varphi_{\mathrm{NL}})}\right|^2} , \tag{4.4}$$

where the so-called Fabry-Perot phase φ_{FP} is the phase of the Stokes wave after a single passage of the resonator. Near the resonance, i.e., for a small detuning $\Delta\lambda_{\mathrm{S}}$ from the resonance wavelength, we can approximate the Fabry-Perot phase as

$$\varphi_{\mathrm{FP}} \approx - \frac{2\pi\, n_{\mathrm{S}}\, L \cos\vartheta_{\mathrm{S}}}{\lambda_{\mathrm{S}}^2} \Delta\lambda_{\mathrm{S}} = - \frac{2\pi\, n_{\mathrm{S}}\, L}{\lambda_{\mathrm{S}}^2} \Delta\lambda_{\mathrm{S}} , \tag{4.5}$$

as is demonstrated in Eq. (B.15) in appendix B. Here, we have also inserted $\vartheta_{\mathrm{S}} = 0$. All the nonlinear optical effects which have been described in sections 2.2 and 2.3 modify either the intensity or the phase of the Stokes wave (or both) during its propagation in the microcavity. This is taken into account by the gain coefficient G and the nonlinear phase shift $\Delta\varphi_{\mathrm{NL}}$ in Eq. (4.4), as is explained in more detail in the following sections.

Gain and phase shift due to stimulated Raman scattering

The influence of stimulated Raman scattering is described by the Raman susceptibility. As has been shown in section 2.2.3, the stimulated Raman scattering affects the intensity as well as the phase of the probe (Stokes) beam. The effect of SRS on the *intensity* is described by the gain coefficient G_{R}, which can be expressed as

$$G_{\mathrm{R}} = \gamma_{\mathrm{R}}\, M_{\mathrm{P}}\, I_{\mathrm{P}}(t') = \bar\gamma_{\mathrm{R}}\, \frac{1}{1 + \Delta^2}\, M_{\mathrm{P}}\, I_{\mathrm{P}}(t + \Delta t) , \tag{4.6}$$

where $\bar\gamma_{\mathrm{R}}$ is the Raman gain coefficient of the material, M_{P} is the intensity magnification factor introduced in section 2.4.2, and I_{P} is the incident pump intensity (i.e., the intensity of the pump beam). The parameter Δt describes the delay between pump and probe pulses. As can be clearly seen from the above equation, the stimulated Raman scattering only occurs when pump and probe pulse have a significant temporal overlap (i.e., for $\Delta t \approx 0$), which is consistent with our physical understanding of the Raman scattering as an *instantaneous*[1] process. The magnification factor

---

[1] We can calculate the characteristic time scale of Raman scattering from the linewidth of the Raman resonance by using the uncertainty relationship $\Delta E \Delta t \approx \hbar$. With $\Delta E = hc\, \delta\bar\nu_{\mathrm{R}}$ and a Raman linewidth of $\delta\bar\nu_{\mathrm{R}} = 3$ cm^{-1} for GaAs [102], we obtain the characteristic time of about 2 ps, which can be interpreted as the lifetime of the phonons in the semiconductor lattice, and which is significantly shorter than the duration of the pump and probe pulses.

describes the enhancement of the pump intensity inside the cavity at resonance. As can be seen from Eq. (2.104), it is a function of the reflectivities $R_{1,\mathrm{P}}$ and $R_{2,\mathrm{P}}$ of the two Bragg mirrors for the pump wave. Using the results of the simulations presented in section 4.1 (i.e., $R_{1,\mathrm{P}} = 0.9817$ and $R_{2,\mathrm{P}} = 0.9974$), we calculate

$$M_{\mathrm{P}} \;=\; \frac{(1 - 0.9738)\,(1 + 0.9946)}{\left(1 - \sqrt{0.9738 \times 0.9946}\right)^2} \;=\; 333 \;,$$

which means a more than 300-fold increase of the pump intensity in the microcavity. According to Eq. (2.53), the Raman-induced *phase shift* of the probe wave after one passage of the microcavity (i.e., at $z = L$) is given by

$$\Delta\varphi_{\mathrm{R}}(L) = \frac{\bar{\gamma}_{\mathrm{R}}}{2} \frac{\Delta}{1 + \Delta^2} M_{\mathrm{P}}\, I_{\mathrm{P}}(t + \Delta t)\, L \;. \qquad (4.7)$$

Equations (4.6) and (4.7) both depend on the detuning parameter Δ, which has already been discussed in section 2.2.2. This parameter describes the detuning of the pump frequency ω_{P} from the *optimal* pump frequency ω_{P}^*, which corresponds exactly to the Raman resonance. For a given probe (Stokes) frequency ω_{S}, the optimal pump frequency can be calculated according to $\omega_{\mathrm{P}}^* = \omega_{\mathrm{S}} + \Omega_{\mathrm{R}}$, where Ω_{R} is the Raman frequency. In the vicinity of the Raman resonance, i.e., for pump frequencies close to the optimal pump frequency ($\omega_{\mathrm{P}} \approx \omega_{\mathrm{P}}^* = \omega_{\mathrm{S}} + \Omega_{\mathrm{R}}$), we approximate the frequency-dependent (or wavelength-dependent, respectively) parameter Δ in terms of the detuning $\Delta\omega_{\mathrm{P}} = \omega_{\mathrm{P}} - (\omega_{\mathrm{S}} + \Omega_{\mathrm{R}})$. Based on the expression presented in Eq. (2.27), we obtain

$$\Delta \approx -2\frac{\Delta\omega_{\mathrm{P}}}{\delta\Omega_{\mathrm{R}}} = -2\frac{\Delta\nu_{\mathrm{P}}}{\delta\bar{\nu}_{\mathrm{R}}} \approx -\frac{2}{c\,\delta\bar{\nu}_{\mathrm{R}}} \frac{c}{\lambda_{\mathrm{P}}^2}\,\Delta\lambda_{\mathrm{P}} = -\frac{2}{\delta\bar{\nu}_{\mathrm{R}}\,\lambda_{\mathrm{P}}^2}\,\Delta\lambda_{\mathrm{P}} \;, \qquad (4.8)$$

where we have used the relationship $\nu = c\,\bar{\nu}$ between the frequency and the wave number of a light wave, as well as the relationship $\Delta\nu \approx (c/\lambda^2)\,\Delta\lambda$. The *pump wavelength detuning* $\Delta\lambda_{\mathrm{P}}$ represents the detuning of the pump wavelength from Raman resonance,

$\Delta\lambda_{\mathrm{P}}$
$$\Delta\lambda_{\mathrm{P}} \;=\; \lambda_{\mathrm{P}} \;-\; \lambda_{\mathrm{P}}^* \;,$$

where the *optimal* pump wavelength λ_{P}^* can be calculated for a given probe (Stokes) wavelength λ_{S} according to

λ_{P}^*
$$\omega_{\mathrm{P}}^* = \omega_{\mathrm{S}} + \Omega_{\mathrm{R}} \qquad \Longleftrightarrow \qquad \lambda_{\mathrm{P}}^* = \left(\frac{1}{\lambda_{\mathrm{S}}} + \bar{\nu}_{\mathrm{R}}\right)^{-1} \;.$$

Here, we have again used the relationship $\omega = 2\pi\,\nu = 2\pi\,c\,\bar{\nu} = 2\pi\,c/\lambda$ between angular frequency, frequency, wavenumber, and wavelength.

In the above paragraphs, we have presented the definitions of λ_{S}^*, $\Delta\lambda_{\mathrm{S}}$, λ_{P}^*, and $\Delta\lambda_{\mathrm{P}}$, which are related to two different sorts of resonances : the Fabry-Perot resonance in the *microcavity* and the *Raman* resonance of the semiconductor material. For the understanding of the modeling (and of the experiments in section 4.5), these definitions should not be confused with one another.

The starting point of the model is a microcavity of a thickness L whose tenth-order resonance corresponds to the so-called optimal probe wavelength λ_{S}^*. The probe beam has a wavelength λ_{S} which can be equal to λ_{S}^* (i.e., exactly at resonance in the microcavity), but it in general, it can also be slightly off resonance. In the latter case, the wavelength detuning of the probe beam from the *microcavity* resonance is denoted by $\Delta\lambda_{\mathrm{S}}$. Based on the actual wavelength λ_{S} of the probe beam, we can

calculate the pump wavelength that corresponds exactly to the *Raman* resonance, which is called the optimal pump wavelength λ_P^*. The wavelength of the pump beam λ_P can be equal to this optimal pump wavelength (i.e., exactly at Raman resonance). However, the pump wavelength λ_P can also be slightly off Raman resonance for the given probe wavelength. In that case, the detuning of the pump wavelength from the *Raman* resonance (not to be confused with the microcavity resonance) is denoted by $\Delta\lambda_P$. It should be noted that the pump beam can always be made resonant in the *microcavity* by changing the angle of incidence of the pump beam accordingly. This is the key advantage of a planar microcavity.

For GaAs at room temperature, we use a Raman gain coefficient[2] $\bar{\gamma}_R = 50 \times 10^{-11}$ m/W, a Raman shift given by the wave number $\bar{\nu}_R = 292$ cm^{-1}, and a Raman linewidth (FWHM) of $\delta\bar{\nu}_R = 3$ cm^{-1} [102].

Free charge carriers created by the pump pulses

Having defined the pulse shape of the pump beam in Eq. (4.3), we can describe the time dependence of the free carrier density N_{FC}. For this purpose, we use the differential equation (2.72) describing the number of free carriers per unit volume. The lifetime τ_e of the free carriers in GaAs is in the nanosecond range [45], which is much longer than the pulse duration ($\tau_e \gg \tau_P$) and much shorter than the time between two pulses ($\tau_e \ll T$). For our model, we can approximate the carrier lifetime as infinitely long, $\tau_e \to \infty$, so that we can easily integrate Eq. (2.72), yielding

$$N_{FC}(t) = \frac{\beta_{TPA}}{2\hbar\omega_P} \int_{-\infty}^{t} \left(M_P \, I_P(t') \right)^2 \, dt' \,.$$

By inserting the explicit form of the pump pulse given by Eq. (4.3), we obtain the time dependence of the free carrier density in the time frame of the probe pulses

$$N_{FC}(t + \Delta t) = \frac{\beta_{TPA}}{4\pi\hbar c} \frac{\lambda_P \, \tau_P}{4\sqrt{\ln 2}} \sqrt{\frac{\pi}{2}} \left[1 + \text{erf}\left(\sqrt{8\ln 2} \, \frac{t + \Delta t}{\tau_P} \right) \right] M_P^2 \, I_{P,0}^2 \,. \qquad (4.9)$$

For GaAs we use a value of $\beta_{TPA} = 23$ cm/GW^2 [105]. Figure 4.5 illustrates the time dependence of the free carrier density in the context of the present model for different pump intensities $I_{P,0}$. By inserting the limit $t \to \infty$, we calculate the number of free carriers generated during one pump pulse with a wavelength of $\lambda_P = 924$ nm and, for example, a peak pump intensity of $I_{P,0} = 10$ MW/cm^2 to be $N_{FC}^{total} = 4.6 \times 10^{24}$ m^{-3}.

---

[2]This value has been extrapolated from the spontaneous Raman scattering efficiency reported in [104] and using [41] for the calculation of $\bar{\gamma}_R$.
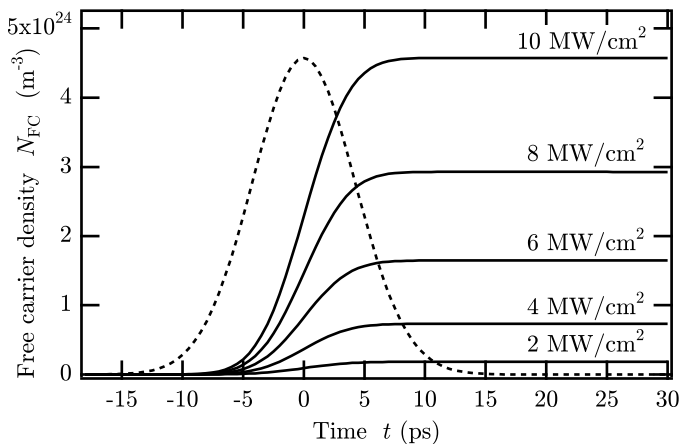

Fig. 4.5. Illustration of the time dependence of the free carrier density N_{FC} according to Eq. (4.9) for different pump intensities $I_{P,0}$. The dotted line represents the Gaussian pump pulse.

Two photon absorption and absorption by free carriers

The free charge carriers are created by the self-induced two photon absorption (TPA) of the *pump* wave. The *probe* wave, however, is affected by the *cross*-two photon absorption (XTPA), as described by Eq. (2.71),

$$\frac{\mathrm{d}}{\mathrm{d}z}I_\mathrm{S} = -2\,\beta_\mathrm{XTPA}\,I_\mathrm{P}I_\mathrm{S}\,.$$

Under the assumption of a non-depleted pump beam, this equation can be easily integrated, yielding

$$I_\mathrm{S} = I_\mathrm{S,0}\,e^{-2\,\beta_\mathrm{XTPA}\,I_\mathrm{P}\,z}\,.$$

In analogy to Eq. (4.6) for the Raman gain, we can thus describe the cross-two photon absorption by a negative gain coefficient,

$$G_\mathrm{XTPA} \;=\; -2\,\beta_\mathrm{XTPA}\,I_\mathrm{P}(t') \;\approx\; -2\,\beta_\mathrm{TPA}\,I_\mathrm{P}(t+\Delta t)\,, \tag{4.10}$$

where we have ignored dispersion, i.e., we have set $\beta_\mathrm{XTPA} \approx \beta_\mathrm{TPA}$ (see also section 2.3.2).

In a very similar way, we can express the free carrier absorption (FCA) by a negative gain coefficient as

$$G_\mathrm{FCA} \;=\; -\alpha_\mathrm{FC} \;=\; -\sigma_\mathrm{a}\,N_\mathrm{FC}\,,$$

where the free carrier absorption coefficient α_FC has already been introduced in Eq. (2.82). As has been explained in section 2.3.3, the inverse of α_FC is a measure of the penetration depth of the material. The factor σ_a can be calculated with Eq. (2.75). For the effective masses and mobilities of electrons and holes in GaAs, we use the values shown in Tab. 4.1, where m_0 is the electron mass $m_0 = 9.11 \times 10^{-31}$ kg. With these values, we obtain $\sigma_\mathrm{a} \approx 4.3 \times 10^{-22}$ m^2. Knowing that the number of free carriers generated by one pump pulse is of the order of 10^{24} m^{-3} (e.g., 4.6×10^{24} m^{-3} for a pump intensity $I_\mathrm{P,0} = 10$ MW/cm^2), the penetration depth is of the order of a millimeter. This is very long compared to the resonator length of $L \approx 1.3$ μm so that we can henceforth ignore the free carrier absorption (FCA) in this model, i.e., $G_\mathrm{FCA} \approx 0$.

$$m_\mathrm{e} = 0.0632\,m_0$$
$$m_\mathrm{h} = 0.5\,m_0$$
$$\mu_\mathrm{e} = 6500 \times 10^{-4}\ \mathrm{m^2V^{-1}s^{-1}}$$
$$\mu_\mathrm{h} = 400 \times 10^{-4}\ \mathrm{m^2V^{-1}s^{-1}}$$
$$E_\mathrm{g} = 1.42\ \mathrm{eV} = 2.72 \times 10^{-19}\ \mathrm{J}$$

Tab. 4.1. Effective masses and mobilities of electrons and holes in GaAs [45].

Refractive index change by free carriers and cross-Kerr effect

In section 2.3.3, we have introduced the phase shift of the Stokes wave that is induced by the free carriers in the semiconductor material. Since the carriers are created by the *pump* pulse, whereas here, we consider the phase shift of the *Stokes* (i.e., the *probe*) wave, we have to take into account the delay Δt between the probe and the pump pulse. Thus, we can calculate Stokes phase shift after one passage of the microcavity ($z = L$) with Eq. (2.79) as

$$\Delta\varphi_\mathrm{FC}(L) = \frac{2\pi}{\lambda_\mathrm{S}}\sigma_n N_\mathrm{FC}(t+\Delta t)\,L\,. \tag{4.11}$$

The coefficient σ_n can be calculated with Eq. (2.74). Using again the values listed in Tab. 4.1, we find $\sigma_n \approx -1.35 \times 10^{-26}$ m^3.

According to Eq. (2.65) in section 2.3.1, the Stokes phase shift that is caused by the cross-Kerr effect is described by the nonlinear refractive index n_2K. For simplicity,

we ignore dispersion and approximate the value of n_{2X} by the nonlinear refractive index of the normal Kerr effect n_2. We obtain the cross-Kerr phase shift after one passage of the microcavity,

$$\Delta\varphi_{XK}(L) \approx \frac{2\pi}{\lambda_S}\, 2\, n_2\, I_P(t + \Delta t)\, L \; . \tag{4.12}$$

As before, the time delay between pump and probe beam has been taken into account. Although we have not found a published value of the nonlinear refractive index n_2 for GaAs for the wavelengths used here (i.e., between 920 and 950 nm), we can estimate a reasonable value by using the results of a fairly complex analytical model [106] with an experimental reference value of $n_2 \approx -3 \times 10^{-17}$ m^2/W at 1064 nm [107]. Without presenting the whole calculation here, we obtain a value of $n_2 \approx -4 \times 10^{-17}$ m^2/W.

4.2.2 Analytical model of the nonlinear transmission

Before presenting the results of the model, we summarize briefly the key findings of the previous section. The model that we present here describes the nonlinear transmission of the microcavity at the Stokes (probe) wavelength, which is given by

$$T_S = \frac{(1 - R_{1,S})(1 - R_{2,S})\, e^{GL}}{\left|1 - \sqrt{R_{1,S}R_{2,S}}\, e^{GL}\, e^{2i(\varphi_{FP} + \Delta\varphi_{NL})}\right|^2} \; .$$

The Fabry-Perot phase φ_{FP} is given by Eq. (4.5) as a function of the detuning from the microcavity resonance $\Delta\lambda_S$ as

$$\varphi_{FP} \approx -\frac{2\pi\, n\, L}{\lambda_S^2}\, \Delta\lambda_S \; .$$

The total nonlinear phase shift $\Delta\varphi_{NL}$ at the Stokes wavelength is caused by the Raman effect, the cross-Kerr effect, and the free carriers. It can be expressed as the sum $\Delta\varphi_R + \Delta\varphi_{XK} + \Delta\varphi_{FC}$, yielding

$$\Delta\varphi_{NL} = \left(\frac{\bar{\gamma}_R}{2}\frac{\Delta}{1 + \Delta^2}\, L + \frac{2\pi}{\lambda_S}\, 2\, n_2\, L\right) I_P(t + \Delta t) + \left(\frac{2\pi}{\lambda_S}\, \sigma_n L\right) N_{FC}(t + \Delta t) \; ,$$

where the Δ parameter is proportional to the pump wavelength detuning $\Delta\lambda_P$ according to Eq. (4.8), which is

$$\Delta \approx -\frac{2}{\delta\bar{\nu}_R \lambda_P^2}\, \Delta\lambda_P \; .$$

The pump intensity I_P and the free carrier density N_{FC} are given by Eqs. (4.3) and (4.9). As mentioned above, the gain G is essentially composed of the Raman gain G_R given by Eq. (4.6) and the negative XTPA contribution G_{XTPA} described by Eq. (4.10),

$$G \approx (\gamma_R - 2\,\beta_{TPA})\, I_P(t + \Delta t) = \left(\bar{\gamma}_R\frac{1}{1 + \Delta^2} - 2\,\beta_{TPA}\right) I_P(t + \Delta t) \; , \tag{4.13}$$

whereas we can neglect the influence of the free carrier absorption (FCA) here. As has been explained in detail in the previous section, it is important to distinguish between the detuning from the *microcavity* resonance $\Delta\lambda_S$, which determines the starting point of the *probe* wavelength, and the detuning $\Delta\lambda_P$ from the *Raman* resonance, which indicates by how much the *pump* wavelength is detuned from the optimum pump wavelength λ_P^*.

The above set of equations represents an analytical nonlinear model of the probe transmission (i.e., Stokes transmission) T_S of the microcavity, including stimulated Raman scattering (SRS), the cross Kerr effect (X-Kerr), cross-two photon absorption (XTPA), and free carrier refraction (FCR). The free carrier absorption (FCA) is not taken into account for reasons that have been discussed above. The model depends on several independent parameters, which are the probe wavelength detuning $\Delta\lambda_S$, the pump wavelength detuning $\Delta\lambda_P$, the pump intensity $I_{P,0}$, and the probe-pump delay Δt. We therefore express the nonlinear probe transmission as

$$T_S = T_S\Big(\Delta\lambda_S, \Delta\lambda_P, I_{P,0}, \Delta t\Big).$$

It is worth noting here that only the stimulated Raman scattering depends on the parameter Δ and thus on the pump wavelength λ_P. For all other nonlinear effects, the exact value of the pump wavelength does not play a crucial role (as long as it is approximately in the range between 900 and 950 nm).

Linear transmission as special case of nonlinear transmission

From this general, nonlinear model, we can easily derive the *linear* case, where we do not take into account the nonlinear effects, by setting $I_{P,0} = 0$. In that case, there is no pump beam at all ($I_P \equiv 0$), and therefore the free carrier density vanishes, too ($N_{FC} \equiv 0$). Consequently, the gain G and the nonlinear phase shift $\Delta\varphi_{NL}$ are both zero, and the resulting linear probe transmission is only a function of the probe wavelength detuning $\Delta\lambda_S$, yielding an Airy function (see appendix B) given by

$$T_S = T_S(\Delta\lambda_S) = \frac{(1 - R_{1,S})(1 - R_{2,S})}{\left|1 - \sqrt{R_{1,S}R_{2,S}}\, e^{-2i\,(2\pi nL/\lambda_S^2)\,\Delta\lambda_S}\right|^2}. \tag{4.14}$$

In Fig. 4.6 we show the resulting linear transmission spectrum of the microcavity according to Eq. (4.14). This transmission curve indicates the linear transmission T_S of the microcavity for the probe beam as a function of the probe wavelength detuning $\Delta\lambda_S$ (or the probe wavelength λ_S, respectively).

Influence of nonlinear effects on the microcavity transmission

In the following, we discuss the different components of the *nonlinear* model, i.e., we show how all the different nonlinear optical effects affect the probe transmission T_S. In order to do that, we divide the nonlinear effects into two groups, which have

Fig. 4.6. Simulated linear transmission spectrum of the GaAs microcavity according to the analytical model of the probe (i.e., Stokes) beam propagation. The curve correponds to an Airy function, as given by Eq. (4.14).
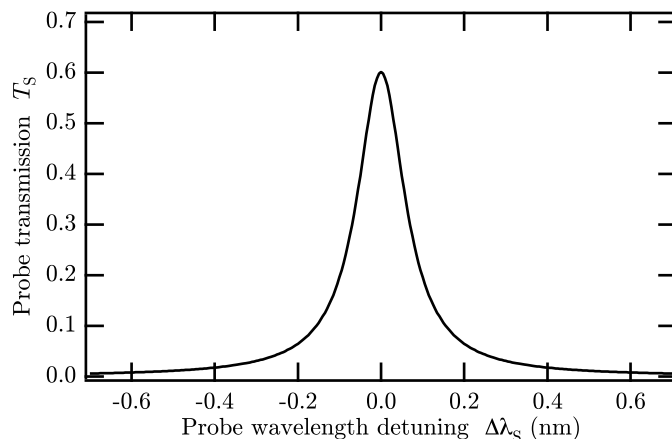
already been mentioned above : the effects affecting the *intensity* of the probe wave and the effects changing its *phase.*

In the fist group, we consider the cross-two photon absorption (XTPA) and the stimulated Raman scattering (SRS). The influence of these two effects on the probe transmission is obvious. The XTPA is an absorptive effect and thus reduces the probe transmission, while the SRS is basically an amplifying process which can therefore lead to an enhanced transmission (as mentioned in section 2.4.2, the "transmission" can even be greater than unity in this case).

The second group, i.e., the effects modifying the phase of the probe beam, is composed of the cross Kerr effect (X-Kerr), the free carrier refraction (FCR), and again the stimulated Raman scattering (SRS) through the real part of the Raman susceptibility. As opposed to the first group, their influence on the probe transmission is indirect. These effects induce a phase shift $\Delta\varphi_{\mathrm{NL}}$, which is then translated into a modification of the transmission by "walking" up or down on the linear resonance curve (Airy function) shown in Fig. 4.6. To illustrate this translation process, we consider the Airy curve as a function of the *phase* φ_{FP} (instead of the wavelength detuning as in Eq. (4.14)),

$$T_{\mathrm{S}}\big(\varphi_{\mathrm{FP}}\big) \;=\; \frac{(1-R_{1,\mathrm{S}})(1-R_{2,\mathrm{S}})}{\big|1-\sqrt{R_{1,\mathrm{S}}R_{2,\mathrm{S}}}\,e^{2i\,\varphi_{\mathrm{FP}}}\big|^2} \;=\; \frac{T_{\max}}{1+\frac{4}{\pi^2}\,\mathcal{F}^2\sin^2(\varphi_{\mathrm{FP}})}\;, \qquad (4.15)$$

which is derived and discussed in detail in appendix B and which is plotted in Fig. 4.7. The finesse $\mathcal{F}$ is the ratio between the free spectral range $\Delta\nu_{\mathrm{FSR}}$ of the microcavity and the full width at half maximum $\delta\nu_{1/2}$ of the resonance curve in the frequency domain. The free spectral range corresponds to a phase shift $\varphi_{\mathrm{FP}}=\pi$, which is the periodicity of the Airy function. Therefore, we can define the phase $\delta\varphi_{1/2}$ corresponding to the full width at half maximum (FWHM) of the resonance curve in the *phase* domain according to

$$\mathcal{F} \;=\; \frac{\Delta\nu_{\mathrm{FSR}}}{\delta\nu_{1/2}} \;=\; \frac{\pi}{\delta\varphi_{1/2}} \qquad \Longleftrightarrow \qquad \delta\varphi_{1/2} \;=\; \frac{\pi}{\mathcal{F}}\;. \qquad (4.16) \qquad\qquad \delta\varphi_{1/2}$$

The physical meaning of $\delta\varphi_{1/2}$ is illustrated in Fig. 4.7. We suppose that the initial phase of the electromagnetic wave in the microcavity is such that the transmission is exactly half the maximum transmission, i.e., $T_{\max}/2$, as is illustrated by point A. By shifting the phase of the wave towards the right, we move up on the transmission curve, and the transmission thereby increases. For a phase shift of $\delta\varphi_{1/2}/2$, we reach
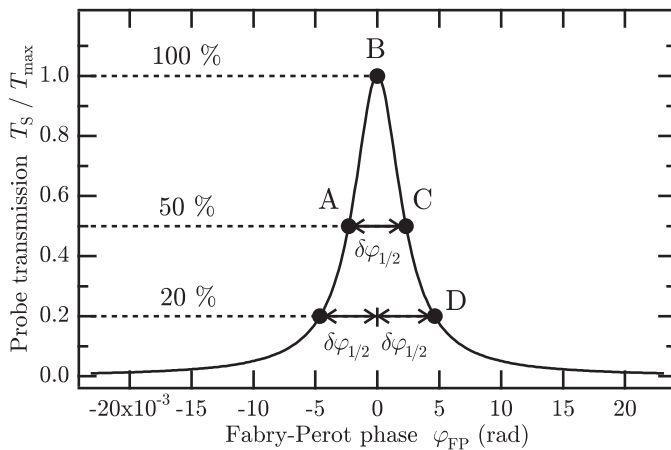

Fig. 4.7. Normalized simulated linear transmission spectrum of the GaAs microcavity as a function of the phase φ_{FP} according to Eq. (4.15). Basically, the graph shows the same curve as Fig. 4.6. Only the ordinate is normalized to the maximum transmission $T_{\max}$, and the abscissa is given as a phase instead of a wavelength. For more explanations see text.

the maximum $T_{\max}$ of the transmission curve in point B. By moving further to the right, the transmission becomes again $T_{\max}/2$ in point C, which corresponds exactly to a total phase shift of $\delta\varphi_{1/2}$.

Besides the meaning as the linewidth (FWHM) of the resonance, there is another useful interpretation of $\delta\varphi_{1/2}$. If we start our considerations at point B, then a phase shift of $\delta\varphi_{1/2}$ leads to point D, which causes a *significant* drop in the microcavity transmission. To quantify this drop, we insert $\delta\varphi_{1/2}$ into Eq. (4.15). Since the finesse $\mathcal{F}$ is usually much greater than π, we can approximate the sine function by its argument, $\sin(\pi/\mathcal{F}) \approx \pi/\mathcal{F}$, so that the resulting transmission in point D is only one fifth (i.e., 20 %) of the maximum transmission,

$$T_{\mathrm{S}}(\delta\varphi_{1/2}) \;\approx\; \frac{T_{\max}}{1 + \frac{4}{\pi^2}\mathcal{F}^2\,\frac{\pi^2}{\mathcal{F}^2}} \;=\; \frac{T_{\max}}{1 + 4} \;=\; \frac{1}{5}\,T_{\max}\;.$$

In both of the above-described interpretations, $\delta\varphi_{1/2}$ represents a characteristic quantity for the given resonance curve, i.e., for the given microcavity with its reflectivities of the two mirrors. Therefore, we use $\delta\varphi_{1/2}$ in the following considerations as a reference, i.e., as a sort of unit of phase shifts.

We are now interested in the contributions of the different nonlinear effects to the total nonlinear phase shift $\Delta\varphi_{\mathrm{NL}}$ that we have included in our model. As has been shown in section 4.2.1, the phase shifts induced by the cross Kerr effect (X-Kerr), the free carrier refraction (FCR), and the stimulated Raman scattering (SRS) are given by Eqs. (4.12), (4.11), and (4.7), respectively. Essentially, all three phase shifts are a function of the time delay Δt and of the pump intensity $I_{\mathrm{P},0}$ (either directly or indirectly through the free carrier density N_{FC}). The SRS-induced phase shift depends additionally on the pump wavelength detuning $\Delta\lambda_{\mathrm{P}}$. In Fig. 4.8, we illustrate the time dependence of the three phase shifts according to the above-mentioned equations for a pump intensity $I_{\mathrm{P},0} = 2$ MW/cm^2. As stated above, the phase shifts are given in units of $\delta\varphi_{1/2}$.

For the sake of convenience, we will omit the "X" in "X-Kerr" and "XTPA" in the remainder of this chapter because we only consider the *probe* beam here, and thus it is clear that only the *non*-degenerate effects XTPA and X-Kerr (as opposed to the self-induced effects TPA and Kerr) are of interest for the discussion.

As can be clearly seen from the graphs in Fig. 4.8, the (cross) Kerr effect and the stimulated Raman scattering are instantaneous effects. That means that they occur only as long as the pump pulse is present in the microcavity, i.e., around $\Delta t = 0$ in the center of the graphs. The free carrier refraction, however, is a long-term effect that depends on the free carrier lifetime in the microcavity, as has already been discussed in section 2.3.3. It is thus fairly easy to identify the contribution of the free carriers, simply by looking at the long-term behavior.

While the Kerr and FCR phase shifts are purely negative (which is caused by the material properties of GaAs), the SRS-induced phase shift can be positive or negative, as the three graphs on the right hand side of Fig. 4.8 show. The three graphs correspond to three different pump wavelengths : exactly at Raman resonance ($\Delta\lambda_{\mathrm{P}} = 0$), slightly off Raman resonance towards longer wavelengths ($\Delta\lambda_{\mathrm{P}} = +0.12$ nm), and slightly off Raman resonance towards shorter wavelengths ($\Delta\lambda_{\mathrm{P}} = -0.12$ nm). The latter two cases, i.e., $\Delta\lambda_{\mathrm{P}} = \pm0.12$ nm, have been chosen for illustration purposes because they show the strongest positive and negative phase shift, respectively. As can be seen from the real part of the Raman susceptibility (cf. Fig. 2.3), beyond this maximum, i.e., for a higher detuning $|\Delta\lambda_{\mathrm{P}}| > 0.12$ nm, the phase shift becomes less strong.
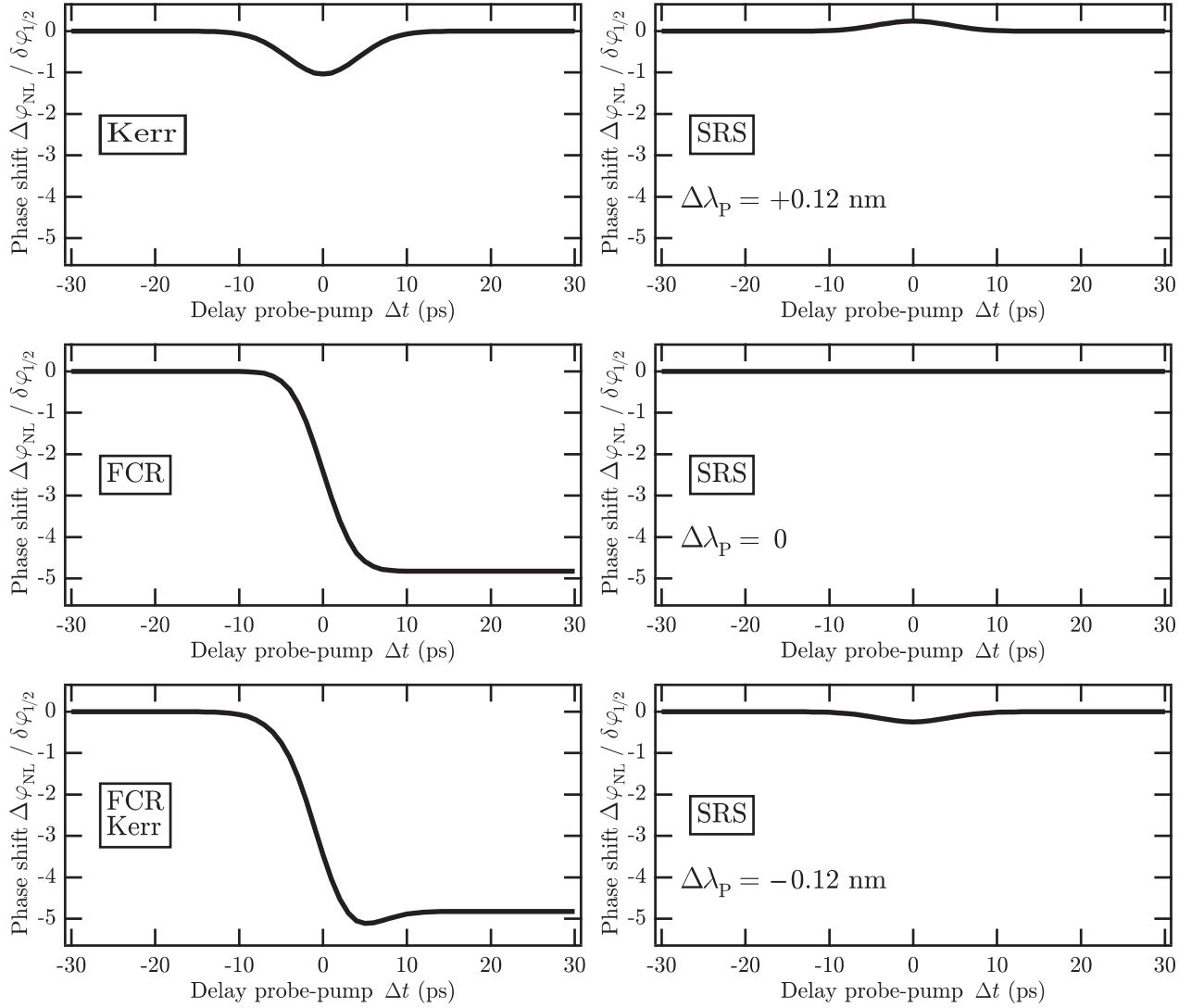
Fig. 4.8. Calculated time dependence of the phase shifts induced by different nonlinear optical effects (Kerr, FCR, SRS) in units of $\delta\varphi_{1/2}$. The phase shifts have been calculated with Eqs. (4.12), (4.11), and (4.7), respectively, for a pump intensity $I_{P,0} = 2$ MW/cm^2. The three graphs on the right hand side correspond to three different pump wavelength detunings $\Delta\lambda_P$, where $\Delta\lambda_P = \pm 0.12$ nm show the strongest positive and negative phase shift.

A comparison between the different graphs clearly shows that the FCR phase shift is by far the strongest one, followed by the Kerr-induced phase shift, which is the second strongest one. The lower left-hand graph in Fig. 4.8 illustrates the combination of these two effects. Compared to this, the phase shift due to SRS is very weak and appears only as a small perturbation. All the curves in Fig. 4.8 have been calculated for a moderate pump intensity of 2 MW/cm^2. Since the FCR contribution depends on the free carrier density, which in turn is a function of the *square* of the pump intensity (while Kerr and SRS are only linear in I_P), the discrepancy between the relative strengths of the different contributions is even more pronounced for higher pump intensities.

The phase shifts in Fig. 4.8 are given in units of $\delta\varphi_{1/2}$. Thus, we can see the influence of the different nonlinear effects on the microcavity transmission directly from the graphs. Supposing that the initial state of the resonator is point B (in Fig. 4.7), the negative phase shift caused by the Kerr effect leads to a decrease of the transmission as we move down on the resonance curve to the left. For a pump intensity of $I_{P,0} = 2$ MW/cm^2, the maximum Kerr shift (i.e., at $\Delta t = 0$) causes the transmission to drop to about 20 % of its maximum value because $\Delta\varphi_{XK} \approx -\delta\varphi_{1/2}$,

as is indicated by the upper left graph in Fig. 4.8. The FCR-induced phase shift for the same pump intensity is five times stronger so that we move even further to the left on the resonance curve in Fig. 4.7 to almost zero transmission. As mentioned above, the SRS contribution is almost negligible compared to the other two effects.

If, as opposed to the above considerations, the initial state of the microcavity is given by point C (in Fig. 4.7), the negative phase shifts induced by the Kerr effect and the free carriers cause the transmission first to rise up to the maximum and then to roll over the maximum to smaller values. Here again, the FCR contribution is much stronger ($\Delta\varphi_{\mathrm{FC}} \approx -5\,\delta\varphi_{1/2}$) and leads to an almost zero transmision.

In both of the above cases, the Kerr phase shift returns to $\Delta\varphi_{\mathrm{XK}} = 0$ after the pump pulse has passed the microcavity, whereas the FCR-induced phase shift persists over the much longer free carrier lifetime.

4.2.3   Simulations of the pump-probe experiments

In the previous section, we have analyzed the different mathematical components of our model and their influence on the intensity and the phase of the probe (Stokes) wave in the semiconductor microcavity. We have also determined the resulting consequences for the probe transmission T_{S}. Based on these considerations, we now show some simulations of the pump-probe experiments presented in section 4.5.

Figures 4.9 and 4.10 on pages 96 and 97 show the results of the simulations. Each figure contains ten graphs which show the influence of the different nonlinear optical effects on the probe transmission T_{S}. The graphs on the left-hand side of both figures show all the nonlinear effects (i.e., TPA, Kerr, FCR, and SRS) *separately*, for illustration purposes, whereas the graphs on the right-hand side represent various *combinations* of these four effects. As we have shown in section 4.2.2, our model of the probe transmission T_{S} has four independent parameters,

$$T_{\mathrm{S}} \;=\; T_{\mathrm{S}}\!\Big(\Delta\lambda_{\mathrm{S}}, \Delta\lambda_{\mathrm{P}}, I_{\mathrm{P},0}, \Delta t\Big),$$

whose influence on the transmission can be seen in the graphs. Each graph in Figs. 4.9 and 4.10 shows T_{S} versus the time delay Δt for several pump intensities $I_{\mathrm{P},0}$ between 0 and 2 MW/cm^2 (as multiple traces per graph). Regarding the probe wavelength detuning $\Delta\lambda_{\mathrm{S}}$, we consider two different situations, which have already been discussed in the previous section : a probe wavelength that is exactly at resonance in the microcavity ($\Delta\lambda_{\mathrm{S}} = 0$, point B in Fig. 4.7) and a situation where the probe beam is halfway off resonance ($\Delta\lambda_{\mathrm{S}} = -0.07$ nm, point C in Fig. 4.7). It should be noted here that according to Eq. (4.5), the Fabry-Perot phase φ_{FP} has the opposite sign of the probe wavelength detuning $\Delta\lambda_{\mathrm{S}}$. The influence of stimulated Raman scattering is shown for two different pump wavelength detunings : one exactly at Raman resonance ($\Delta\lambda_{\mathrm{P}} = 0$) and one far off the Raman resonance ($\Delta\lambda_{\mathrm{P}} = +2.4$ nm).

When considering only *one* nonlinear effect at a time, i.e., the five graphs on the left-hand side of each figure, we find that the time dependence of the probe transmission T_{S} in these graphs corresponds exactly to the discussion in the previous section. In other words, we clearly see the expected influence of the nonlinear effects on the intensity and on the phase of the probe (Stokes) wave in the microcavity.

As the top left graphs illustrate, TPA reduces the transmission by attenuating the probe intensity directly inside the microcavity (we consider the non-degenerate TPA, or cross-TPA, here). The Kerr effect and the FCR both induce a phase shift of the probe wave in the microcavity, which is translated by the resonance curve (Airy function) into a variation of the probe transmission, as has been demonstrated

in the previous section. In Fig. 4.9, where the probe beam is initially exactly at resonance (i.e., $T_\mathrm{S} = T_\mathrm{max}$), both effects force the transmission to decrease. However, in Fig. 4.10, where the starting point is halfway off the microcavity resonance (i.e., $T_\mathrm{S} = T_\mathrm{max}/2$), the transmission first rises to the maximum, in the vicinity of $\Delta t \approx 0$, and then decreases by moving down on the Airy curve. In either case, it is clearly visible that the Kerr phase shift returns very fast to the initial state, whereas the FCR induced phase shift keeps the transmission low in the long-term.

The fourth graph on the left-hand side of both figures shows clearly that the microcavity transmission is not influenced by SRS if the pump wavelength is far off the Raman resonance (i.e., $T_\mathrm{S}(\Delta t) \approx \mathrm{const.}$). This means that for $\Delta\lambda_\mathrm{P} \gg 0$ or $\Delta\lambda_\mathrm{P} \ll 0$, SRS can be ignored. However, as can be seen from bottom left graphs, the transmission can be significantly enhanced (i.e., amplified) if the pump wavelength is exactly at Raman resonance (i.e., if $\Delta\lambda_\mathrm{P} = 0$). In that case (see Fig. 4.9), our model predicts a more than 120-fold amplification (by considering *only* SRS and no other nonlinear effect). For sure, this theoretical result would *not* be obtained in an experiment because the analytical model presented here does *not* take into account the depletion of the pump beam (due to the energy transfer to the probe beam), *nor* does it include any transient phenomena occurring during the nonlinear interaction (such as a chirp of the pump pulse etc.).

The upper three graphs on the right-hand side of each figure illustrate the combinations TPA with Kerr, TPA with FCR, and FCR with Kerr. These graphs serve only as an illustration of the combined influence of two effects at the same time.

The main interest of the analytical model that we have developed in this section is to simulate the pump-probe experiments presented in section 4.5. For this purpose, we have to take into account all three effects (i.e., TPA, Kerr, and FCR) and additionally SRS. The bottom right graph in both figures shows a case that corresponds to the pump-probe experiments where the pump wavelength is exactly at Raman resonance (i.e., $\Delta\lambda_\mathrm{P} = 0$). The fourth graph (on the right-hand side) shows the combination of TPA, FCR, and Kerr, which is practically the same as the combination of all four effects (i.e., TPA, FCR, Kerr, and SRS) in the case that the pump wavelength is far off the Raman resonance (i.e., $\Delta\lambda_\mathrm{P} \gg 0$ or $\Delta\lambda_\mathrm{P} \ll 0$). Thus, the lower two graphs on the right-hand side of each figure are the ones that effectively simulate the pump-probe experiments *without* and *with* stimulated Raman scattering (SRS).

By analyzing the bottom right graph in both figures (i.e., all four effects at the same time) in more detail, we do *not* see the strong amplification that we would expect from SRS alone (see bottom left graph) although the pump beam is exactly at Raman resonance. We first consider the case of Fig. 4.9, where the initial probe wavelength is exactly at resonance. For delays slightly below $\Delta t = 0$ (i.e., when the pump pulse enters the microcavity), the refractive nonlinear effects (Kerr, FCR) start moving the position of the resonance curve (in terms of frequency or wavelength, respectively) so that pump and probe are not at resonance in the microcavity any more. As a result, the enhancement of the electric fields (and intensities) of the pump and the Stokes wave drop significantly, and thus, there is only a very weak influence of SRS. This is the reason why, by comparing the fourth and the fifth graph on the right-hand side of Fig. 4.9, we hardly see any difference between the situations *without* and *with* SRS. From an experimental point of view, this fact makes it difficult to demonstrate the presence of SRS in the measurement results because the signature of SRS is likely to be of the same order of magnitude as the measurement uncertainty.

In Fig. 4.10, we compensate the Kerr- and FCR-induced displacement of the res-
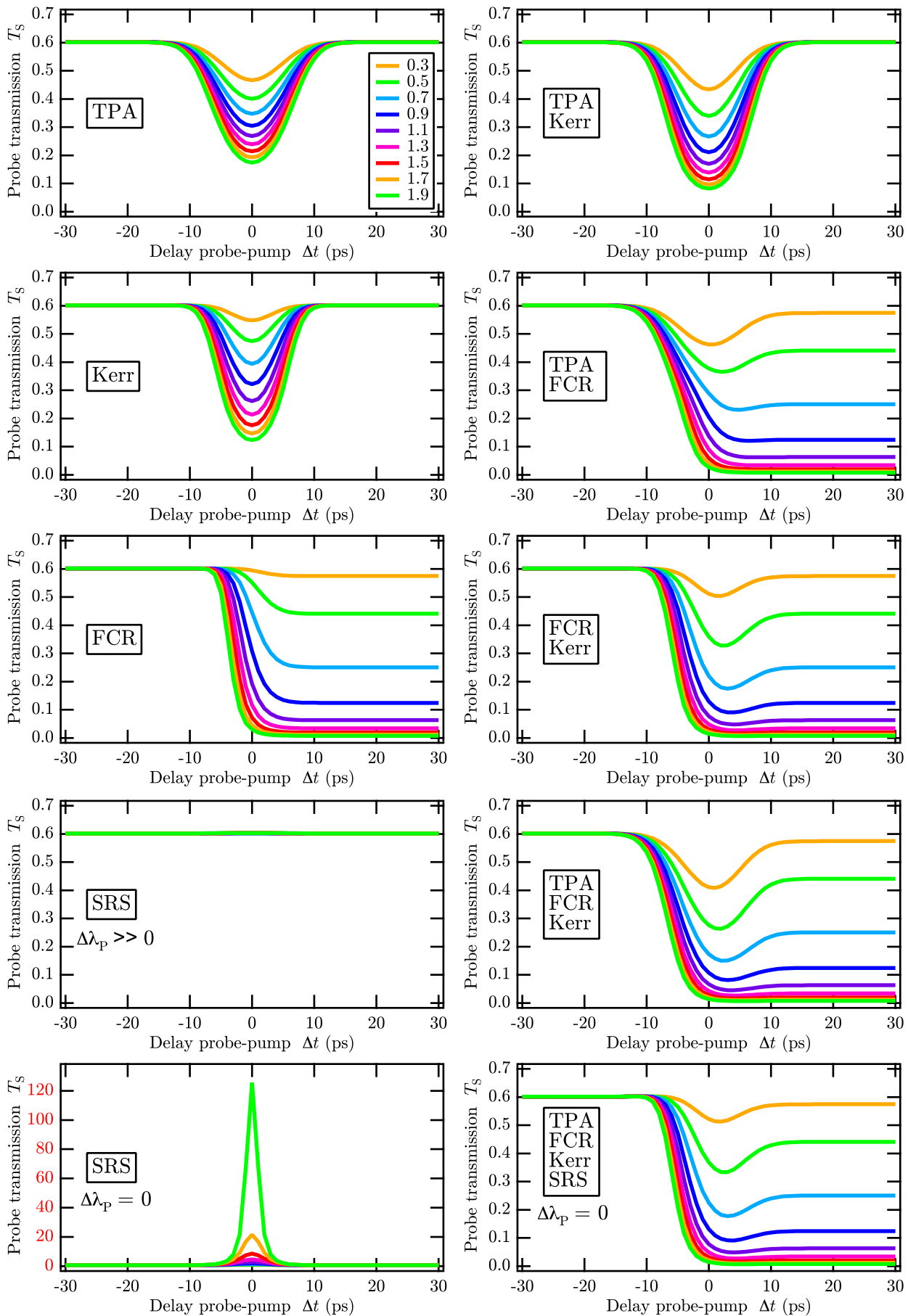
Fig. 4.9. Simulations of the pump-probe experiments for $\Delta\lambda_S = 0$. Time dependence of the probe transmission T_S of the semiconductor microcavity for pump intensities $I_{P,0}$ between 0.3 and 1.9 MW/cm^2 (indicated by the different colors of the traces). The graphs show the influence of the different nonlinear optical effects and their combinations. It should be noted that the vertical scale of the bottom left graph (SRS, $\Delta\lambda_P = 0$) is different from the other graphs (up to 130).
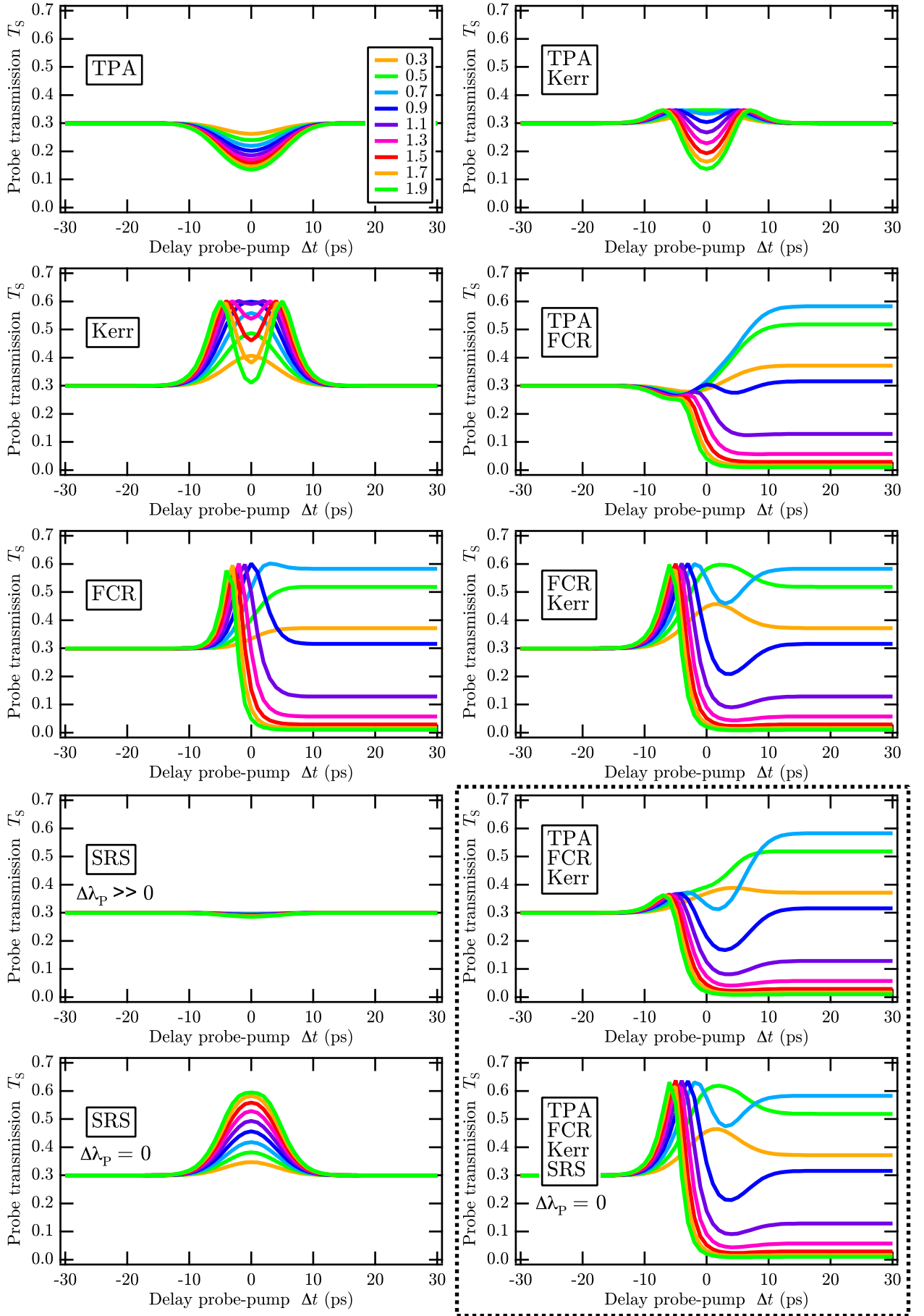
Fig. 4.10. Simulations of the pump-probe experiments for $\Delta\lambda_S = -0.07$ nm. Time dependence of the probe transmission T_S of the semiconductor microcavity for pump intensities $I_{P,0}$ between 0.3 and 1.9 MW/cm^2 (indicated by the different colors of the traces). The graphs show the influence of the different nonlinear optical effects and their combinations. The dotted frame indicates the two graphs that correspond to the pump-probe experiments presented in section 4.5.

onance curve by setting the initial probe wavelength already half-way off resonance. For delays of $\Delta t \approx 0$, the center of the resonance curve is then moved towards the wavelength of the probe beam, and this leads to a visible increase of the transmission of the microcavity. Therefore, when comparing the fourth and the fifth graph on the right-hand side of Fig. 4.10 (where the initial probe transmission is only half the maximum transmission, i.e., $T_S \approx T_{max}/2$), there is a clear difference in the simulated time dependences *without* and *with* SRS. Although this increase does not really correspond to an net *amplification* of the probe beam (because even the maximum value is not significantly higher than the maximum T_{max} of the *linear* transmission), the influence of SRS is clearly visible in the simulations and should, therefore, also be measurable in the experiments.

Thus, we conclude that is reasonable to carry out the pump-probe measurements with an initial probe wavelength detuning $\Delta \lambda_S$ which is halfway off the resonance towards shorter wavelengths (i.e., point C in Fig. 4.7).

As all the graphs clearly show, the **long-term behavior** of the microcavity transmission is **exclusively determined by the free carrier density** because all the other nonlinear effects taken into account by our model are considered as instantaneous. The pump intensities $I_{P,0}$ that have been used for the simulations vary between 0.3 and 1.9 MW/cm^2 (see the different traces in each graph). This range has been chosen because it illustrates very well the dependence of the probe transmission on the pump intensity. In all the graphs including FCR, one can clearly see the superposition of the two or three traces corresponding to the highest intensities. This means that for even higher intensities, the shape of the traces would not change significantly and that the transmission drops to values below 1%. We can, therefore, consider these traces as a sort of asymptotic limit indicating the final state of the microcavity.

As we will see in the following sections, the above-presented model and the simulations do *not perfectly* describe the pump-probe measurements that have been carried out with the real sample. Given the simplicity of the model, in particular the fact that it does not take into account such important things as self phase modulation etc., this is not surprising. However, the simulations yield some valuable insights that are essential for the practical realization of the experiments and for the interpretation and general understanding of the the results.

- Based on the discussion of the simulations, we know how to set the initial wavelengths λ_S and λ_P of both beams in order to compensate for the Kerr- and FCR-induce nonlinear phase shift and, thus, to see a measurable signature of stimulated Raman scattering (SRS) in the measurement data.

- Although stimulated Raman scattering can, in general, lead to a *net amplification* of the Stokes (probe) beam, the simulations clearly show that the above-mentioned signature of SRS consists only in a (clearly) visible *increase of the transmission* of the microcavity, which does *not* significantly exceed the maximum linear transmission T_{max}.

- The simulations provide a good overview of the general time dependence of the probe transmission T_S, describing the key features of the transmission curves, such as the behavior for delays around $\Delta t = 0$, as well as the asymptotic long-time behavior that is determined by the free carriers.

With these findings, we learn very much about *how* we should design and carry out the experiments and *what*, approximately, we are expected to observe.

4.3   Experimental setup and methods

In this section we describe the experimental setup that is used for the pump-probe measurements. We start with a description of the picosecond light source that generates the pump and the probe pulses. Furthermore, the whole experimental setup is explained, i.e., how the two beams are prepared for the experiment, how they are injected in the sample, and what kind of signals are detected. The section closes by describing how the raw data are acquired, digitized, and processed in order to yield the transmission of the sample for the pump and the probe beam.

4.3.1   Two synchronous optical parametric generators

The light source that is used for the pump-probe experiments has been designed by Robert FREY, a senior researcher in our group (MANOLIA), and it was improved by former PhD students for previous research projects. It consists of a modified commercial Nd:YAG picosecond laser, a frequency doubling and tripling stage, two lines of optical parametric generators (one for the pump and one for the probe beam), and an additional amplifier stage for the pump beam.

Since it is a self-made light source (i.e., no commercial turn-key system), I have spent a significant amount of time on several modifications of the source and on the correct alignment all the mechanical and optical components. Also, it has required very much practice and a lot of time to conduct the experiments that are presented in the following sections.

Frequency-tripled Nd:YAG picosecond laser

The first element in the chain of the pulse generation is a commercial picosecond laser of the type PY61C-10, manufactured by the company Continuum. The laser has been modified for previous research projects in order to provide two output beams instead of only one. In total, the modified laser is composed of three stages : an oscillator, a preamplifier, and an amplifier. It provides two pulsed output beams : the so-called **signal beam** and the so-called **amplifier beam**. Both beams have a diameter of about 6 mm. They consist of pulses of a duration of about 12 ps at a wavelength of 1064 nm, and the pulse energies of both beams are about 8 to 13 mJ. The pulses are generated with a repetition rate of 10 Hz. The laser also provides an electric signal that is used to synchronize the data acquisition and processing etc. (sync signal).

Both output beams of the laser are converted to 355 nm by frequency tripling. The conversion comprises three steps : spatial filtering, frequency doubling, and frequency tripling. For the spatial filtering, we cannot use the lens-and-pinhole method since the pulse energy of both beams is too high. Focussing would ionize the air and/or damage the pinhole. Therefore, we use the central part of the far field of the beams. Thus, both beams propagate over 30 meters in free space by being reflected several times by a set of mirrors, as depicted in Fig. 4.11. In order to compensate for mechanical instabilities or drifts, the pointing of the beams is controlled with two quadrant photodiodes (QPD). An electronic servo system reads out the position information from the quadrant photodiodes and controls two pairs of step motors which are connected to two mirror mounts (one for each beam).

Both beams are then guided through a combination of two nonlinear crystals for the frequency conversion. The crystals can be rotated to adjust the optimal phase matching angle. In a first step, the 1064 nm pulses are partly converted to 532 nm by second harmonic generation in a KDP crystal. In a second step, the remainder of the light at 1064 nm and the light at 532 nm are combined in a second KDP crystal
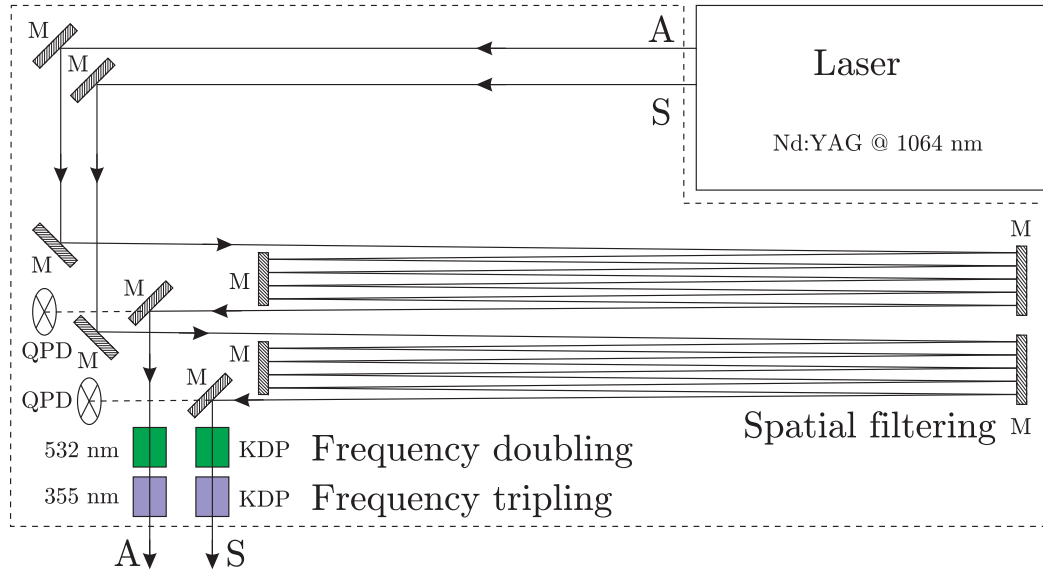
Fig. 4.11. Spatial filtering and frequency tripling of the pulsed laser beams that are generated by the modified Nd:YAG laser. Both the signal beam (S) and the amplifier beam (A) are guided over several mirrors (M) and thereby propagate more than 30 meters in free space before passing two KDP crystals. In the first KDP crystal, the 1064-nm infrared pulses are converted to 532 nm, and in the second crystal this green light and the remainder of the infrared light are converted to 355 nm by sum frequency generation (SFG). The pointing of both beams is monitored by two quadrant photodiodes (QPD) and stabilized by step motor actuators in two of the mirror mounts. The signal beam is used to pump the two optical parametric generators, while the amplifier beam pumps the optical parametric amplifier stage.

to generate pulses at 355 nm by sum frequency generation. The overall efficiency of this two-step approach, using two second-order nonlinear effects, is higher than using direct third harmonic generation, which would be a third-order nonlinear effect. So, after the passage of the two crystals, both the signal beam and the amplifier beam are converted to 355 nm [108].

Two independent parametric generators and amplifiers

The signal beam is divided into two equally powerful parts by a 50:50 beam splitter in order to generate two independent beams (signals) whose wavelengths can be tuned continuously over a large range from the ultraviolet to the infrared. One of the two parts is henceforth called the *pump beam*, the other one is referred to as the *probe beam*. The wavelength tuning is achieved by two independent optical parametric generators. Their design, which is identical for both beams, has been developed by HUANG [109]. It uses a sequence of two second-order nonlinear optical effects : optical parametric fluorescence (OPF) and optical parametric amplification (OPA).

In each of the two optical parametric generators, the pulses at 355 nm are guided through two nonlinear barium beta-borate crystals (β-BaB$_2$O$_2$, BBO). In the first BBO crystal, they induce **optical parametric fluorescence**. Due to this effect, the ultraviolet input beam interacts with the crystal in a nonlinear way so that a photon at 355 nm spontaneously "decays" into two new photons which have to fulfill the conservation of energy,

$$\hbar\omega_1 = \hbar\omega_2 + \hbar\omega_3 \quad \Longleftrightarrow \quad \omega_1 = \omega_2 + \omega_3 \quad \Longleftrightarrow \quad \frac{1}{\lambda_1} = \frac{1}{\lambda_2} + \frac{1}{\lambda_3} \ . \qquad (4.17)$$

Due to the birefringence of the crystal, there is for each combination of wavelengths λ_2 and λ_3 (or frequencies ω_2 and ω_3, respectively) a combination of propagation

(a) Optical parametric fluorescence

OPF principle

OPF cone of light

(b) Optical Parametric Amplification

OPA principle
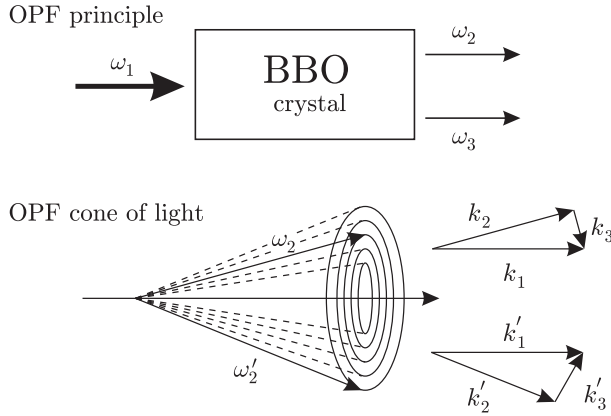
Fig. 4.12. **(a)** Optical parametric fluorescence (OPF). A strong electromagnetic wave at the frequency ω_1 is incident upon a nonlinear crystal (e.g., BBO) and its photons "decay" spontaneously into pairs of photons at the frequencies ω_2 and ω_3. Because of the phase matching condition between the three interacting light waves, a rainbow-like cone of light is generated behind the crystal.

(b) Optical parametric amplification (OPA). Besides the strong electromagnetic wave at the frequency ω_1, a weak wave at ω_2 is incident upon a nonlinear crystal. Due to the nonlinear interaction of the waves with the crystal, the weak wave is amplified and the complementary wave at ω_3 is created.

directions that leads to an efficient generation of the new waves. These propagation directions are given by the so-called phase matching condition

$$\hbar \vec{k}_1 = \hbar \vec{k}_2 + \hbar \vec{k}_3 \qquad \Longleftrightarrow \qquad \vec{k}_1 = \vec{k}_2 + \vec{k}_3 \ , \tag{4.18}$$

which corresponds to the conservation of momentum of the three interacting waves. As a result, a cone of light appears behind the first BBO crystal. In its center, the phase matching condition is fulfilled for all three wave vectors being parallel. By rotating the crystal, one can alter the constraints imposed by the phase matching condition and, thus, freely choose this combination of wavelengths (λ_2, λ_3) which propagate in the same direction as the input wave at λ_1. Figure 4.12(a) illustrates the principle of the optical parametric fluorescence and the generation of the phase matching cone.

In the second BBO crystal, the selected waves at λ_2 and λ_3 interact again with the remainder of the ultraviolet wave at λ_1. The second crystal is rotated by the same angle with respect to the propagation direction as the first crystal, but in the inverse direction. As a result, both wavelengths are amplified by the so-called **optical parametric amplification**, as is illustrated in Fig. 4.12(b). Thus, after the passage of the two BBO crystals, the initial ultraviolet beam at 355 nm is converted into two waves with two wavelengths λ_2 and λ_3 which can be freely chosen within a large spectral range by rotating the two BBO crystals.

The ultraviolet beam is, however, not entirely depleted. The remaining ultraviolet light at 355 nm is separated from the other two waves by a dichroic mirror. It is sent back by another mirror in order to pass again the two BBO crystals in the opposite direction. The other two waves at λ_2 and λ_3 are guided onto a diffraction grating at grazing incidence. Figure 4.13 illustrates the course of the different beams. The first order of diffraction of one of the waves, say λ_2, is reflected back onto the grating by a movable mirror. This reflected light is again diffracted on the grating. Due to the symmetry of the diffraction process, part of this diffracted light propagates back through the two BBO crystals. The result of this so-called Littman setup [110] is a
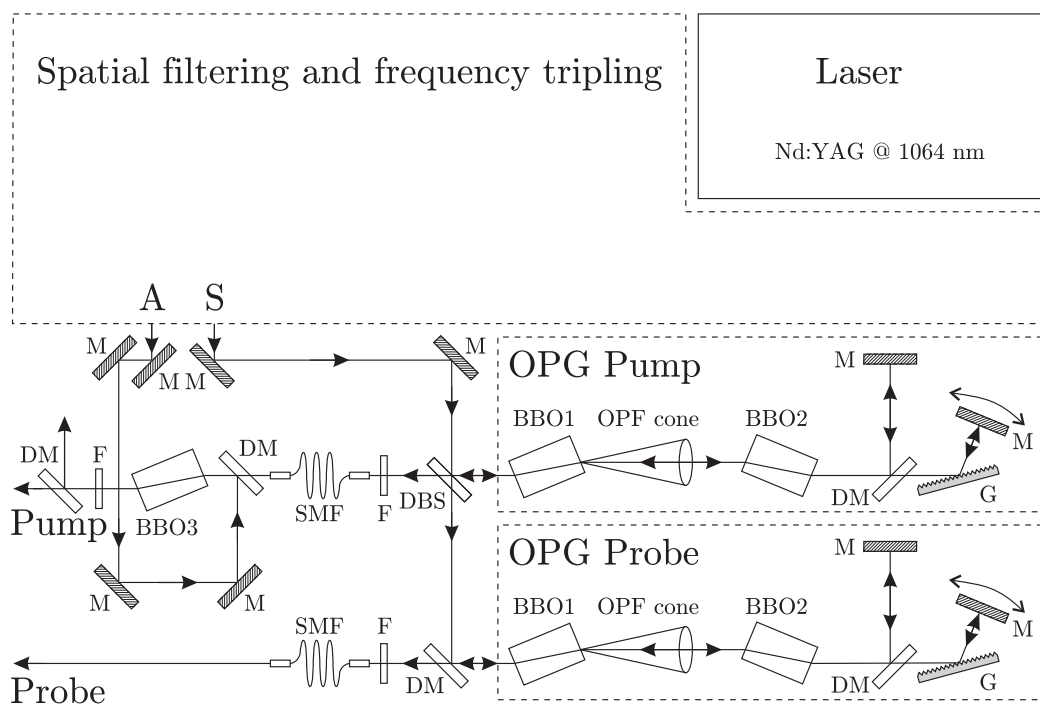
Fig. 4.13. Optical parametric generators and optical parametric amplifier. The so-called signal beam (S) from the frequency-tripled Nd:YAG laser is guided over two mirrors (M). It is split into two parts by a dichroic 50:50 beamsplitter (DBS). The two parts are then converted by two optical parametric generators (OPG) into the pump beam and the probe beam. Each of the two OPGs is composed of two BBO crystals, a dichroic mirror (DM), a grating (G) and two mirrors (M). After the OPGs, pump and probe beam pass a colored glass filter (F) in order to block the unwanted wavelengths. Both beams are then injected into single mode fibers (SMF) for spatial filtering. The pump beam is further amplified in another BBO crystal which is pumped by the so-called amplifier beam (A) from the frequency-tripled Nd:YAG laser. Behind this amplifier stage for the pump beam, another colored glass filter (F) and a dichroic mirror (DM) block the UV pump light of the amplifier beam and the complementary wave so that only the desired pump wavelength λ_P passes. For detailed explanations see the text.

high-resolution spectral filtering.

The distances between all the optical components of the Littman setup are such that the ultraviolet beam at 355 nm and the spectrally filtered beam (λ_2) are again spatially and temporally superimposed in the BBO crystals. (It should be noted that we work with picosecond pulses which have a physical length of only several millimeters.) During the second passage of the crystals, the spectrally filtered wave at λ_2 is strongly amplified by optical parametric amplification. As a side effect, the complementary wave at λ_3, given by $1/\lambda_3 = 1/\lambda_1 - 1/\lambda_2$, is recreated and also amplified by optical parametric amplification. Since we only need one of the two wavelengths for the experiments, we use a colored glass filter to block the unwanted one. In the present case, we actually block the wave at λ_2 that is generated by the Littman system (somewhere in the yellow spectral range) and use the complementary wave at λ_3 in the near infrared (between 900 nm and 950 nm).

After this *spectral* filtering, both beams (pump and probe) are *spatially* filtered in order to obtain a good beam profile. Therefore, each beam generated by the optical parametric generators is injected with a microscope objective into a single-mode fiber which is about 10 centimeters long and which is appropriately chosen for the wavelength used. After the passage through the fiber, another microscope objective extracts the beam. The *pump* beam is then again amplified in another optical parametric amplifier. For this purpose, the amplifier beam (i.e., the second beam provided by the laser and the frequency doubling and tripling stage) is superimposed

with the pump beam in a third BBO crystal. Here again, the complementary wavelength is recreated, as in the case of the optical parametric generators. Therefore, a dichroic mirror and a colored glass filter are put behind the crystal in order to isolate the wavelength of interest. As a result, the pump pulses have a pulse energy of about 20 to 30 μJ at a well-defined, freely choosable wavelength λ_P. The wavelength of the probe beam can also be freely tuned and is henceforth called λ_S (because it corresponds to the Stokes beam in the process of the stimulated Raman scattering). The pulse energy of the probe beam is too weak to be measured (certainly in the sub-microjoule range).

In total, the sequence of the Nd:YAG laser, the spatial filtering and frequency tripling, the two optical parametric generators, and the optical parametric amplifier for the pump beam provides an appropriate light source for the pump-probe experiments. It delivers two output beams of almost Fourier-transform limited gaussian pulses. One of the beams (pump) is significantly stronger than the other (probe). Both beams are wavelength-tunable over a wide spectral range from about 400 nm to more than 2.5 μm. In the present case we work in the near infrared spectral range. The pulse duration is about 12 ps at a repetition rate of 10 Hz. Since both beams are initially generated by the same Nd:YAG pump laser, their pulses have a fixed time delay with respect to one another, which allows us to use them for pump-probe measurements.

However, it is important to note that, despite the fact that both beams originate from the same pump laser, there is no correlation between the intensities of the two beams. This is due to the fact that little variations of the beam positions in the frequency doubling and tripling stages can lead to strong variations in the output intensities of the beams after the optical parametric generators. The fluctuations of the final pump and probe intensities can be even higher because of varying coupling efficiencies into the single mode fibers. These variations have to be taken into account in the transmission measurements that are presented below.

Pump and probe wavelengths and spectra

In order to measure the wavelengths of the two beams, we use a monochromator from Jobin Yvon. A CCD line camera is mounted at the exit of the monochromator. The line camera is connected to a computer (PC) and triggered by the sync signal of the laser. The data from the camera are read by a data acquisition program which has been developed by other PhD students and researchers for previous research projects in the programming language Pascal. This program has been modified in order to be useful for the experiments presented here. As a result, we can save complete spectra with a resolution of 0.026 nm. Furthermore, we can record time series of the barycenter wavelength of the central peak. In order to measure the pump wavelength λ_P and the probe wavelength λ_S, we record a series of at least 600 barycenter wavelengths (corresponding to one minute of recording at a repetition rate of 10 Hz) and determine its average value and standard deviation.

It should be noted that the spectral range which can be covered by the CCD line camera without rotation of the diffraction grating in the monochromator is about 14 nm. Since the pump and the probe wavelengths are separated by approximately 25 nm (921 nm and 946 nm, respectively) we have to rotate the grating manually in order to switch from a *pump* wavelength measurement to a *probe* wavelength measurement, and vice versa.

In order to guide the *pump* beam into the monochromator, we utilize the fact that the dichroic mirror that is introduced behind the pump beam amplifier (i.e.,

Fig. 4.14. Spectra of the pump beam (a) and the probe beam (b). The markers represent the experimental data that have been measured with the monochromator and the data acqustion program. The blue lines are gaussian functions that are fitted to the data. From the spectra, we determine linewidth (FWHM) of the pump beam $\delta\lambda_\mathrm{P} = 0.22$ nm and the linewidth (FWHM) of the probe beam $\delta\lambda_\mathrm{S} = 0.18$ nm.
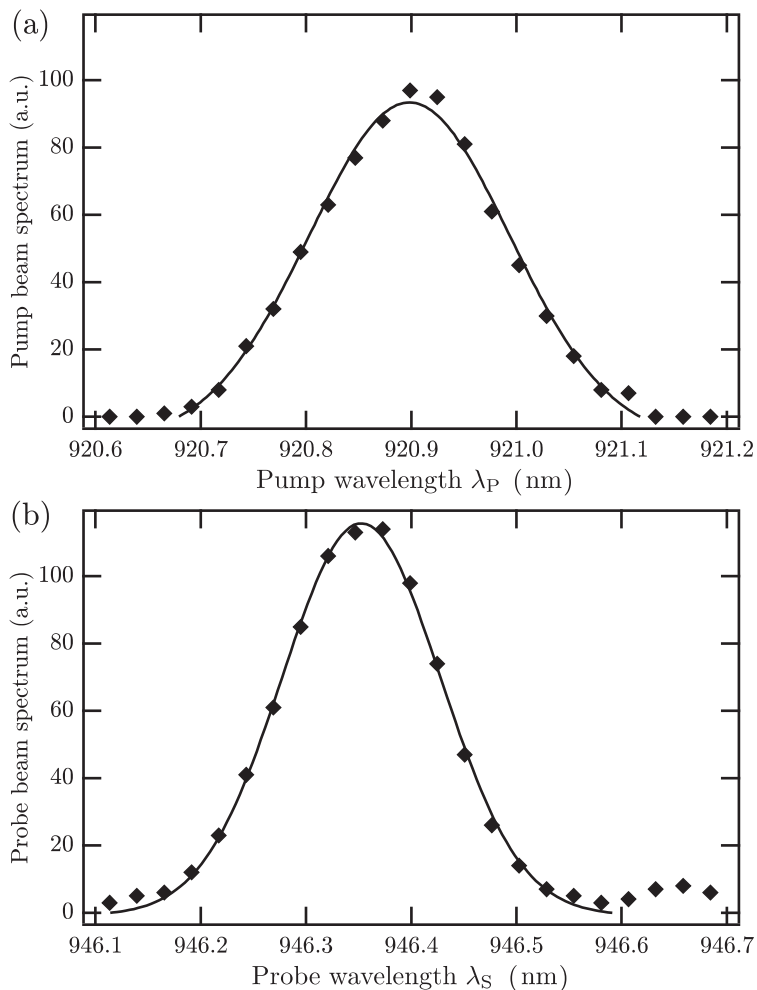
behind the third BBO crystal) provides a weak reflection of the pump beam because its reflectivity at the pump wavelength is not exactly zero. This reflection is guided over several mirrors into the monochromator. An advantage of this setup is that it allows us to monitor the pump wavelength in real-time (i.e., during the experiments).

We can also guide the *probe* beam into the monochromator. For this purpose, we use a little mirror on a flip mount, which can be introduced into the probe beam. The light is guided over several mirrors, including another flip mirror, into the monochromator. It is not possible to monitor the probe wavelength in real time during the experiments.

Figure 4.14 shows two typical spectra of the pump and the probe beam along with Gaussian fits. From the fits, we determine linewidth (FWHM) of the pump beam $\delta\lambda_\mathrm{P} = 0.22$ nm and the linewidth (FWHM) of the probe beam $\delta\lambda_\mathrm{S} = 0.18$ nm. For all the experiments presented in this chapter, the measurement uncertainty (standard deviation) of the wavelength measurements is $\Delta\lambda = 0.06$ nm for both beams. It is worth noting that this corresponds approximately to one third of the linewidth of the microcavity resonance.

4.3.2 Preparation and superposition of pump and probe beam

The aim of the experiments is to measure the probe transmission T_S of the sample as a function of several parameters, such as the probe wavelength λ_S, the pump wavelength λ_P, the pump intensity I_P, and the time delay between the pump and the probe pulses Δt. Other parameters of these measurements are the angle of incidence

of the probe beam, which is at normal incidence for all experiments (i.e., $\vartheta_\mathrm{S} \equiv 0$), the angle of incidence of the pump beam ϑ_P, which can be adjusted to make the pump beam resonant in the cavity, and the probe beam intensity I_S, whose exact value does not matter here. As explained in section 4.3.1, the pump and the probe intensities and wavelenghts show intrinsic random variations that are not correlated with one another. This has implications for the determination of the probe transmission (and also the pump transmission), as is explained in the following.

Transmission measurement with a stable light source

In the case of a light source with a stable output power (i.e., all pulses contain the same pulse energy), the simplest method to determine the transmission of the sample would be to mount a photo detector behind the sample holder and to measure the average light power (i.e., average pulse energy) for two different configurations : *with* and *without* the sample. The ratio of the two measured values yields the intensity transmission T of the sample, as given by

$$ T = \frac{\left\langle \hat{I}_\mathrm{with} \right\rangle}{\left\langle \hat{I}_\mathrm{w/o} \right\rangle} = \frac{\left\langle \hat{P}_\mathrm{with} \right\rangle}{\left\langle \hat{P}_\mathrm{w/o} \right\rangle} = \frac{\left\langle E_\mathrm{with} \right\rangle}{\left\langle E_\mathrm{w/o} \right\rangle} \; . \tag{4.19} $$

Here, the angle brackets $\left\langle \ldots \right\rangle$ denote the time average value, "w/o" stands for "without" the sample, and the relationship between the peak intensity $\hat{I}$, the peak power $\hat{P}$, and the pulse energy E,

$$ \hat{I} = \frac{\hat{P}}{\pi \, (d/2)^2} = \frac{E/\tau}{\pi \, (d/2)^2} \; , \tag{4.20} $$

of a Gaussian pulse with a beam diameter d and pulse duration τ (FWHM) has been used. However, because of the intrinsic variations of the pump and probe intensities, this method does not work in the present case because the incident intensity is not the same from one pulse to the next. Therefore, we have to measure the incident as well as the transmitted intensity (or pulse energy, respectively) for each single pulse individually, as is explained in more detail below.

Opto-mechanical setup of pump and probe beams

For the pump-probe experiments, the pulses of the pump beam and the probe beam have to be superimposed spatially as well as temporally in the sample (i.e., in the semiconductor microcavity). Moreover, we have to prepare the two beams in such a way that they have the correct polarization states, maximum intensities, and angles of incidence. The whole experimental setup, including the beam preparation, the beam superposition, and the different detectors, has been specifically designed and built for the experiments presented in this chapter. It is illustrated in Fig. 4.15. A considerable amount of time has been spent on its construction and testing as well as on the development of the data acquisition and processing programs (in LabVIEW from National Instruments and IGOR Pro from Wavemetrics).

The *pump beam* from the optical parametric generator and amplifier is guided over several mirrors and then passes an afocal lens system (telescope) to reduce the beam diameter. The beam is then guided through a half wave plate and a Glan-Taylor polarizer. For all the experiments, the polarizer is oriented in such a way that the output beam is polarized horizontally (i.e., TM-polarized). By rotating the half-wave plate, we can control the optical power of the pump beam. After passing the polarizer, the beam is weakly focused by a convex lens with a focal length of 50 cm.

In the focal point of the lens, the sample holder is placed, in which the semiconductor microcavity can be fixed. On the sample, the pump beam has a diameter of about 1 mm. The sample holder itself is fixed on a 50 cm long mechanical rail (Newport MicroContrôle X25) that is mounted on a rotation stage. The rail is used to guide the probe beam onto the sample, as is explained below. Therefore, the sample holder is positioned in such a way that the sample (when it is fixed in the holder) is exactly on the vertical rotational axis of the rotation stage, and it is oriented at a right angle to the rail. Hence, the angle between the rail and the pump beam is equal to the external angle of incidence ϑ'_{P} of the pump beam, which can therefore be read on the scale of the rotation stage.

A plane glass plate is placed between the 50-cm lens and the sample holder. It is slightly tilted with respect to the propagation direction of the pump beam and provides a weak reflection that is focused on a photodiode. The signal of this photodiode, which is referred to as photodiode 1 (PD1), serves as a measure of the *incident* pump intensity. Behind the sample holder the pump beam is focused on another photodiode, called photodiode 2 (PD2). The signal of this photodiode is a measure of the *transmitted* pump intensity. See Fig. 4.15 for a graphical illustration.

The *probe beam* coming from the optical parametric generator passes a movable retroreflector that serves as a delay line. By changing the position of the retroreflector, we can control the time delay Δt between the probe and the pump pulses. A displacement r of the retroreflector corresponds to an increase (or decrease) of the delay of

$$\Delta t = 2r/c \, , \tag{4.21}$$

where c is the speed of light in air. This yields, for example, a time shift of 20 ps for a displacement of 3 mm.

The probe beam is then injected by a fiber collimator into a polarization maintaining fiber. The fiber has a length of about 1 meter. At the other end of the fiber, the light is extracted with another fiber collimator. This collimator is fixed on the above-mentioned mechanical rail that is mounted on the rotation stage. In order to adjust the polarization of the beam correctly, we use a half wave plate before the fiber entry and a Glan-Taylor polarizer behind the fiber exit. A convex lens with a focal length of 12 cm is mounted behind the polarizer and focuses the probe beam on the sample. The distance between the lens and the sample is equal to the focal length (i.e., 12 cm) and the polarization of the probe beam is horizontal (i.e., the probe beam is TM-polarized). In the focal point, the probe beam has a diameter of about 40 μm.

The mechanical setup is very carefully aligned so that the focused probe beam and the weakly focused pump beam are superimposed on the sample, which is positioned on the rotational axis of the rotation stage. This means that the probe beam is always at normal incidence. The angle of incidence of the pump beam can be chosen by turning the mechanical rail, while both beams remain superimposed on the sample.

In order to obtain a measurement of the probe beam intensity that is incident upon the sample, a thin plane glass plate is mounted behind the Glan-Taylor polarizer. It is slightly rotated with respect to the beam, in order to provide a weak reflection, which is then focused on a photodiode. The signal that is measured with this photodiode, which is referred to as photodiode 3 (PD3), is a reference of the *incident* probe intensity. Behind the sample (or the sample holder), another lens is mounted and focuses the transmitted light on another photodiode, which is referred to as photodiode 4 (PD4). This photodiode yields a measure of the *transmitted* probe intensity. In order to minimize any scattered light on this photodiode, especially the scattering of the strong pump beam, an iris diaphragm is mounted between the sam-
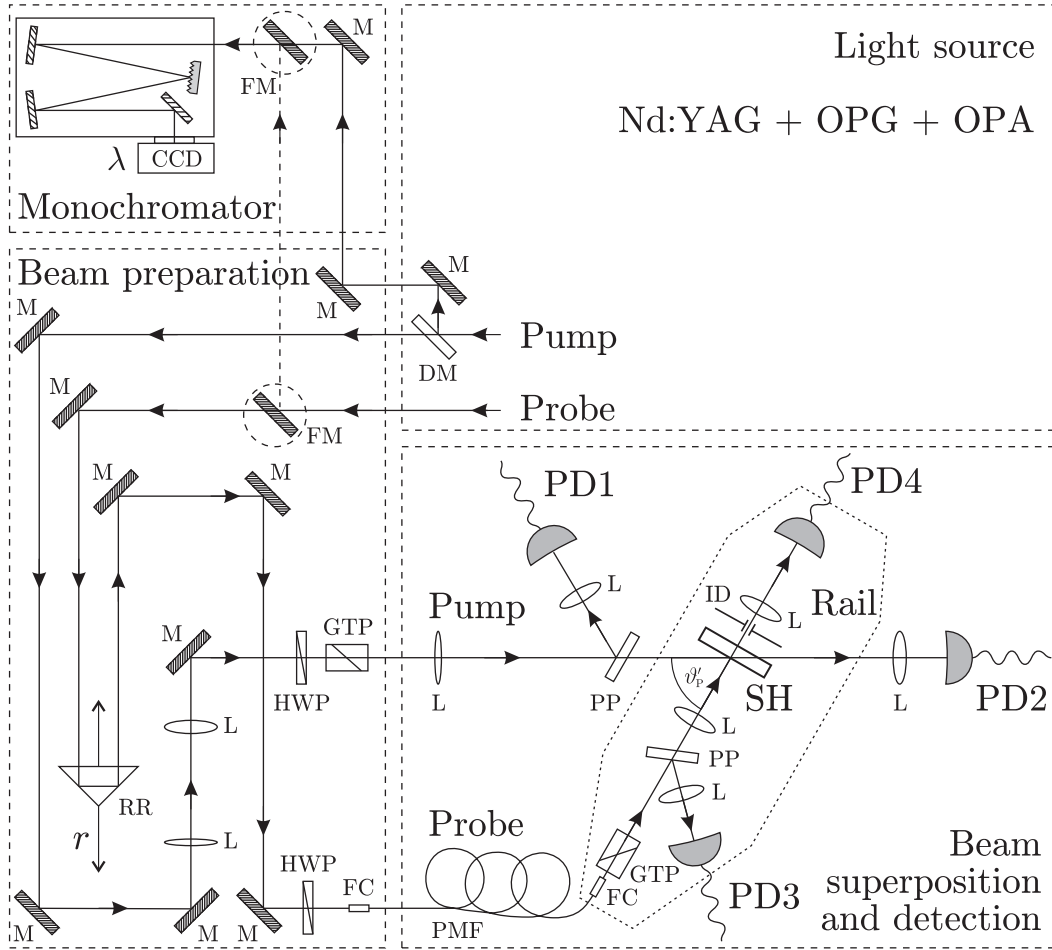
Fig. 4.15. Beam preparation and experimental setup. Both the pump (P) and the probe (S) beam come from the optical parametric generators shown in Fig. 4.13. As explained in section 4.3.1, a monochromator is used to measure the wavelengths and to record spectra of both beams. The beam preparation stage prepares both beams for the pump-probe experiments by setting the correct polarization (TM, i.e., horizontal for both beams), maximum intensity, and time delay. See text for a more detailed explanation. M mirror, DM dichroic mirror, FM mirror on flip mount, RR retroreflector, L lens, GTP Glan-Taylor polarizer, HWP half wave plate, FC fiber collimator, PMF polarization-maintaining fiber, PP plane glass plate, ID iris diaphragm, **SH** sample holder (in which the semiconductor sample can be fixed), **PD1, PD2, PD3, PD4** photodiodes. All optical and mechanical components inside of the dotted line are fixed on a mechanical rail (X25), which can be turned in order to adjust the angle of incidence ϑ'_{P} of the pump beam. The four photodiodes measure the incident and the transmitted intensities of both beams.

ple and the collecting lens. The diaphragm can be closed and aligned in such a way that only the probe beam passes and any scattered light is blocked, except for the light that is scattered exactly in the direction of the probe beam, which is only a very small fraction.

Since all four photodiodes are silicon-based, they are, in principle, also sensitive to visible light from the laboratory environment (i.e., parasites). Therefore, they are all protected with colored glass filters which are fixed directly on the photodiodes and which do not transmit light of the visible spectral range. Moreover, we install cardboard and rubber tubes between the aluminum housings of the photodiodes and the lenses that focus the light on the detectors. The lenses are partly covered with black insulating tape so that light passes only in the center of the lenses. As a result of all these measures, which are not explicitly shown in Fig. 4.15 for the sake of clarity, we successfully reduce parasite signals on the photodiodes to a minimum.

The above-described experimental setup, consisting of the parametric light source, the beam preparation, and the beam superposition, allows for setting the wavelengths λ_P and λ_S of the pump and the probe beam, the angle of incidence of the pump beam ϑ'_P, and the time delay Δt between the the pulses. The angle of incidence of the probe beam is fixed at $\vartheta_S = 0$, and both beams are TM-polarized. The intensities I_P and I_S of both beams are subject to intrinsic variations that have to be taken into account in the data processing.

4.3.3   Photodiode signals and sample transmission

In the above description of the experimental setup there are four different photodiodes that we want to use to measure the incident and transmitted intensities of the pump and the probe beam. However, it is not possible to use the time average of the four photodiode signals because the repetition rate of the light source is 10 Hertz, and thus the average signal is null. Therefore, we use a so-called boxcar integrator from Stanford Research Systems in order to determine the total optical energy that is deposited in a photodiode by one pulse.

Pulse integration at 10-Hz repetition rate

For this purpose, the boxcar integrator reads the signals from the photodiodes and integrates these signals over a pre-defined time period. The starting point of the integration is triggered by the sync signal that is generated by the Nd:YAG laser. Besides the length of the integration window (i.e., the duration), we can also control the offsets of the photodiode signals as well as the measurement sensitivity. Figure 4.16 shows an example of a photodiode signal and the integration window as a function of time. We use a boxcar integrator with four channels (one for each photodiode), which therefore issues four signals between -10 V and +10 V, called $PD1$, $PD2$, $PD3$, and $PD4$. These boxcar signals correspond to the integrals of the photodiode signals and thus to the pulse energies measured by the photodiodes. They can be read out from the boxcar integrator between two sync signals (i.e., during 100 ms, which is the time between two pulses at a repetition rate of 10 Hz). In the following, these four boxcar signals are the ones that we use for the further data processing.

Fig. 4.16. Example of a boxcar integration. The red line is a typical signal of the photodiode 2 as a function of time. The blue line corresponds to the integration window of the boxcar integrator. The resulting boxcar signal $PD2$ is the integral of the red signal from the rising edge of the blue signal until the falling edge of the blue signal.
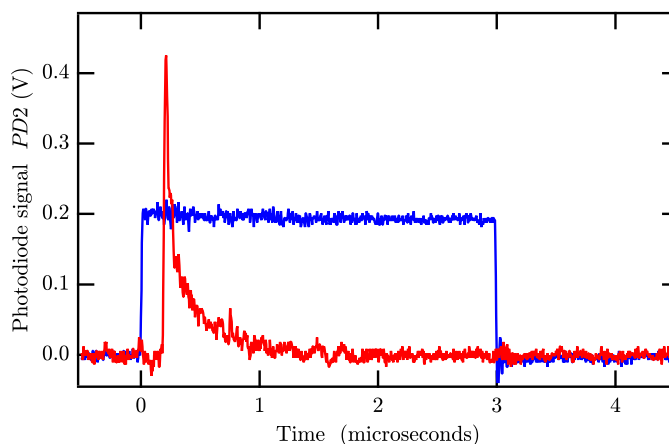
Determination of the sample transmission

The idea behind the above-described experimental setup is to measure for every pair of pump and probe pulses (i.e., for every pulse of the initial Nd:YAG laser) the incident and the transmitted intensities of both beams, yielding the four voltage values $PD1$, $PD2$, $PD3$, and $PD4$. In the following, we briefly describe the method we use to determine the transmission of the sample for one of the two beams, say, the probe beam. It works in the same way for the pump beam.

The signal $PD3$ is a measure for the incident probe intensity, the signal $PD4$ corresponds to the transmitted probe intensity. Suppose that we perform many measurements of these two values with varying incident intensities (because of the intrinsic variations). If there is *no sample* in the sample holder, the transmitted light is proportional to the incident light, and thus the ratio of $PD4$ to $PD3$ should be always the same. This means that we can plot the $PD4$ data versus the corresponding $PD3$ data and obtain a straight line through the origin. The slope of the line can be determined by fitting a linear function to the data. If the offset settings of the boxcar integrator are not correctly adjusted, the points are still on a straight line, which does, however, not pass through the origin. In any case, we are interested in the slope $M_{4,3}$ of the line.

We carry out the same measurement again, but this time *with a sample* in the sample holder. The plot of $PD4$ versus $PD3$ gives again a straight line whose slope is determined by a linear fit to the data. Figure 4.17 shows an example of such a graph. By comparing the slopes of the two measurements, i.e., *with* the sample ($M_{4,3,\text{with}}$) and *without* the sample ($M_{4,3,\text{w/o}}$), we calculate the intensity **transmission of the sample for the probe beam** by forming the ratio

$$T_{\text{S}} = \frac{M_{4,3,\text{with}}}{M_{4,3,\text{w/o}}} \ . \tag{4.22}$$

With this method we calibrate, so to speak, the slope of the sample by the slope of air (i.e., no sample), which yields the transmission coefficient of the sample. As mentioned above, we apply the same procedure to determine the **transmission of the sample for the pump beam**, yielding

$$T_{\text{P}} = \frac{M_{2,1,\text{with}}}{M_{2,1,\text{w/o}}} \ , \tag{4.23}$$

where $M_{2,1,\text{with}}$ and $M_{2,1,\text{w/o}}$ are the slopes of the straight lines in the $PD2$ versus $PD1$ plots with and without the sample, respectively. This means that the measurement of the transmission of the sample (for both beams) actually consists in a
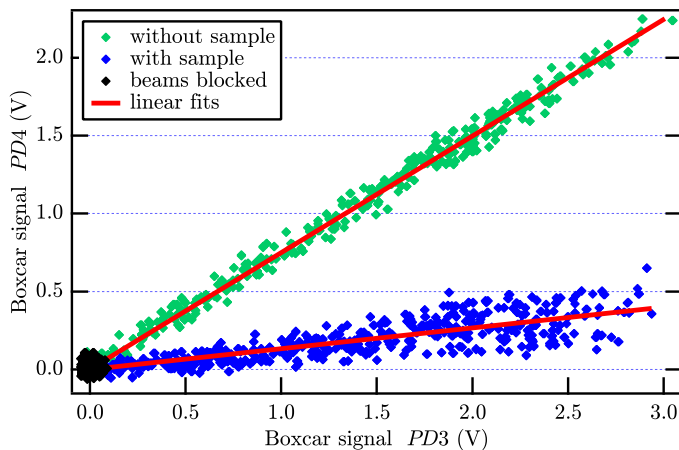
Fig. 4.17. Determination of the transmission of the sample for the probe beam. The markers represent the experimental data *without* and *with* sample in the sample holder, as well as a measurement of the noise level of the detection system. The red lines are the corresponding linear fits, yielding the slopes $M_{4,3,\text{with}}$ and $M_{4,3,\text{w/o}}$. These data have been measured with the avalanche photodiodes of the type Hamamatsu C5460 (see page 110 for more details).

measurement of the slopes of the $PD2$ vs. $PD1$ and $PD4$ vs. $PD3$ graphs. If we carry out a **measurement series** (i.e., a series of measurements with different delays) we measure these slopes and then calibrate all the slopes with one reference measurement. The reference measurement is done without the sample, and it is therefore independent of the delay or the wavelength etc. It can be performed before or after all the measurements of the series (usually before).

In the present work, we use the above-described method to measure the transmission of a microcavity. It should be noted that in the vicinity of the resonance of the cavity, the transmission is highly wavelength sensitive. Therefore, a little spectral jitter (i.e., an intrinsic random variation of the wavelength) can translate into a large spread of the transmitted intensities ($PD2$, $PD4$). This means that the points in the $PD2$-$PD1$ and $PD4$-$PD3$ graphs are no longer on a well-defined straight line, but they rather form a cone that opens towards the upper right-hand corner. In this case, a linear fit to the data still provides a good estimate of the transmission, as shown by the blue points (*with* sample) in Fig. 4.17. However, close to the resonance maximum, such a fit systematically underestimates the transmission. An example and a more detailed discussion of this case is given in section 4.4.2.

Photodiodes with and without noise

For all the experimental results presented in the remainder of this chapter, the photodiodes PD1 and PD2 are silicon p-i-n photodiodes of the type S1721 from Hamamatsu. They are mounted in small aluminum housings that can be positioned with manual micrometer actuators. A standard lab power supply is used to apply an operating voltage of 30 V to the photodiodes. It is sensible to use two photodiodes of the same type because two different photodiodes (with different rise times and decay times) could have different influences on the integration in the boxcar integrator, which could lead to a nonlinear $PD2$-$PD1$ dependence and therefore to a poorly defined slope $M_{2,1}$. The same argument holds, of course, also for the photodiodes 3 and 4 of the probe beam. Therefore, for all the experiments presented here those are also of identical type. We have the choice between silicon p-i-n photodiodes of the type S1721 from Hamamatsu (as PD1 and PD2) and silicon-based avalanche photodiode modules of the type C5460, also from Hamamatsu. The former ones are used with a standard lab power supply, as the photodiodes 1 and 2. The avalanche photodiodes come with an electronic circuit and an integrated pre-amplifier and are much more sensitive than the normal photodiodes. Because of the high sensitivity, they have to be protected from external electromagnetic influences. Therefore, the avalanche photodiodes are mounted in copper housings in which two lead batteries of the type NP2-12 from Yuasa are installed as a power supply. The batteries can be charged overnight with a lead battery charger. Fully charged, they provide enough electricity for about three days of experiments.

Since the signal of the photodiode 3 is only a *weak* reflection of the *weak* probe beam, it is clearly the weakest of all four photodiode signals. Therefore, when we use the normal Si photodiodes for PD3 and PD4, the boxcar signal $PD3$ shows significant noise, which is of the same order of magnitude as the signal itself.

Depending on the choice of the photodiodes for the signals $PD3$ and $PD4$, the experimental setup and the data processing change slightly. The normal Si photodiodes are mounted in small and light aluminum housings that are fixed directly on the mechanical rail on the rotation stage and therefore do not need to be realigned after turning the rail. The avalanche photodiodes in their bigger copper housings, including the lead batteries, are too heavy for the rail and are therefore mounted separately
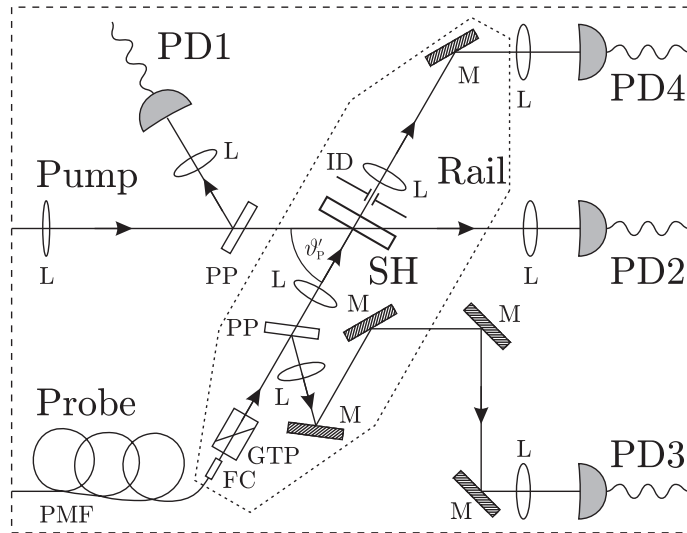
Fig. 4.18. Modified experimental setup using the avalanche photodiodes for the signals $PD3$ and $PD4$. See text for a more detailed explanation. M mirror, L lens, FC fiber collimator, GTP Glan-Taylor polarizer, PMF polarization-maintaining fiber, PP plane glass plate, ID iris diaphragm, **SH** sample holder (in which the semiconductor sample can be fixed), **PD1, PD2, PD3, PD4** photodiodes. The components inside the dotted line are fixed on the mechanical rail.

on x-y-z translation stages on the optical table. Several mirrors are used to guide the weak reflection from the glass plate and the transmitted light on the photodiodes, as is depicted in Fig. 4.18. These mirrors have to be realigned after each change of the angle of incidence of the pump beam (i.e., after turing the rail). Because of several alignment aids, such as pinholes at fixed positions, this realignment is achieved with a high precision and a good reproducibility.

Data acquisition and processing

The four signals issued by the boxcar integrator are recorded with a data acquisition card from National Instruments that is installed in a computer (PC). For this purpose, I have developed a LabVIEW program which digitizes the four voltage values at a repetition rate of 10 Hz (triggered by the sync signal from the Nd:YAG laser). The program stores the values in several arrays and creates the $PD2$ vs. $PD1$ and $PD4$ vs. $PD3$ graphs. Therefore, it allows for a real-time monitoring of the relationships between these signals. The contents of the arrays can be saved on the hard disk as data files (i.e., tab-separated text files), which can then be read and further processed with some data analysis software, in our case mainly IGOR Pro from Wavemetrics.

The further data processing consists of the determination of the slopes of the linear fits to the $PD2$-$PD1$ and $PD4$-$PD3$ graphs as well as the calibration with the reference measurement without sample, as described above. When we use the avalanche photodiodes for PD3 and PD4, the noise is reasonably weak compared to the signals (cf. Fig. 4.17) so that we can adjust the offsets of the $PD3$ and $PD4$ signals correctly and force the linear fit through the origin. The advantage of this method is that we need only approximately 50 measurement points to obtain a well-defined slope. However, when we use the normal silicon photodiodes, the noise is too strong to define the offsets (and therefore the origin) of the $PD4$-$PD3$ graph correctly. In this case, it is not sensible to force the fit through the origin. Therefore, we acquire more data points (about 600 to 800) in order to have sufficiently good statistics to determine the slope with the linear fit.

## 4.4 Linear characterization of the GaAs sample

The first result we present here is a linear transmission spectroscopy of the sample, i.e., a measurement of the transmission of the sample as a function of the wavelength. More precisely, we present two linear spectroscopies : one with the *probe* beam at

normal incidence and one with the *pump* beam at an external angle of incidence of $\vartheta'_P = 57°$. In order to avoid any nonlinear effects, these linear measurements have been carried out at weak intensities. The choice of angles corresponds approximately to the configuration used for the nonlinear pump-probe experiments presented in section 4.5. Besides the resulting transmission spectra, this section illustrates the above-described method of the determination of the sample transmission.

4.4.1   Linear transmission spectroscopies of the sample

The principle of the measurement is simple : one of the two beams is incident upon the sample, and the other one is blocked. The pump beam is attenuated by turning the half-wave plate that is mounted before the Glan-Taylor prism. A reference measurement without the sample yields the reference slope of the $PD2$-$PD1$ plot (and $PD4$-$PD3$ plot, respectively), which is needed for the calibration. After fixing the sample in the sample holder, the wavelength is set to different values in the vicinity of the expected resonance wavelength. The wavelength tuning is achieved with the respective optical parametric generator by turning the mirror behind the Littman grating and the BBO crystals (see the description of the light source in section 4.3.1). For each wavelength, we determine the slope of $PD2$-$PD1$ graph (when we use the pump beam) or of the $PD4$-$PD3$ graph (when we use the probe beam). This slope is then divided by the corresponding reference slope, yielding the transmission of the sample at that wavelength. The resulting transmission curves for the pump and the probe beam are shown in Fig. 4.19. As explained above, the uncertainty of the wavelength measurement is 0.06 nm (for each wavelength).

Fig. 4.19. Linear spectroscopy of the sample (a) at an external angle of incidence of $\vartheta' = 57°$, measured with the pump beam, and (b) at $\vartheta' = 0°$ (normal incidence), measured with the probe beam. The solid line in each graph represents a fit of an Airy function to the experimental data.
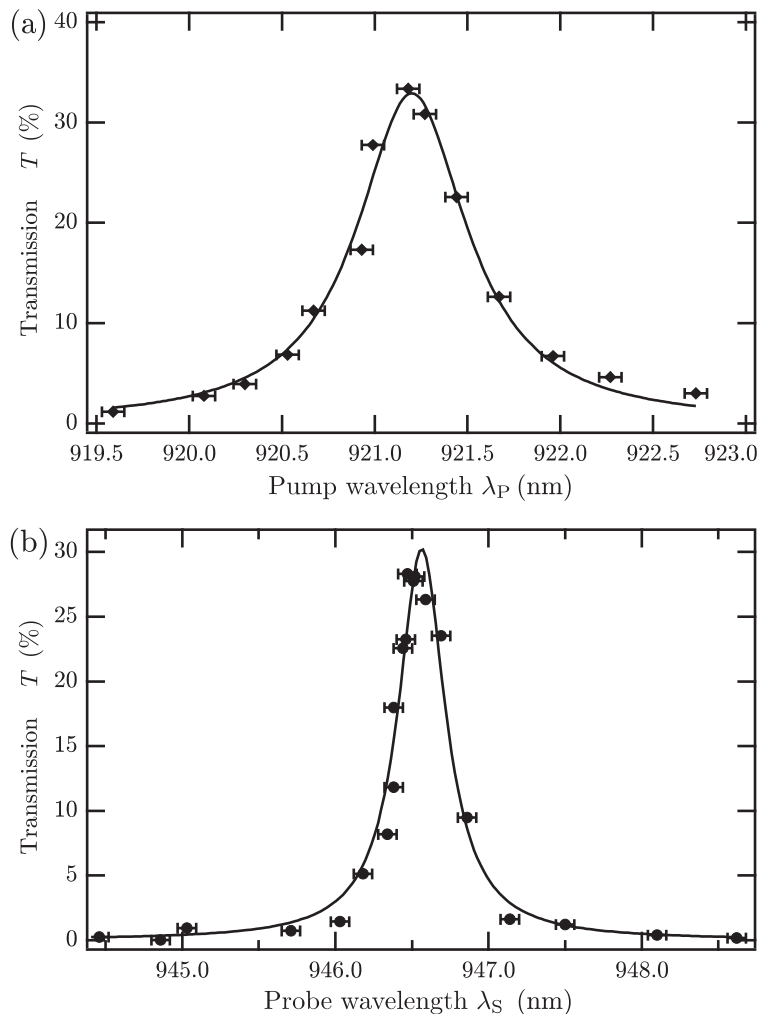
Each graph also shows the fit of an Airy function, as given by Eq. (B.9) in appendix B,

$$T(\lambda) = \frac{T_{\mathrm{max}}}{1 + \frac{4}{\pi^2}\,\mathcal{F}^2\,\sin^2\left(10\,\pi\,\frac{\lambda_0}{\lambda}\right)} \tag{4.24}$$

to the data, where we have inserted the Fabry-Perot phase $\varphi_{\mathrm{FP}} = nkL\cos\vartheta = 10\,\pi\,\lambda_0/\lambda$ (see Eq. (B.11) in the appendix) with the resonator length $L = 5\,\lambda_0/n$. The fit provides the resonance wavelength λ_0, the maximum transmission $T_{\mathrm{max,fit}}$, and the finesse $\mathcal{F}_{\mathrm{fit}}$. With λ_0 and $\mathcal{F}_{\mathrm{fit}}$, we can calculate the linewidth (full width at half maximum) of the resonance according to

$$\delta\lambda_{\mathrm{fit}} = \frac{\lambda_0}{10\,\mathcal{F}_{\mathrm{fit}}}\;. \tag{4.25}$$

The following table summarizes the resulting values, which have been obtained with the pump beam at an external angle of incidence $\vartheta'_{\mathrm{P}} = 57°$ (corresponding to an internal angle of incidence of $\vartheta_{\mathrm{P}} \approx 14°$) and with the probe beam at $\vartheta'_{\mathrm{S}} = \vartheta_{\mathrm{S}} = 0°$:

Beam	ϑ'	λ_0/nm	$T_{\mathrm{max,fit}}$	$\mathcal{F}_{\mathrm{fit}}$	$\delta\lambda_{\mathrm{fit}}$/nm
Probe	0°	946.56	0.30	253	0.37
Pump	57°	921.20	0.33	128	0.72

It is important to note, however, that these results represent a characterization of the whole sample, and not only semiconductor microcavity that is under study here. Moreover, the results are possibly biased by systematic imperfections of our measurement method, as is explained in more detail in the following section.

4.4.2 Characteristics of the semiconductor microcavity

In order to obtain the key characteristics of the semiconductor microcavity alone, the above results have to be further processed. As we show in the following, this means that several corrections have to be applied to the finesse values as well as to the maximum transmissions.

Corrections to the finesse values

The measured resonance curves do *not* correspond to pure Airy functions. Theoretically, they represent convolution integrals of the microcavity resonance (Airy function) with the spectral shapes of the pump and the probe beam (Gaussian functions). Since the linewidth of the microcavity resonance and the linewidths of the pump and probe beam are of the same order of magnitude, the finesse values $\mathcal{F}_{\mathrm{fit}}$ determined by the fit do not correspond to the real finesse $\mathcal{F}$ of the microcavity. In order to obtain the latter, it would actually be necessary to perform a deconvolution of the measured spectra. This is, however, rather complicated and not very meaningful, given the little number of measurement points.

As a reasonable approximation, we can estimate the real linewidth of the microcavity resonance by considering the latter as a Gaussian function (instead of the mathematically correct Airy function). As is well known, the convolution of two Gaussian functions yields another Gaussian function, and the linewidth of the resulting function is described by

$$\delta\nu_{\mathrm{total}}^2 = \delta\nu_1^2 + \delta\nu_2^2\;,$$

where $\delta\nu_1$ and $\delta\nu_2$ are the linewidths of the two convolved functions. Using the relationship $\delta\nu = (c/\lambda^2)\,\delta\lambda$, we can thus calculate the real linewidth of the microcavity resonance in the wavelength domain by

$$\delta\lambda_{\mathrm{MC}} = \sqrt{\delta\lambda_{\mathrm{fit}}^2 - \delta\lambda_{\mathrm{P/S}}^2}\;,$$

where we have assumed that all involved wavelengths are of the same order of magnitude and where $\delta\lambda_{\mathrm{P/S}}$ corresponds to the spectral linewidth of the pump beam or the probe beam, respectively. As shown in section 4.3.1, the pump linewidth is $\delta\lambda_{\mathrm{P}} = 0.22$ nm, and the probe linewidth is $\delta\lambda_{\mathrm{S}} = 0.18$ nm. Using again Eq. (4.25), we can also calculate the real finesse of the microcavity according to $\mathcal{F} = \lambda_0/(10\,\delta\lambda_{\mathrm{MC}})$. The resulting calculated values are presented below.

Corrections to the maximum transmission values

It is also important to note that the maximum transmission $T_{\mathrm{max,fit}}$ provided by the fit does *not* correspond to the maximum transmission of the microcavity. This is for two reasons : The first reason is that our measurement method systematically underestimates the transmission in the vicinity of the resonance maximum, as has already been mentioned in section 4.3.3. In order to illustrate this behavior, we show in Fig. 4.20 the $PD2$-$PD1$ graph for $\lambda \approx 921.20$ nm (i.e., at the resonance maximum), measured with the pump beam. As can be seen from the graph, there are many points for which the ratio $PD2/PD1$ is higher than the slope of the linear fit. This can be explained by the intrinsic spectral jitter, i.e., by the intrinsic variations of the wavelength of the pulses. These variations, which have already been explained in the description of the parametric light source in section 4.3.1, are of the same order of magnitude as the resonance linewidth. Thus, only for those pulses whose wavelength is exactly 921.20 nm, the microcavity shows its maximum transmission. These pulses are visible in the graph as the points with the highest $PD2/PD1$ ratio, indicated by the thin black line in Fig. 4.20. For all other pulses (for which $\lambda \neq 921.20$ nm), the ratio $PD2/PD1$ and therefore also the transmission is lower. Hence, the *maximum* transmission has to be determined with the *extreme* points (maximum of the ratio $PD2/PD1$) instead of the linear fit through all data points. By dividing the slope of the thin black line by the slope of the reference measurement (without sample), we obtain the real maximum transmission at an angle of incidence of $\vartheta' = 57°$ of $T^*_{\mathrm{max}} = 40$ %.

A similar analysis of the measurement at normal incidence (measured with the probe beam) shows that the real maximum transmission in this case is $T^*_{\mathrm{max}} = 30$ %, which is actually equal to the value provided by the fit of the Airy function.

The second correction that we have to take into account is the fact that the experimentally determined values of the transmission correspond to the transmission of the whole *sample*, including the GaAs microcavity (with the two Bragg mirrors) and also the 500-μm thick GaAs substrate. Thus, in order to obtain the transmission of

Fig. 4.20. Plot of the boxcar integrated signal $PD2$ versus $PD1$ (measured with the pump beam) at the resonance maximum (i.e., for $\lambda \approx \lambda_0$). As is clearly visible, there are many points for which the ratio $PD2/PD1$ is higher than the slope of the linear fit through all the points. The thin black line indicates the maximum transmission of the sample.
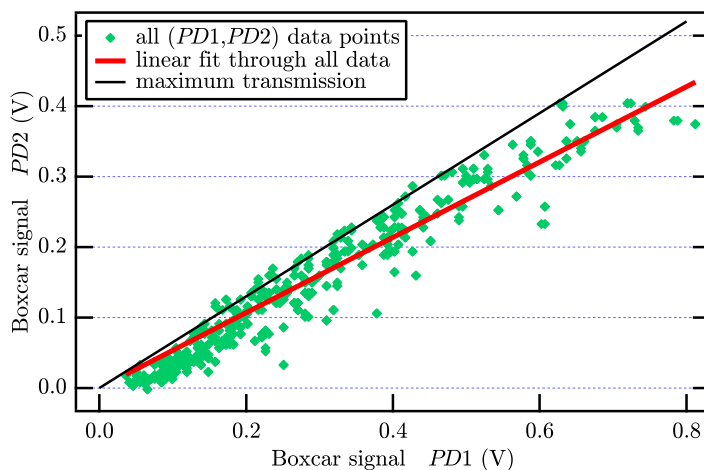
the *microcavity* alone, the propagation of the light in the substrate and the reflection at the optical interface between the substrate and the air have to be considered. This leads to the following expression for the maximum transmission of the sample

$$T^*_{\mathrm{max}} \; = \; T_{\mathrm{max}} \, \exp(-\alpha \, L_{\mathrm{sub}}) \, \left(1 - \frac{(n-1)^2}{(n+1)^2} \right) \; ,$$

where T_{max} stands for the maximum transmission of the microcavity, α is the linear absorption coefficient of GaAs, L_{sub} is the thickness of the substrate layer, and n is the refractive index of GaAs. With $L_{\mathrm{sub}} = 500 \ \mu$m, $\alpha \approx 2$ cm^{-1} [45] and $n \approx 3.5$ (for wavelengths around 1 μm), we determine the maximum transmission of the microcavity according to

$$T_{\mathrm{max}} \; = \; T^*_{\mathrm{max}}/0.63 \; . \tag{4.26}$$

Experimentally determined microcavity characteristics

Based on the corrections to the finesse and maximum transmission values, we can also determine the reflectivities R_1 and R_2 of the two Bragg mirrors for the pump and the probe beam. For this purpose, we follow the calculation that has already been presented in section 4.1.2.

Taking all the above-described corrections into account, the linear transmission measurements provide the key characteristics of the semiconductor microcavity, which are summarized in the following table :

ϑ'	$\lambda_0/$nm	T^*_{max}	T_{max}	$\mathcal{F}$	$\delta\lambda/$nm	R_1	R_2
0°	946.56	0.30	0.44	300	0.32	$R_{1,\mathrm{S}} = 0.9818$	$R_{2,\mathrm{S}} = 0.9973$
57°	921.20	0.40	0.63	139	0.66	$R_{1,\mathrm{P}} = 0.9643$	$R_{2,\mathrm{P}} = 0.9911$

As these numbers show, the sample that we use for the experiments does not exactly correspond to the design that we have determined with the numerical simulations presented in section 4.1. This might be due to imprecisions in the fabrication. We clearly see, however, that the initial requirements regarding the sample (cf. section 4.1.1) are still satisfied. Since the focus of the present work is essentially on the experiments and *not* on the simulations, we use in the following the experimentally determined values rather than the theoretical ones.

4.5 Nonlinear pump-probe measurements

Using the GaAs/AlGaAs/AlAs sample described in section 4.1 and the experimental setup presented in section 4.3, I have carried out several series of nonlinear pump-probe experiments. As is demonstrated in the following, these measurements show some totally unexpected results, which yield some insight in the interaction between electrons in the conduction band and the coherently excited phonons generated by amplified spontaneous Raman scattering.

4.5.1 Pump-probe measurements of the probe transmission

As has been extensively discussed in section 4.2, the key quantity of interest in the experiments is the transmission of the sample T_{S} for the probe beam, which is essentially a function of the probe wavelength λ_{S}, the pump wavelength λ_{P}, the pump intensity I_{P}, and the probe-pump delay Δt. The transmission is determined with the method that has been described in section 4.3.3, i.e., by measuring the slope

$M_{4,3}$ *with* and *without* the sample in the sample holder. In the remainder of this chapter, we will refer to a *measurement* as the determination of the transmission for *one* single set of parameters $(\lambda_S, \lambda_P, \Delta t)$ for different pump intensites $I_{P,0}$. It should be noted here that we work with almost Fourier-transform limited Gaussian pump (and probe) pulses. Therefore, for the experiments (as for the analytical model), the pump intensity is fully characterized by its peak value $I_{P,0}$ (and by the pulse duration, which is constant for all measurements).

Measurement of the transmission for different pump intensites

As explained in section 4.3.1, we cannot avoid the intrinsic variations of the intensity, and therefore they are always present in the measurements. In order to extract the intensity information from the measurement data, we have to process the raw data correspondingly, as is described in the following. Since we want to study the influence of the pump intensity on the nonlinear effects, we are mainly interested in the *intracavity* pump intensity. Therefore, we use the signal of photodiode 2 (i.e., the transmitted pump power) as a reference information because the intracavity intensity and the transmitted intensity are always related to one another by a fixed ratio, as has been shown by Eq. (2.101). Hence, for each pair of pump and probe pulses that is injected into the microcavity (i.e., for each pulse of the Nd:YAG laser), we record a data set consisting of the four boxcar signals $PD1$, $PD2$, $PD3$, and $PD4$, and we analyze in particular the signal $PD2$. In the experiments presented here, the latter varies intrinsically between 0 V and 1.3 V.

The key idea of the data processing is that we define a certain number of bins, corresponding to different sub-ranges of the $PD2$ signals, in which all the measurement data are sorted. In the present case, there are 10 bins, which are simply called "bin00" to "bin09", where bin00 covers the range $0 \text{ V} \leq PD2 < 0.13 \text{ V}$, bin01 contains all the values $0.13 \text{ V} \leq PD2 < 0.26 \text{ V}$, and so on. Technically these bins are realized in the programming language LabVIEW by defining ten different arrays in which the data are stored. Since each data set consists of four values ($PD1$ to $PD4$), each array is actually a two-dimensional array with (so to say) 4 columns and up to 1200 rows. So, when a data set is read from the data acquisition card (National Instruments), the program looks at the $PD2$ signal (for example $PD2 = 1.1 \text{ V}$), determines in which sub-range this value falls (for $PD2 = 1.1 \text{ V}$, this would be the range from 1.040 to 1.170 V), and then appends this data set to the corresponding array (here the array bin08). By using this method, we finally obtain ten (two-dimensional) arrays, which each contain up to 1200 data sets of four values. When the measurement is finished, we apply the transmission determination method described in section 4.3.3, yielding the probe transmission T_S for the given set of parameters $(\lambda_S, \lambda_P, \Delta t)$ and for the ten different pump intensity ranges $I_{P,0}$. As a result, we have the full information

$$T_S = T_S\Big(\lambda_S, \lambda_P, I_{P,0}, \Delta t\Big),$$

which depends on the same set of parameters as the analytical model presented in section 4.2. To illustrate the data processing, we show in Fig. 4.21 the raw data of $PD4$ vs. $PD3$ for all ten bins (i.e., pump intensity ranges) for $\Delta t \approx 200$ ps. The red lines in the graphs show the linear fit through the data points. Since these measurements have been made with the avalanche photodiodes (Hamamatsu C5460), which have a low noise level, the fits are forced through the origin (although the lines in the graphs are not drawn through the origin). Besides the measurement data, the graphs also contain two dashed lines, which are identical for all bins (i.e., in all graphs). The upper dashed line illustrates the theoretical maximum transmission.
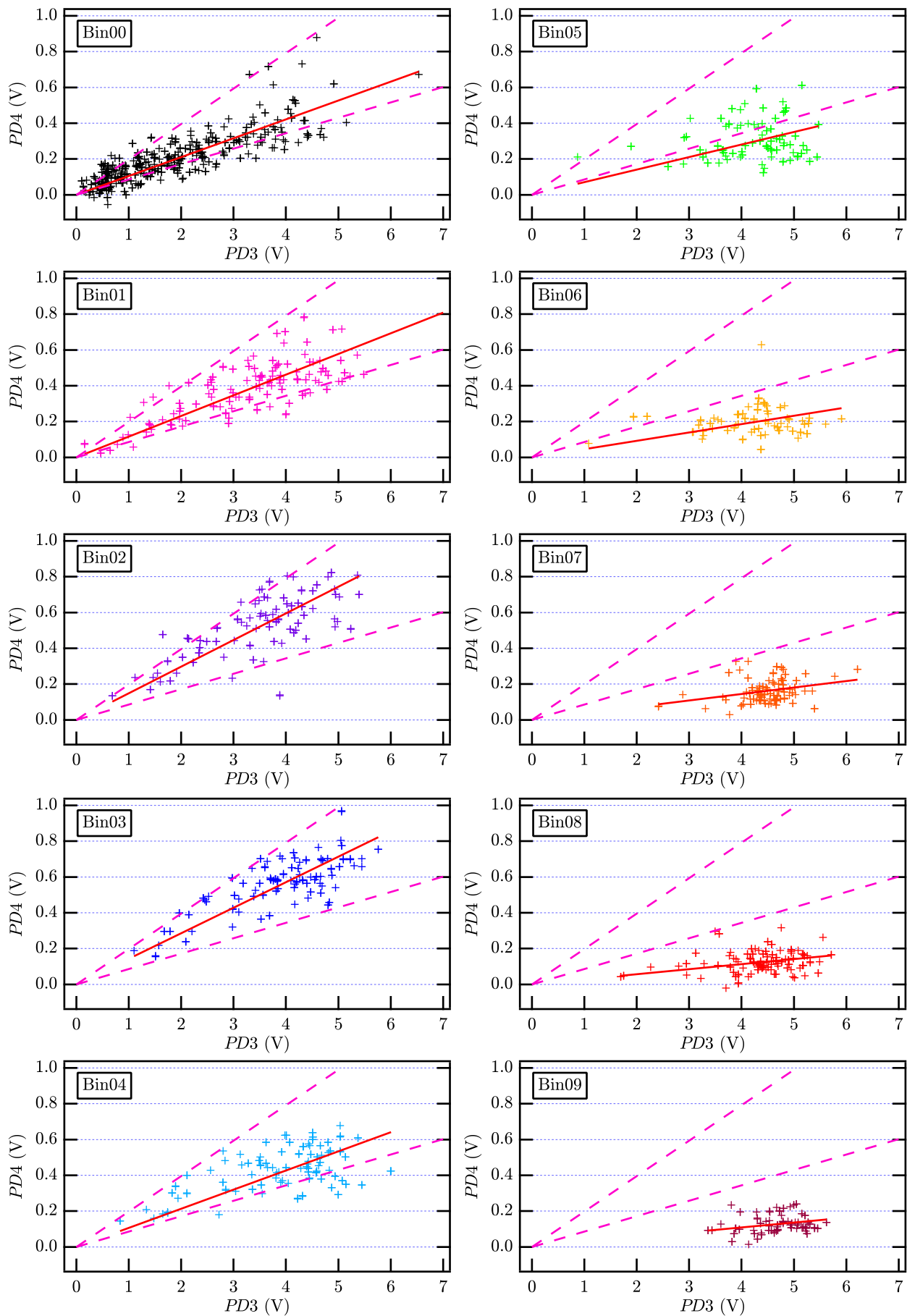
Fig. 4.21. Illustration of the $PD4$-$PD3$ raw data of one *measurement*, i.e. for one set of the parameters (λ_S, λ_P, Δt) for $\Delta t \approx 200$ ps. Each graph shows the data points corresponding to one bin, which represents a certain pump intensity $I_{P,0}$. The red lines show the linear fits (which are forced through the origin) that yield the $M_{4,3}$ slopes. The upper dashed lines correspond to the maximum transmission T^*_{max}, and the lower dashed lines illustrate the initial state.

Fig. 4.22. Illustration of the probe transmission T_S as a function of the bin number for the measurement whose raw data are shown in Fig. 4.21 (i.e. for $\Delta t \approx$ 200 ps).
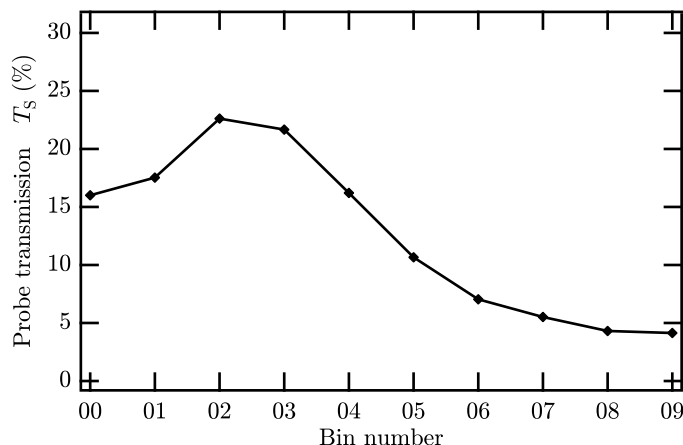
Its slope is calculated with Eq. (4.22), i.e. by multiplying the maximum probe transmission $T_{\max}^* = 30$ % with the reference slope. The lower dashed line corresponds to the initial situation without pump beam, which is calculated by multiplying the reference slope with the linear transmission at the probe wavelength $T_S(\lambda_S)$.

The graphs do not only illustrate how the probe transmission is determined, they also give an impression of the influence of the spectral jitter of the probe wavelength. As can be clearly seen, the data points are not aligned on well-defined straight lines, but they form cones or clouds of points. This is caused by the intrinsic variation of the probe wavelength, as has been explained in section 4.3.3 (see page 110).

By dividing all the slopes of the linear fits (red lines) by the reference slope $M_{4,3}$ *without* sample, we obtain the absolute values of the probe transmission T_S for each bin, which are shown in Fig. 4.22. We clearly see from the graph that the probe transmission first increases and then decreases with the bin number, where the latter is assumed to be proportional to the intracavity pump intensity. The maximum is somewhere between bin02 and bin03, and the transmission does not change much between bin07 and bin09, indicating an asymptotic behavior for the highest bin numbers. Since these data correspond only to one single measurement (i.e., one single set of λ_S, λ_P, and Δt), it is not very meaningful to enter into a detailed discussion of these results at this point. We will, however, present such a detailed analysis including the discussion of possible physical origins of the increase and decrease of the transmission, when investigating the time dependence of the ten different transmission values T_S (corresponding to the ten bins), as is presented below.

Intracavity pump intensity and transmitted pump intensity

As mentioned above, we assume that the *transmitted* pump intensity is a measure of the *intracavity* pump intensity because the two are always proportional to one another. However, this assumption is only true as long as the propagation of the pump beam in the microcavity is *not significantly* modified by the nonlinear effects. Thus, to apply the above-described binning method, we have to make sure that our measurements are not biased by a nonlinearity in the pump transmission. Therefore, for each measurement, we also determine the pump transmission T_P according to the method described in section 4.3.3 (i.e., by measuring the slope $M_{2,1}$ *with* and *without* the sample). Figure 4.23 shows the raw data of the boxcar signals $PD2$ vs. $PD1$ for the same measurement whose $PD4$-$PD3$ data are shown in Fig. 4.21. The colors of the bins are the same. As can be seen from the graph, the data points form a sort of cone whose upper limit is very well defined. For the lower and middle bin numbers, the limit is described by a straight line that corresponds to the maximum pump
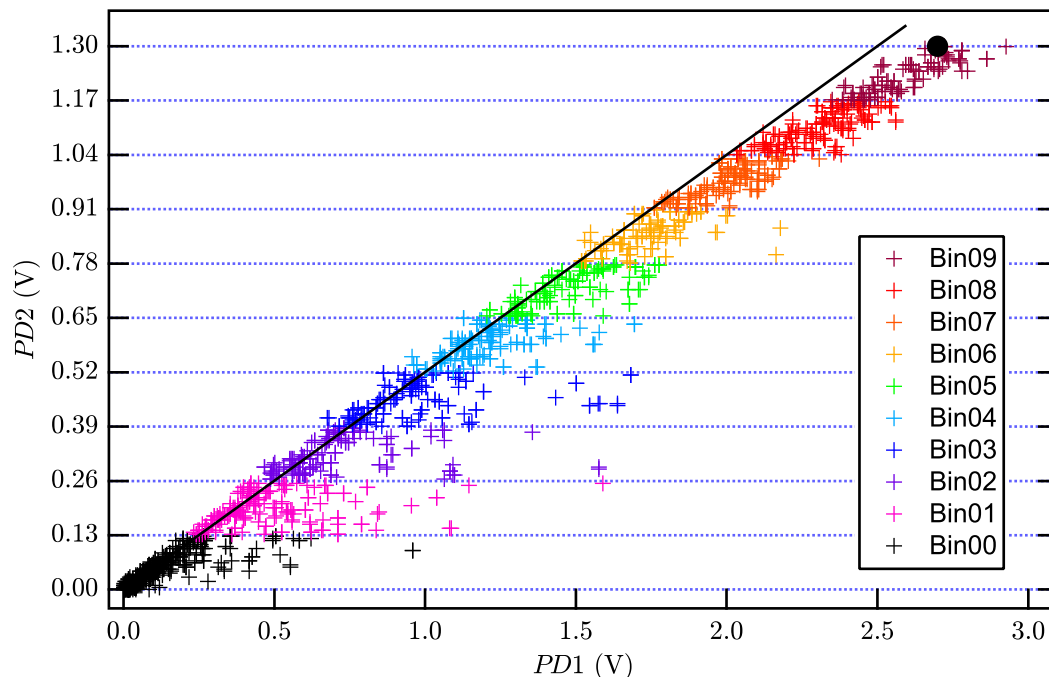
Fig. 4.23. Example of a $PD2$-$PD1$ graph illustrating the binning of the measurement data. The black line illustrates the maximum transmission of the pump beam of $T^*_{\max} \approx 40$ %, and the thick black marker in the upper right-hand corner represents the pump transmission T_P for the highest intracavity pump intensity (bin09).

transmission $T^*_{\max} = 40$ % of the sample, illustrated by the black straight line in the graph. Only for the highest bins, the pump transmission shows a slightly nonlinear behavior (i.e., a deviation from the straight line), which is due to the self-induced nonlinear effects of the pump beam, such as the two photon absorption (TPA) and the Kerr effect.

It should be noted here that these effects are only half as strong for the pump beam as for the probe beam because of the different degeneracy factors (see also the introduction of these effects in section 2.3). Since the pump-probe experiments aim at measuring the nonlinear effects induced by the pump beam on the probe beam, we have to use sufficiently high pump intensities. Consequently, it is practically impossible to avoid such self-induced nonlinearities completely. We only have to be sure that they are not too strong. Therefore, we determine the slope of the straight line in Fig. 4.23, yielding 0.52. The ratio $PD2/PD1$ of the extreme point representing bin09 (indicated by the black marker in the graph) has the value 0.48. By comparing these two, we find that even for the highest pump intensites (bin09), the deviation from the linear $PD2$-$PD1$ relationship is only about 7 %, which is reasonably small. For all the experiments presented in the following, it has been verified that the pump intensities show a quasi-linear behavior (i.e., the possibly occurring nonlinearity is only negligible small, as demonstrated above).

Measurement series for different pump wavelengths

By keeping the combination of the two wavelengths λ_S and λ_P constant while varying the probe-pump delay Δt (by moving the optical delay stage), we obtain a *measurement series*. Thus, a measurement series consists of many measurements of T_S for different delays Δt and, by using the above-described binning method, for different pump intensities $I_{P,0}$, which are represented by the different bins. As a result, we obtain the time dependence of the probe transmission, which we can then compare

to the results of the simulations in section 4.2.3 (see Figs. 4.9 and 4.10). Thus, for the experiments, there are two parameters that have to be chosen appropriately : the probe wavelength λ_S and the pump wavelength λ_P.

As the simulations of the experiments in section 4.2.3 have clearly shown, it is reasonable to choose an initial probe wavelength λ_S which is slightly detuned from the exact resonance wavelength λ_S^* towards shorter wavelengths. According to the linear characterization of the sample presented in section 4.4, the ideal probe wavelength is $\lambda_\mathrm{S}^* = 946.56$ nm. Thus, we choose $\lambda_\mathrm{S} = 946.33$ nm, for which the resulting linear transmission is about half of the maximum transmission.

Regarding the pump wavelength λ_P, we are essentially interested in the difference between the two situations *with* and *without* stimulated Raman scattering (SRS). By referring again to the simulations presented in section 4.2.3, this means that it

$\lambda_{\mathrm{P},1} = 918.89$ nm	$\ll$	λ_P^*
$\lambda_{\mathrm{P},2} = 920.78$ nm	$<$	λ_P^*
$\lambda_{\mathrm{P},3} = 920.87$ nm	$\approx$	λ_P^*
$\lambda_{\mathrm{P},4} = 920.99$ nm	$>$	λ_P^*
$\lambda_{\mathrm{P},5} = 922.71$ nm	$\gg$	λ_P^*

Tab. 4.2. Pump wavelengths used for the nonlinear pump-probe experiments.

would be sufficient, in principle, to carry out two measurement series : one exactly at Raman resonance and one far off Raman resonance. However, in order to be sure not to "miss" the signature of SRS, we choose three pump wavelengths in the vicinity of the theoretical ideal pump wavelength λ_P^*, which is given by $\lambda_\mathrm{P}^* = (1/\lambda_\mathrm{S} + \bar{\nu}_\mathrm{R})^{-1} = 920.88$ nm. Moreover, we want to see if there is any difference between the situation where the pump beam is far off the Raman resonance towards *longer* wavelengths and the situation where it is far detuned towards *shorter* wavelengths. So, in total, this leads to five measurement series for five different pump wavelengths λ_P, which are listed in Tab. 4.2. The results of these five measurement series are shown in Figs. 4.24 and 4.25 on the next two pages.

All the measurement series are carried out according to the same experimental procedure, which is described in the following. First, the pump wavelength is set to the desired value with the parametric light source (optical parametric generator and amplifier), while it is measured with the monochromator. Then, the sample is removed from the sample holder, and the data acquisition program is started to measure the two reference slopes $M_{2,1}$ and $M_{4,3}$ *without* the sample. Third, the sample is fixed in the sample holder, and the data acquisition program is used to provide a real time view of the $PD2$-$PD1$ graph (as shown in Fig. 4.23). The power of the pump beam is reduced by turning the half-wave plate of the beam preparation stage, and the angle of incidence ϑ_P' of the pump beam is adjusted in such a way that the $PD2$-$PD1$ shows a well-defined *linear* upper limit whose slope corresponds to the maximum transmission of $T_\mathrm{max}^* = 40$ %. Finally, the half-wave plate is rotated back into its initial position in order to attain sufficiently high pump intensities for the pump-probe measurements, and the optimal spatial overlap of the pump and the probe beam on the sample are verified with a CCD camera that is placed at a fixed and reproducible reference position. Before the first measurement series, this optimal overlap has been determined for a pump wavelength λ_P far off Raman resonance at a long delay Δt by minimizing the probe transmission as much as possible (which is what we expect according to the simulations).

Then the measurement series starts by setting the position r of the retroreflector to different values between 0 and 40 mm (the absolute value of r does not matter here). For each value of r, we carry out a *measurement* as described above. This means that the data acquisition program reads continuously the $PD1$, $PD2$, $PD3$, and $PD4$ signals from the boxcar integrator with a repetition rate of 10 Hz and performs the binning of the data sets according to the method described above. While the data acquisition is running, we monitor the filling of the different bins, i.e., we check that all bins contain enough data points to be able to perform a linear fit that yields a meaningful slope $M_{4,3}$. As a preliminary test has shown, a minimum of 50 data points per bin provides good enough statistics for a reasonable fit (when
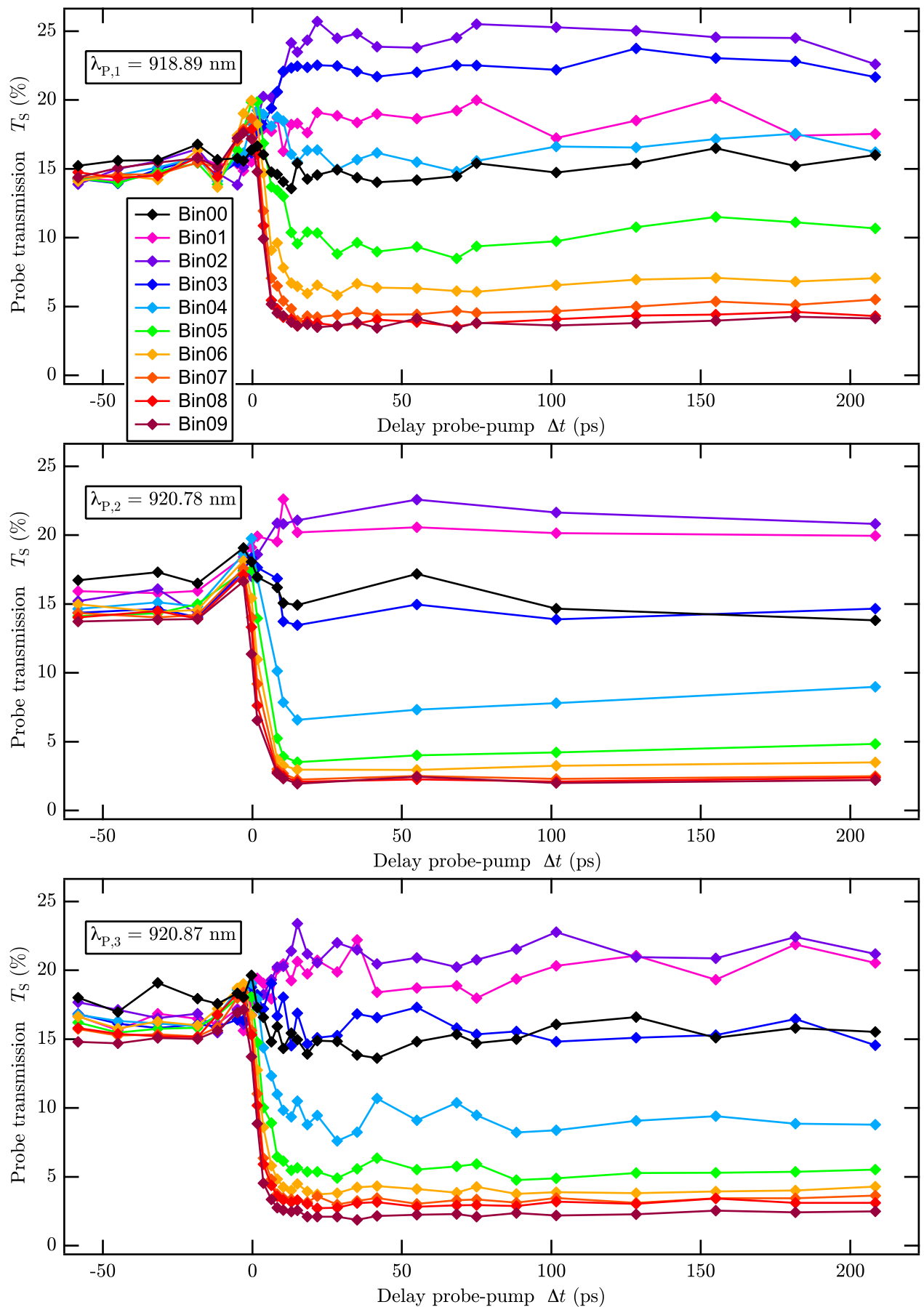
Fig. 4.24. Pump-probe measurement series for $\lambda_S = 946.33$ nm. Time dependence of the probe transmission T_S of the semiconductor microcavity for different pump intensities $I_{P,0}$, represented by the different bins (bin00 ... bin09) as the colored traces. For an estimation and discussion of the measurement uncertainties (error bars), see text.
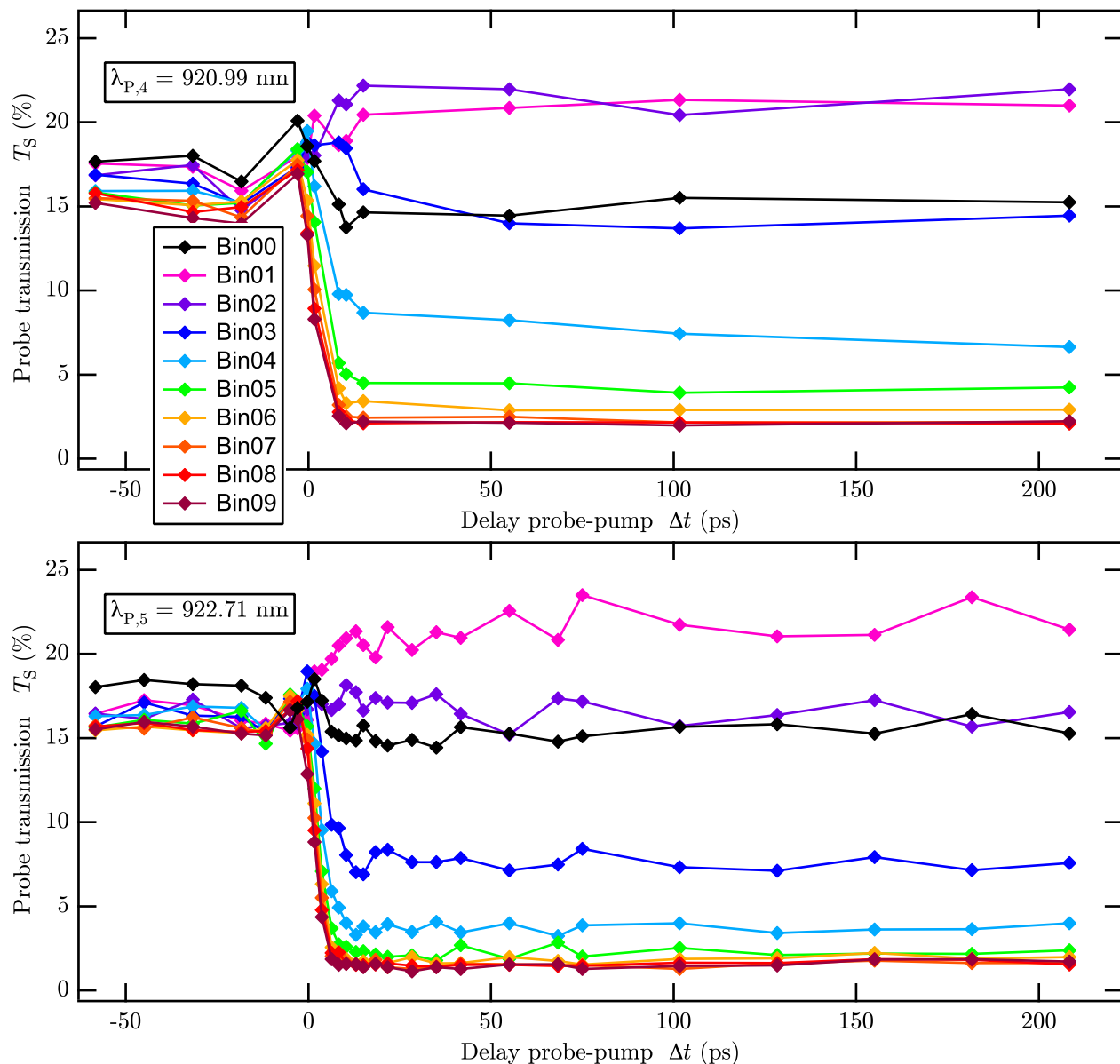
Fig. 4.25. Pump-probe measurement series for $\lambda_S = 946.33$ nm. Time dependence of the probe transmission T_S of the semiconductor microcavity for different pump intensities $I_{P,0}$, represented by the different bins (bin00 ... bin09) as the colored traces. For an estimation and discussion of the measurement uncertainties (error bars), see text.

using the avalanche photodiodes of the type Hamamatsu C5460). Moreover, we also check for each measurement the $PD2$-$PD1$ graph in real time and verify that the pump beam does *not* show a *significant* nonlinear behavior, as has been discussed above. As a result, each measurement yields the ten different probe transmissions T_S (one for each bin) for the given value of r. After the completion of the first measurement series, the position r of the delay stage is calibrated (i.e., the zero position is determined) based on the observed time dependence of T_S. As a result, we find that the different values of r correspond to probe-pump delays Δt between -58 and +208 ps. It should be noted that this choice of the position $\Delta t = 0$ is only an estimation. However, the *relative* time scale (i.e., the scale of time *differences*) is simply given by the speed of light according to $\Delta t = r/c$ and, therefore, very precise.

All the five graphs in Figs. 4.24 and 4.25 (i.e., all the five time dependencies of T_S) show a similar behavior. For negative probe-pump delays Δt (for which the probe pulse arrives before the pump pulse), the probe transmission T_S is constant at the

initial value of about 15 %, which is physically logical for causality reasons. The little differences between the curves of the different bins for these delays can*not* be explained by any nonlinear optical effect because the pump pulse arrives *after* the probe pulse. Except for the first graph ($\lambda_P = 918.89$ nm), it seems that the curves corresponding to the higher bin numbers are systematically lower than the curves of the lower bin numbers. One reason for these differences might be the fact that the initial probe wavelength λ_S corresponds to a position half-way off the resonance curve of the microcavity. Thus, the intrinsic wavelength variations are translated into a large spread of the data points in the $PD4$-$PD3$ graph (which yields the slope $M_{4,3}$ and thus also the transmission T_S), and this translation is highly sensitive to possibly asymmetric distributions of the randomly varying wavelength values around the measured probe wavelength λ_S. Since the ten bins are usually *not* filled with the same number of data sets (i.e., the $PD4$-$PD3$ graphs of the different bins do usually *not* contain the same number of data points), the determination of the slopes $M_{4,3}$ is based on different statistics for the different bins. In general, the bins with the lower bin numbers (i.e., weak pump intensities) contain systematically less data points than the bins with higher bin numbers (i.e., high pump intensities), which is due to technical reasons (the intrinsic intensity variations of the pump pulses are not uniformly distributed). This might explain the apparently systematic differences between the different bins.

Around $\Delta t = 0$ (i.e., where the pump and probe pulses have their maximum temporal overlap), the transmission rises to a maximum. The height of the maximum as well as the further behavior for higher delays Δt depend on the bin number (i.e., on the pump intensity). For the lower bin numbers, the transmission rises relatively slowly and reaches a stable optimum value, whereas for middle and high bin numbers, the transmission passes the maximum and then decreases. For the upper bin numbers, it even drops to values which are lower than the initial transmission of about 15 %. In all five graphs, the curves corresponding to the highest bin numbers group together so that we can reasonably conclude that for even higher pump intensities, the time dependence of the probe transmission T_S would not be significantly different from the curve of bin09 (burgundy / dark red curve).

Because of the method that is used to determine the transmission values (see also section 4.3.3), the measurement uncertainty of the probe transmission T_S is, in general, a function of the value of T_S itself. It basically depends on how much the spectral jitter (i.e., the randomly varying wavelength) of the probe beam leads to a spread of the transmission values. For delays $\Delta t \ll 0$, the probe wavelength is on the wing of the resonance curve of the microcavity, and thus the latter is highly sensitive on wavelength variations. Hence, we estimate the uncertainty of the transmission in this Δt range to be between 2% and 3% (absolute values in terms of the transmission). However, for very low values of T_S (i.e., mainly for long delays $\Delta t \gg 0$ and high bin numbers), the transmission should be rather insensitive to wavelength variations so that here, we can estimate the uncertainty to be of the order of 1% (absolute value).

Essentially, the five graphs correspond to two different situations that we have already studied with the simulations presented in section 4.2.3 : *with* SRS (i.e., λ_P is *at* Raman resonance) and *without* SRS (i.e., λ_P is *off* Raman resonance). The simulations of these two situations are indicated by a dotted frame in the lower right corner of Fig. 4.10 and shown again in Fig. 4.26 (for the sake of convenience). The experimental results shown in the first and fifth graph in Figs. 4.24 and 4.25 show the situation far *off Raman resonance* ($\lambda_{P,1} = 918.89$ nm $\ll \lambda_P^*$ and $\lambda_{P,5} = 922.71$ nm $\gg \lambda_P^*$, where $\lambda_P^* = 920.88$ nm). The second, third, and fourth graph are close or equal to

Fig. 4.26. Simulations of the pump-probe experiments for an initial probe wavelength half-way off resonance. Time dependence of the probe transmission T_S of the semiconductor microcavity for pump intensities $I_{P,0}$ between 0.3 and 1.9 MW/cm^2 (indicated by the different colors of the traces). The top graph shows the situation *without* SRS (i.e., far off Raman resonance), whereas the bottom graph illustrates the case *with* SRS (i.e., at Raman resonance). These two graphs are also shown in Fig. 4.10.
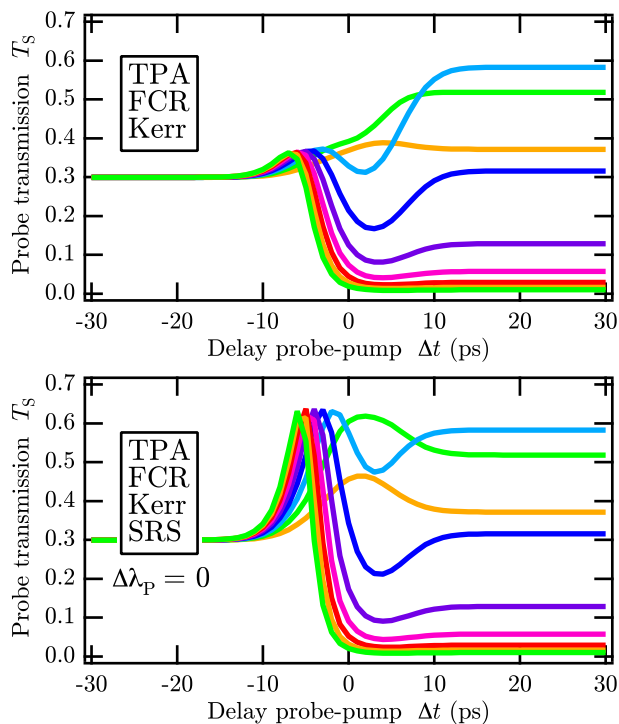
the situation *at Raman resonance* ($\lambda_{P,2} = 920.78$ nm $< \lambda_P^*$, $\lambda_{P,3} = 920.87$ nm $\approx \lambda_P^*$, and $\lambda_{P,4} = 920.99$ nm $> \lambda_P^*$).

By comparing the experimental results to the simulations, we find that the measurements correspond *approximately* to the predictions of the simulations. However, there are several important differences that have to be discussed in more detail. Because of these differences, it is not possible to fit the theoretical curves of the analytical model (see section 4.2) to the experimental data, although the model takes into account all nonlinear effects that we expect to observe in the experiments. Therefore, in the following, we compare the simulations and the measurements by looking only at the essential properties of the curves. For this purpose, we present in Fig. 4.27 a zoom of the five graphs of Figs. 4.24 and 4.25 between $\Delta t = -30$ ps and $\Delta t = 70$ ps, which makes the comparison easier.

Starting our analysis with the situation *at Raman resonance*, i.e., the graphs for $\lambda_{P,2}$, $\lambda_{P,3}$, and $\lambda_{P,4}$, we find that all three graphs are very similar (except for the fact that the two graphs slightly detuned from the ideal pump wavelength have a lower time resolution, which is due to practical reasons). However, none of these graphs shows exactly the behavior that has been predicted by the simulations (see bottom graph in Fig. 4.26). First, we do *not* observe that the probe transmission of all bins reaches its maximum value for probe-pump delays $\Delta t \approx 0$, as the simulations have shown. This means that we do actually *not* find the signature of stimulated Raman scattering (i.e., an increase of the probe transmission) as it is described by the analytical model. Second, we see that the transmission of the highest bins does *not* drop as much in the measurement data as in the simulations. Although we clearly observe an asymptotic behavior of the curves as a function of the pump intensity (i.e., bin number), the measured minimum transmission is between 2 and 3 % instead of almost zero, as the simulation graph shows. This observation will in the following be the key element of our analysis of the experimental data. A third observation is that the Kerr/TPA dip is not as pronounced in the measurement results as it is in the simulations. To find an explanation for these differences between theory and experiment, it is insightful
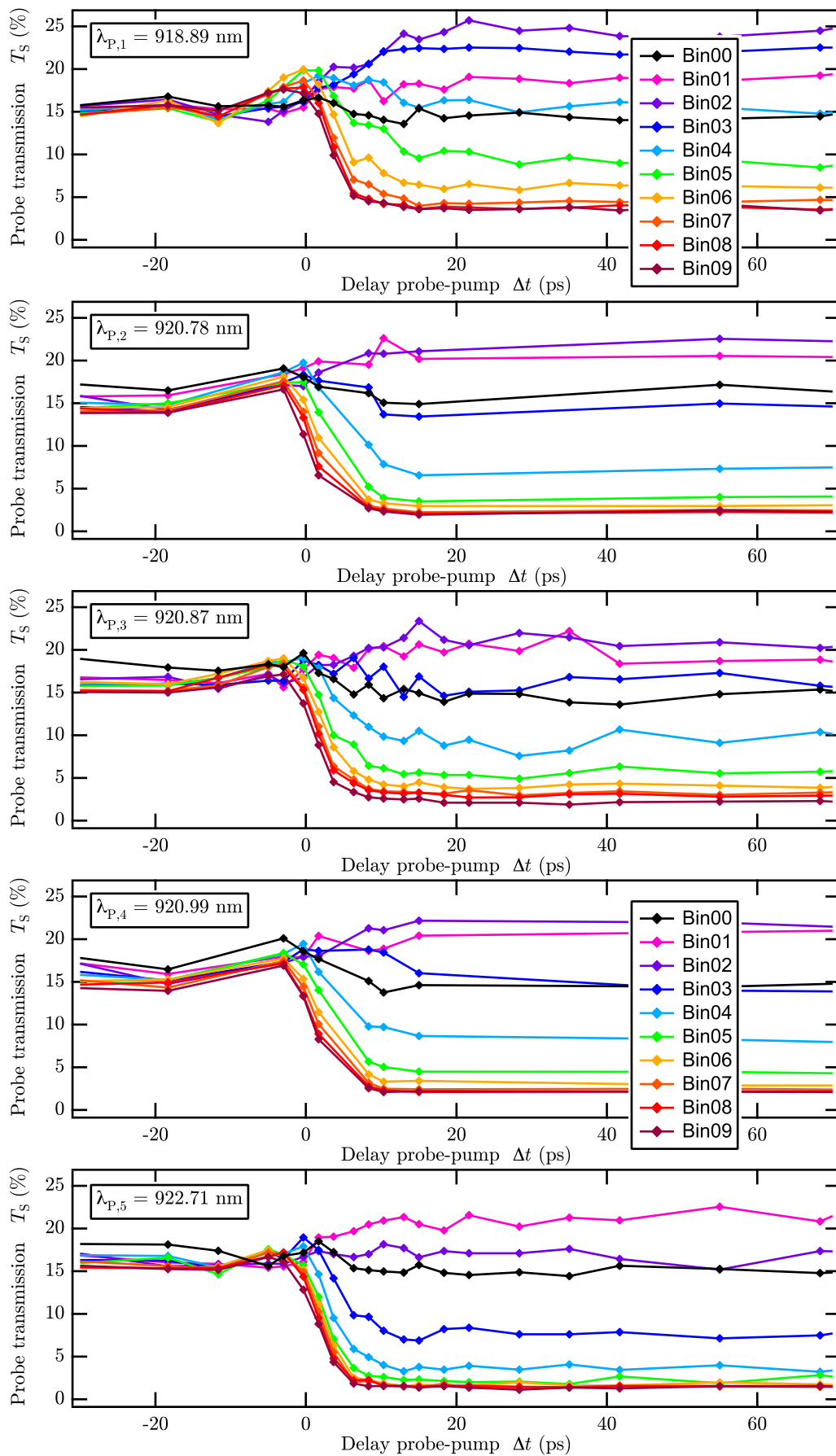
**Fig. 4.27.** Zoom of the experimental results of the pump-probe measurement series presented in Figs. 4.24 and 4.25 (i.e., for $\lambda_S = 946.33$ nm). Time dependence of the probe transmission T_S of the semiconductor microcavity for different pump intensities $I_{P,0}$, represented by the different bins as the colored traces. The five graphs correspond to the different pump wavelengths λ_P (see Tab. 4.2).

to look in more detail at the other two graphs.

When comparing the experimental results for $\lambda_{P,1}$ (i.e., far off Raman resonance towards *shorter* wavelengths), which are shown in the first graph in Fig. 4.27, to the corresponding simulation (see top graph in Fig. 4.26), we make slightly different observations. Around $\Delta t = 0$, the simulations predict a weak increase of the probe transmission by only several percent, corresponding to approximately a fifth of the initial transmission. This is exactly what we see in the experimental results. Moreover, the simulations have shown that for some of the lower bins, the transmission continues to increase for long delays. This can also be seen from the experimentally determined curves. The purple curve (bin02), for example, rises to an optimum transmission of 26 %, which is very close to the theoretical maximum value of $T_{\max}^* = 30$ % (it should be kept in mind here that our measurement method always underestimates the microcavity transmission near the maximum, as has been explained in section 4.4.2), and it stays at this optimum value for delays $\Delta t \gg 0$, exactly as predicted by the model. The most important observation, however, is that the asymptotic minimum transmission reached by the experimental curves of the highest bins is about 4 %, which is clearly higher than in the three graphs discussed above. Finally, one could mention that it is again difficult to identify the Kerr/TPA dip in the experimental data, as in the previous case.

The measurement results for $\lambda_{P,5}$ (i.e., far off Raman resonance towards *longer* wavelengths), which are depicted in the fifth graph in Fig. 4.27, show an interesting behavior. In principle, one would expect that this graph should be similar to one for $\lambda_{P,1}$ (i.e., far off Raman resonance towards *shorter* wavelengths). However, as opposed to these expectations, we observe that the asymptotic minimum transmission of the highest bins is less than 2 %. Since we can assume a measurement uncertainty of about 1% here (see discussion on page 123), this value is in agreement with the simulations (which have predicted values of less than 1%). The fact that we do not see any curve here that rises to transmission values of more than 25 % might be caused by the binning steps (i.e., maybe we would see such a curve if we had chosen the binning intervals slightly differently). As opposed to the other four graphs, we can identify the Kerr/TPA dip on the dark blue and light blue curves (bin03 and bin04).

> To summarize the above findings, we can state that in many aspects, the experimental results of the pump-probe measurements are *approximately* well described by the analytical model presented in section 4.2. However, we clearly find several major differences between the theoretical and experimental behaviors of the time dependencies of the probe transmission T_S. First, we do *not* see the signature of an amplification through stimulated Raman scattering (SRS) that is predicted by the simulations around $\Delta t = 0$. Second, and **most importantly**, the asymptotic value of the transmission for the highest bins depends on the pump wavelength λ_P. Third, the asymptotic values of the probe transmission measured for $\lambda_{P,1}$ and $\lambda_{P,5}$ (i.e., far below and far above Raman resonance) are clearly different from one another.

It is important to note here that, although we do *not* see the SRS signature that we expect according to the model, the five different graphs show a clear dependence on λ_P. Given that TPA, the Kerr effect, and the free carrier effects (FCA, FCR) are not sensitive to the pump wavelength, we can further conclude that this dependence

must be caused by SRS. In other words, we actually observe an *unexpected* signature of SRS, which we study in more detail in the following.

So far, we have discussed all the experimental results in terms of the bin number, which serves as a measure for the pump intensity $I_{P,0}$. In order to determine the exact relationship between the bin numbers and $I_{P,0}$, several calibration measurements have been carried out. For these measurements, a highly sensitive optical energy meter (with a sensitivity of several μJ) has been placed at the position of the sample holder in the experimental setup, and the measured values have been compared with the reference boxcar signal $PD1$. By combining these measurements with an experimental determination of the pump beam diameter, we find that the highest bin number (i.e., bin09) corresponds to a pump intensity of several MW/cm^2. It has not been possible to determine this relationship with a higher precision because of two reasons. First, the energies of the pump pulses have been very close to the measurement sensitivity of the energy meter. And second, the comparisons between the value from the energy meter and the reference boxcar signal have been done "by naked eye", thus with a high intrinsic uncertainty.

Another (and maybe better) calibration of the bin numbers is provided by the experimental results themselves. Since we clearly see that the general behavior of the experimental T_S-Δt curves, especially the asymptotic state for the highest bin numbers, is also predicted by the simulations, we can conclude that the pump intensity ranges in the simulations and in the experiments are approximately the same. Supposing that we can trust the nonlinear coeffients (β_{TPA}, n_2, σ_n, σ_a), we see *approximately* a good agreement between the model and the measurements. Thus, we assume that bin09 corresponds to a pump intensity of $I_{P,0} \approx 2$ MW/cm^2.

Unexpected signature of SRS in the experimental results

As a closer look at the experimental data shows, the stimulated Raman scattering has a very subtle influence on the time dependence of the probe transmission. More precisely, it affects the speed with which the transmission T_S passes the maximum and approaches the asymptotic state. To illustrate this influence, we show in Fig. 4.28 the probe transmission T_S as a function of the bin number (which represents the pump intensity) for all five pump wavelengths λ_P used in the pump-probe experiments at a delay of $\Delta t \approx 8$ ps. As can be very clearly seen from the graph, the curves show a *significantly* different behavior. The red trace ($\lambda_{P,5}$) passes very quickly the maximum and reaches the asymptotic state in bin05. The three traces that are (approximately) at Raman resonance ($\lambda_{P,1}$, $\lambda_{P,2}$, and $\lambda_{P,3}$) also pass the maximum in a very similar way as the red curve, but this happens for higher pump intensities. Moreover, the transmission does not drop as strongly as for the red trace. In the case far off Raman resonance towards shorter wavelengths ($\lambda_{P,1}$), shown as the blue trace, the probe transmission needs even higher pump intensities to pass the maximum, and the curve does not decrease as much as in the other cases. In summary, we see three different behaviors : the one of the red trace ($\lambda_P \ll \lambda_P^*$), the one of the three traces approximately at Raman resonance ($\lambda_P \approx \lambda_P^*$), and the one of the blue trace ($\lambda_P \gg \lambda_P^*$). Therefore, we will focus in the following on these three situations, which are represented by $\lambda_{P,1}$ (red), $\lambda_{P,3}$ (green), and $\lambda_{P,5}$ (blue).

As mentioned above, the differences between the curves have to be related to SRS because they depend on the pump wavelength. However, without knowing exactly how SRS influences the transmission of the microcavity, the question arises why the red trace and the blue trace do *not* show a similar behavior (they are both far off

Fig. 4.28. Illustration of an *unexpected* signature of SRS in the experimental data. The graph shows the probe transmission T_S as a function of the bin number (corresponding to the pump intensity) for $\Delta t \approx 8$ ps for all five pump wavelengths λ_P (see Tab. 4.2).
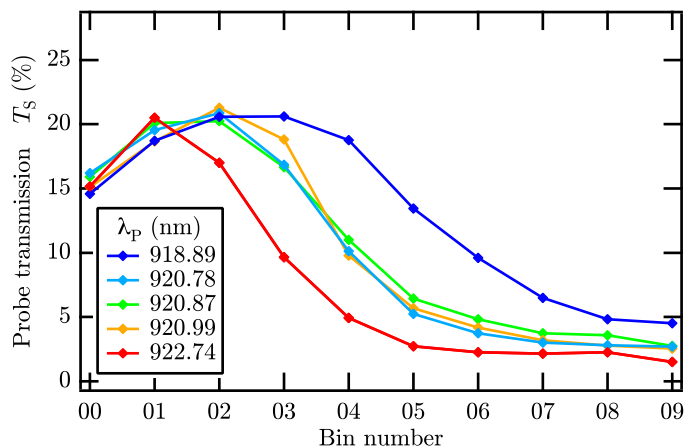
Raman resonance and, thus, expected to undergo the same physical effects). The key to the understanding of these differences is the fact that the resonance wavelength of a Fabry-Perot resonator depends on the angle of incidence. As is demonstrated in appendix B, by increasing the angle of incidence ϑ of an electromagnetic wave (we only consider plane waves here), the resonance wavelength becomes shorter. This fact has some important implications for the present situation.

Considering that the pump beam is very strong, one has to take into account the effect of the *spontaneous* Raman scattering in the central GaAs layer of the semiconductor sample. In a situation where the Stokes photons (generated through *spontaneous* Raman scattering) are coupled into a resonant mode of the microcavity, they should be amplified through SRS. It is important to note that the Stokes wave, which is resonant in the microcavity, can interact nonlinearly with the pump wave through stimulated Raman scattering (SRS) *without* the presence of the probe beam. Thus, in this particular case, the probe beam does not take part in the Raman scattering process and only serves as a *probe* (in the literal sense of the word) to measure the transmission of the semiconductor sample. Therefore, the wavelength of the *Stokes* photons generated through **amplified spontaneous Raman scattering** might differ from the wavelength of the *probe* beam (as opposed to the general assumption that these two are equal). However, the Stokes wave can only be resonant in the microcavity if its wavelength is shorter or equal to the ideal probe wavelength λ_S^* because the latter is the longest possible resonance wavelength for the given resonator length (assuming that the resonance order m is conserved).

For the pump wavelength $\lambda_{P,5}$, the corresponding Stokes wavelength would be $\lambda_S = (1/\lambda_P - \bar{\nu}_R)^{-1} = 948.26$ nm. Since this wavelength can under no circumstances be resonant in the microcavity, we cannot observe any enhancement of the amplification of the spontaneous Raman scattering. The Stokes wavelength for $\lambda_{P,3}$ (and also $\lambda_{P,2}$ and $\lambda_{P,4}$) is around $\lambda_S \approx 946.32$ nm, which can be resonant at almost normal incidence. Therefore, in that case, there can be a nonlinear interaction between pump and Stokes in the form of SRS. Finally, for $\lambda_{P,1}$, we calculate the Stokes wavelength to be $\lambda_S = 944.23$ nm. Contrary to the situation for $\lambda_{P,5}$, we can expect an enhancement of the amplified spontaneous Raman scattering because the corresponding Stokes wave coincides with a resonance of the cavity (which has a non-zero angle of incidence). In that case, we expect an increase of the number of Raman phonons with an energy $\hbar\Omega_R$ that are generated in the central layer of the microcavity.

> We conclude that the difference between the asymptotic states in the T_S-Δt measurements for $\lambda_{P,1}$ and $\lambda_{P,5}$ (i.e., far off Raman resonance) is related to the enhancement of the amplification of the Stokes photons generated by spontaneous Raman scattering in the central GaAs layer of the semiconductor sample.

With this important result, we still have to address the question *how* SRS influences the microcavity transmission. For this purpose, we must have a closer look at the key mechanisms that influence the transmission T_S. These are, as has been extensively discussed in section 4.2, absorption/amplification on the one hand and, on the other hand, the nonlinear phase shift. In all the measurement data, we do *not* observe any amplification, and we have demonstrated in the simulations (and also seen in the measurements) that the nonlinear phase shift induced by SRS is negligibly small. Hence, this question cannot be fully explained with our analytical model. However, as the discussion of the different nonlinear effects and their influence on the probe transmission in section 4.2.2 has shown, the impact of the phase shifts on T_S is higher than the one of the two photon absorption. Since a phase shift can also be considered as an effective modification Δn of the refractive index of the microcavity (i.e., of the central GaAs layer), we have to look for other physical effects that influence the refractive index of the semiconductor microcavity. Therefore, we have to determine by how much the refractive index changes.

4.5.2 Modified electron relaxation dynamics due to SRS

To determine the refractive index change Δn from the measurement data, we would have to isolate the absorptive effects from the refractive effects. In principle, however, this is not possible because we have only measured the transmission T_S of the microcavity, which is affected by both sorts of effects simultaneously. Since we have previously shown that the absorption effect of the free carriers (FCA) can be neglected (see section 4.2.1), we can reasonably assume the variation of the transmission at long delays ($\Delta t \gg 0$) is only due to the variation of the refractive index induced by the free carriers (FCR). Although for short delays $\Delta t > 0$, the probe transmission is biased by two photon absorption (TPA), we can still compare the different measurement series to each other in order to discuss the *relative* differences (instead of the absolute behavior). This is possible because TPA is independent of the pump wavelength λ_P. For this comparison, we apply the following method.

Refractive index change for three different pump wavelengths

Considering the red, the green, and the blue trace in Fig. 4.28, we see that all of them start at bin00 with approximately the same transmission $T_S \approx 15$ %. This transmission corresponds to the initial state of the microcavity, which is given by the probe wavelength detuning $\Delta\lambda_S = -0.13$ nm ($\lambda_S = 946.33$ nm). Since all the curves rise to the maximum and then fall to lower transmissions, we can translate the T_S values into the refractive index change Δn by comparing the behavior of the traces to the resonance curve of the microcavity, as is illustrated in Fig. 4.29. This translation actually happens in two steps : first, we have to determine the phase φ (i.e., the horizontal position in the graph) to a given value of T_S (vertical axis), and second, we calculate the corresponding modification Δn based on the phase φ.

The resonance curve in Fig. 4.29 is described by an Airy function of the form

$$T_S(\varphi) = \frac{T_{max}}{1 + \frac{4}{\pi^2}\,\mathcal{F}^2\sin^2(\varphi)}\,,$$

Fig. 4.29. Illustration of the method that is used to determine the nonlinear refractive index change based on the transmission measurements presented in Figs. 4.24 and 4.25.
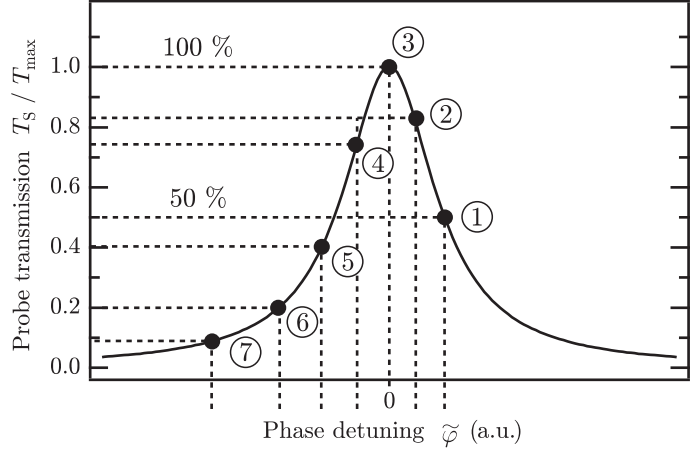
which we have already used in the discussion of the analytical model (see Eq. (4.15) in section 4.2.2). Since we want to determine the phase φ based on the transmission T_S, we rewrite this equation in the form

$$\sin(\varphi) = \pm \sqrt{\frac{\pi^2}{4\mathcal{F}^2}\left(\frac{T_{\max}}{T_S} - 1\right)} \; .$$

Since the Airy function has a periodicity of π (because of the $\sin^2$ function in the denominator), we can restrict our considerations to the φ range around the tenth-order resonance. Therefore, we decompose the phase into

$$\varphi = \bar{\varphi} + \widetilde{\varphi} \qquad \text{with} \qquad \bar{\varphi} = 10\pi \; , \tag{4.27}$$

where $\widetilde{\varphi}$ is the variation of the phase around the center of the tenth-order resonance. Because of the periodicity of the sine function, we obtain $\sin(\varphi) = \sin(10\pi + \widetilde{\varphi}) = \sin(\widetilde{\varphi})$, and since we assume $\widetilde{\varphi}$ to be small, we can calculate the phase by

$$\widetilde{\varphi} \approx \sin(\widetilde{\varphi}) = \sin(\varphi) = \pm \sqrt{\frac{\pi^2}{4\mathcal{F}^2}\left(\frac{T_{\max}}{T_S} - 1\right)} \tag{4.28}$$

As this expression and the shape of the resonance curve in Fig. 4.29 show, there is an ambiguity regarding the sign of the phase. In other words, the above equation does *not* tell us on which side of the resonance we are. In order to overcome this problem, we have to utilize the fact that we know the initial state of the microcavity, as is explained in more detail below.

In general (see appendix B), the phase φ can also be expressed by Eq. (B.11) as

$$\varphi = \frac{2\pi\, n_S\, L\, \cos(\vartheta_S)}{\lambda_S} = 10\pi\, \frac{n_S\, \lambda_S^*}{n_S^*\, \lambda_S} \; , \tag{4.29}$$

where we have inserted the angle of incidence of the probe beam $\vartheta_S = 0$ and the length of the microcavity $L = 5\lambda_S^*/n_S^*$. It should be noted that the refractive index n_S is considered *variable* here (it is exactly *this* variation of n_S that we want to determine), while n_S^* denotes the bulk refractive index of GaAs at the ideal probe wavelength λ_S^*. By introducing the refractive index change Δn_S through $n_S = n_S^* + \Delta n_S$ and by using the relationship $\lambda_S = \lambda_S^* + \Delta\lambda_S$, the fraction on the right hand side of the above expression can be transformed to

$$\frac{n_S\, \lambda_S^*}{n_S^*\, \lambda_S} = \frac{(n_S^* + \Delta n_S)\, \lambda_S^*}{n_S^*\,(\lambda_S^* + \Delta\lambda_S)} = \frac{n_S^* + \Delta n_S}{n_S^*}\, \frac{\lambda_S^*}{\lambda_S^* + \Delta\lambda_S} = \frac{1 + \Delta n_S/n_S^*}{1 + \Delta\lambda_S/\lambda_S^*} \; , \tag{4.30}$$

which depends on the relative refractive index change $\Delta n_{\mathrm{S}}/n_{\mathrm{S}}^*$ and the relative probe wavelength detuning $\Delta\lambda_{\mathrm{S}}/\lambda_{\mathrm{S}}^*$. We assume both of these quantities to be small compared to unity so that this expression can be expanded into a power series around the point $(\Delta n_{\mathrm{S}} = 0, \Delta\lambda_{\mathrm{S}} = 0)$, yielding the first-order approximation

$$\frac{1 + \Delta n_{\mathrm{S}}/n_{\mathrm{S}}^*}{1 + \Delta\lambda_{\mathrm{S}}/\lambda_{\mathrm{S}}^*} \approx 1 + \frac{\Delta n_{\mathrm{S}}}{n_{\mathrm{S}}^*} - \frac{\Delta\lambda_{\mathrm{S}}}{\lambda_{\mathrm{S}}^*} . \tag{4.31}$$

By inserting Eqs. (4.29), (4.30), and (4.31) into Eq. (4.27), we obtain an expression for the phase detuning $\widetilde{\varphi}$ from resonance, given by

$$\widetilde{\varphi} = \varphi - \bar{\varphi} = 10\pi\left(\frac{n_{\mathrm{S}}\,\lambda_{\mathrm{S}}^*}{n_{\mathrm{S}}^*\,\lambda_{\mathrm{S}}} - 1\right) = 10\pi\left(\frac{\Delta n_{\mathrm{S}}}{n_{\mathrm{S}}^*} - \frac{\Delta\lambda_{\mathrm{S}}}{\lambda_{\mathrm{S}}^*}\right) . \tag{4.32}$$

In the initial state of the microcavity (i.e., for $\Delta t \to -\infty$ or for bin00, respectively), the refractive index change is assumed to be $\Delta n_{\mathrm{S}} = 0$. Moreover, we know that the probe wavelength detuning in the present case is negative ($\Delta\lambda_{\mathrm{S}} = -0.13$ nm). Thus, by inserting this into the above equation, we find that in the initial state, the phase detuning is positive, $\widetilde{\varphi} > 0$. In the graphs where we plot T_{S} vs. Δt (see Fig. 4.27) and T_{S} vs. the bin number (see Fig. 4.28), we observe that the traces pass the maximum of the transmission. Thus, the phase detuning $\widetilde{\varphi}$ decreases and reaches the center position of the resonance curve at $\widetilde{\varphi} = 0$ (see Fig 4.29). After the maximum, the phase detuning becomes negative and decreases further until it reaches the asymptotic value.

As a result of these considerations, we have found an additional piece of information that we can use to solve the ambiguity of Eq. 4.28. Thus, starting with bin00, we can calculate for each delay Δt the phase detunings $\widetilde{\varphi}$ for each bin by following the traces that are illustrated in Fig. 4.28. Before the maximum, we know that $\widetilde{\varphi}$ must be positive, and after the maximum, it has to be negative. Therefore, we distinguish between the two possible versions of Eq. (4.28) as follows

$$\text{before maximum}: \quad \widetilde{\varphi} \approx +\sqrt{\frac{\pi^2}{4\mathcal{F}^2}\left(\frac{T_{\max}}{T_{\mathrm{S}}} - 1\right)} \tag{4.33a}$$

$$\text{after maximum}: \quad \widetilde{\varphi} \approx -\sqrt{\frac{\pi^2}{4\mathcal{F}^2}\left(\frac{T_{\max}}{T_{\mathrm{S}}} - 1\right)} . \tag{4.33b}$$

In some cases, for example in case of the red trace in Fig. 4.28, we cannot precisely determine if the highest T_{S} value of a trace is before or after the maximum. This introduces an uncertainty for $\widetilde{\varphi}$ values around the maximum. Moreover, as is illustrated in Fig. 4.29, the method only works properly if the transmission always rises up to the highest possible value $T_{\max}^* \approx 30$ %, which is not the case in our measurement data because of the two photon absorption (TPA). Therefore, around the zero delay $\Delta t \approx 0$, the calculated phase detunings $\widetilde{\varphi}$ are strongly biased. However, since TPA, as well as the Kerr effect and the free carrier effects, do *not* depend on the pump wavelength λ_{P}, the above-described method still allows for a comparison between the three situations given by $\lambda_{\mathrm{P},1}$, $\lambda_{\mathrm{P},3}$, and $\lambda_{\mathrm{P},5}$ to determine the relative differences (as mentioned above).

Having calculated all the values of the phase detuning $\widetilde{\varphi}$, we can then easily determine the corresponding modification of the refractive index by using again Eq. (4.32), yielding

$$\Delta n_{\mathrm{S}} = n_{\mathrm{S}}^*\left(\frac{\widetilde{\varphi}}{10\pi} + \frac{\Delta\lambda_{\mathrm{S}}}{\lambda_{\mathrm{S}}^*}\right) . \tag{4.34}$$

This has been done by programming several data processing functions that have been used to extract these information from the measurement data. The results are shown in Fig. 4.30 as a function of the probe-pump delay Δt for the different bins (the traces for bin00 are not shown because they are constant at ~ 15 %, which is due to the data processing method). As mentioned above, for delays around $\Delta t = 0$, the values are biased by TPA and, therefore, they are not very meaningful for the analysis. However, by comparing the three graphs for delays $\Delta t > 0$, we clearly see that the modification of the refractive index occurs significantly faster in the bottom graph ($\lambda_{P,5}$), where there cannot be any Stokes wave resonant in the microcavity, than in the other two graphs. Moreover, by looking at the behavior for long delays $\Delta t \gg 0$, we see that the amplitude of the refractive index change is clearly higher in the bottom graph than in the top graph ($\lambda_{P,1}$), while the graph in the middle ($\lambda_{P,3}$) shows an intermediary behavior between the two others. These results confirm the observation that the presence of a (spontaneously generated) resonant Stokes wave has an influence on the behavior of the microcavity. More precisely, the results indicate that if there is a Stokes wave resonant in the microcavity, the refractive index changes significantly slower than in the case where there cannot be any resonant Stokes wave, and the maximum modification of the refractive index for long delays is weaker.

In conclusion, we have developed a method to extract from the measurement data the modification Δn_{S} of the refractive index of the GaAs microcavity experienced by the probe beam. Although this method does *not* provide the physically correct values of the refractive index change around $\Delta t = 0$ (because we cannot remove the influence of the two photon absorption from the measurement data), a comparison between the time dependencies of Δn_S for the three different situations given by $\lambda_{P,1}$, $\lambda_{P,3}$, and $\lambda_{P,5}$ shows major differences. As a result, we find that the presence of a resonant Stokes wave in the microcavity slows down the dynamics with which the modification of the refractive index occurs, and it reduces the maximum refractive index change for long delays. In this sense, the presence of the Stokes wave effectively reduces the influence of the free carrier refraction (FCR).

This result raises the question *how* the Stokes wave modifies the dynamics of the refractive index change. In order to answer this question, it is necessary to include the semiconductor material itself (i.e., GaAs) into our considerations, as is explained in the following.

Slowing down of the electron relaxation through Raman phonons

The refractive index n_S that is experienced by the probe wave is essentially modified by the Kerr effect and the free carrier refraction. At long delays, $\Delta t \gg 0$, we can ignore the Kerr effect because we consider it as an instantaneous effect that only occurs around $\Delta t = 0$. Thus, the long-term behavior of the refractive index is determined by the free carrier density in the central GaAs layer of the microcavity.

Since GaAs is a polar material, the free carriers (we restrict our considerations here to the electrons in the conduction band) interact with the Stokes photons through the vibrations of the crystal lattice, i.e., the phonons. As becomes clear in the following, this interaction is strongly influenced by a coherent population of Raman phonons that is created by amplified spontaneous Raman scattering.
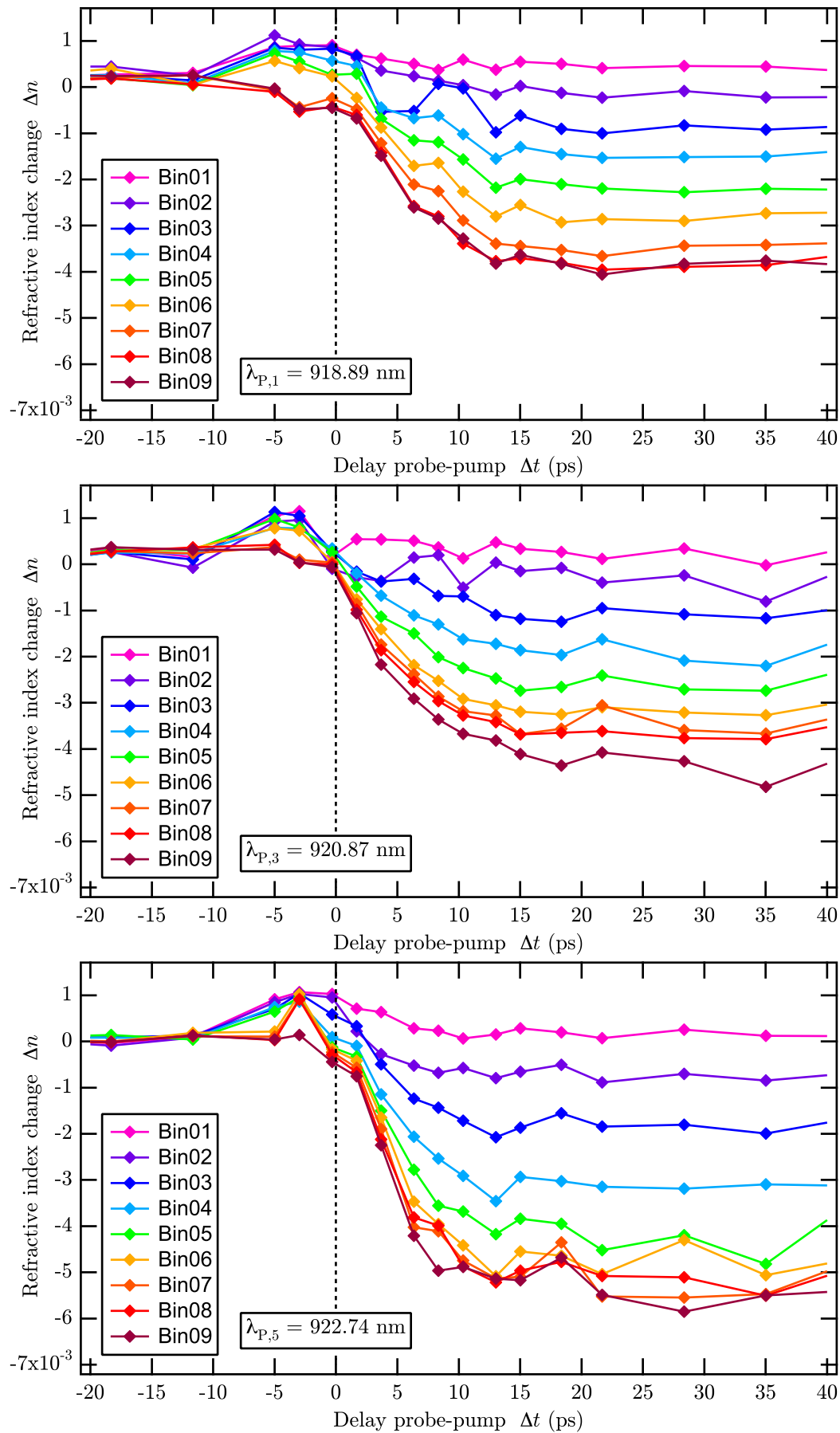
Fig. 4.30. Time dependence of the refractive index change that is caused by the nonlinear effects. The three graphs show the modification Δn of the refractive index as a function of the probe-pump delay Δt for the three different pump wavelengths $\lambda_{P,1}$, $\lambda_{P,3}$, and $\lambda_{P,5}$. The refractive index change has been determined with the method described in the text. Thus, it is only meaningful for $\Delta t > 0$.

In our considerations so far, we have assumed that *all* free carriers, i.e., all electrons that are excited by TPA into the conduction band, contribute to the effect of the free carrier refraction (FCR), i.e., to the FCR-induced phase shift. Since the energies of the pump and the probe photons are not very far from the band gap energy (see discussion in section 4.1), the (cross-)two photon absorption excites the electrons to high energy levels in the conduction band, where they form a so-called hot electron plasma. The hot electrons then undergo a relaxation in the band structure until they reach the band edge, where they contribute to the FCR-induced modification of the refractive index Δn_S. It is important to note that this relaxation usually occurs to a great extent through the creation/excitation of phonons in the semiconductor lattice,which happens on sub-picosecond time scales (i.e., faster than the light pulses used in the experiments).

For each Stokes *photon* that is created in the microcavity by spontaneous Raman scattering, there is also a Raman *phonon* with the frequency Ω_R (i.e., with the energy $\hbar\Omega_R$) and a quasi-wave vector $\vec{K}_R$ (defined by the phase matchning condition for Raman scattering) generated in the central GaAs layer. Moreover, since these phonons are created through the interaction between the pump photons (which are coupled into a well-defined mode of the microcavity given by ω_P and $\vec{k}_P$) and the Stokes photons (which are also coupled into a microcavity mode given by ω_S and $\vec{k}_S$), these phonons can thus be considered as *coherent* because they are generated in phase with the pump and Stokes photons and coupled into a mode defined by $\Omega_R = \omega_P - \omega_S$ and $\vec{K}_R = \vec{k}_P - \vec{k}_S$. Moreover, the Raman scattering process is excited by the pump photons, which are wave packets (pulses) whose linewidth (and duration) is of the same order of magnitude as the linewidth of the Raman resonance (corresponding to the lifetime of the LO phonons in GaAs). Hence, we can expect the presence of a very high density of coherent phonons in the central semiconductor layer of the microcavity. This Raman phonon population can interact with the population of hot electrons in the conduction band during their relaxation process, as is discussed in the following.

Consider an electron which is excited by TPA to a high energy level E_n in the conduction band. It starts its relaxation by the generation of a phonon, thereby falling down to the energy level E_{n-1}. From there, the electron falls to the level E_{n-2} through the excitation of another phonon. In the "normal" case, where the electrons interact with an ensemble of *in*coherent phonons that are distributed over a wide range of different modes, this continues until the electron reaches the band edge of the conduction band. However, in the present case, where we assume the presence of a coherent Raman phonon population in a single, well-defined mode, this relaxation of the hot electrons can be significantly modified.

We suppose that the high density of coherent phonons influences the evolution of the electron-phonon system. We imagine that in the presence of such a high coherent phonon density, it is possible that the interaction between electrons and phonons totally perturbs the way it reaches its thermodynamic equilibrium. This perturbation is reached through successive exchanges of energy between the electrons and the phonons. More precisely, the relaxation of the electrons can continuously re-excite/re-create the Raman phonons, which then can be re-absorbed by the electrons, which, in turn, can then again decay under the creation of a Raman phonon, and so on. As a result, the electrons and phonons undergo a cyclic re-creation/re-excitation process that considerably slows down the thermalization of the hot electrons towards the band edge. At the same time, the cyclic re-excitation causes the lifetime of the Raman phonons in the well-defined mode to be be much longer than the typical lifetimes of LO phonons in GaAs (i.e., without the high coherent phonon density).

We make the hypothesis that the differences in the dynamics of the refractive index change can be explained with a simple model of the electron relaxation in the conduction band of the central GaAs layer of the microcavity. The presence of a highly populated Raman phonon mode that is coherently excited through enhanced amplified spontaneous Raman scattering in the microcavity can lead to a re-exitation of the electrons to higher energy levels. Although these re-excitations do not completely prevent the electrons from reaching the band edge of the conduction band, where they contribute to the free carrier refraction (FCR), they can significantly slow down the relaxation of the hot electron plasma. This interaction between electrons and coherent phonons might explain why the measurement series for $\lambda_{P,1}$ and $\lambda_{P,3}$ show effectively a weaker influence of the FCR, while the data for $\lambda_{P,5}$ correspond rather well to the predictions of the analytical model presented in section 4.2.

4.5.3 Confirmation of the phonon-electron hypothesis

Apart from the experiments presented in section 4.5.1, where the photodiodes 3 and 4 were highly sensitive avalanche photodiodes (Hamamasu C5460) with a low noise level, I have also carried out several nonlinear pump-probe measurement series with a preliminary version of the experimental setup, which uses the standard silicon photodiodes (Hamamasu S1721) as the photodiodes 3 and 4, as has been described in section 4.3.3 (see page 110). Because of the poor signal-to-noise ratio of the standard photodiodes, we cannot force the linear fits in the $PD4$-$PD3$ graphs through the origin. Therefore, it has been necessary to acquire much more data points, leading to minimum of about 300 data sets per bin (i.e., per $PD4$-$PD3$ graph). Moreover, as a result of the high noise level, the determination of the slopes $M_{4,3}$ do never yield values close to zero. Thus, especially for the highest pump intensities (i.e., bin numbers), the probe transmission T_S is systematically overestimated, i.e., it never falls to values below ~ 10 % although the corresponding $PD4$-$PD3$ graphs clearly indicate that many of the data points would yield an almost zero slope.

In this preliminary version of the experimental setup, the four BBO crystals in the two optical parametric generators are different from the ones used for the experiments presented in section 4.5.1. They are older and provide a poorer efficiency for the generation of the pump and the probe beam, probably because of less good surface coatings and the less developed crystal growth technologies at the time when they were fabricated. As a result, they require a much better stability of the Nd:YAG pump laser and the frequency doubling and tripling stages, which makes the experiments more sensitive on external factors such as the air conditioning in the laboratory etc. Thus, in terms of experimental practicability, these old BBO crystals impose some unnecessary constraints, which is the reason why they have been replaced by new and more efficient crystals. However, the spectra of the pump and the probe beam generated with the old crystals seemed to be slightly better (i.e., closer to a Gaussian profile), and they were more reproducible from one pulse to the next, which can be expressed by standard deviations of the wavelength measurements (with the monochromator) of about 0.04 nm (instead of 0.06 nm with the new crystals).

Four different measurement series of T_S as a function of the probe-pump delay Δt have been carried out for four different pump wavelengths λ_P. As in case of the above-presented measurements, the probe wavelength is set to $\lambda_S = 946.33$ nn, and three of the four pump wavelengths have been chosen exactly at the Raman resonance, $\lambda_P = 920.88$ nm, and slightly off Raman resonance to both sides, i.e., $\lambda_P = 920.73$ nm

and $\lambda_{\mathrm{P}} = 921.03$ nm. The fourth pump wavelength, which is $\lambda_{\mathrm{P}} = 922.65$ nm, corresponds to the case where there cannot be any Stokes wave resonant in the microcavity. The resulting time dependencies of the probe transmission T_{S} for the four different measurement series are depicted in Fig. 4.31.

The bottom graph, which corresponds to the pump wavelength $\lambda_{\mathrm{P},5}$ in section 4.5.1, looks fairly similar to the respective graphs in Figs. 4.25 and 4.27 and, thus, also to the simulation results. The curves for the strongest intensities are grouped together at low transmission and remain unchanged for higher delays Δt. However, as can be clearly seen, the two graphs slightly off Raman resonance do not show this superposition of the high-intensity curves. It seems that in these two cases, the modification of the refractive index of the semiconductor (GaAs) is less efficient, even for high pump intensities. The graph where the pump wavelength is exactly at Raman resonance shows a *completely different* behavior. Obviously, the curves of all bins rise up to the maximum transmission, but no curve shows a significant drop of the transmission T_{S}. So, according to the model of the electron relaxation presented in section 4.5.2, the measurement series presented here indicate an extremely slow relaxation of the hot electrons to the band edge.

To illustrate the differences between the four different measurement series (i.e., pump wavelengths), we can rearrange the measurement data and show one graph per bin (instead of one graph per pump wavelength), where each graph contains the curves for all four wavelengths, as depicted in Fig. 4.32. Here, it becomes even clearer how the Raman scattering affects the refractive index change of the microcavity. The top graph shows the time dependence of the probe transmission T_{S} for a moderate pump intensity (bin04). As can be seen from the graph, all four traces, including the red trace (for which there cannot be any Stokes wave resonant in the microcavity), rise to the maximum and stay there, also for long delays Δt. However, when looking at the three other graphs, which correspond to the three highest pump intensities (i.e., bins), we see very clearly how the red trace shows the expected behavior (i.e., drops to low transmission values), whereas the two traces slightly off Raman resonance (i.e., the light blue trace and the yellow trace) do not drop as much as the red trace. Their minimum transmission depends on the bin number (i.e., on the pump intensity), and in bin09, they reach almost the same low level as the measurement series far off Raman resonance. As already mentioned above, since all the curves remain on the same transmission value even for long probe-pump delays Δt, the reason for the observed behavior must be related to the free carrier refraction (FCR). Since the FCR is apparently less strong than our simulations would predict, we confirm with these measurements that there is some other physical effect which reduces the number of free carriers that participate in the modification of the refractive index. This effect is even stronger in the situation exactly *at Raman resonance*, represented by the green trace, which stays a the maximum transmission for all delays $\Delta t > 0$. Here, the FCR is so weak that even for the highest pump intensities, the microcavity does not "roll over" the maximum of the resonance curve.

The experimental results that have been obtained with a preliminary version of the experimental setup, using other detectors and a slightly different light source than in case of the previously presented measurements, confirm the hypothesis of the modified electron relaxation that we have developed in section 4.5.2. These experiments show much more clearly the difference between the case *at* Raman resonance and *off* Raman resonance and even illustrate very well the transition between these two situations when the pump wavelength is only *slightly off* Raman resonance.
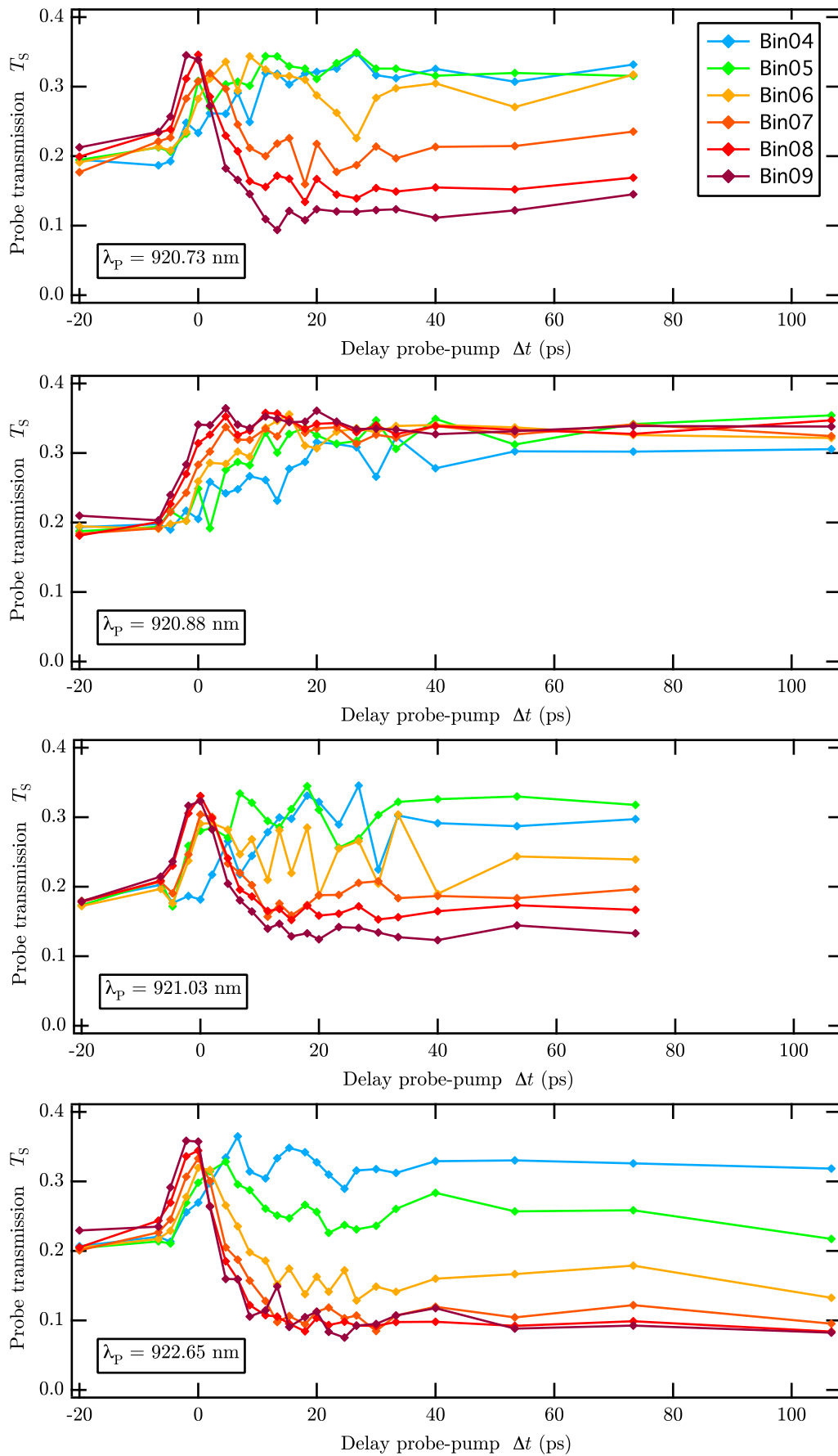
Fig. 4.31. Pump-probe measurement series for $\lambda_S = 946.33$ nm with the preliminary experimental setup. Time dependence of the probe transmission T_S of the semiconductor microcavity for different pump intensities $I_{P,0}$, represented by the different bins (bin00 ... bin09) as the colored traces.
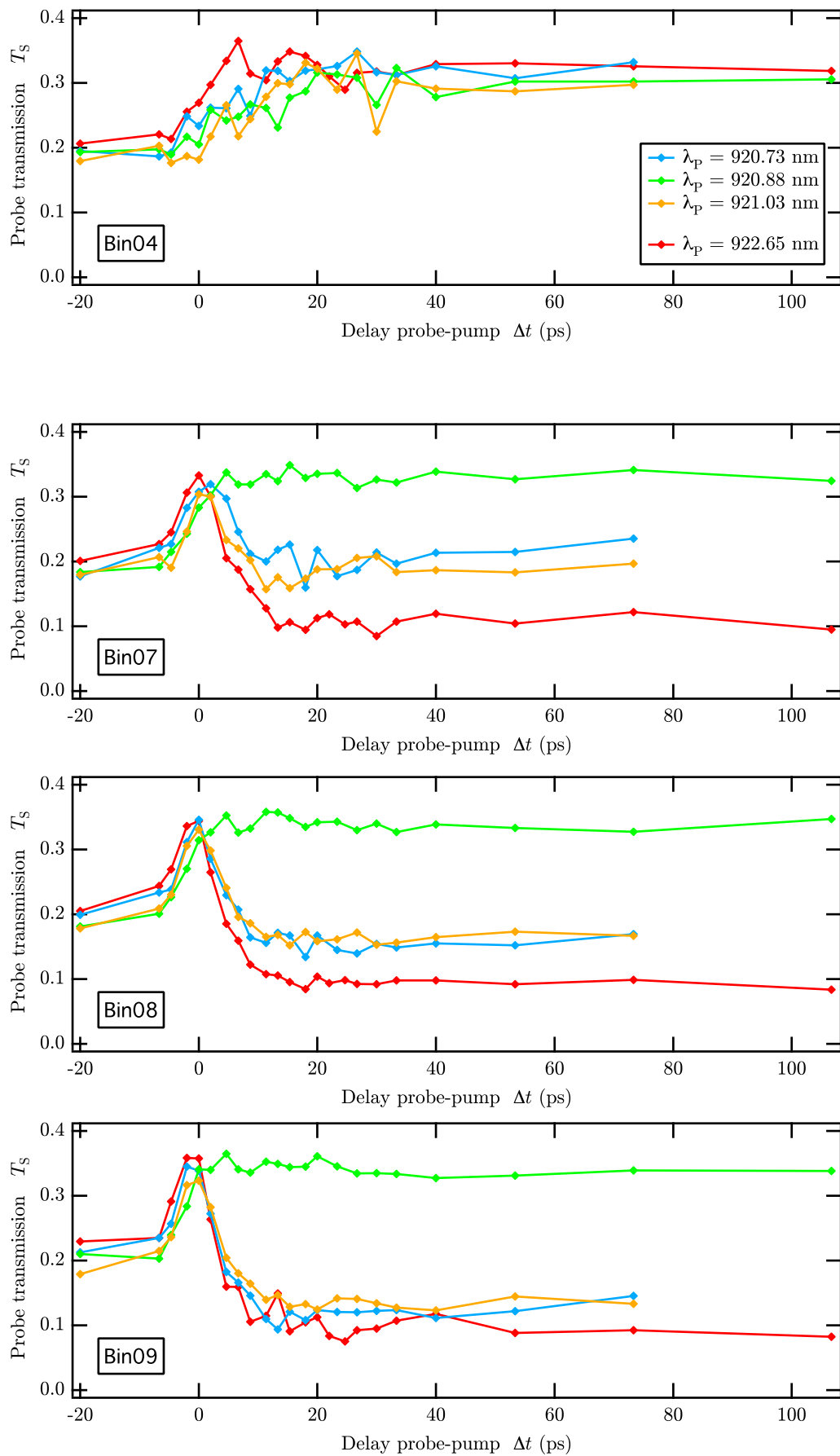
Fig. 4.32. Pump-probe measurement series for $\lambda_S = 946.33$ nm with the preliminary experimental setup. Time dependence of the probe transmission T_S of the semiconductor microcavity for different pump wavelengths λ_P as the colored traces. Rearrangement of the data already shown in Fig. 4.31.

By comparing the experimental results shown in section 4.5.1 to the measurement series presented here, the question arises why we do *not* observe the same behavior in both cases. More precisely, given that all the parameters taken into account by our analytical model are equal in the two cases, it is unclear why we do *not* see such a clear difference between the situation *at* and *off* Raman resonance when using the technically better experimental setup (i.e., in section 4.5.1). Although there is no simple answer to this question, we can see three possible reasons that might explain some differences in the results.

First, it should be noted that the experimental setup illustrated in Fig. 4.15 is only a schematic representation indicating in which order all the optical and mechanical components have been arranged. Although this illustration applies to both versions of the experimental setup (i.e., the setup for the measurements in section 4.5.1 *and* the one for the experiments shown here), the beam preparation and superposition of the final version have been completely rebuild in order to integrate the avalanche photodiodes etc. Also, in order to optimize several practical aspects of the experimental procedure, the setup has become more complex in the final version, including some alignment aids and check points to monitor the pump intensity as well as the coupling into the polarization maintaing fiber etc. While great attention has been paid to make sure that the two setups provide comparable results, it cannot be said with certainty that all the important parameters are exactly identical. So, it is, in principle, possible that a tiny detail of the experimental setup is different in the two versions, and that this detail causes the differences in the results.

Second, as mentioned above, the spectra of the pump and probe beam were more stable in the preliminary version of the setup. This might explain why we see a clear difference between the three series around the Raman resonance (i.e., slightly off Raman resonance towards shorter wavelengths, exactly at Raman resonance, and slightly off resonance to the other side) with the preliminary setup, while in case of the final version, the larger spread of the pump wavelengths blurs these differences and makes all three measurements look rather similar.

Third, it is possible that in the experiments presented in section 4.5.1, we have simply used a pump beam whose intensity is too strong, so that the resolution of the binning is not fine enough to exhibit the clear differences that we see in the measurements presented here. Since in the latter case, the pump intensity has not been properly calibrated, we cannot precisely check if this hypothesis is true or not. By looking at the graph far off resonance (i.e., the bottom graph in Fig. 4.32), we see that only three traces group together at low transmission, while in the respective graph of the measurements with the avalanche photodiodes (i.e., the bottom graph in Fig. 4.31), there are at least four traces. This might be an indicator for a slightly different maximum intensity (corresponding to bin09), but we can assume the difference to be small.

So, despite the above reasons that could explain some of the differences we observe, the question why we do *not* see the behavior of the green trace (in Fig. 4.32) in the results presented in section 4.5.1 remains open at this point and might be the subject of further studies.

4.6 Experimental characterization of the Raman phonons

In the previous sections, we have presented a hypothesis about the interaction between the hot electron plasma and the Raman phonons in the central GaAs layer of the microcavity. The key element of this hypothesis is the existence of a strongly excited phonon mode. The coherent population of Raman phonons in this phonon

mode is created through amplified *spontaneous* Raman scattering, and it is, thus, *independent* of the presence of the probe beam in the microcavity.

Although this hypothesis seems to explain the experimental observations very well, the pump-probe measurements of the sample transmission T_S can only be considered as an *indirect* proof of the hypothesis. Therefore, it is desirable to find a way to prove the existence of this highly populated Raman phonon mode *directly*. For this purpose, we have developed a new experiment that uses a different geometry. In the following, we describe the idea of this new experiment.

As a starting point of our considerations, we assume that there is a highly excited population of Raman phonons with the energy $\hbar\Omega_R$. The phonons are created through spontaneous Raman scattering by a strong pump wave of an angular frequency ω_P, which also generates a Stokes wave with an angular frequency ω_S at normal incidence in the microcavity. We now consider another monochromatic electromagnetic wave (laser beam) with an angular frequency ω_L that is incident upon the sample. Since the phonon mode is assumed to be highly populated, this wave can interact with the phonons in another spontaneous Raman scattering process by creating an *Anti-Stokes* wave with the angular frequency ω_{AS}. In summary, this leads to a cascade of two scattering processes, which is illustrated in the energy diagram that is shown in Fig. 4.33. Its energy balance can be expressed in the form

$$\omega_P = \omega_S + \Omega_R \qquad \text{and} \qquad \omega_L + \Omega_R = \omega_{AS} .$$

4.6.1 Stokes scattering process

In the first Raman scattering process (Stokes scattering), the conservation of energy and the conservation of the (quasi)-momentum of the interacting electromagnetic waves and the phonon mode can be expressed in the form

$$\frac{1}{\lambda_P} = \frac{1}{\lambda_S} + \bar{\nu}_R \tag{4.35a}$$

$$\vec{k}_P = \vec{k}_S + \vec{K}_R , \tag{4.35b}$$

where $\bar{\nu}_R = 292 \text{ cm}^{-1}$ is the Raman shift of GaAs at room temperature and $\vec{K}_R$ is the quasi wave vector of the phonon mode. As in the experiments presented in the previous sections, we assume that the pump beam is incident upon the sample in the x-z plane and the Stokes wave is at normal incidence (i.e., parallel to the z direction). In a component-wise notation, this is described by

$$\vec{k}_P = \begin{pmatrix} k_P \sin\vartheta_P \\ 0 \\ k_P \cos\vartheta_P \end{pmatrix} \qquad \vec{k}_S = \begin{pmatrix} 0 \\ 0 \\ k_S \end{pmatrix} \qquad \vec{K}_R = \begin{pmatrix} K_{R,x} \\ K_{R,y} \\ K_{R,z} \end{pmatrix} , \tag{4.36}$$

Fig. 4.33. Energy diagram illustrating the spontaneous Anti-Stokes scattering of an incident light wave of an angular frequency ω_L with a highly populated phonon mode with a Raman frequency Ω_R. The latter is populated by spontaneous Raman scattering of an incident pump wave with an angular frequency ω_P. The Stokes wave of the initial spontaneous Raman scattering has an angular frequency ω_S.
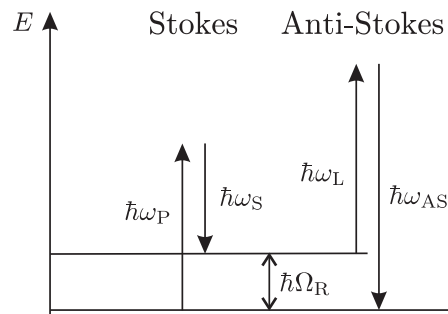
where ϑ_P is the angle of incidence of the pump beam. By inserting this into Eq. (4.35b), we obtain

$$K_{R,x} = k_P \sin \vartheta_P \tag{4.37a}$$
$$K_{R,y} = 0 \tag{4.37b}$$
$$K_{R,z} = k_P \cos \vartheta_P - k_S . \tag{4.37c}$$

The wave vectors of both pump and Stokes wave are supposed to be resonant in the microcavity, which imposes two further constraints on the wave vectors, given by

$$\vec{k}_P \cdot \hat{z}\, L = m\,\pi , \tag{4.38a}$$
$$\vec{k}_S \cdot \hat{z}\, L = m\,\pi , \tag{4.38b}$$

where $\hat{z} = (0,0,1)$ is the unit vector in z direction, m is the order of resonance (here $m = 10$), and $L = 5\,\lambda_S/n_S$ is the resonator length (i.e., the thickness of the central GaAs layer). By inserting the component-wise notation of $\vec{k}_P$ given in Eq. (4.36) into Eq. (4.38a), we obtain

$$\begin{pmatrix} k_P \sin \vartheta_P \\ 0 \\ k_P \cos \vartheta_P \end{pmatrix} \cdot \begin{pmatrix} 0 \\ 0 \\ 1 \end{pmatrix} L = L\, k_P \cos \vartheta_P = m\,\pi = k_S\, L , \tag{4.39}$$

where, in the last step, Eq. (4.38b) has been used. The above equation means that

$$k_S = k_P \cos \vartheta_P , \tag{4.40}$$

which we insert into Eq. (4.37c), yielding the result

$$K_{R,z} = 0 . \tag{4.41}$$

Thus, according to Eqs. (4.37b) and (4.41), the quasi-wave vector $\vec{K}_R$ of the Raman phonons is parallel to the central GaAs layer of the microcavity, i.e., $\vec{K}_R = (K_R, 0, 0)$ with $K_R = k_P \sin \vartheta_P$. Moreover, by inserting $k_P = 2\pi\, n_P/\lambda_P$ and $k_S = 2\pi\, n_S/\lambda_S$ into Eq. (4.40) and by assuming that $n_P \approx n_S$, we find the relationship

$$\lambda_P = \lambda_S \cos \vartheta_P \quad \Longrightarrow \quad \vartheta_P = \arccos\left(\frac{\lambda_P}{\lambda_S} \right) . \tag{4.42}$$

As a result of all the above considerations, we have fully determined all relevant parameters of the first spontaneous Raman scattering process. In the order of their determination, these are

$$\begin{array}{ll} \lambda_S & \text{given by Eq. (4.38b)} \\ \lambda_P & \text{given by Eq. (4.35a)} \\ \vartheta_P & \text{given by Eq. (4.42)} \\ K_{R,x} & \text{given by Eq. (4.37a)} \\ K_{R,y} & \text{given by Eq. (4.37b)} \\ K_{R,z} & \text{given by Eq. (4.41)} . \end{array}$$

With the above equations, the phonon mode of the Raman phonons is fully defined in terms of the experimentally accessible parameters λ_P, λ_S, and ϑ_P.

4.6.2 Anti-Stokes scattering process

With the information about $\Omega_R = 2\pi\,\bar{\nu}_R$ and $\vec{K}_R$, we now consider the second (Anti-Stokes) Raman scattering process. The conservation of energy and the conservation of the (quasi)-momentum in the Anti-Stokes scattering process can be expressed in the form

$$\frac{1}{\lambda_L} + \bar{\nu}_R \;=\; \frac{1}{\lambda_{AS}} \tag{4.43a}$$

$$\vec{k}_L + \vec{K}_R \;=\; \vec{k}_{AS} \,. \tag{4.43b}$$

As in the previous case, both waves should be resonant in the microcavity, which is expressed by

$$\vec{k}_L \cdot \hat{z}\, L \;=\; \vec{k}_{AS} \cdot \hat{z}\, L \;=\; k_S\, L \,, \tag{4.44}$$

where the last step simply reuses the resonance condition of the Stokes wave at normal incidence given by Eq. (4.38b). By inserting $k_L = 2\pi\,n_P/\lambda_L$ and $k_{AS} = 2\pi\,n_{AS}/\lambda_{AS}$ into the above equation and by assuming $n_L \approx n_{AS} \approx n_S$, we obtain

$$\frac{1}{\lambda_L}\cos\vartheta_L \;=\; \frac{1}{\lambda_{AS}}\cos\vartheta_{AS} \;=\; \frac{1}{\lambda_S} \,. \tag{4.45}$$

For the following considerations, we use ϑ_L as an independent parameter. Thus, according to Eq. (4.45), the wavelength λ_L of the second laser beam is given by

$$\lambda_L \;=\; \lambda_S \cos\vartheta_L \tag{4.46}$$

Then, the wavelength of the Anti-Stokes wave that is generated through spontaneous Raman scattering is given by Eq. (4.43a) as

$$\lambda_{AS} \;=\; \left(\frac{1}{\lambda_L} + \bar{\nu}_R\right)^{-1} . \tag{4.47}$$

By using again Eq. (4.45), we determine the angle ϑ_{AS} as

$$\vartheta_{AS} \;=\; \arccos\left(\frac{\lambda_{AS}}{\lambda_S}\right) \tag{4.48}$$

To summarize the above considerations, all experimentally accessible parameters of the Anti-Stokes scattering process depend on the angle ϑ_L. These are

$$\begin{aligned}
\lambda_L & \quad \text{given by Eq. (4.46)} \\
\lambda_{AS} & \quad \text{given by Eq. (4.47)} \\
\vartheta_{AS} & \quad \text{given by Eq. (4.48)} \,.
\end{aligned}$$

In principle, the laser beam with the wave vector $\vec{k}_L$ is not restricted to the x-z plane. Therefore, we can express it in spherical coordinates $\vec{k}_L = (k_L, \vartheta_L, \varphi_L)$ with, in general, a non-zero angle φ_L. Consequently, this also applies to the wave vector of the Anti-Stokes wave, which can thus be expressed as $\vec{k}_{AS} = (k_{AS}, \vartheta_{AS}, \varphi_{AS})$. Both wave vectors are related through the Raman phonon mode according to Eq. (4.43b), as is graphically illustrated Fig. 4.34.

In order to find explicit expressions for the two angles φ_L and φ_{AS}, we consider the projections of Eq. (4.43b) to the x axis and the y axis, which yields

$$k_{AS}\sin\vartheta_{AS}\cos\varphi_{AS} \;=\; k_L\sin\vartheta_L\cos\varphi_L + K_{R,x} \tag{4.49a}$$

$$k_{AS}\sin\vartheta_{AS}\sin\varphi_{AS} \;=\; k_L\sin\vartheta_L\sin\varphi_L + 0 \,. \tag{4.49b}$$
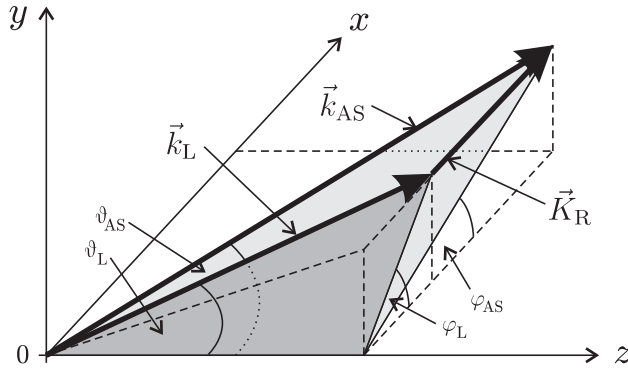
Fig. 4.34. Illustration of the geometric relationships between the wave vectors of the laser beam $\vec{k}_\mathrm{L}$, the Anti-Stokes wave $\vec{k}_\mathrm{AS}$, and the Raman phonons $\vec{K}_\mathrm{R}$. The latter are generated through amplified spontaneous Raman scattering of the pump wave. The graph also shows the spherical coordinates $(\vartheta_\mathrm{L}, \varphi_\mathrm{L})$ and $(\vartheta_\mathrm{AS}, \varphi_\mathrm{AS})$ of the involved wave vectors.

This is a system of two equations with two variables (φ_L and φ_AS). By inserting the expressions for the wave vectors k_L and k_AS, we find the solutions

$$\varphi_\mathrm{L} = \pm \arccos \left[\frac{1}{2} \frac{\lambda_\mathrm{P} \sin \vartheta_\mathrm{L}}{\lambda_\mathrm{L} \sin \vartheta_\mathrm{P}} \left(\left(\frac{\lambda_\mathrm{L} \sin \vartheta_\mathrm{AS}}{\lambda_\mathrm{AS} \sin \vartheta_\mathrm{L}} \right)^2 - \left(\frac{\lambda_\mathrm{L} \sin \vartheta_\mathrm{P}}{\lambda_\mathrm{P} \sin \vartheta_\mathrm{L}} \right)^2 - 1 \right) \right] \quad (4.50)$$

$$\varphi_\mathrm{AS} = \arcsin \left[\frac{\lambda_\mathrm{AS} \sin \vartheta_\mathrm{L}}{\lambda_\mathrm{L} \sin \vartheta_\mathrm{AS}} \sin \varphi_\mathrm{L} \right] , \quad (4.51)$$

which depend only on the previously determined wavelengths λ_P, λ_L, λ_AS and on the angles ϑ_P, ϑ_L, ϑ_AS.

In the above derivations, we have considered ϑ_L as an independent parameter that determines all the other experimentally relevant parameters. For a given value of ϑ_L, we can calculate λ_L and φ_L (laser beam) and λ_AS, ϑ_AS, and φ_AS (Anti-Stokes wave) according to Eqs. (4.46), (4.47), (4.48), (4.50), and (4.51). From an experimental point of view, it is more interesting to consider the *external* angles of incidence (or propagation) ϑ'_L and ϑ'_AS instead of the *internal* angles ϑ_L and ϑ_AS. The external angles can be easily calculated with the help of SNELL's law. Figure 4.35 shows the dependencies of all the above-mentioned parameters on the *external* angle of incidence ϑ'_L.

4.6.3 Experimental setup of the Anti-Stokes experiment

As the above two sections have shown, we should be able to demonstrate experimentally the existence of a highly populated Raman phonon mode in the central GaAs layer of the microcavity through a second Raman scattering process. The idea behind this is the following: if there is such a strong population of coherent Raman phonons, this should significantly increase the probability of the Anti-Stokes scattering process. In other words, there should be a strong difference in the Anti-Stokes scattering efficiency between the two cases *with* and *without* the strong Raman phonon population.

In order to measure the intensity of the Anti-Stokes wave, I have designed a real experimental setup that uses the freely tunable picosecond light source which has been described in detail in section 4.3.1. The pump beam of the light source is used in exactly the same manner as in the pump-probe experiments presented in section 4.5 (this part of the experimental setup is identical to the previous pump-probe measurements). The pump beam is incident upon the sample at an angle of incidence ϑ_P. If the angle of incidence allows for a Stokes wave that is resonant in the microcavity, we assume that the Raman scattering process generates the highly populated Raman phonon mode in the central GaAs layer.
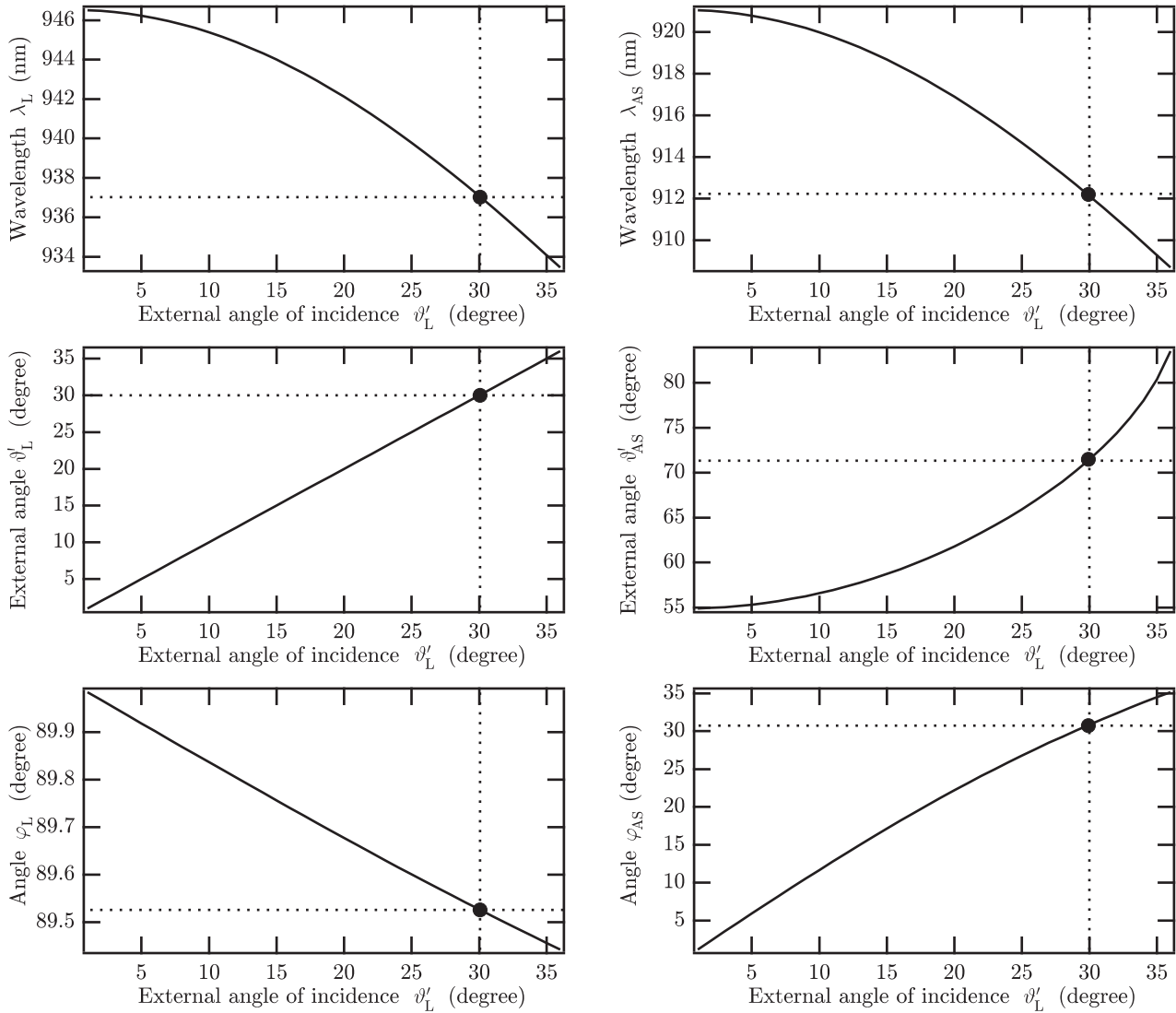
Fig. 4.35. Calculated dependencies of the experimental parameters of the Anti-Stokes scattering experiment on the external angle of incidence ϑ_L' of the laser beam that is used to demonstrate the existence of the strongly excited Raman phonon mode in the central GaAs layer of the microcavity.

The other beam of the picosecond light source (i.e., the so-called "probe" beam) is now used as the laser beam that initiates the Anti-Stokes scattering. It should be noted that *here*, the probe beam is used in a completely different way compared to the pump-probe measurements in section 4.5, where it was used with the aim to induce *stimulated* Raman scattering (i.e., where it was chosen to be almost identical to the Stokes wave). Since the intensity of the Anti-Stokes wave is expected to be very weak compared to the pump beam, it is, from an experimental point of view, desirable to separate the Anti-Stokes beam geometrically from the x-z plane. Therefore, I have chosen an angle $\vartheta_L = 30°$ for the experimental setup. As has been shown in section 4.6.2, this choice of ϑ_L determines all the other experimental parameters. The resulting values are also shown as the thick markers in Fig. 4.35.

According to these results, I have built a complete experimental setup, including the preparation of pump and probe beam, the positioning of the required photodiodes to measure the intensities of the pump, Stokes, probe, and Anti-Stokes beams, as well as a sophisticated method to measure and set the angles ϑ_L, ϑ_{AS}, φ_L, and φ_{AS}. By varying the time delay Δt between the probe pules and the pump pulses, it should be possible to show the existence of the strong Raman phonon population, as well

as its prolonged lifetime. Both these results would strengthen the interpretation of the pump-probe measurements presented in section 4.5.

However, because of time constraints, I have not had the time to practically carry out the measurements to verify (or falsify) the hypothesis of the highly populated Raman phonon mode. This will hopefully be done by future PhD students in the group Manolia at the Laboratoire Charles Fabry de l'Institut d'Optique.

4.7 Conclusion and outlook

The main objective of the work presented in this chapter has been to study the interplay between several nonlinear optical effects—in particular stimulated Raman scattering (SRS), (cross-)two photon absorption (TPA), the (cross-)Kerr effect, and the free carrier refraction (FCR)—under the influence of strong light localization in a semiconductor material. For this purpose, I have developed an analytical model that describes the influence of these effects (with a focus on SRS) on the transmission of a semiconductor microcavity. Moreover, I have built a highly complex experimental setup for pump-probe measurements working with a 10-Hz repetition rate in order to track each pair of pump and probe pulses individually. The determination of the microcavity transmission T_S for the probe beam (and T_P for the pump beam) has been done by using two pairs of photodiodes, measuring the incident and the transmitted optical power of both beams. In order to extract the transmission values from the raw data, I have further developed a data processing method that traces the relationship between the transmitted power and the incident power and calibrates, so to speak, this relationship with a reference measurement without the microcavity.

I have carried out several series of nonlinear pump-probe measurements of the transmission of a planar GaAs microcavity for different pump wavelengths. Conversely to the predictions of several simulations that I have calculated with the help of the analytical model, these measurements do *not* show the expected signature of stimulated Raman scattering, which corresponds to a clearly visible increase of the sample transmission for probe-pump delays around $\Delta t = 0$. As the key result of the experiments, I have presented a very promising hypothesis that explains the observed behavior with a perturbation of the electron relaxation dynamics in the conduction band of the semiconductor, which is due to a cyclic re-excitation process between the TPA-generated hot electron plasma and a highly populated, well-defined phonon mode of the polar semiconductor crystal lattice (GaAs). As a side effect of this coherent electron-phonon interaction, the lifetime of the Raman phonons might be significantly prolonged. This hypothesis has been confirmed by a number of preliminary measurement series that even demonstrate the gradual onset of the modification of the electron relaxation for increasing pump intensity and that also show very clearly a wavelength dependence corresponding to the shape of the Raman resonance. It is worth noting here that this unexpected observation has not been the initial purpose of the experiments, but it opens the route towards a whole new and exciting field of physics, which clearly needs further experimental and theoretical investigation.

The results of the pump-probe experiments have shown that, even when setting the initial pump wavelength λ_P in such a way that we compensate for the nonlinear phase shift induced by the Kerr effect and FCR, we do *not* observe the signature of stimulated Raman scattering (SRS) that we would expect according to the analytical model. One possible explanation for this is the fact that SRS depends critically on the exact value of the pump frequency ω_P (more precisely on the difference Ω between the pump and the probe frequency), as mentioned in section 4.2.2. It should be

noted that in the whole discussion of the simulation results and the experiments, we have only considered the intensity and the phase of the probe (Stokes) wave in the microcavity. However, to understand the absence of the SRS signature, we also have to take into account the instantaneous frequencies ω_S and ω_P of the probe and the pump wave. The instantaneous frequency ω is, in general, given by the time derivative of the instantaneous phase φ, which is composed of the Fabry-Perot phase φ_{FP} and the time-dependent nonlinear phase shift $\Delta\varphi_{NL}$, so that we obtain

$$\omega(t) = \frac{d}{dt}\Big(\varphi_{FP} + \Delta\varphi_{NL}(t)\Big) = \frac{d}{dt}\Big(\varphi_{FP}\Big) + \frac{d}{dt}\Big(\Delta\varphi_{NL}(t)\Big) = \frac{d}{dt}\Big(\Delta\varphi_{NL}(t)\Big) .$$

The nonlinear phase shift $\Delta\varphi_{NL}$ is essentially caused by the Kerr phase shift and the free carrier phase shift, where the former is proportional to the pump intensity (Gaussian time dependence), and the latter is given by the free carrier density (which rises steeply but decreases very slowly). Without going into the numbers, it is clear from the above equation that both of these effects modify the instantaneous frequency. They do, however, not only change the frequeny ω_S of the probe beam, but also the pump frequency ω_P. As we have demonstrated in Eqs. (2.62) and (2.65) in section 2.3.1, the *auto*-induced Kerr phase shift for the pump wave is only half as strong as the *cross*-Kerr phase shift for the probe wave. This means that for delays around $\Delta t = 0$, the instantaneous frequencies of pump and probe wave are affected differently, and thus, they are *not* at Raman resonance (i.e., $\omega_P - \omega_S \neq \Omega_R$) although the initial pump wavelength detuning $\Delta\lambda_P$ might be such that it perfectly compensates the Kerr- and FCR-induced nonlinear phase shift. This is the reason why we do *not* observe the strong enhancement of the probe transmission T_S in the experiments. One might argue that it should be possible to compensate for this effect by a good choice of the initial pump wavelength. That is true, but since the Kerr and FCR-induced nonlinear phase shifts depend also on the intensity, this intentional detuning from the Raman resonance is also intensity dependent, which makes it effectively impossible to find a combination of wavelenghts λ_S and λ_P for which we can be sure to observe a strong Raman signature.

In order to see exactly how the intensity, the phase, and also the instantaneous frequency of the pump and the probe wave evolve in time (especially for delays around $\Delta t = 0$) and how their time dependence affects the different nonlinear effects, it would be necessary to develop a *transient* model of the nonlinear interactions in the semiconductor microcavity. Since such a model could not any longer be solved analytically, it would require to perform numerical simulations. Although this has been beyond the scope of the present work, WONG *et al.* have published such numerical simulations [100] for which they assume a fixed value of γ_R and a spectral shape of the Raman resonance that is independent of the pump spectrum. However, as I have demonstrated in chapter 3, the self phase modulation of the pump wave strongly modifies the lineshape of the Raman gain and, thus, also the *effective* Raman gain experienced by the probe beam. Therefore, this modification and its detrimental effect on the effective Raman gain should be taken into account by future simulations of the transient behavior of the microcavity transmission.

It should be noted that the gain coefficient used for the simulations in section 4.2.3 is expressed as

$$G \approx (\gamma_R - 2\beta_{TPA}) I_P(t + \Delta t) ,$$

where $(\gamma_R - 2\beta_{TPA})$ is given by the material-dependent parameters γ_R and β_{TPA}. Using the values $\gamma_R = 50$ cm/GW and $\beta_{TPA} = 23$ cm/GW for gallium arsenide (GaAs) at Raman resonance (i.e., for $\Delta = 0$, which means $\gamma_R = \bar{\gamma}_R$), we obtain $G \approx 4$ cm/GW. As we have seen in chapter 3, the two-photon absorption

coefficient β_{TPA} of silicon (Si) is only of the order of 1 cm/GW. Therefore, it would be possible to achieve higher effective gains by choosing other materials, such as silicon (Si), for which we have determined in the previous chapter a value of $G = (\gamma_{\mathrm{R}} - 2\,\beta_{\mathrm{TPA}}) \approx 6.3$ cm/GW (see Eqn. (3.54)). Thus, in order to realize a doubly resonant semiconductor microcavity with the only objective of enhancing the effect of stimulated Raman scattering (or Raman amplification, respectively), it would be more appropriate to use Si than to take GaAs.

Actually, this becomes even more true when we look again at our estimation of the Raman gain coefficient of GaAs. The only data that can be found in the literature come from an indirect determination of the Raman gain that is based on a measurement of the of Stokes wave generated by amplified spontaneous Raman scattering in a photonic crystal waveguide in GaAs [111], yielding a value of 6.9 cm/GW for a Stokes wavelength of 1300 nm. Since the wavelengths used for the experiments are between 900 and 950 nm, it is necessary to extrapolate the Raman gain coefficient for these wavelengths by taking into account the frequency dependence of $\bar{\gamma}_{\mathrm{R}}$, leading to a value of about 10 cm/GW. Obviously, this value is much smaller than our estimation of 50 cm/GW that we have used throughout this chapter, and by subtracting $2\,\beta_{\mathrm{TPA}}$, we obtain an effective gain for the Stokes wave of $G \approx -36$ cm/GW, which corresponds to a strong absorption (instead of an amplification). So, another reason why we have *not* observed an increase of the probe transmission T_{S} in the experiments may be the fact that we have largely overestimated the Raman gain coefficient $\bar{\gamma}_{\mathrm{R}}$ of GaAs.

Nevertheless, as the pump-probe measurements presented in this chapter show, this does not mean that a GaAs-based sample is not a good candidate for the study of the coupling between the electrons and the coherent phonons. It is, however, necessary to take into account the coupling constant of the electron-phonon interaction.

The experiments presented in this chapter have essentially been motivated by an interest in the interplay between different effects from the field of *optics*. However, the above-presented interpretation of the experimental results leads into the domain of *solid state physics*. A more detailed explanation and modeling of the relaxation processes and their influence on the refractive index require extensive knowledge of the electron dynamics in semiconductors, which is beyond the scope of the present PhD thesis. In a collaboration with Christos FLYTZANIS from the Laboratoire Pierre Aigrain de l'École Normale Supérieure de Paris, we have started to work on a more sophisticated model of the relaxation process, based on a random-walk with a trap (i.e., a preferred transition). Although this new model is still work in progress, it could be worthwhile to improve and include it in future studies and PhD theses on this exciting subject.

* * *

Chapter 5

Summary

The present PhD thesis addresses the central question how the localization of light affects certain optical nonlinearities in semiconductors. The focus has been on the effect of stimulated Raman scattering (SRS), which is a promising method for purely optical amplification and lasing in semiconductor materials.

For this purpose, several pump-probe experiments have been carried out to study experimentally two different types of light localization. In these experiments, a strong light beam (pump) excites the nonlinear optical effects in a suitably fabricated semiconductor sample, whose response to this excitation is then measured with another, weaker, light beam (probe).

The first type of light localization is the reduction of the group velocity of light pulses in a slow-mode nanowaveguide in silicon or, more precisely, in silicon-on-insulator (SOI). As has been shown in chapter 3, the Raman amplification that is experienced by a narrow-band probe beam undergoes a saturation effect for increasing pump intensities. This saturation of the Raman amplification corresponds to a steady decrease of the effective Raman gain for increasing pump intensities, which is caused by the fact that the pump wave experiences a spectral broadening that is induced by the Kerr effect and the free carrier refraction (FCR). It is important to note that the strength of the stimulated Raman scattering (SRS) and the other nonlinear effects, such as TPA, the Kerr effect and the free carrier effects, is *enhanced* because of the localization of the light in the nanowveguide.

An analytical model has been developed to describe the effective Raman gain for picosecond pump pulses, and it shows an excellent agreement with the experimental results and, further, allows for a determination of the Raman gain coefficient of silicon. The analytical model, however, does *not* address the question *how strong* the pump wave is broadened, i.e., it does not describe the origin of the self phase modulation. Moreover, it does not describe how certain *transient* phenomena (such as a chirp) affect the nonlinear effects. Thus, in order to obtain a better understanding of these aspects and find answers to these questions, it is necessary to extend the proposed model and carry out *numerical* simulations, which has been started in our working group in the context of another PhD thesis (Alexandre Baron).

Althought the experiments have studied a situation with only a weak localization, the obtained results are also applicable to much higher levels of localization (e.g., slow-mode waveguides, photonic crystal structures). This makes the present study very useful to develop highly integrated all-optical functions in silicon or SOI. However, one of the key results of the present study is the observation that the light localization induces an *intrinsic limitation* of the attainable Raman gain because it

affects not only SRS, but also the other nonlinear effects, and in case of FCR (fifth-order effect), this enhancement is even stronger than for SRS (third-order effect).

The second light localization type is the enhancement of the intensities of the involved light waves (pulses) in a semiconductor microcavity. In chapter 4, an experimental pump-probe study of this localization type is presented. As opposed to the case of a nanowaveguide (chapter 3), the light localization in a microcavity is generally very sensitive to variations of the phase of the light waves inside the resonator because of the resonance condition. Therefore, in order to estimate the influence of the different nonlinear optical effects, including those effects that affect the phase of the probe wave, an analytical model has been developed and applied to the case of a planar GaAs microcavity whose resonator is only five wavelengths long. The simulation results have clearly shown that the transmission of the cavity, and thus the intracavity intensity, of the probe pulses is strongly influenced by the two photon absorption and, more importantly, by a nonlinear phase shift that is induced by the Kerr effect and the free carrier refraction. Thus, although the latter effects do not directly affect the *intensity* of the probe wave, they have a high impact on the *localization* of the probe light in the microcavity. This impact is determined by the pump intensity and by the delay between probe and pump pulses.

Several series of pump-probe experiments have been carried out to measure the transmission of a real GaAs microcavity sample. Although the experimental results have *not* shown the expected signature of stimulated Raman scattering (SRS), which could be explained with an overestimation of the Raman gain coefficient of GaAs, a detailed analysis of the time dependence of the transmission (especially the long-term behavior) indicates that the electron relaxation dynamics in the GaAs layer of the microcavity is strongly influenced by amplified spontaneous Raman scattering. A hypothesis is presented that describes how a coherently excited population of Raman phonons interacts with the electrons in the conduction band through the polar crystal lattice of the GaAs semiconductor material. A new experiment has been developed to measure this highly populated phonon mode independently of the Stokes wave that is created in the microcavity through the Raman scattering.

These exciting results open the route to a totally unknown effect in the field of semiconductor physics, whose systematic modeling and experimental investigation have, unfortunately, been beyond the scope of the present PhD thesis. They may, however, lead the way for numerous interesting future studies and PhD theses. The next step towards a Raman microlaser would be to use doubly resonant microcavities in silicon (e.g., in ridge waveguides like the one presented in chapter 3). Such experiments would require an extremely high fabrication precision because it means that two waves (pulses) must be resonant in the mircocavity at the same time, while frequencies of the two waves have a difference of 15.6 THz with an absolute accuracy of 105 GHz (Raman linewidth). This corresponds to a relative accuracy of about 1%, which still represents a challenge for the fabrication.

Interestingly, with the interaction between electrons and phonons and its highly wavelength-sensitive influence on the transmission of the microcavity, it might be possible to design an (ultra-)fast Raman switch that uses the pump wavelength (instead of the pump intensity) to trigger the transition from open to closed.

In summary, the present PhD thesis can certainly be considered as a valuable contribution to the state-of-the-art knowledge in the fields of silicon photonics and all-optical information processing, two research domains that will, most probably, in the future become the "shoulders" on which the coming scientific challenges and technological developments are standing.

Classical derivation of stimulated Raman scattering

In this appendix, we present a classical derivation of the nonlinear polarization of stimulated Raman scattering (SRS). It includes all the steps from a simple harmonic oscillator model of a microscopic dipole to the final expression of the nonlinear polarization.

The result of this derivation illustrates very well the resonance nature of the Raman scattering, which is of vital importance for the interpretation of the experiments presented in chapter 3 because it is a key element of the model developed in section 3.1.

Classical harmonic oscillator with electromagnetic driver

As in the case of the *spontaneous* Raman scattering (see section 2.2.1), we can describe the *stimulated* Raman scattering with a simple classical model [36]. This description yields some valuable insight in the underlying processes and into the properties of the material constant describing the Raman scattering, the so-called Raman susceptibility.

We consider a microscopic dipole with an vibrational eigen-frequency Ω_{R}. The dipole can be described by the equation of motion of a driven harmonic oscillator of the form

$$\frac{\mathrm{d}^2}{\mathrm{d}t^2}\,q \,+\, 2\Gamma\frac{\mathrm{d}}{\mathrm{d}t}\,q \,+\, \Omega_{\mathrm{R}}^2\,q = \frac{F(t)}{m} \tag{A.1}$$

where q is the displacement of the oscillator from its equilibrium position, Γ is a damping constant, m is the mass of the oscillator, and $F(t)$ is a time-dependent driving force. The latter (i.e. the driving force) corresponds to the electromagnetic waves that are incident upon the dipole. It can be expressed as the gradient of the energy W that is necessary to set the oscillator in motion,

$$F(t) = \frac{\mathrm{d}W(t)}{\mathrm{d}q} \ . \tag{A.2}$$

This energy W, in turn, is given by

$$W(t) = \frac{1}{2}\,\langle p(z,t) \cdot E(z,t)\rangle \ , \tag{A.3}$$

where the angle brackets denote the time average of the scalar product of dipole moment and electric field strength. According to Eq. (2.10), we can express the

dipole moment of the dipole as

$$p(z,t) = \alpha(q)\,\vec{E}(z,t) \tag{A.4}$$

so that the energy W of the dipole oscillation becomes

$$W(t) = \frac{1}{2}\,\langle \alpha(q)\,E(z,t) \cdot E(z,t)\rangle = \frac{1}{2}\,\langle \alpha(q)\,E^2(z,t)\rangle \;. \tag{A.5}$$

The polarizability $\alpha(q)$ can be written as a Taylor series expansion according to Eq. (2.9) as

$$\alpha(q) = \alpha_0 + \left(\frac{\partial\alpha}{\partial q}\right)_0 q + \dots \;. \tag{A.6}$$

We insert Eqs. (A.5) and (A.6) into Eq. (A.2) and obtain an expression for the driving force of the harmonic oscillator (i.e., the dipole), given by

$$
\begin{aligned}
F(t) = \frac{\mathrm{d}W(t)}{\mathrm{d}q} &= \frac{1}{2}\left(\frac{\mathrm{d}}{\mathrm{d}q}\,\langle \alpha(q)\,E^2(z,t)\rangle\right) \\
&= \frac{1}{2}\left(\frac{\mathrm{d}}{\mathrm{d}q}\left[\alpha_0 + \left(\frac{\partial\alpha}{\partial q}\right)_0 q\right]\right)\langle E^2(z,t)\rangle \\
&= \frac{1}{2}\left(\frac{\partial\alpha}{\partial q}\right)_0 \langle E^2(z,t)\rangle \;.
\end{aligned}
\tag{A.7}
$$

Consider two incident laser beams with frequencies ω_P and ω_S. They can be described by their electric field strengths

$$
\begin{aligned}
E_P(z,t) &= A_P\,e^{i(k_P z - \omega_P t)} + A_P^*\,e^{-i(k_P z - \omega_P t)} = E_P + E_{\text{-}P} & (A.8a)\\
E_S(z,t) &= A_P\,e^{i(k_P z - \omega_P t)} + A_S^*\,e^{-i(k_S z - \omega_S t)} = E_S + E_{\text{-}S} & (A.8b)
\end{aligned}
$$

where we have introduced the notation $E_P = A_P\,e^{i(k_P z - \omega_P t)}$. Thus, the electric field can be expressed as the superposition of the two incident waves,

$$E(z,t) = E_P(z,t) + E_S(z,t)\;, \tag{A.9}$$

so that the square of the electric field in Eq. (A.7) becomes

$$
\begin{aligned}
E^2(z,t) &= \Big(E_P(z,t) + E_S(z,t)\Big)^2 = \Big(E_P + E_{\text{-}P} + E_S + E_{\text{-}S}\Big)^2 \\
&= E_P E_P + E_P E_{\text{-}P} + 2\,E_P E_S + \underline{2\,E_P E_{\text{-}S}} + E_S E_S + E_S E_{\text{-}S} + \underline{\text{c.c.}}\;.
\end{aligned}
$$

We are interested in the time-varying part at the beat frequency $\omega_P - \omega_S$, which is given by the underlined terms in the above equation. Thus, according to Eq. (A.7), the driving force is given by

$$F(t) = \left(\frac{\partial\alpha}{\partial q}\right)_0 \left[A_P\,A_S^*\,e^{i((k_P - k_S)z - (\omega_P - \omega_S)t)} + \text{c.c.}\right]\;. \tag{A.10}$$

By introducing the notation

$$K = k_P - k_S \qquad \text{and} \qquad \Omega = \omega_P - \omega_S\;, \tag{A.11}$$

we can simplify Eq. (A.10), yielding

$$F(t) = \left(\frac{\partial\alpha}{\partial q}\right)_0 \left[A_P\,A_S^*\,e^{i(Kz - \Omega t)} + \text{c.c.}\right]\;. \tag{A.12}$$

We insert Eq. (A.12) into the equation of motion (A.1) and obtain

$$\frac{\mathrm{d}^2}{\mathrm{d}t^2}\, q \,+\, 2\Gamma \frac{\mathrm{d}}{\mathrm{d}t}\, q \,+\, \Omega_\mathrm{R}^2\, q = \frac{1}{m}\left(\frac{\partial\alpha}{\partial q}\right)_0 \left[A_\mathrm{P}\, A_\mathrm{S}^*\, e^{i(Kz-\Omega t)} \,+\, \mathrm{c.c.}\right]. \qquad (A.13)$$

This is the equation of motion of a harmonic oscillator with a harmonic driver. As is well known from classical mechanics, the solutions to such a system are also harmonic functions with the same frequency as the driver. Therefore, we make the following ansatz for the displacement q of the oscillator (i.e., the dipole) :

$$q = q(\Omega)\, e^{i(Kz-\Omega t)} \,+\, \mathrm{c.c.}\,. \qquad (A.14)$$

By inserting Eq. (A.14) into Eq. (A.13), we obtain

$$-\Omega^2\, q(\Omega) - 2i\Omega\Gamma\, q(\Omega) + \Omega_\mathrm{R}^2\, q(\Omega) = \frac{1}{m}\left(\frac{\partial\alpha}{\partial q}\right)_0 A_\mathrm{P}\, A_\mathrm{S}^* \qquad (A.15)$$

and, thus, we find that the amplitude of the dipole vibration is given by

$$q(\Omega) = \frac{(1/m)\, (\partial\alpha/\partial q)_0}{\Omega_\mathrm{R}^2 - \Omega^2 - 2i\Omega\Gamma}\, A_\mathrm{P}\, A_\mathrm{S}^*\,. \qquad (A.16)$$

With Eqs. (A.14) and (A.16) we have found a solution to the equation of motion of our model oscillator, i.e., a single *microscopic* dipole.

Nonlinear polarization of stimulated Raman scattering

In order to describe a *macroscopic* medium such as a solid (e.g., a semiconductor crystal), we want to calculate the dipole moment per unit volume, or polarization P, of the medium. With the density N of dipoles, the polarization of the material is given by

$$
\begin{aligned}
P(z,t) \;=\;& N\, p(z,t) = N\, \alpha(z,t)\, E(z,t) \\[2mm]
=\;& N\left[\alpha_0 + \left(\frac{\partial\alpha}{\partial q}\right)_0 q(z,t)\right] E(z,t) \\[2mm]
=\;& N\left[\alpha_0 + \left(\frac{\partial\alpha}{\partial q}\right)_0 \left(q(\Omega)\, e^{i(Kz-\Omega t)} + \mathrm{c.c.}\right)\right] \\[2mm]
& \times \left[A_\mathrm{P}\, e^{i(k_\mathrm{P}z-\omega_\mathrm{P}t)} + A_\mathrm{S}\, e^{i(k_\mathrm{S}z-\omega_\mathrm{S}t)} + \mathrm{c.c.}\right] \qquad (A.17)
\end{aligned}
$$

where we have used Eqs. (A.4),(A.6), (A.10), and (A.14). This result can be physically interpreted as follows. The first factor (in square brackets) is the polarizability of the medium at the difference frequency $\Omega = \omega_\mathrm{P} - \omega_\mathrm{S}$. Therefore, it represents the response of the material to an applied light field, which is given by the second factor (the second pair of square brackets). Both factors together create a macroscopic diplole moment P, which is the source of another electromagnetic wave. Since we want to derive an expression for the stimulated Raman scattering (SRS), we are only interested in the Stokes components, i.e., in the frequency components that are oscillating at a frequency ω_S. By expanding all the parentheses in Eq. (A.17), we find two Stokes terms. The first one corresponds to the *linear* response of the material to the incident Stokes wave, given by

$$P_\mathrm{S}^\mathrm{L}(z,t) = N\, \alpha_0\, A_\mathrm{S}\, e^{i(k_\mathrm{S}z-\omega_\mathrm{S}t)} \,+\, \mathrm{c.c.}\,. \qquad (A.18)$$

The second Stokes term is the *nonlinear* response of the material, where the oscillating exponential functions of the polarizability and the electric field interact with one another. We obtain

$$
\begin{aligned}
P_{\mathrm{S}}^{\mathrm{NL}}(z,t) &= N\left(\frac{\partial \alpha}{\partial q}\right)_0 q^*(\Omega)\, e^{-i((k_{\mathrm{P}}-k_{\mathrm{S}})z-(\omega_{\mathrm{P}}-\omega_{\mathrm{S}})t)} A_{\mathrm{P}}\, e^{i(k_{\mathrm{P}}z-\omega_{\mathrm{P}}t)} \;+\; \mathrm{c.c.} \\
&= N\left(\frac{\partial \alpha}{\partial q}\right)_0 q^*(\Omega) A_{\mathrm{P}}\, e^{i(k_{\mathrm{S}}z-\omega_{\mathrm{S}}t)} \;+\; \mathrm{c.c.} \,,
\end{aligned}
\tag{A.19}
$$

which can also be expressed as

$$
P_{\mathrm{S}}^{\mathrm{NL}}(z,t) = P^{\mathrm{NL}}(\omega_{\mathrm{S}})\, e^{-i\omega_{\mathrm{S}}t} \;+\; \mathrm{c.c.}
\tag{A.20}
$$

with a complex amplitude given by

$$
P^{\mathrm{NL}}(\omega_{\mathrm{S}}) = N\left(\frac{\partial \alpha}{\partial q}\right)_0 q^*(\Omega) A_{\mathrm{P}}\, e^{ik_{\mathrm{S}}z} \,.
\tag{A.21}
$$

By inserting the expression (A.16) for $q(\Omega)$ into the above equation, we obtain

$$
P^{\mathrm{NL}}(\omega_{\mathrm{S}}) = \frac{(N/m)\,(\partial \alpha/\partial q)_0^2}{\Omega_{\mathrm{R}}^2 - \Omega^2 + 2i\Omega\Gamma}\, |A_{\mathrm{P}}|^2\, A_{\mathrm{S}}\, e^{ik_{\mathrm{S}}z} \,.
\tag{A.22}
$$

We now define the so-called **Raman susceptibility** as

$$
\chi_{\mathrm{R}}(\omega_{\mathrm{S}}) = \frac{1}{6\epsilon_0}\, \frac{(N/m)\,(\partial \alpha/\partial q)_0^2}{\Omega_{\mathrm{R}}^2 - \Omega^2 + 2i\Omega\Gamma} = \frac{Q_0}{\Omega_{\mathrm{R}}^2 - \Omega^2 + 2i\Omega\Gamma} \,,
\tag{A.23}
$$

where we have introduced $Q_0 = (N/6\, m\, \epsilon_0)\, (\partial \alpha/\partial q)_0^2 \in \mathbb{R}$ for the sake of convenience. Thus, the complex amplitude of the **nonlinear Stokes polarization** can then be written as

$$
P^{\mathrm{NL}}(\omega_{\mathrm{S}}) = 6\,\epsilon_0\, \chi_{\mathrm{R}}(\omega_{\mathrm{S}})\, |A_{\mathrm{P}}|^2\, A_{\mathrm{S}}\, e^{ik_{\mathrm{S}}z} \,.
\tag{A.24}
$$

The ϵ_0 in Eq. (A.24) has been introduced to keep the result of our simple classical model consistent with the physical meaning of a susceptibility as it has been introduced in section 2.1. The factor 6 is the so-called degeneracy factor, which is properly introduced and explained in section 2.1.3.

Equations (A.23) and (A.24) are the classical expressions describing the nonlinear polarization of stimulated Raman scattering (SRS). These expressions are needed to solve the nonlinear propagation equation (2.4). As mentioned in the introduction to this appendix, the classical derivation presented here shows very well the frequency dependence of the Raman susceptibility given by Eq. (A.23), which corresponds to a typical resonance function. For more details and a graphical illustration of the resonance curve, see section 2.2.2.

Appendix B

Transmission of a Fabry-Perot resonator with optical gain

In this appendix, we derive an equation describing the intensity transmission coefficient T of a Fabry-Perot resonator containing a gain medium (e.g., a Raman-active nonlinear material). The resulting formula can be considered as the general form of the widely known Airy function, describing the resonance behavior of an optical resonator.

Consider a Fabry-Perot resonator consisting of two planar mirrors with reflectivities r_1 and r_2 for the electric field strength E. The medium between the two mirrors has a refractive index n and provides an optical gain g for the electric field strength. A plane monochromatic electromagnetic wave

$$\vec{E} = A \exp\left\{ i\vec{k} \cdot \vec{r} - i\omega t \right\} \quad + \text{ c.c.} \tag{B.1}$$

is injected under an angle ϑ' into the resonator, where it propagates under an angle ϑ back and forth many times. The situation is illustrated in Figure B.1. The wave enters the resonator at point A, propagates to point B, is reflected to point C, where it is again reflected to point D, and so on and so forth. During the propagation, the wave experiences a phase shift and, because of the gain, a change of the field amplitude. Hence, after the propagation from point A to point B, the wave has the form

$$\vec{E} \quad \longrightarrow \quad \vec{E}' = \vec{E}\, e^{gl}\, e^{i\varphi} \;, \tag{B.2}$$
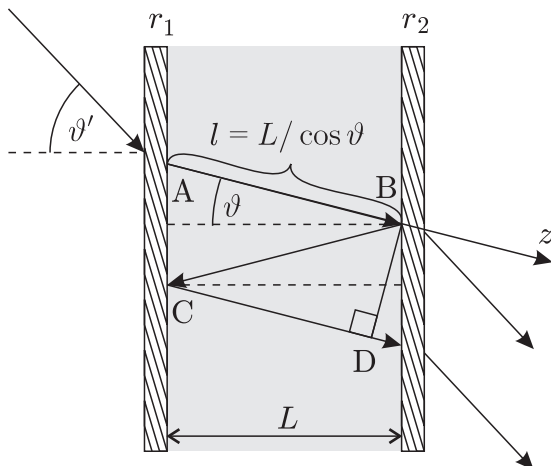

Fig. B.1. Propagation of an electromagnetic wave in a Fabry-Perot resonator containing a gain medium. The amplitude reflectivities of the mirrors are r_1 and r_2. The wave enters the resonator at point A, propagates to point B, is reflected to point C, where it is again reflected to point D, and so on and so forth. During the propagation the wave experiences a phase shift and, because of the gain, a change of the field amplitude. The z axis indicates the propagation direction inside the resonator.

where l is the effective path length,

$$l = L/\cos\vartheta \ , \tag{B.3}$$

and L is the distance between the two mirrors, i.e., the resonator length.

We consider the electric field strength of an incident electromagnetic wave $\vec{E}_\mathrm{i}$. Depending on the reflectivity r_1 of the first mirror, the incident field is partially reflected, $\vec{E}_\mathrm{r} = r_1 \vec{E}_\mathrm{i}$. Inside the resonator, we consider a forward propagating wave $\vec{E}_\mathrm{f}$ and a backward propagating wave $\vec{E}_\mathrm{b}$. The field strength that leaves the resonator through the second mirror is $\vec{E}_\mathrm{t}$. For the rest of this derivation we assume that the mirrors have no losses. Figure B.2 shows the different electric fields as a function of the position z along the propagation direction of the wave. We find an expression for the forward propagating electric field at $z = 0$, given by

$$
\begin{aligned}
\vec{E}_\mathrm{f}(0) &= t_1 \vec{E}_\mathrm{i} - r_1 \vec{E}_\mathrm{b}(0) \\
&= t_1 \vec{E}_\mathrm{i} - r_1 e^{gl} e^{i\varphi} \vec{E}_\mathrm{b}(l) \\
&= t_1 \vec{E}_\mathrm{i} + r_1 r_2 e^{gl} e^{i\varphi} \vec{E}_\mathrm{f}(l) \\
&= t_1 \vec{E}_\mathrm{i} + r_1 r_2 e^{gl} e^{i\varphi} e^{gl} e^{i\varphi} \vec{E}_\mathrm{f}(0) \\
&= t_1 \vec{E}_\mathrm{i} + r_1 r_2 e^{2gl} e^{2i\varphi} \vec{E}_\mathrm{f}(0) \ ,
\end{aligned}
$$

where the minus sign in the first and the second line is convention [49]. The above equation yields a relationship between the forward propagating electric field and the incident electric field,

$$t_1 \vec{E}_\mathrm{i} = \left(1 - r_1 r_2 \, e^{2gl} e^{2i\varphi}\right) \vec{E}_\mathrm{f}(0) \quad \Longrightarrow \quad \vec{E}_\mathrm{f}(0) = \frac{t_1}{\left(1 - r_1 r_2 \, e^{2gl} e^{2i\varphi}\right)} \, \vec{E}_\mathrm{i} \ ,$$

so that the transmitted electric field can be expressed as

$$\vec{E}_\mathrm{t} = t_2 \, \vec{E}_\mathrm{f}(l) = t_2 \, e^{gl} e^{i\varphi} \, \vec{E}_\mathrm{f}(0) = \frac{t_1 t_2 \, e^{gl} e^{i\varphi}}{\left(1 - r_1 r_2 \, e^{2gl} e^{2i\varphi}\right)} \, \vec{E}_\mathrm{i} \ .$$

Thus, by using the relationship between the intensity and the electric field strength of an electromagnetic wave, $I = 2nc\epsilon_0 |\vec{E}|^2$, we can express the intensity transmission of the resonator as

$$T = \frac{I_\mathrm{t}}{I_\mathrm{i}} = \frac{|\vec{E}_\mathrm{t}|^2}{|\vec{E}_\mathrm{i}|^2} = \frac{t_1^2 t_2^2 \, e^{2gl} \, |e^{2i\varphi}|^2}{\left|1 - r_1 r_2 \, e^{2gl} \, e^{2i\varphi}\right|^2} = \frac{T_1 T_2 \, e^{Gl}}{\left|1 - \sqrt{R_1}\sqrt{R_2} \, e^{Gl} \, e^{2i\varphi}\right|^2} \ , \tag{B.4}$$

where we have introduced the **intensity gain coefficient** $G = 2g$ (as opposed to the *amplitude* gain coefficient g) as well as the transmission and reflectivity coefficients

Fig. B.2. Self-consistency conditions of the electric fields in a Fabry-Perot resonator (with gain). The graph illustrates the relationship between the incident electric field $\vec{E}_\mathrm{i}$, the reflected field $\vec{E}_\mathrm{r}$, the forward and backward propagating intra-cavity fields $\vec{E}_\mathrm{f}$ and $\vec{E}_\mathrm{b}$, and the transmitted electric field $\vec{E}_\mathrm{t}$ as a function of the propagation along z.
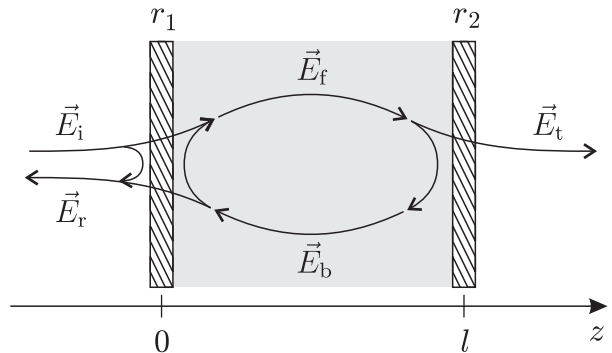
$T_1 = t_1^2$, $T_2 = t_2^2$, $R_1 = r_1^2$, and $R_2 = r_2^2$ for the intensity of the electromagnetic wave. The mirrors are assumed to be loss-free, which means that $T_1 + R_1 = 1$ and $T_2 + R_2 = 1$. We can thus express the **transmission of a resonator containing a gain medium** as a function of the intensity reflectivities as

$$T = \frac{(1 - R_1)(1 - R_2)\, e^{Gl}}{\left| 1 - \sqrt{R_1 R_2}\, e^{Gl}\, e^{2i\varphi} \right|^2} \,. \tag{B.5}$$

In the special case of a zero gain $G = 0$, we obtain

$$T = \frac{(1 - R_1)(1 - R_2)}{\left| 1 - \sqrt{R_1 R_2}\, e^{2i\varphi} \right|^2} \,. \tag{B.6}$$

The denominator of the above equation can also be expressed as

$$\begin{aligned}
\left| 1 - \sqrt{R_1 R_2}\, e^{2i\varphi} \right|^2 &= 1 + R_1 R_2 - 2\sqrt{R_1 R_2}\, \cos(2\varphi) \\
&= \left(1 - 2\sqrt{R_1 R_2} \right)^2 \left(1 + \frac{4}{\pi} \mathcal{F}^2 \sin^2(\varphi) \right),
\end{aligned} \tag{B.7}$$

where we have introduced the so-called **finesse** $\mathcal{F}$ of the resonator as

$$\mathcal{F} = \frac{\pi \sqrt[4]{R_1 R_2}}{1 - \sqrt{R_1 R_2}} \,. \tag{B.8}$$

$\mathcal{F}$

Thus, we can write Eq. (B.6) in the form of the so-called **Airy function** as

$$T = \frac{(1 - R_1)(1 - R_2)}{\left(1 - 2\sqrt{R_1 R_2} \right)^2 \left(1 + \frac{4}{\pi} \mathcal{F}^2 \sin^2(\varphi) \right)} = \frac{T_{\max}}{1 + \frac{4}{\pi} \mathcal{F}^2 \sin^2(\varphi)} \,, \tag{B.9}$$

which is characterized by the finesse $\mathcal{F}$ and the **maximum transmission** $T_{\max}$

$$T_{\max} = \frac{(1 - R_1)(1 - R_2)}{\left(1 - 2\sqrt{R_1 R_2} \right)^2} \,. \tag{B.10}$$

$T_{\max}$

In order to be resonant in the cavity, the electric fields at the points B and D in Fig. B.1 have to interfere constructively. As a geometrical derivation shows, the phase difference between the points B and D is given by

$$\delta = 2\, n\, L\, k \cos \vartheta \,.$$

This is the phase difference after one round trip in the resonator, which corresponds to 2φ. Therefore, we can express the phase of the electromagnetic wave after half a round trip, which is called the **Fabry-Perot phase**, as

$$\varphi_{\mathrm{FP}} = \frac{\delta}{2} = n\, L\, k \cos \vartheta = \frac{2\pi\, n\, L \cos \vartheta}{\lambda} \,. \tag{B.11}$$

φ_{FP}

At resonance, the electromagnetic wave has to satisfy the resonance condition

$$\delta = 2\pi\, m \quad \Longrightarrow \quad \varphi_{\mathrm{FP}} = \pi\, m \qquad \text{with} \quad m \in \mathbb{N} \,, \tag{B.12}$$

where m is called the **order of the resonance**. Hence, for a given order m, cavity length L, and refractive index n, the above equations (B.11) and (B.12) yield a

m

Fig. B.3. Resonant modes of a Fabry-Perot resonator in the frequency domain. The graph shows the first ten resonances. (i.e., the resonance orders $m = 1$ to $m = 10$). The resonances are characterized by the maximum transmission $T_{\max}$ and the spectral linewidth $\delta\nu_{1/2}$. They are separated by the so-called **free spectral range** $\Delta\nu_{\mathrm{FP}}$.
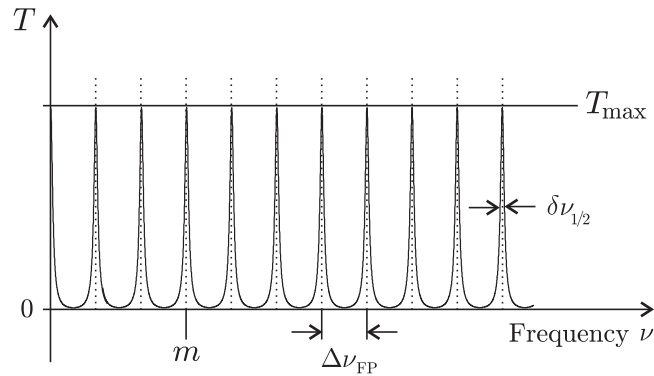
relationship between the angle of incidence ϑ and the resonance wavelength $\lambda = 2\pi/k$, which is given by

$$\lambda = \frac{2nL}{m}\cos\vartheta \; . \tag{B.13}$$

Since the cosine function is bounded ($\cos\varphi \leq 1$), there is for a given resonance order m a longest possible resonance wavelength, which corresponds to normal incidence ($\vartheta = 0$). All other resonant wavelengths are shorter.[1] Their angle of incidence is given by $\vartheta = \arccos(m\lambda/2nL)$.

As can be seen from Eq. (B.9), the Airy function has a periodicity of π, which is given by the periodicity of the $\sin^2$ function. Figure B.3 illustrates the Airy function and its periodicity as a function of the frequency $\nu = c/\lambda$. It also shows the key characteristics of the Fabry-Perot resonances, which are their linewidth $\delta\nu_{1/2}$ (FWHM), the maximum transmission $T_{\max}$, and the free spectral range $\Delta\nu_{\mathrm{FP}}$. The latter corresponds to the difference between two adjacent resonance frequencies. Without further proof, we state here that the ratio of the free spectral range and the linewidth is given by the finesse $\mathcal{F}$,

$$\mathcal{F} \;=\; \frac{\Delta\nu_{\mathrm{FP}}}{\delta\nu_{1/2}} \, , \tag{B.14}$$

which is therefore a measure of the "sharpness" of the resonance peaks.

Since the Airy function (which describes the transmission of the resonator), is periodic in π, it is often useful to approximate the Fabry-Perot phase φ_{FP} near the resonances by a Taylor series, yielding

$$\varphi_{\mathrm{FP}} \;\approx\; -\,\frac{2\pi nL}{\lambda^2}\,\Delta\lambda \, , \tag{B.15}$$

where $\Delta\lambda$ is the (small) wavelength detuning from the resonance wavelength given by Eq. (B.13). It should be noted that this expression is negative for a positive detuning $\Delta\lambda$, and vice versa.

---

[1] *Remark:* This result might contradict our intuitive expectation, since, because of the geometry, each individual beam in the resonator travels along an elongated path $l = L/\cos\vartheta$. Therefore one could be tempted to conclude that the resonance wavelength also increases with the angle of incidence. However, exactly the opposite occurs : Higher angles ϑ correspond to shorter resonance wavelengths λ. This property of the Fabry-Perot resonator can be used to make two beams with different wavelengths simultaneously resonant in the cavity by injecting them with two different angles of incidence. In chapter 4, we use this important result to obtain a **doubly resonant cavity**, in which the Stokes wave is at normal incidence whereas the pump wave propagates with an angle of incidence $\vartheta \neq 0$.

Bibliography

[1] DULKEITH, E., GRUNERT, K., AND VAN DER MERWE, S. From the Village Lane to the Highway. *Detecon Management Report 5*, 1 (2009).

[2] SOREF, R. A., AND LORENZO, J. P. All-silicon active and passive guided-wave components for 1.3 and 1.6 micrometer. *IEEE J. Quantum Electron. 22*, 6 (1986), 873–879.

[3] LIPSON, M. Guiding, modulating, and emitting light on silicon - Challenges and opportunities. *JOURNAL OF LIGHTWAVE TECHNOLOGY 23*, 12 (DEC 2005), 4222–4238.

[4] BOYRAZ, O., KOONATH, P., RAGHUNATHAN, V., AND JALALI, B. All optical switching and continuum generation in silicon waveguides. *Opt. Express 12* (2004), 4094–9102.

[5] JUGESSUR, A. S., POITTIER, P., AND DE LA RUE, R. M. Engineering the filter response of photonic crystal microcavitiy filters. *Opt. Express 12*, 7 (April 2004), 1304–1312.

[6] LIPSON, M. Switching of light on a silicon chip. *Opt. Mat. 27* (2005), 731–739.

[7] COCORULLO, C., IODICE, M., RENDINA, I., AND SARRO, P. M. Silicon thermo-optical micro-modulator with 700 kHz-3 dB bandwidth. *IEEE Photon. Technol. Lett. 4*, 363–365 (April 7).

[8] PRUESSNER, M. W., STIEVATER, T. H., FERRARO, M. S., AND RABI-NOVICH, W. S. Thermo-optic tuning and switching in SOI waveguide Fabry-Perot microcavities. *Opt. Express 15*, 12 (Jun 2007), 7557–7563.

[9] BARRIOS, C. A., ALMEIDA, V. R., PANEPUCCI, R., AND LIPSON, M. Electrooptic Modulation of Silicon-on-Insulator Submicrometer-Size Waveguide Devices. *Journal of Lightwave Technology 21*, 10 (Oct 2003), 2332–2339.

[10] SCHMIDT, B., XU, Q., SHAKYA, J., MANIPATRUNI, S., AND LIPSON, M. Compact electro-optic modulator on silicon-on-insulator substrates using cavities with ultra-small modal volumes. *Opt. Express 15*, 6 (March 2007), 3140–3148.

[11] GU, L., JIANG, W., CHEN, X., WANG, L., AND CHEN, R. T. High speed silicon photonic crystal waveguides modulator for low voltage operation. *Appl. Phys. Lett. 90* (2007), 071105.

[12] Jones, R., Liu, A., Rong, H., Paniccia, M., Cohen, O., and Hak, D. Lossless optical modulation in a silicon waveguide using stimulated Raman scattering. *Opt. Express 13*, 5 (MAR 7 2005), 1716–1723.

[13] Tanabe, T., Notomi, M., Mitsugi, S., Shinya, A., and Kuramochi, E. All-optical switches on a silicon chip realized using photonic crystal nanocavities. *Appl. Phys. Lett. 87* (2005), 151112.

[14] Tanabe, T., Notomi, M., Mitsugi, S., Shinya, A., and Kuramochi, E. Fast bistable all-optical switch and memory on a silicon photonic crystal on-chip. *Opt. Lett. 30*, 19 (2005), 2575–2577.

[15] Pavesi, L., Dal Negro, L., Mazzoleni, C., Franzo, G., and Priolo, F. Optical gain in silicon nanocrystals. *Nature 408* (2000), 440–444.

[16] Foster, M., Turner, A., Sharping, J., Schmidt, B., Lipson, M., and Gaeta, A. Broad-band optical parametric gain on a silicon photonic chip. *Nature 441*, 7096 (JUN 22 2006), 960–963.

[17] Liu, A., Rong, H., Jones, R., Cohen, O., Hak, D., and Paniccia, M. Optical Amplification and Lasing by Stimulated Raman Scattering in Silicon Waveguides. *Journal of Lightwave Technology 24*, 3 (2006), 1440–1455.

[18] Jalali, B., Raghunathan, V., Dimitropoulos, D., and Boyraz, O. Raman-based silicon photonics. *Selected Topics in Quantum Electronics, IEEE Journal of 12*, 3 (MAY-JUN 2006), 412–421.

[19] Frandsen, L. H., Lavrinenko, A. V., Fage-Pedersen, J., and Borel, P. I. Photonic crystal waveguides with semi-slow light and tailored dispersion properties. *Opt. Express 14*, 20 (2006), 9444–9450.

[20] Settle, M. D., Engelen, R. J. P., Salib, M., Michaeli, A., Kuipers, L., and Krauss, T. F. Flatband slow light in photonic crystals featuring spatial pulse compression and terahertz bandwidth. *Opt. Express 15*, 1 (2007), 219–226.

[21] Kubo, S., Mori, D., and Baba, T. Low-group-velocity and low-dispersion slow light in photonic crystal waveguides. *Opt. Lett. 32*, 20 (2007), 2981–2983.

[22] Li, J., White, T. P., O'Faolain, L., Gomez-Iglesias, A., and Krauss, T. F. Systematic design of flat band slow light in photonic crystal waveguides. *Opt. Express 16*, 9 (2008), 6227–6232.

[23] Broderick, N. G. R., Millar, P., Richardson, D. J., Aitchson, J. S., Rue, R. D. L., and Krauss, T. Spectral features associated with nonlinear pulse compression in Bragg gratings. *Opt. Lett. 25*, 10 (2000), 740–742.

[24] Razzari, L., Trager, D., Astic, M., Delaye, P., Frey, R., Roosen, G., and Andre, R. Kerr and four-wave mixing spectroscopy at the band edge of one-dimensional photonic crystals. *Applied Physics Letters 86*, 23 (2005), 231106.

[25] Roussey, M., Baida, F. I., and Bernal, M.-P. Experimental and theoretical observations of the slow-light effect on a tunable photonic crystal. *J. Opt. Soc. Am. B 24*, 6 (2007), 1416–1422.

[26] ASTIC, M., DELAYE, P., FREY, R., ROOSEN, G., ANDRÉ, R., BELABAS, N., SAGNES, I., AND RAJ, R. Time resolved nonlinear spectroscopy at the band edge of 1D photonic crystals. *Journal of Physics D: Applied Physics 41*, 22 (2008), 224005.

[27] KRAUSS, T. F. Slow light in photonic crystal waveguides. *Journal of Physics D: Applied Physics 40*, 9 (2007), 2666.

[28] BARON, A., RYASNYANSKIY, A., DUBREUIL, N., DELAYE, P., TRAN, Q. V., COMBRIÉ, S., DE ROSSI, A., FREY, R., AND ROOSEN, G. Light localization induced enhancement of third order nonlinearities in a GaAs photonic crystal waveguide. *Opt. Express 17*, 2 (2009), 552–557.

[29] MONAT, C., CORCORAN, B., EBNALI-HEIDARI, M., GRILLET, C., EGGLETON, B. J., WHITE, T. P., O'FAOLAIN, L., AND KRAUSS, T. F. Slow light enhancement of nonlinear effects in silicon engineered photonic crystal waveguides. *Opt. Express 17*, 4 (Feb 2009), 2944–2953.

[30] MONAT, C., CORCORAN, B., PUDO, D., EBNALI-HEIDARI, M., PELUSI, M. D., MOSS, D. J., EGGLETON, B. J., WHITE, T. P., O'FAOLAIN, L., AND KRAUSS, T. F. *Slow Light Enhanced Nonlinear Optics in Silicon Photonic Crystal Waveguides*, vol. 16. IEEE Journal of Selected Topics in Quantum Electronics, January/February 2010.

[31] SONG, B., NODA, S., ASANO, T., AND AKAHANE, Y. Ultra-high-Q photonic double heterostructure nanocavity. *Nature Mater. 4* (2005), 207.

[32] KURAMOCHI, E., NOTOMI, M., MITSUGI, S., SHINYA, A., TANABE, T., AND WATANABE, T. Ultrahigh-Q photonic crystal nanocavities realized by the local width modulation of a line defect. *Appl. Phys. Lett. 88*, 4 (2006), 041112.

[33] VELHA, P., PICARD, E., CHARVOLIN, T., HADJI, E., RODIER, J., LALANNE, P., AND PEYRADE, D. Ultra-High Q/V Fabry-Perot microcavity on SOI substrate. *Opt. Express 15*, 24 (2007), 16090–16096.

[34] WEIDNER, E., COMBRIE, S., TRAN, N.-V.-Q., ROSSI, A. D., NAGLE, J., CASSETTE, S., TALNEAU, A., AND BENISTY, H. Achievement of ultrahigh quality factors in GaAs photonic crystal membrane nanocavity. *Appl. Phys. Lett. 89*, 22 (2006), 221104.

[35] KIPPENBERG, T., SPILLANE, S., MIN, B., AND VAHALA, K. Theoretical and experimental study of stimulated and cascaded Raman scattering in ultrahigh-Q optical microcavities. *Selected Topics in Quantum Electronics, IEEE Journal of 10*, 5 (sep. 2004), 1219–1228.

[36] BOYD, R. W. *Nonlinear Optics*, 3rd ed. Academic Press, 2008.

[37] SUTHERLAND, R. L. *Handbook of Nonlinear Optics*, 2nd ed. Marcel Dekker, 2003.

[38] RAMAN, C. V., AND KRISHNAN, K. S. A New Type of Secondary Radiation. *Nature 121* (March 1928), 501–502.

[39] JALALI, B., CLAPS, R., DIMITROPOULOS, D., AND RAGHUNATHAN, V. *Silicon Photonics*, vol. 94 of *Topics in Applied Physics*. Springer, 2004, ch. 5.

[40] BLOEMBERGEN, N. The Stimulated Raman Effect. *American Journal of Physics 35*, 11 (1967), 989.

[41] Ralston, J. M., and Chang, R. K. Spontaneous Raman Scattering Efficiency and Stimulated Scattering in Silicon. *Phys. Rev. B 2*, 6 (Sep 1970), 1858–1862.

[42] Lin, Q., Painter, O. J., and Agrawal, G. P. Nonlinear optical phenomena in silicon waveguides: Modeling and applications. *Opt. Express 15*, 25 (DEC 10 2007), 16604–16644.

[43] Yin, L., and Agrawal, G. P. Impact of two-photon absorption on self-phase modulation in silicon waveguides. *Opt. Lett. 32*, 14 (July 2007), 2031–2033.

[44] Ulmer, T. G., Tan, R. K., Zhou, Z., Ralph, S. E., Kenan, R. P., and Verber, C. M. Two-photon absorption-induced self-phase modulation in GaAs-AlGaAs waveguides for surface-emitted second-harmonic generation. *Opt. Lett. 24*, 11 (June 1999), 756–758.

[45] Delaye, P. *Étude des non-linéarités photoréfractives dans les composés semi-isolants III-V et II-VI.* PhD thesis, Univerité de Paris-Sud, 1993.

[46] Meschede, D. *Optics, Light and Lasers.* Wiley-VCH, 2004.

[47] Flytzanis, C. *Quantum Electronics*, vol. I, part A. Academic Press, New York, 1975, ch. Theory of nonlinear optical susceptibilities.

[48] Frey, R., Delaye, P., and Roosen, G. *Third Order Optical Nonlinearities in Photonic Crystals.* Wiley-ISTE, 2006, ch. 6.

[49] Siegman, A. E. *Lasers.* Universtiy Science Books, 1986.

[50] Bogaerts, W., Baets, R., Dumon, P., Wiaux, V., Beckx, S., Taillaert, D., Luyssaert, B., Van Campenhout, J., Bienstman, P., and Van Thourhout, D. Nanophotonic Waveguides in Silicon-on-Insulator Fabricated With CMOS Technology. *J. Lightw. Technol. 23*, 1 (Jan 2005), 401–412.

[51] Claps, R., Dimitropoulos, D., Raghunathan, V., Han, Y., and Jalali, B. Observation of stimulated Raman amplification in silicon waveguides. *Opt. Express 11*, 15 (2003), 1731–1739.

[52] Boyraz, O., and Jalali, B. Demonstration of a silicon Raman laser. *Opt. Express 12*, 21 (2004), 5269–5273.

[53] Rong, H., Jones, R., Liu, A., Cohen, O., Hak, D., Fang, A., and Paniccia, M. A continuous-wave Raman silicon laser. *Nature 433*, 7027 (FEB 17 2005), 725–728.

[54] Rong, H., Xu, S., Kuo, Y.-H., Sih, V., Cohen, O., Raday, O., and Paniccia, M. Low-threshold continuous-wave Raman silicon laser. *Nature Photonics 1*, 4 (Apr 2007), 232–237.

[55] Claps, R., Raghunathan, V., Dimitropoulos, D., and Jalali, B. Influence of nonlinear absorption on Raman amplification in silicon waveguides. *Opt. Express 12*, 12 (Jun 2004), 2774–2780.

[56] Rong, H., Kuo, Y.-H., Xu, S., Liu, A., Jones, R., and Paniccia, M. Monolithic integrated Raman silicon laser. *Opt. Express 14*, 15 (Jul 2006), 6705–6712.

[57] DEKKER, R., USECHAK, N., FORST, M., AND DRIESSEN, A. Ultrafast nonlinear all-optical processes in silicon-on-insulator waveguides. *Journal of Physics D: Applied Physics 40*, 14 (JUL 21 2007), R249–R271.

[58] XU, Q., ALMEIDA, V., AND LIPSON, M. Time-resolved study of Raman gain in highly confined silicon-on-insulator waveguides. *Opt. Express 12*, 19 (2004), 4437–4442.

[59] LIU, A., RONG, H., PANICCIA, M., COHEN, O., AND HAK, D. Net optical gain in a low loss silicon-on-insulator waveguide by stimulated Raman scattering. *Opt. Express 12*, 18 (2004), 4261–4268.

[60] LIANG, T., AND TSANG, H. Efficient Raman amplification in silicon-on-insulator waveguides. *Appl. Phys. Lett. 85*, 16 (OCT 18 2004), 3343–3345.

[61] XU, Q., ALMEIDA, V. R., AND LIPSON, M. Demonstration of high Raman gain in a submicrometer-size silicon-on-insulatorwaveguide. *Opt. Lett. 30*, 1 (2005), 35–37.

[62] WRIGHT, N. M., THOMSON, D. J., LITVINENKO, K. L., HEADLEY, W. R., SMITH, A. J., KNIGHTS, A. P., DEANE, J. H. B., GARDES, F. Y., MASHANOVICH, G. Z., GWILLIAM, R., AND REED, G. T. Free carrier lifetime modification for silicon waveguide based devices. *Opt. Express 16*, 24 (2008), 19779–19784.

[63] TURNER-FOSTER, A. C., FOSTER, M. A., LEVY, J. S., POITRAS, C. B., SALEM, R., GAETA, A. L., AND LIPSON, M. Ultrashort free-carrier lifetime in low-loss silicon nanowaveguides. *Opt. Express 18*, 4 (2010), 3582–3591.

[64] MCMILLAN, J. F., YU, M., KWONG, D.-L., AND WONG, C. W. Enhanced Raman Scattering in Slow-Light Photonic Crystals for Chip-Scale Frequency Conversion and Optical Amplification. *Journal of Nanoscience and Nanotechnology 10*, 3, Sp. Iss. SI (MAR 2010), 2243–2247.

[65] MCMILLAN, J. F., YU, M., KWONG, D.-L., AND WONG, C. W. Observation of spontaneous Raman scattering in silicon slow-light photonic crystal waveguides. *Appl. Phys. Lett. 93*, 25 (2008), 251105.

[66] CHECOURY, X., KURDI, M. E., HAN, Z., AND BOUCAUD, P. Enhanced spontaneous Raman scattering in silicon photonic crystal waveguides on insulator. *Opt. Express 17*, 5 (2009), 3500–3507.

[67] TSANG, H. K., AND LIU, Y. Nonlinear optical properties of silicon waveguides. *Semiconductor Science and Technology 23*, 6 (2008), 064007.

[68] KROEGER, F., RYASNYANSKIY, A., BARON, A., DUBREUIL, N., DELAYE, P., FREY, R., ROOSEN, G., AND PEYRADE, D. Saturation of the Raman amplification by self-phase modulation in silicon nanowaveguides. *Appl. Phys. Lett. 96* (2010).

[69] TEMPLE, P. A., AND HATHAWAY, C. E. Multiphonon Raman spectrum of silicon. *Phys. Rev. B 7* (1973), 3685–3697.

[70] HART, T. R., AGGARWAL, R. L., AND LAX, B. Temperature dependence of Raman scattering in silicon. *Phys. Rev. B 1* (1970), 638–642.

[71] ZWICK, A., AND CARLES, R. Multiple-order Raman scattering in crystalline and amorphous silicon. *Phys. Rev. B 48* (1993), 6024–6032.

[72] DULKEITH, E., XIA, F., SCHARES, L., GREEN, W. M. J., AND VLASOV, Y. A. Group index and group velocity dispersion in silicon-on-insulator photonic wires. *Opt. Express 14*, 9 (May 2006), 3853–3863.

[73] AGRAWAL, G. P. *Nonlinear Fiber Optics*, 4th ed. Academic Press, 2007.

[74] VELHA, P., RODIER, J. C., LALANNE, P., HUGONIN, J. P., PEYRADE, D., PICARD, E., CHARVOLIN, T., AND HADJI, E. Ultracompact silicon-on-insulator ridge-waveguide mirrors with high reflectance. *Appl. Phys. Lett. 89*, 17 (2006), 171121.

[75] RYASNYANSKIY, A., DUBREUIL, N., DELAYE, P., FREY, R., AND ROOSEN, G. Fourier transformed picosecond synchonously pumped optical parametric oscillator without spectral filtering element. *Journal of the European Optical Society - Rapid Publications 3* (2008).

[76] VLASOV, Y. A., AND MCNAB, S. J. Losses in single-mode silicon-on-insulator strip waveguides and bends. *Opt. Express 12*, 8 (2004), 1622.

[77] BASS, M., Ed. *Handbook of Optics*, 2nd ed., vol. 2. McGraw-Hill, 1994.

[78] PINAULT, S. C., AND POTASEK, M. J. Frequency broadening by self-phase modulation in optical fibers. *J. Opt. Soc. Am. B 2*, 8 (1985), 1318–1319.

[79] PASSARO, V. M. N., AND DE LEONARDIS, F. Space-time modeling of Raman pulses in silicon-on-insulator optical waveguides. *Journal of Lightwave Technology 24*, 7 (JUL 2006), 2920–2931.

[80] DINU, M., QUOCHI, F., AND GARCIA, H. Third-order nonlinearities in silicon at telecom wavelengths. *Appl. Phys. Lett. 82*, 18 (May 2003), 2954–2956.

[81] BRISTOW, A. D., ROTENBERG, N., AND VAN DRIEL, H. M. Two-photon absorption and Kerr coefficients of silicon for 850-2200 nm. *Appl. Phys. Lett. 90* (2007), 191104.

[82] RAGHUNATHAN, V., BOYRAZ, O., AND JALALI, B. 20 dB on-off Raman amplification in silicon waveguides. In *2005 Conference on Lasers & Electro-Optics (CLEO), Vols 1-3* (2005), pp. 349–351. Conference on Lasers and Electro-Optics (CLEO), Baltimore, MD, MAY 22-27, 2005.

[83] BANDELOW, U., DEMIRCAN, A., AND KESTING, M. Simulation of Pulse Propagation in Nonlinear Optical Fibers. *WIAS Reports (Weierstrass Institute for Applied Analysis and Stochastics Berlin), ISSN 0946-8838 23* (2003).

[84] BARON, A., DUBREUIL, N., DELAYE, P., AND AGRAWAL, G. P. Raman amplification of optical pulses in silicon waveguides: impact of spectral broadening of pump pulses. *submitted*.

[85] ZHANG, Z., AND QIU, M. Small-volume waveguide-section high Q microcavities in 2D photonic crystal slabs. *Opt. Express 12*, 17 (AUG 23 2004), 3988–3995.

[86] RYU, H., NOTOMI, M., KIM, G., AND LEE, Y. High quality-factor whispering-gallery mode in the photonic crystal hexagonal disk cavity. *Opt. Express 12*, 8 (APR 19 2004), 1708–1719.

[87] AKAHANE, Y., ASANO, T., SONG, B., AND NODA, S. High-Q photonic nanocavity in a two-dimensional photonic crystal. *Nature 425*, 6961 (OCT 30 2003), 944–947.

[88] WEIDNER, E., COMBRIE, S., DE ROSSI, A., TRAN, N.-V.-Q., AND CASSETTE, S. Nonlinear and bistable behavior of an ultrahigh-Q GaAs photonic crystal nanocavity. *Appl. Phys. Lett. 90*, 10 (2007), 101118.

[89] TANAKA, Y., KAWASHIMA, H., IKEDA, N., SUGIMOTO, Y., KUWATSUKA, H., HASAMA, T., AND ISHIKAWA, H. Optical Bistable Operations in AlGaAs-Based Photonic Crystal Slab Microcavity at Telecommunication Wavelengths. *Photonics Technology Letters, IEEE 18*, 19 (oct.1, 2006), 1996 –1998.

[90] COMBRIÉ, S., ROSSI, A. D., TRAN, Q. V., AND BENISTY, H. GaAs photonic crystal cavity with ultrahigh Q: microwatt nonlinearity at 1.55 μm. *Opt. Lett. 33*, 16 (2008), 1908–1910.

[91] CAIRO, F., DE MARTINI, F., AND MURRA, D. QED-vacuum confinement of inelastic quantum scattering at optical frequencies: A new perspective in Raman spectroscopy. *Phys. Rev. Lett. 70*, 10 (Mar 1993), 1413–1416.

[92] SNOW, J. B., QIAN, S.-X., AND CHANG, R. K. Stimulated Raman scattering from individual water and ethanol droplets at morphology-dependent resonances. *Opt. Lett. 10*, 1 (1985), 37–39.

[93] BOYRAZ, O., AND JALALI, B. Demonstration of directly modulated silicon Raman laser. *Opt. Express 13*, 3 (FEB 7 2005), 796–800.

[94] RONG, H., LIU, A., JONES, R., COHEN, O., HAK, D., NICOLAESCU, R., FANG, A., AND PANICCIA, M. An all-silicon Raman laser. *Nature 433*, 7023 (JAN 20 2005), 292–294.

[95] JONES, R., RONG, H., LIU, A., FANG, A., PANICCIA, M., HAK, D., AND COHEN, O. Net continuous wave optical gain in a low loss silicon-on-insulator waveguide by stimulated Raman scattering. *Opt. Express 13*, 2 (JAN 24 2005), 519–525.

[96] FAINSTEIN, A., AND JUSSERAND, B. Phonons in semiconductor planar microcavities: A Raman scattering study. *Phys. Rev. B 54*, 16 (Oct 1996), 11505–11516.

[97] FAINSTEIN, A., JUSSERAND, B., AND THIERRYMIEG, V. Raman efficiency in a planar microcavity. *Phys. Rev. B 53*, 20 (MAY 15 1996), 13287–13290.

[98] FAINSTEIN, A., JUSSERAND, B., AND THIERRY-MIEG, V. Raman Scattering Enhancement by Optical Confinement in a Semiconductor Planar Microcavity. *Phys. Rev. Lett. 75*, 20 (Nov 1995), 3764–3767.

[99] YANG, X., AND WONG, C. W. Design of photonic band gap nanocavities for stimulated Raman amplification and lasing in monolithic silicon. *Opt. Express 13*, 12 (JUN 13 2005), 4723–4730.

[100] YANG, X., AND WONG, C. W. Coupled-mode theory for stimulated Raman scattering in high-Q/V-m silicon photonic band gap defect cavity lasers. *Opt. Express 15*, 8 (APR 16 2007), 4763–4780.

[101] CHECOURY, X., HAN, Z., AND BOUCAUD, P. Stimulated Raman scattering in silicon photonic crystal waveguides under continuous excitation. *Phys. Rev. B 82*, 4 (JUL 26 2010).

[102] MOORADIAN, A., AND WRIGHT, G. B. First order Raman effect in 3-V compounds. *Solid State Communications 4*, 9 (1966), 431–&.

[103] DELAYE, P., ASTIC, M., AND ROOSEN, G. Transfer-matrix modeling of four-wave mixing at the band edge of a one-dimensional photonic crystal. *Journal of the Optical Society of America B 22*, 11 (November 2005), 2494–2504.

[104] GRIMSDITCH, M. H., OLEGO, D., AND CARDONA, M. Absolute cross-section of 1st-order Raman Scattering in GaAs. *Phys. Rev. B 20*, 4 (1979), 1758–1761.

[105] VAN STRYLAND, E. W., WOODALL, M. A., VANHERZEELE, H., AND SOILEAU, M. J. Energy band-gap dependence of two-photon absorption. *Opt. Lett. 10*, 10 (1985), 490.

[106] HUTCHINGS, D. C., AND WHERRETT, B. S. Theory of the dispersion of ultrafast nonlinear refraction in zinc-blende semiconductors below the band edge. *Phys. Rev. B 50*, 7 (1994).

[107] SHEIK-BAHAE, M., HUTCHINGS, D. C., HAGAN, D. J., AND VAN STRYLAND, E. W. Dispersion of Bound Electronic Nonlinear Refraction in Solids. *IEEE Journal of Quantum Electronics 27*, 6 (1991).

[108] BANFI, G. B., GHIGLIAZZA, M., AND DI TRAPANI, P. Bandwidth and beam quality of barium borate parametric oscillator synchronously pumped by an active-passive modelocked Nd:YAG laser. *Opt. Comm. 89* (1992).

[109] HUANG, J. Y., ZHANG, J. Y., SHEN, Y. R., CHEN, C., AND WU, B. High-power, widely tunable, picosecond coherent source from optical parametric amplification in barium borate. *Appl. Phys. Lett. 57* (1990).

[110] LITTMAN, M. G., AND METCALF, H. J. Spectrally narrow pulsed Dye Laser without Beam Expander. *Applied Optics 17*, 14 (July 1978), 2224–2227.

[111] ODA, H., AND INOUE, K. Observation of Raman scattering in GaAs photonic-crystal slab waveguides. *Opt. Express 14*, 15 (JUL 24 2006), 6659–6667.